Zonal Jets and Shear: Transport Properties of Two-Dimensional Fluid Flows

Submitted by

Sam Durston

to the University of Exeter as a thesis for the degree of Doctor of Philosophy in Mathematics, July 2015.

This thesis is available for Library use on the understanding that it is copyright material and that no quotation from the thesis may be published without proper acknowledgement.

I certify that all material in this thesis which is not my own work has been identified and that no material has previously been submitted and approved for the award of a degree by this or any other University.

Sam Durston

Abstract

It is well known that instabilities in rotational flows, such as those found on planets or in the solar tachocline, lead to the formation of long-lived zonal jets. Pioneered by the work of Rhines, after whom the fundamental length scale of these jets is named [34], much work has been put into simulating these formations for various situations. These models are often motivated by applications such as the cloud bands of Jupiter, or the geophysical stratospheric polar night jet [15].

The exploration of a driven flow under rotational effects provides a fascinating subject for investigation. Many aspects of fluid behaviour can be observed; from the interaction of mean flows with small-scale turbulence, to the effects of wave-like motion and the transport of potential vorticity (PV). The gradient of PV produces anisotropic behaviour and an inverse energy cascade [46] forming zonal jets with properties governed by the nonlinearity of the system [40].

Starting on the basis of a simple two-dimensional β-plane system (incompressible Navier-Stokes) under the effects of a body force, we implement a shearing box coordinate system in order to study the competing effects of shear and rotation. We use this in combination with spectral methods to numerically simulate the flow. Following the work of Moffatt [25], we use the flux of a passive scalar field to calculate and compare the effective diffusivity of the system over a range of the parameter space. In particular, we investigate the effect shear has of disrupting the formation of β-plane jets, and the resulting modification to transport.

We use quasi-linear analysis to further explore these systems. In doing so, we establish important mechanisms bought about by key parameters. We extend the scope of our investigation to include general mean flows. We show relationships

between the mean flow and its feedback on the fluid, particularly regarding the perpetuation of zonal jets. We give important modifications to the flow bought about by frictional forces such as viscosity, and show the inherently complicated effect β has on the mean flow feedback.

We make an extension to the above work by looking at the corresponding magnetohydrodynamic system, investigating the effect of adding a magnetic field to a sheared/rotating flow. We find that the magnetic field disrupts β-plane jets, creating a resonance-like peak in transport, suppressing it when the field strength is increased. We discuss the three predominant quantities governing the feedback for an MHD flow analytically; the Reynolds stress, Lorentz force and magnetic flux. We find that the magnetic flux allows for interactions between the vorticity gradient and magnetic field which potentially allow for zonal features in the mean field; we observe these in our numerical simulations.

Acknowledgements

I would like to express my utmost gratitude to Prof. Andrew Gilbert for his continuous support, guidance and patience throughout this project. It has been a privilege to work with such an enthusiastic and gifted mathematician, whose hard work has helped me tremendously over the past four years.

I am profoundly grateful to my wife, Effie, for supporting my decision to pursue this degree. Without her, my ambitions would have little meaning. I also offer my thanks to my parents and siblings, for their unwavering love and encouragement, and for being such brilliant, inspiring people.

Lastly, I would like to give specific thanks to my Mum for bribing me to take the 11-plus, and to my Gran for giving me £5 for each commendation I subsequently earnt at school.

Contents

List of Figures

List of Tables

Chapter 1

Introduction

1.1 Geophysical and Astrophysical Fluid Dynamics

Zonal jets, persistent banded flows of alternating relative velocity, are ubiquitous in observations of large-scale fluid motion. They can be seen on the surfaces of the giant planets, of which the atmosphere of Jupiter has been subject of much recent investigation [39]. They also appear in a variety of geophysical flows, including the stratospheric polar vortex [15], and as the three zonal bands in the Antarctic circumpolar current [41]. Other astrophysical phenomena in which jets play a key role include the formation of accretion disks [2], and the generation of a dynamo mechanism by the solar tachocline [44]. These flows often consist of plasmas under the influence of strong magnetic fields, as is the case in nuclear tokamaks where plasma drift waves are associated with jet-like behaviour [49]. Indeed, any flow where there exist barriers to the transport of angular momentum, heat or chemical substances can be related to zonal jets. Note that these quantities can be subject to their own governing equations, and may feed back on the fluid, or remain a passive element in the flow [16].

Jets of this type generally occur in flows where strong rotation, often of a spherical body, is taking place. The Coriolis force leads to a gradient of vorticity across the latitudinal axis of the flow, the strength of which relates directly to the rate of rotation. Many of these flows exhibit little radial variation, and so it is common to take a two-dimensional approximation of the flow. Traditional two-dimensional turbulence is characterized by an inverse cascade of energy from small to large scales, however a background vorticity gradient introduces Rossby waves, which may disrupt the cascade and trigger the zonal flows [49]. It also selects a preferred direction in which waves propagate, and determines a characteristic length scale of motion in the system.

It is common to take a slice of the fluid, representing a region on the surface of the sphere, and assign a periodic Cartesian coordinate system. This is known as a β-plane model, where β refers to the coefficient of the background vorticity

gradient, corresponding to the strength of rotation [11]. Various forms of the governing equations have been explored, with a variety of additional effects which can be used to investigate jets in different phenomena.

The jets are known for their persistence across a wide range of potential vorticity supporting systems, for many different types of forcing. As such, their formation can likely be attributed to a fundamental dynamic mechanism common to each of these systems. However, despite their similarities, many differences also occur between individual experiments/observations of zonal flows. Key features of the flow, such as characteristic length and time scales, jet strength (typical velocities), position and stability all have the potential to vary across different simulations [35].

It is generally accepted that the length scale of the jets, or the spacing between them, is determined by the characteristic scale, the 'Rhines scale' given by $L_{Rh} = \sqrt{U/\beta}$, where U represents a typical velocity inside the jet [34]. Of the different quantities of the flow discussed above, this is probably the best understood, although modifications for specific cases have been discussed, e.g. [17]. However, the Rhines scale still only gives an order of magnitude estimate for the number of jets in a system, allowing for variation across different observations which may be linked to parameters other than U and β.

One approach to explaining the formation and existence of jets is to look at the distribution of potential vorticity (PV). Stirring the PV leads to the formation of 'vorticity staircases', idealised step-like structures which allow for jets to occur at regions with small gradients of PV, with strong mixing being present at the large gradients [26]. Dritschel and McIntyre propose that the mechanism behind this is 'Rossby wave elasticity', a positive feedback continuously regulating vertical transport in the centre of the jet. This is reported as being analagous to the Philips effect in stably stratified fluids with a background buoyancy gradient [15].

Without the background vorticity gradient, the investigation reverts to one of two-dimensional turbulence, a subject of continuing interest to the scientific community. These two types of behaviour, zonal jets and turbulence, are naturally connected due to their simultaneous occurence in many physical phenomena. As

such it is common to find methods and models with roots in turbulence modelling dispersed throughout the zonal jet literature. Studies of turbulence are typically concerned with the spectral transfer of energy across wavenumbers with well known -5/3 upscale and -3 downscale cascades having been established. The former refers to the transfer of energy to large-scale motion as vortices merge, while the latter gives the transfer of enstrophy to small scales and dissipation by viscous forces [45]. However, applying the same techniques to β-plane turbulence is not necessarily useful, due to the zonal mean component of the flow; the emphasis is shifted to properly understanding the transport processes in such a system [17].

Taking the approach of a two-dimensional β-plane framework, the PV is defined as $PV = \beta y + \omega$, where ω represents perturbations of vorticity to the background gradient. It is then possible to investigate the evolution of the vorticity perturbations, with the longitudinally averaged profile of ω providing important information about the formation of zonal flows. Roughly sinusoidal profiles of the vorticity perturbations will lead to a staircase-like structure of PV, with sharper profiles encouraging well defined jets.

Often the statistics of such a flow are of greater interest than the dynamics. Several authors have used this to formulate statistics based models, where a variety of statistical methods are used to solve a modified set of equations. This can include methods which separate large and small-scale behaviour, statistically evolving the small-scale flow, while integrating over the more important larger scales. Novel and interesting work has been done by Tobias et al., who use sets of cumulant equations to obtain entirely statistical results [42]. While not directly relevant to our planned investigations, we emphasize the importance of statistical observations in the results of this thesis.

In studies of turbulence, careful analytical work has often been used to support numerical calculations. Srinivasan and Young take this approach when investigating the onset of jet formation, caused by what they call 'zonostrophic instability' [40]. Taking a quasi-linear (QL) approach (ignoring the second order nonlinear terms, while retaining the first order corrections), they look at the second order

cumulant expansion of the QL equations and the corresponding linear stability problem. They compare this analysis with numerical results obtained from a geophysical model under the influence of both Ekman drag and hyperdiffusion; the Ekman drag is considered the main source of energy removal in the model, while the hyperdiffusion is used as a means to remove energy at small scales for numerical convenience. A 'narrow band' or ring body force (see section 4.7), delta-correlated in time, is implemented, the properties of which are made use of in the analysis. The authors explore the parameter plane made of the strength of the vorticity gradient, β, and the coefficient of Ekman drag.

The authors find that length scales of jets formed in the QL system are comparable to those in the full nonlinear system; this follows logically from Rhines' work [34]. They also offer important scaling laws relating the energy of the jets to the Ekman drag (which will be discussed later in this thesis). Their deterministic equation, while not yielding jets, does support the stability curve of the QL system. However, neither of these stability curves match that of the nonlinear system, implying that nonlinear interactions are critical to jet formation.

An interesting approach is taken by Haynes et al., who take a step back from traditional models (often following the two-dimensional turbulence approach), and look at a prescribed barrier flow subject to disruptions in two different cases; a kinematic and a dynamically consistent model [22]. The kinematic model consists of a relatively simple two-dimensional time dependent map, periodic in x and unbounded in y. The dynamically consistent model is an integration of the vorticity equation, with hyperdiffusion replacing traditional viscosity. The authors look at both two-dimensional turbulence ($\beta = 0$) and geophysical flows, but use different forms of body force for each case. For the former, they implement a topographic forcing (one which is carried by the flow, i.e. can be included in the vorticity term), whereas for the geophysical flow they opt for a simpler time-stochastic force. The use of topographic forcing is particularly interesting, and something that has not been widely covered in the literature.

The authors measure the time taken for particles to cross the 'last barrier'

in the flow, which can be correlated with the persistence and stability of jets in geophysical flows. After discussing the range of parameters at which the kinematic and dynamically consistent cases are valid for comparison, they find that in general the barriers in the dynamically consistent model tend to be stronger than those in the kinematic model. This supports the idea that the persistence of zonal jets in geophysical flows is a feature fundamentally rooted in the dynamics of the system.

1.2 Magnetohydrodynamics

Of the various motivations for exploring zonal jets mentioned previously, several include situations where the fluid is electrically conducting and in the presence of relatively strong magnetic fields. Such systems require the use of magnetohydrodynamic (MHD) equations for the evolution of both the flow and the magnetic field. Whereas β-plane systems allow the propagation of large-scale Rossby waves, the MHD system also allows for the existence of Alfvén waves, which act as a restoring force to the fluid, propagating along the magnetic field lines. The magnetic potential (which is to the magnetic field as a stream function is to the fluid velocity), while comparable to that of a passive scalar in its evolution, actively feeds back on the flow, typically acting to disrupt vortical motion via stretching (as will be seen in chapter 7).

On the topic of the solar tachocline, the theoretical region of possibly jet-like behaviour between the sun's radiate and convective zones, Tobias et al., implement an MHD version of the β-plane model in order to investigate how transport is modified by the magnetic field [44]. Using numerical simulations of the two-dimensional incompressible β-plane MHD equations (with standard viscosity), they discuss the effect of increasing the strength of the magnetic field on a system which, in the purely hydrodynamical (HD) case, contains strong zonal jets. The field acts to disrupt the jets, lowering their strength and reducing the flow to a turbulent state. The authors find that in general, the Maxwell stresses exerted on the flow by the magnetic field cancel the Reynolds stress (which for the HD case has an anti-frictional effect; see section 2.6), and establish a scaling law between the field strength and

magnetic diffusivity.

1.3 Shear Flows

When examining two-dimensional turbulence, the simplest extension mathematically is to a system with a linear background shear flow. This type of system has received less attention recently than other extensions (including those of the geophysical and magnetohydrodynamical variety) from the classical fluid dynamics community. Despite this, theories regarding large-scale background shear flows (linear or not) can be applied to a range of physical phenomena, including the transport of chemicals, heat and angular momentum, as well as the dissipation of magnetic fields [28].

Authors to have investigated the effect of shear on two-dimensional turbulent transport include Newton and Kim. In early results they found that under certain conditions resonances occur for time dependent shear flows, which encourage transport across the system [28]. The requirements and form of the resonance were found to be primarily dependent upon the correlation time of the oscillating shear flow, with no resonances occuring as the correlation time tended towards the zero limit. In more recent papers they have looked at time dependent shear flows, examining the evolution of such a shear flow and making comparisons between the flow's resultant structure and that of the zonal flows on the giant planets [31].

On the topic of simpler, time-independent shear flows, Newton and Kim investigate the turbulent diffusion (or *effective diffusivity*) of decaying passive scalar fields under the influence of two different types of background flow; a 'uniform' (linear) flow and a sinusoidal flow [30]. For each case, a ring forcing is implemented with two possible time scales; finite, or delta correlated. Using numerical simulations they establish scaling laws relating the turbulent diffusivity to the strength of the shear. Note, however, that these simulations make use of normal viscosity, albeit applied with different strengths to different modes; a type of hyperdiffusion. Using a mean field approach, another quasi-linear technique, they support their findings with analysis, after adopting a renormalization scheme to make the two

comparable.

Extending the system discussed above to one which supports a background magnetic field carried by an electrically conducting fluid, the authors investigate the effect of a sinusoidal shear flow on the turbulent dissipation rate of the field [29]. The numerical methods are similar to those given in the purely hydrodynamical investigation described above, although little analysis is given to support the results. A variety of cases are investigated, with the authors initially discussing the case of no shear, and relating the turbulent diffusivity to the strength of the background field via a power law. Following this they look at sheared 'kinematic' MHD, where the magnetic field does not feed back on the flow, essentially becoming a passive scalar. Lastly they investigate full sheared MHD, finding resonances which alleviate a general reduction in transport by the shear flow.

Shear plays a crucial role in the evolution of accretion disks, the thin (two-dimensional) circular regions of rotating unorganized matter drawn in by gravitational collapse taking place in the formation of stars [2]. Later in their life, gravity causes matter in the disk to clump together, forming planets and moons [23]. However, early in the disks formation matter is adequately dispersed such that it acts as a continuous fluid (with astronomically large length and time scales). A large amount of work has been done by the astrophysics community in mathematically modelling the flows theoretically found in these systems. Taking a two-dimensional slice of the rotating disk, it is reasonable to implement a periodic box with a background shear related to the total rotation of the disk [5]. Given that the length of the box along the axis of shear is relatively small compared to the radius of the disk, and that the (differential) rate of rotation is also small, one can assume that the background shear is linear across the box. Historically, numerically modelling fast shear flows has been difficult due to the strain put on the computation by the dynamics. However, novel methods have been researched with which one can track the flow from a frame of reference following the shear. The so called 'shearing box coordinate system' also allows the use of spectral methods in a system periodic with respect to the sheared coordinates (which is physically more logical than one

periodic with regards to regular Cartesian coordinates when a shear flow is present) [21]. This is a matter which we will implement and discuss at length in chapter 4.

This shearing box method has also been applied to geophysical flows. Chung and Matheou, for example, use these methods to investigate the effect of shear on stratified turbulence [10]. Using numerical simulations of the three-dimensional Boussinesq equations (validated by comparison to experimental wind tunnel results), they look at the 'flux gradient' relationships of the perturbations to the mean flow, and back up these results analytically using Monin-Obukhov similarity theory. Despite different physical motivations between their investigation and that of this thesis, their paper demonstrates how the shearing box coordinate system can be effective in researching geophysical phenomena.

1.4 Thesis Plan

In this thesis we aim to investigate the combined effects of a background shear flow, vorticity gradient and magnetic field on two-dimensional turbulence. Drawing on the work of several of the authors mentioned in this introduction, we plan to use direct numerical simulations (DNS) to demonstrate the dynamics of these systems for a variety of individual parameter choices, while covering the parameter regime more comprehensively with a statistical description of the flow. We also aim to use quasi-linear methods to provide an analytical perspective which can be compared to the results of the DNS. Throughout the thesis we will emphasize the issues regarding transport in the flow, with the vertical (y-directional) flux of several quantities playing a key role. A break down of the thesis in more detail is as follows.

In chapter 2 we take a quasi-linear approach to the evolution of a flow on a β-plane with general background mean flow, $U(y)$, subject to Ekman drag and/or viscosity. We investigate several forms of $U(y)$, as well as different values for the coefficients of the vorticity gradient, drag and viscosity. Note that it is well known, due to the Orr-mechanism, that transport in an inviscid freely decaying flow is uneffected by shear flows of the form $U(y) = \alpha y$ (with constant α). We consider

both large-scale and short-time expansions of the governing equations, and focus on the feedback of the flow on to the mean via Reynolds stresses. We also look at turning points in the mean flow with regard to the parameter β in more detail.

We make an extension to this work in chapter 3, where we discuss the equivalent quasi-linear approximation to the MHD β-plane system. This introduces additional feedbacks to both the large-scale flow and magnetic field in the form of Lorentz force and magnetic stresses. Including a magnetic field makes analysis of this problem much more complicated, and as such we only investigate the short-time expansion of the quasi-linear MHD equations, as well as briefly discussing the feedback on the evolution of the magnetic field by a linear shear flow.

In chapter 4 we discuss the nonlinear two-dimensional β-plane system under the influence of a linear background shear, $U(y) = \alpha y$, and viscosity, dropping the Ekman drag. We put energy into the system by a body force which, in spectral space, takes the form of a ring and follows the shear. Energy is removed from the system via a combination of the viscosity and the shear-diffuse mechanism. We look at the vertical flux of a passive scalar field carried by the flow, which can be used to give the effective diffusivity of the system. We describe the discretization of the governing equations and the implementation of the shearing box coordinate system in a numerical model of the flow. Rather than attempt to run a small number of high powered simulations at very large Reynolds number, we instead make it our aim to run a vast ensemble of simulations in order to gain well established statistical results regarding the fluid system.

Following this, we discuss the results of our numerical simulations in chapter 5. We start with a system with no shear, and vary β in order to investigate the occurence and characteristics of β-plane jets. We establish a scaling law relationship between transport of a passive scalar and the strength of the vorticity gradient, while paying close attention to the behaviour of the flow at the small β limit. We then look at the effect the shear flow has on forced two-dimensional turbulence without the background vorticity gradient. Lastly, we look at what happens when we apply shear (at varying levels) to a β-plane system, and how the shear can

disrupt the formation of zonal flows.

In chapter 6 we look at the magnetohydrodynamic extension to the purely hydrodynamic problem posed in chapter 4. We discuss the flux of the various quantities relevant to the MHD system (which can be compared to those in chapter 3), noting that the passive scalar and magnetic fluxes are equivalent under certain conditions. We set up the numerical scheme and look at the non-dimensionalization of the governing equations.

Similarly to chapter 5, we look at the results of our MHD simulations in chapter 7. The emphasis moves to the strength of the background magnetic field, which we vary across a variety of sheared β-plane systems. We start by looking at the effect the field has on two-dimensional turbulence, before adding a shear flow for more complicated behaviour. With a vorticity gradient, we observe the influence the magnetic field has on a jet-supporting system.

Lastly, we present a summary of the results of the thesis in chapter 8, the conclusion. We compare and contrast the different scaling laws and behaviours found in each chapter, and refer to results from other works in the literature. We make comment on the applications and relevance of our results, and discuss future investigations and projects that might come about from this work.

Chapter 2

Quasi-linear Analysis

2.1 Introduction

In this chapter we introduce the quasi-linear equations describing a flow subject to a background vorticity gradient and frictional forces. In the process, we separate the mean flow from perturbations to it, and look at the effect of launching waves on this background flow. In particular, we look at the feedback the perturbations have on the mean flow via the vertical flux of vorticity.

We first look at a linear shear flow, which doesn't produce any flux, and hence has zero feedback on the mean. We then look at a large-scale expansion, that is, we investigate the case of launching small-scale waves on a large-scale background flow. We establish the general form in which the mean flow feeds back on itself, noting that complicated behaviour occurs at points where the gradient of the mean velocity, U(y), is zero. We then look at the effect of introducing certain features to the flow, including drag, viscosity and a vorticity gradient. The latter results in particularly complicated fluxes, which we aim to more thoroughly investigate later in the chapter.

To explore the turning points of the mean flow in more detail, we look at flows quadratic in form, again rescaling the quasi-linear governing equations. Going back to the original quasi-linear equation, we then implement a short-time expansion in order to investigate the vorticity gradient further. From this, we gain further insight into the complications of the feedback, and also on the sometimes anti-frictional dynamics of the standard flow.

2.2 Governing Equations

An incompressible, two-dimensional, viscously decaying fluid on a β-plane, as found in [45], with the added effect of a frictional bottom drag, can be described by the following equation:

$$\partial_t \Omega = J(\Psi, \Omega) + \beta \partial_x \Psi - \lambda \Omega + \nu \nabla^2 \Omega, \tag{2.1}$$

where $\Omega(x, y, t)$ is the normal component of the fluid vorticity, $\Psi(x, y, t)$ is the corresponding stream function, β is the gradient of the Coriolis force and λ is the

coefficient of drag. The fluid viscosity, ν, can be thought of as an inverse Reynolds number, $\mathrm{Re} = UL\nu^{-1}$, with U and L representing typical velocities and length scales of the system respectively. The determinant of the Jacobian of Ψ and Ω is given by

$$J(\Psi,\Omega) = (\partial_x\Psi)(\partial_y\Omega) - (\partial_y\Psi)(\partial_x\Omega), \tag{2.2}$$

and the vorticity is related to the stream function by

$$\Omega = -\nabla^2\Psi = -\left(\partial_x^2\Psi + \partial_y^2\Psi\right). \tag{2.3}$$

The components of the fluid velocity are related to the stream function by

$$\mathbf{u} = (\partial_y\Psi, -\partial_x\Psi). \tag{2.4}$$

The inherent nonlinearity of equation (2.1) leads to difficulty in solving and analysing it. However, as we are interested in the effect of large-scale background flows on the statistics of the fluid, we can make a quasi-linear approximation; we include nonlinear effects involving large-scale flows, but ignore the smallest scale nonlinear interactions, often called eddy-eddy interactions [40].

We start by splitting our variables into separate parts; contributions from the mean flow and the perturbations about it. We write

$$\Omega(x,y,t) = \widetilde{\Omega}(x,y,t) + \bar{\Omega}(y,t) = \widetilde{\Omega}(x,y,t) - \partial_y U(y,t), \tag{2.5}$$

$$\partial_y\Psi(x,y,t) = \partial_y\widetilde{\Psi}(x,y,t) + \partial_y\bar{\Psi}(y,t) = \partial_y\widetilde{\Psi}(x,y,t) + U(y,t), \tag{2.6}$$

where we take the barred quantities to be the x-averaged profiles of their respective variables, for example

$$\bar{\Omega}(y,t) \equiv \langle\Omega(x,y,t)\rangle_x. \tag{2.7}$$

Likewise, the vorticity perturbations are related to the stream function perturbations by $\widetilde{\Omega} = -\nabla^2\widetilde{\Psi}$. From now on, we choose to work with the variable $U(y,t)$, the mean profile of the velocity of our fluid. The β-plane vorticity equation becomes

$$\begin{aligned}\partial_t\left(\widetilde{\Omega} - \partial_y U\right) = {} & J\left(\widetilde{\Psi},\widetilde{\Omega}\right) - \partial_y^2 U\partial_x\tilde{\Psi} - U\partial_x\widetilde{\Omega} + \beta\partial_x\widetilde{\Psi} \\ & - \lambda\left(\widetilde{\Omega} - \partial_y U\right) + \nu\nabla^2\widetilde{\Omega} - \nu\partial_y^3 U,\end{aligned} \tag{2.8}$$

where the Jacobian term is defined as in (2.2).

We now assume that solutions to equation (2.8) are spatially wave-like in the horizontal direction:

$$\widetilde{\Omega}(x,y,t) = \omega(y,t)e^{imx} + c.c., \tag{2.9}$$

$$\widetilde{\Psi}(x,y,t) = \psi(y,t)e^{imx} + c.c., \tag{2.10}$$

where *c.c.* refers to the complex conjugate of the preceding terms. Note that while the above only represents a single wave, we can sum such contributions over a range of m-values to represent a general fluid system. While applying this to our previous equations, and equating powers of e^{imx}, we neglect the contributions from e^{2imx} and the corresponding complex conjugate parts, hence the label 'quasi-linear'. This leaves three equations (truncated to two), the first giving the evolution of the mean from the e^0 terms

$$\partial_t \partial_y U = -im\partial_y \left(\psi\omega^\star - \psi^\star\omega\right) - \lambda\partial_y U + \nu\partial_y^3 U, \tag{2.11}$$

where * represents the complex conjugate of the corresponding variable. The second equation, obtained by equating the e^{imx} terms, governs the perturbations:

$$\partial_t\omega + imU\omega = im\left(\beta - \partial_y^2 U\right)\psi - \lambda\omega - \nu\left(m^2 - \partial_y^2\right)\omega. \tag{2.12}$$

As mentioned, the third equation, taken from the e^{-imx} terms, gives us no new information about the flow as it is equivalent to equation (2.12).

We introduce a new quantity, F, which we define as being the x-averaged flux of vorticity (compare (2.11)):

$$F(y,t) = \langle v\omega\rangle_x = im\left(\omega\psi^\star - \omega^\star\psi\right). \tag{2.13}$$

As the name implies, F describes the vertical exchange of vorticity throughout the fluid profile (i.e. across y). However, it is worth noting that unlike the vertical flux of a passive-scalar quantity, such as temperature, or the concentration of a dye, the vorticity has a feedback on how it is distributed.

Rewriting equation (2.11) in terms of the mean part of the vorticity and the flux, whilst assuming the fluid is inviscid with no drag ($\nu = \lambda = 0$) gives

$$\partial_t\bar{\Omega} + \partial_y F = 0, \tag{2.14}$$

which can also be written as $\partial_t \partial_y U = \partial_y F$. We expect the evolution of the mean profile of vorticity to depend on the gradients of the vorticity flux, or more generally the vertical transport properties of the flow.

It is worth looking into this feedback in more detail. In particular, we can compare the above equation (2.14) to that of the diffusion equation for a general quantity, such as a passive scalar field, θ:

$$\partial_t \theta = \nabla \cdot (\kappa \nabla \theta) \,, \tag{2.15}$$

where κ is the coefficient of diffusivity, and $\kappa > 0$ corresponds to diffusive behaviour, whereas $\kappa < 0$ corresponds to anti-diffusive behaviour. If we restrict θ to depend only on y and t, and κ to be constant, this reduces to

$$\partial_t \theta = \partial_y \left(\kappa \partial_y \theta\right). \tag{2.16}$$

For comparison, we can write (2.14) as

$$\partial_t U' = \partial_y \left(\left(\frac{F}{U''} \right) U'' \right), \tag{2.17}$$

where for simplicity of notation, we have set $U' \equiv \partial_y U$. By comparison with equation (2.16), we can see that the diffusive or anti-diffusive behaviour of the fluid is determined by the sign of F/U'', with

$$\begin{aligned} &\frac{F}{U''} > 0 \Rightarrow \text{diffusive}, \\ &\frac{F}{U''} < 0 \Rightarrow \text{anti-diffusive}. \end{aligned} \tag{2.18}$$

Note that we anticipate that F/U'' will generally be dependent on y and t, and so regions of the flow will exhibit different types of diffusive behaviour as they evolve over time.

An alternate way of looking at the effect of the flux on the mean flow is to integrate equation (2.17) with respect to y. This gives

$$\partial_t U = F \tag{2.19}$$

If we define the time-integrated flux, $\mathcal{F}$ as

$$\mathcal{F}(y,t) = \int_0^t F(y,t) dt, \tag{2.20}$$

we can then take a linear approximation to the integration of equation (2.19), which gives

$$U(y,t) = U(y,0) + \mathcal{F}(y,t). \tag{2.21}$$

As such, we can see the key role the flux (and its time-integral) play in the evolution of the mean flow. For future reference, we also define

$$\mathcal{F}_\infty(y) \equiv \mathcal{F}(y, t \to \infty) = \int_0^\infty F(y,t)dt. \tag{2.22}$$

We now prescribe the background mean flow to be quasi-steady in time, i.e. varying slowly in time relative to the short time scales of the waves in the flow. Then $U = U(y)$, and the stream function relation

$$\omega = \left(m^2 - \partial_y^2\right)\psi, \tag{2.23}$$

along with equation (2.12) give a set of two, spatially one-dimensional partial differential equations. Essentially, we aim to calculate the waves carried by the flow using equations (2.12) and (2.23), find the flux by solving equation (2.13) and then analyze the feedback via the flux using (2.18 – 2.22).

We look for solutions to a particularly simplified form of equation (2.12), which we then use with the full equation in order to pull out individual effects. First, we take the fluid to be inviscid and ignore terms involving ψ, that is assume $\beta = U'' = \nu = 0$:

$$\partial_t\omega + imU\omega = -\lambda\omega. \tag{2.24}$$

Note that the condition $U'' = 0$ implies that we have a linear shear flow, a case which we will look at in more detail in the next section. Solutions to equation (2.24) are given by

$$\omega = e^{-imUt-\lambda t}. \tag{2.25}$$

To remove the fast advection and bottom drag terms from (2.12) (whilst also modifying the stream function relation), we use this solution and write

$$\omega(y,t) = \zeta(y,t)e^{-imUt-\lambda t}, \tag{2.26}$$

$$\psi(y,t) = \phi(y,t)e^{-imUt-\lambda t}, \tag{2.27}$$

which is akin to taking a local Galilean transformation following the shear. We can then calculate the derivatives of ω and ψ as:

$$\partial_t \omega = \left[\partial_t \zeta - (imU + \lambda)\,\zeta\right] e^{-imUt-\lambda t}, \tag{2.28}$$

$$\partial_y \omega = [\partial_y \zeta - imU' t\zeta] e^{-imUt-\lambda t}, \tag{2.29}$$

$$\partial_y^2 \omega = [\partial_y^2 \zeta - imt\,(2U'\partial_y \zeta + U''\zeta) - m^2 U'^2 t^2] e^{-imUt-\lambda t}, \tag{2.30}$$

etc. This gives the following governing equations:

$$\partial_t \zeta = im(\beta - U'')\phi - \nu\mathcal{L}(\zeta), \tag{2.31}$$

$$\zeta = \mathcal{L}(\phi), \tag{2.32}$$

$$\mathcal{L}(\phi) \equiv m^2(1 + U'^2 t^2)\phi + imt\,(U''\phi + 2U'\partial_y \phi) - \partial_y^2 \phi, \tag{2.33}$$

Here, $\mathcal{L}$ is an operator corresponding to the stream function relation between ζ and ψ, or in other words a negative Laplacian taking into account the effect of the removal of the advection and drag terms from the flow.

The flux can be written in terms of the new variables as

$$F(y,t) = im\,(\zeta\phi^\star - \zeta^\star\phi)\, e^{-2\lambda t}. \tag{2.34}$$

We observe that fast-advection terms have no influence on the flux, while drag introduces exponential decay on the time-scale $\mathcal{T}_\lambda \sim 1/\lambda$.

Using the relationship between ζ and ϕ as given in equations (2.32) and (2.33), we can write the flux in terms of $\phi(y,t)$ alone:

$$F = -\left[2m^2 t\partial_y\left(U'|\phi|^2\right) + im\left(\phi^\star\partial_y^2\phi - \phi\partial_y^2\phi^\star\right)\right] e^{-2\lambda t}. \tag{2.35}$$

Further progress on the flux cannot be made without looking for solutions to the system of equations given by (2.31 – 2.33). We aim to do this for various different cases and parameters throughout this chapter.

2.3 Linear Shear and the Orr Mechanism

The form of the background mean flow, $U(y)$, will clearly have strong influence on the flux, and hence the feedback on itself. Although we will look at solutions to the

flux for a general $U(y)$, it is helpful to first look at the simplest non-trivial case; $U(y) = \alpha y$, with constant α.

Given an initially constant initial condition such as $\omega(y, 0) = 1$, we expect a frictionless flow ($\lambda = \nu = 0$) to evolve identically at all points in the y-domain, with only a difference in phase which can be removed from the equations via a Galilean transformation, as taken in (2.26 – 2.27). As such, we can assume that ζ and ϕ are independent of vertical position:

$$\omega(y, t) = \zeta(t)e^{-im\alpha yt}, \tag{2.36}$$

$$\psi(y, t) = \phi(t)e^{-im\alpha yt}, \tag{2.37}$$

which allows us to rewrite equations (2.12) and (2.23) as

$$\partial_t \zeta = im\beta\phi, \tag{2.38}$$

$$\zeta = m^2 \left(1 + \alpha^2 t^2\right) \phi, \tag{2.39}$$

with the initial condition $\zeta(0) = 1$. We can rewrite this as a single equation in ζ:

$$\partial_t \zeta = \frac{im^{-1}\beta}{1 + \alpha^2 t^2}\zeta, \tag{2.40}$$

which is solved by

$$\zeta(t) = e^{(i\beta/m\alpha)\tan^{-1}(\alpha t)}, \tag{2.41}$$

$$\phi(t) = m^{-2} \left(1 + \alpha^2 t^2\right)^{-1} e^{(i\beta/m\alpha)\tan^{-1}(\alpha t)}. \tag{2.42}$$

As in the previous section, the fast-advection terms provide no contribution to the vorticity flux, and so in the absence of bottom drag we have

$$F(y, t) = im \left(\zeta\phi^\star - \zeta^\star\phi\right) e^{-2\lambda t}, \tag{2.43}$$

as found in equation (2.34).

Substituting ζ and ϕ from equations (2.41) and (2.42) into (2.43) gives a key result; that the flux is identically zero for all y and t for a linear background flow. This is not an orginal result; the fact that shear flows produce no feedback on themselves comes from the Orr mechanism, which gives that waves on an inviscid shear flow are continuously tipped over without becoming distorted [32].

Despite being primarily concerned with the y-directional structure of the fluid in this chapter, it is worth briefly discussing the x-directional properties of the flow for this particular simplified case. A single mode of a flow dependent on both x and y directions, as described in equation (2.1), subject to a linear background shear flow (and no background vorticity gradient, $\beta = 0$), can be written in the following form:

$$\Omega(x, y, t) = \zeta(t)e^{imx+iny-im\alpha yt} \tag{2.44}$$

$$= \zeta(t)e^{im(x-\alpha yt)+iny}. \tag{2.45}$$

In the x-direction (taking constant y), we see that the effect of the shear on the waves is that they are translated by $-\alpha yt$. Note that this shift is time-dependent, and as expected the waves will, at different levels of y, be sheared over time.

The results of this section are connected to formulations and results found in chapters 4 and 5. In particular, in section 4.3 we show that the spatial average of vorticity flux of a nonlinear shear flow (subject to viscosity and a vorticity gradient) is zero in a periodic system.

2.4 Large-scale Expansion

We rescale the entire system by introducing the parameter ε:

$$Y = \varepsilon y,\ T = \varepsilon t,$$

$$\tilde{U}(Y) = U(y),\ \tilde{\zeta}(Y, T) = \zeta(y, t),\ \tilde{\phi}(Y, T) = \phi(y, t). \tag{2.46}$$

and write $\partial_Y \left(\tilde{U}(Y, T)\right) \equiv \tilde{U}'$, etc. Omitting the tildes from the appropriate variables, equations (2.31 – 2.33) become:

$$\varepsilon\partial_T\zeta = im(\beta - \varepsilon^2 U'')\phi - \nu\mathcal{L}(\zeta), \tag{2.47}$$

$$\zeta = \mathcal{L}(\phi), \tag{2.48}$$

$$\mathcal{L}(\phi) \equiv m^2(1 + U'^2T^2)\phi + \varepsilon imT\left(U''\phi + 2U'\phi'\right) - \varepsilon^2\phi'', \tag{2.49}$$

where $\partial_Y\phi(Y, T) \equiv \phi'$, etc. Note the change in the operator $\mathcal{L}$ from its previous definition in equation (2.33).

Other than the initial quasi-linear nature of the fluid, no other approximations have been made up to this point, with the transformation given in (2.46) being exact. We now use the notation that has been established to look at limiting behaviour of the system.

We choose for the background flow, $U(Y)$, to be large in scale; $\varepsilon \ll 1$. On the assumption that there is good scale separation, we write

$$\begin{aligned}\zeta(Y,T) =& \zeta_0(Y,T) + \varepsilon\zeta_1(Y,T) + \varepsilon^2\zeta_2(Y,T) + ... \\ \phi(Y,T) =& \phi_0(Y,T) + \varepsilon\phi_1(Y,T) + \varepsilon^2\phi_2(Y,T) + ...\end{aligned} \tag{2.50}$$

This approximation is valid given $\zeta_0 \gg \varepsilon\zeta_1 \gg \varepsilon^2\zeta_2 \gg ...$, etc. We can then solve (2.48) from our system of differential equations by equating powers of ε:

$$\zeta_0 = m^2(1 + U'^2T^2)\phi_0, \tag{2.51}$$

$$\zeta_1 = m^2(1 + U'^2T^2)\phi_1 + imT\left(U''\phi_0 + 2U'\phi_0'\right), \tag{2.52}$$

$$\zeta_2 = m^2(1 + U'^2T^2)\phi_2 + imT\left(U''\phi_1 + 2U'\phi_1'\right) - \phi_0'', \tag{2.53}$$

etc. The flux can be written in terms of the components of ζ and ϕ by

$$\begin{aligned}F(Y,T) &= im\left(\zeta\phi^\star - \zeta^\star\phi\right)e^{-2\lambda T/\varepsilon} \\ &= im\left[\left(\zeta_0\phi_0^\star - \zeta_0^\star\phi_0\right) + \varepsilon\left(\zeta_1\phi_0^\star - \zeta_1^\star\phi_0 + \zeta_0\phi_1^\star - \zeta_0^\star\phi_1\right) + ...\right]e^{-2\lambda T/\varepsilon} \\ &= \left[F_0 + \varepsilon F_1 + \varepsilon^2 F_2 + ...\right]e^{-2\lambda T/\varepsilon},\end{aligned} \tag{2.54}$$

where im has been absorbed into F_0, etc. Note that contributions to the flux come only from the imaginary part of the product of the vorticity and stream function. As such, to $O(1)$, there is no flux; $\zeta_0\phi_0^\star - \zeta_0^\star\phi_0 = 0$ by (2.51). This forms a link to the flux of the linear shear flow given in section 2.3. Essentially what we observe here is that, at leading order, the flow reacts to the large-scale mean flow as though it were a simple linear shear flow. Corrections due to the small and slowly changing curvature of the mean flow will come in at smaller magnitudes.

Considering the flux up to $O(\varepsilon)$, we use (2.51) and (2.52) to write the flux in terms of ζ or ϕ alone (compare to equation (2.35) in section 2.2):

$$F(Y,T) = -2\varepsilon m^{-2}f^2T\left[U''f\left(1 - 3U'^2T^2\right)|\zeta_0|^2 + U'\left(|\zeta_0|^2\right)'\right]e^{-2\lambda T/\varepsilon}, \tag{2.55}$$

where

$$f(Y,T) = \left(1 + U'^2 T^2\right)^{-1}. \tag{2.56}$$

The dependence of the $O(\varepsilon)$ flux on only $O(1)$ terms is of note; in general we expect the $O(n+1)$ flux to depend on $\zeta_n, \zeta_{n-1}, ..., \zeta_0$. This, in conjunction with the expanded (2.47), allows us to tell what magnitude our parameters need to be to have an effect on the flux at leading order, which we will make use of later in this chapter.

We can work out the higher order fluxes in a similar fashion, however these become increasingly complicated and hard to interpret. We will refrain from giving the flux to higher accuracy than $O(\varepsilon^2)$, at which the flux is

$$\begin{aligned} F(Y,T) = &-2m^{-2}f^2T[\varepsilon(U''f(1-3U'^2T^2)|\zeta_0|^2 + U'(|\zeta_0|^2)') \\ &+ 2\varepsilon^2(U''f(1-3U'^2T^2)\mathrm{Re}\{\zeta_0^\star\zeta_1\} + U'\mathrm{Re}\{(\zeta_0^\star\zeta_1)'\} \\ &+ m^{-1}fU'T[4U''f(1-2U'^2T^2)\mathrm{Im}\{\zeta_0^\star\zeta_0'\} + 2U'\mathrm{Im}\{\zeta_0^\star\zeta_0''\}])]e^{-2\lambda T/\varepsilon}. \end{aligned} \tag{2.57}$$

The integrated flux, $\mathcal{F}$, can be written in terms of rescaled variables by

$$\mathcal{F}(Y,T) = \varepsilon^{-1}\int_0^T F(Y,T)dT, \tag{2.58}$$

with a similar definition for $\mathcal{F}_\infty(Y) \equiv \mathcal{F}(Y, T\to\infty)$. Although we could write a general $\mathcal{F}$ in terms of the integral of $|\zeta_0|^2$, the equation is complicated and does nothing to aid understanding of the nature of the flux. As such, we will refer to (2.58) again in subsequent sections.

We now aim to solve (2.47 – 2.49) for various points in our parameter space, evaluate the fluxes given in (2.57 – 2.58), and expand on the results. In particular, we will be looking to see if the fluxes satisfy the conditions needed for diffusive/anti-diffusive behaviour as given in equation (2.18).

2.4.1 $\lambda = \nu = \beta = 0$

Let us first look at the most simple point in our parameter regime: that where we only have the effect of a large-scale background flow on an inviscid fluid, with no

frictional forces. Our system of equations given by (2.47 – 2.48) reduces to

$$\partial_T \zeta = -\varepsilon i m U'' \phi, \tag{2.59}$$

$$\zeta = \mathcal{L}(\phi), \tag{2.60}$$

with $\mathcal{L}$ defined as in equation (2.49).

By expanding in terms of ε and using the initial condition $\zeta(y, 0) = 1$, we find $|\zeta_0|^2 = 1$ and calculate the first order flux to be

$$F = -2\varepsilon m^{-2} f^3 U'' T \left(1 - 3U'^2 T^2\right). \tag{2.61}$$

The most immediate result of this calculation is that the leading order flux is zero when $U'' = 0$, that is when we are dealing with a linear shear flow. This is to be expected, as we have found in section 2.3 that linear background flows produce no vorticity flux.

In figure 2.1 we plot the profile of $\mathcal{F}(Y, T_0)$, where T_0 is a chosen point in time, with $T_0 = 10$ here, as calculated numerically from equations (2.12) and (2.23). We also plot the $O(\varepsilon)$ approximation as calculated in equation (2.61), as well as the limiting behaviour given by (2.65). For comparison, we look at two different mean flows, the first of which takes a sinusoidal form, $U(Y) = -\cos(Y)$.

In this case, the flux is characterised by a spike in magnitude at points where $U'(Y) = 0$. In particular, although not shown in this figure, we observe that while the flux has minima at points $Y = 0, 2\pi, ...$, it will have maxima at $Y = \pi, 3\pi, ...$ With reference to (2.18), we describe this as a region of diffusivity permeated by a spike of strong anti-diffusivity. This enables transport at the peak of the mean flow, possibly allowing for zonal regions of poor mixing to form at either side. Alternatively, using equation (2.21), we see that the flux will modify the mean flow as to further decrease the minima, while also sharpening the gradients either side of it. We expect these types of behaviour to encourage or maintain the occurence of zonal jets in the fluid.

It is well known that instabilities may arise across profiles of perturbed mean flow profiles, such as those investigated here. As our system involves launching waves on top of a mean flow, we are looking at a case where the instabilities would

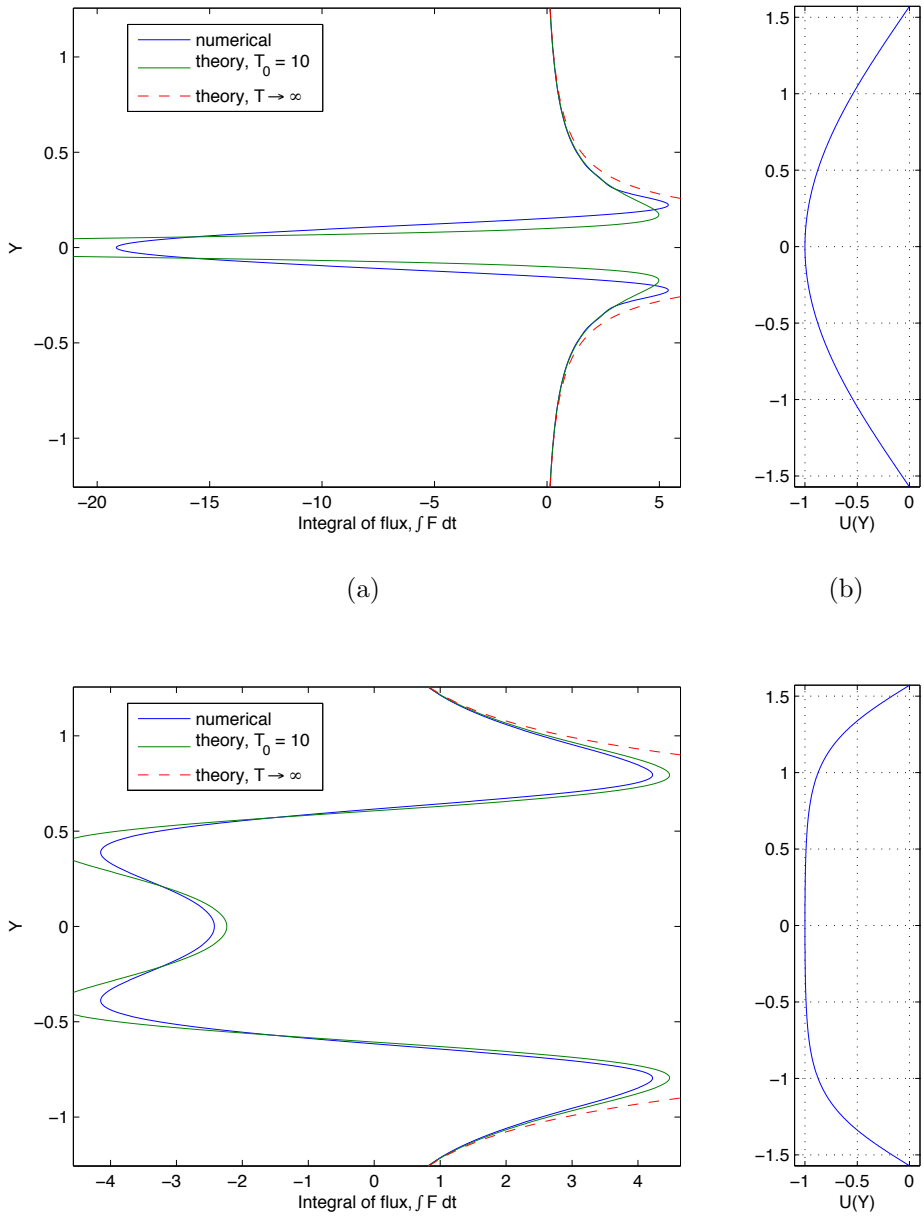

Figure 2.1: Graph of the profile of $\mathcal{F}(Y, T_0)$ for a numerical solution to equations (2.12) and (2.23) with $\lambda = \nu = \beta = 0$, and prescribed mean flow: (a) $U(Y) = -\cos(Y)$ (as shown in (b)), and (c) $U(Y) = \mathrm{sn}(Y^\star)$ (as shown in (d)), where sn is a Jacobi-Elliptic function. Also shown is the $O(\varepsilon)$ approximation to the flux found by directly calculating (2.61) and (2.65).

not have time to trigger, with the mean flow evolving stably. We note that for the $U(Y)$ and range of Y used in figures given in this section, and when introducing large enough β (section 2.4.4), the flow will meet the Rayleigh criterion for stability [45].

For this particular case, the first order approximation and the numerical solution seem to agree particularly well for $|Y| > 0.25$. As previously mentioned, we expect this to be the case for regions where the multi-scale approximation holds (when the terms in the expansion are well-ordered).

The approximation begins to break down when $U'(Y) = 0$, which occurs here at the point $Y = 0$. We can calculate the approximate value of the flux at $Y = 0$ as being

$$F(0, T) = -2\varepsilon m^{-2} T, \tag{2.62}$$

which integrating with respect to t gives

$$\mathcal{F}(0, T_0) = -m^{-2} T_0^2, \tag{2.63}$$

which takes the value $\mathcal{F}(0, 10) = -40$ for our current example. Clearly this is somewhat removed from the value $\mathcal{F}(0, 10) \approx -18$ found by our numerical simulation, and is to be expected due to the breakdown of the approximation. Most importantly, for an appropriately small value of ε, as we continue to increase T towards infinity we find that the approximation tends towards a positive infinite value, as can clearly be seen from equation (2.65) (with $U''(0) = 1$). Meanwhile, the numerical solution tends towards negative infinity, as can be seen from (2.63). However, it is clear that the vertical length of the central negative column of flux in the numerical solution (found at $|Y| \approx 0.2$ in figure 2.1), will tend to zero as $\varepsilon \to 0$.

We find similar behaviour in the second case, figure 2.1c, where we have implemented a more 'step' or 'jet-like' background flow. This is done using Jacobi-Elliptic functions, with $U(Y) = \mathrm{sn}(Y^\star, 0.99)$, where $Y^\star = \frac{2K}{\pi}\left(Y - \frac{\pi}{2}\right)$ is rescaled to translate the flow and give it the the appropriate 2π-periodicity (noting that K is the quarter-period of the Jacobi-Elliptic function corresponding to the root of the elliptic modulus, 0.99). Figure 2.1c shows how the initial flow profile has

a major effect on the flow. Whereas the sinusoidal flow produced a fairly evenly spread flux, the flatter mean flow vertically stretches the jet of negative flux, while squashing the remaining diffusive regions towards the boundaries.

Looking at the flux given in (2.61), general points in the flow are initially anti-diffusive, but for larger times, $T > 3^{-\frac{1}{2}}U'^{-1}$, become positive and diffusive. The integrated flux, $\mathcal{F}$, sheds more light on this:

$$\mathcal{F} = \frac{U''}{m^2 U'^2}\left[1 - f^2\left(1 + 3U'^2T^2\right)\right]. \tag{2.64}$$

Note that as $f^2(1 + 3U'^2T^2) \geq 0$ (see equation (2.56)), the integrated flux tends towards its maximum value as $T \to \infty$:

$$\mathcal{F}_\infty = \frac{U''}{m^2 U'^2}, \tag{2.65}$$

which, as we can see, tends to infinity as the gradient of the background flow tends to zero. However, we have to be careful here, as the terms in the multi-scale approximation of ζ and ϕ can become disordered, leading to a breakdown of the solution. This will be explored in more detail in section 2.5.

Over time, individual points of the integrated flux will change sign. The sign of $\mathcal{F}(Y_0)/U''(Y_0)$ is positive if $f^2(1 + 3U'^2T^2) < 1$, or

$$T > U(Y_0)'^{-1}. \tag{2.66}$$

As mentioned previously (see equation (2.18) in particular), the feedback on the flow from the small-scale perturbations is determined by F/U''. As such, $\mathcal{F}$ tells us if the flow is, in total, diffusive or anti-diffusive up until a specified time. The above relation gives contours of the (Y, T)-plane on which the flow changes between these two effects. The vertical scale selection given in the form of $U'(Y)$ may indeed play an inherent role in the formation of zonal flows associated with these fluids; if anti-diffusive effects dominate certain regions whilst the flow is more diffusive in between these, the driving of jet-like behaviour may be possible.

In figure 2.2 we can see more clearly how the flux evolves over time, and in particular how the central spike of flux continues to narrow, with its width tending to zero as T tends towards infinity. Also demonstrated is how the Jacobi-Elliptic

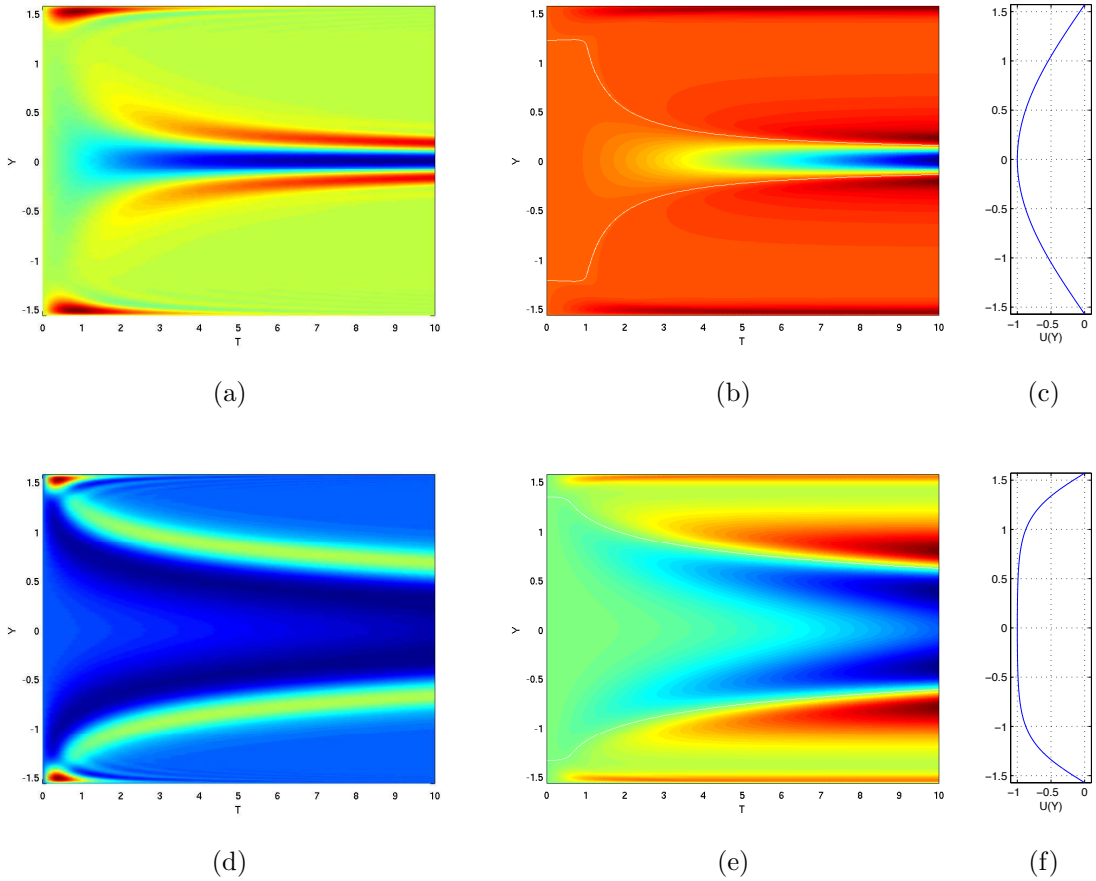

(a) (b) (c)

(d) (e) (f)

Figure 2.2: Contour plots of the profiles of $F(Y,T)$ in (a) and (d), and $\mathcal{F}(Y,T)$ in (b) and (e), for numerical solutions to equations (2.12) and (2.23) with $\lambda = \nu = \beta = 0$, and prescribed mean flow: (a)-(c) $U(Y) = -\cos(Y)$, and (d)-(f), $U(Y) = \mathrm{sn}(Y^\star)$, where sn is a Jacobi-Elliptic function. Red is positive and blue is negative, while for the integrated flux, contours of $\mathcal{F} = 0$ are plotted in white. For scale, please refer to figure 2.1.

profile of background flow decelerates the narrowing of the spike, giving a larger region of anti-diffusive behaviour for short times, such that the scales of the two regions are similar. This indicates that mean flows with a step-like form (for example β-plane jets) may more easily maintain their original scale and structure.

We investigate the general sign of the flux by looking at individual points Y_0, and tracking them throughout time. We write $\tau = U'(Y_0)T$, and note that the division between diffusive and anti-diffusive behaviour is given by $\tau_c = 1$. The

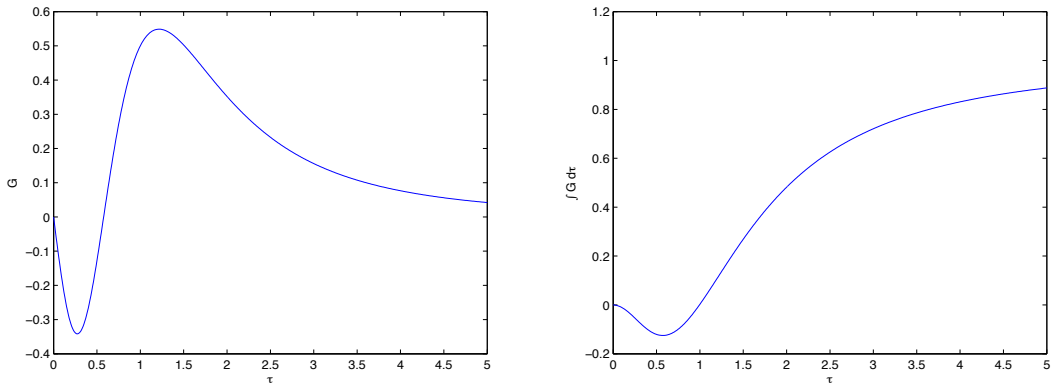

(a) (b)

Figure 2.3: Graph of the reduced form of (a) the flux, $G(\tau)$, and (b) the integrated flux, $\mathcal{G}(\tau)$, as given in equations (2.68) and (2.70) respectively. Note that as $\tau \to \infty$, $\mathcal{G} \to \mathcal{G}_\infty = 1$.

$O(\varepsilon)$ flux can be written as

$$F = \frac{\varepsilon U''}{m^2 U'} G(\tau), \tag{2.67}$$

where

$$G(\tau) = -2\tau(1 - 3\tau^2)(1 + \tau^2)^{-3}. \tag{2.68}$$

For a fixed point in space, τ simply represents a rescaled time variable, whilst the pre-factor to F will be constant. As such, any interesting behaviour in the flux will be dependent on the form of $G(\tau)$. Note that, unlike t, τ can be less than zero. As $G(\tau)$ is odd, results for $\tau < 0$ simply correspond to $-G(|\tau|)$. The approximation to the integrated flux is given by

$$\mathcal{F} = \frac{U''}{m^2 U'^2} \mathcal{G}(\tau), \tag{2.69}$$

where

$$\mathcal{G}(\tau) = \int_0^\tau G(\tau) d\tau = 1 - (1 + 3\tau^2)(1 + \tau^2)^{-2}. \tag{2.70}$$

Again, the nature of the feedback will be determined by the amount of time over which we integrate, with the initial sign being determined by $U''(Y_0)$.

In figure 2.3 we see that for small τ (i.e. small times, T, or flat gradients of U), the function G acts in an anti-diffusive manner. Increasing τ to $\tau > \tau_c = 1$,

the feedback becomes diffusive, with the integrated flux tending toward a limiting value of $\mathcal{G}_\infty = 1$, corresponding to (2.65). We expect that with the addition of drag or viscosity, the flux should decay as the appropriate frictional time-scale is reached. This will be discussed in sections 2.4.2 and 2.4.3.

2.4.2 $\lambda \neq 0,\ \nu = \beta = 0$

As mentioned previously, the presence of surface drag on our fluid has no change on the structure of the flux other than to introduce exponential decay:

$$F = F_{\lambda=0} e^{-2\lambda T/\varepsilon} = -2\varepsilon m^{-2} f^3 U'' T \left(1 - 3U'^2 T^2\right) e^{-2\lambda T/\varepsilon}, \tag{2.71}$$

to $O(\varepsilon)$ accuracy. This additional term will have the important effect of making $\mathcal{G}_\infty < 1$ for $\lambda \neq 0$. Note that for small ε, the flux will tend to zero very quickly unless λ is on the same scale as ε. This is assumed for now, but will be implemented later in our analysis.

We can expand all of the terms in $F_{\lambda=0}$ as a Taylor series in T:

$$F \simeq -2\varepsilon m^{-2} U'' T \left(1 - 6U'^2 T^2 + O(T^4)\right) e^{-2\lambda T/\varepsilon}. \tag{2.72}$$

As such, the integrated flux is

$$\begin{aligned} \mathcal{F} &= \varepsilon^{-1} \int_0^T F_{\lambda=0}\, e^{-2\lambda T/\varepsilon} dT \\ &\simeq -2m^{-2} U'' \int_0^T \left(T - 6U'^2 T^3 + O(T^5)\right) e^{-2\lambda T/\varepsilon} dT. \end{aligned} \tag{2.73}$$

The integral in (2.73) takes the form of a Laplace transform, and is used to find the solution across the entire domain of T (whilst neglecting higher orders of T from the Taylor expansion):

$$\mathcal{F}_\infty \simeq -\frac{U''}{m^2} \left[\frac{1}{2\lambda^2} - \frac{9U'^2}{2\lambda^4} + O(\lambda^{-6})\right]. \tag{2.74}$$

Comparing equation (2.74) to $\mathcal{F}_\infty$ without any drag (as given in equation (2.65)), we can see similarities in the prefactor, with the exception of the U'^2 terms in the denominator. This is to be expected, as frictional forces act to damp extreme behaviour at the limits.

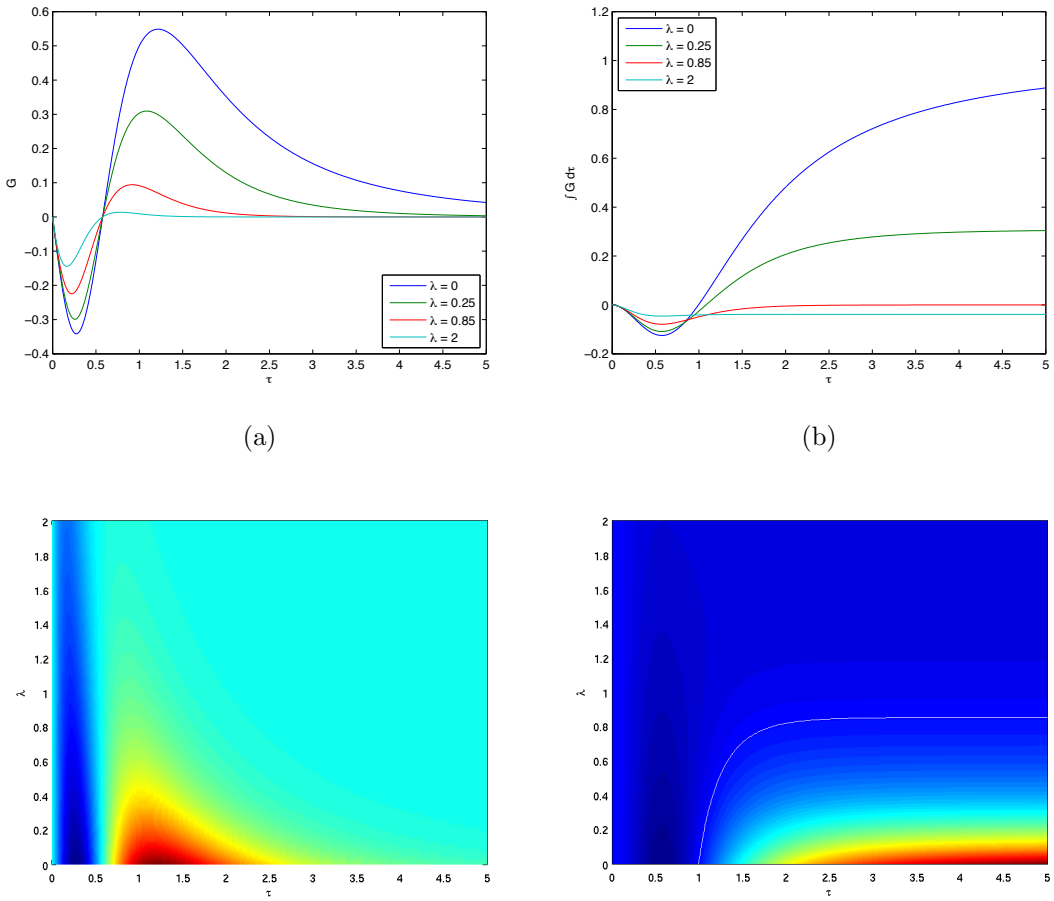

(a) (b)

(c) (d)

Figure 2.4: Graph of the reduced form of (a), (c) the flux, $G(\tau, \bar{\lambda})$ and (b), (d) the integrated flux, $\mathcal{G}(\tau, \bar{\lambda})$ found by calculating and numerically integrating equation (2.76). Plots (a) and (b) give simple line plots of their respective functions for different values of $\bar{\lambda}$, whereas (c) and (d) are contour plots of the parameter space $(\tau, \bar{\lambda})$, with red as positive, blue as negative and the contour line $\mathcal{G} = 0$ overlayed in white. Note that λ in the figure corresponds to $\bar{\lambda}$ in the text. The curve for $\bar{\lambda} = 0$ is the same as found in (2.70) and plotted in figure 2.3.

Similarly to (2.67) in section 2.4.1, we can rewrite equation (2.71) in terms of a simpler function:

$$F = \frac{\varepsilon U''}{m^2 U'} G(\tau, \bar{\lambda}), \tag{2.75}$$

with

$$G(\tau, \bar{\lambda}) = -2\tau(1 - 3\tau^2)(1 + \tau^2)^{-3} e^{-2\bar{\lambda}\tau}, \tag{2.76}$$

where we have introduced a rescaled coefficient of drag, $\bar{\lambda} = \lambda/(\varepsilon U')$, and τ is the rescaled time, as given in the previous section. Again, we can see how the key behaviour of the flux is described by the function G, indeed $\bar{\lambda} = 0$ corresponds exactly to the previous case (see equation (2.68)).

We integrate equation (2.76) to find $\mathcal{G}(\tau, \bar{\lambda})$ and $\mathcal{G}_\infty$, however for non-trivial $\bar{\lambda}$ these can only be written in terms of special functions. Instead, we recall that the total feedback on the mean flow is related to G by

$$\frac{\mathcal{F}}{U''} = \frac{1}{m^2 U'^2} \int G(\tau, \bar{\lambda}) d\tau, \tag{2.77}$$

as in equation (2.69), and so the sign of $\mathcal{G}$ is key to our investigation.

In figure 2.4 we find and plot $G(\tau, \bar{\lambda})$ and $\mathcal{G}(\tau, \bar{\lambda})$ for a range of $\bar{\lambda}$. It is clear from 2.4b that each curve has limiting behaviour as $\tau \to \infty$, as expected from the integral of an exponentially decaying function. Again, the sign of $\mathcal{G}_\infty(\bar{\lambda})$ determines the diffusive/anti-diffusive behaviour. For large $\bar{\lambda}$ the flux is dissipated fast enough that only the anti-diffusive behaviour associated with short time-scales, $\tau \ll 1$, can occur. However, as $\bar{\lambda}$ decreases past a critical value, $\bar{\lambda}_c \simeq 0.85$, the flow persists long enough for diffusive behaviour to begin, as can be seen in 2.4a.

In figures 2.4c and 2.4d we can see how the flux behaves across the entire parameter space of $(\tau, \bar{\lambda})$. In particular, the integrated flux as plotted in 2.4d gives an indication of whether the flux (at a point in τ) behaves in a generally diffusive or anti-diffusive manner, with contours of $\mathcal{G} = 0$ giving the division between these two types of behaviour. In particular, we see that for $\bar{\lambda} > \bar{\lambda}_c$, the flux will always be dissipated before it can produce an overall diffusive effect, i.e. $\mathcal{G} < 0$.

This is the key result for this section; that the frictional drag actually promotes anti-frictional behaviour in the system by killing off the flux before the naturally diffusive nature of the feedback has chance to kick in. This can be an important consequence for many of the models in the literature which use large, often artificial frictional forces to keep simulations in check; depending on the way in which

these are implemented (hyper-viscosity, etc), the flow may become more/less anti-diffusive than is natural. This effect has been observed in numerical simulations, such as those performed by Scott and Polvani in the context of the Jovian atmosphere [36].

2.4.3 $\lambda = 0,\ \nu \neq 0,\ \beta = 0$

The fundamental difference between surface drag and viscosity as frictional forces is that, at any given point in time, viscosity selects and damps different regions of the flow (dependent on scale), while surface drag acts on the flow as a whole. This should become evident whilst looking at the flux for a viscously damped fluid.

In order to solve our large-scale expansion equations, (2.47 – 2.49), with non-zero viscosity, we have to introduce ν at a reduced level. For the viscosity to have an effect on the flux to order ε, it is required to be on the scale of ε, and so we take

$$\nu = \varepsilon\tilde{\nu}, \tag{2.78}$$

and assume $\tilde{\nu}$ is $O(1)$. We then substitute this into equation (2.47).

Solving (2.47 – 2.49), we find that $|\zeta_0|^2 = \exp\{-2\tilde{\nu}m^2T\left(1 + \frac{1}{3}U'^2T^2\right)\}$, and so using (2.55), the $O(\varepsilon)$ flux is

$$F = -2\varepsilon m^{-2}f^2U''T\left[f\left(1 - 3U'^2T^2\right) - \frac{4}{3}\tilde{\nu}m^2U'^2T^3\right]e^{-2\tilde{\nu}m^2T\left(1+\frac{1}{3}U'^2T^2\right)}. \tag{2.79}$$

Similarly to equation (2.71) in the previous section, we now have an exponentially decaying term in the flux, which will make any given point of the flux tend to zero as T increases towards infinity. However, the terms in the exponential are also now dependent on Y, and so different regions of the flux will decay at a different rate.

In particular, we observe that regions close to $U'(Y) = 0$ in the flux will decay with $\exp(-2\tilde{\nu}m^2T)$, whilst for $U'(Y) = O(1)$ we expect F to decay with $\exp(-\frac{2}{3}\tilde{\nu}m^2T^3)$.

Again, we can reduce this to its simplest functional form. We rescale the viscosity such that

$$\bar{\nu} = \frac{\tilde{\nu}m^2}{U'}, \tag{2.80}$$

which gives

$$F = \frac{\varepsilon U''}{m^2 U'} G(\tau, \bar{\nu}), \tag{2.81}$$

where $\tau = U'(Y_0)T$ as previously stated, and

$$G(\tau, \bar{\nu}) = -2\tau \left[(1 - 3\tau^2)(1 + \tau^2)^{-3} - \frac{4}{3}\bar{\nu}\tau^3(1 + \tau^2)^{-2} \right] e^{-2\bar{\nu}\tau(1+\frac{1}{3}\tau^2)}. \tag{2.82}$$

Integrating this to find $\mathcal{G}(\tau, \bar{\nu})$ is impossible analytically, so again we use numerics to investigate further.

Figure 2.5 plots the numerical solution to the integral of (2.82). Characteristically, the curves have much the same appearance as seen in the figure 2.4 for bottom drag, with the critical point for diffusive/anti-diffusive behaviour occuring at $\bar{\nu} \simeq 0.95$. These similarities come about because $\mathcal{G}$ is a simplified function tracking only a single point in the Y domain over time; in order to properly view the mechanisms that make viscosity differ from drag, we need to examine the flux as a function of space.

To do this, we find $\mathcal{F}_\infty(Y)$ for various values of ν (and λ for comparison) by numerically integrating equation (2.79) (and (2.71)).

In figures 2.6 and 2.7 we plot $\mathcal{F}_\infty(Y)$ for two different background flows and several values of λ and ν. As can be seen, the frictional forces have a similar effect on the form of the flux, which is clear when contrasting with figure 2.1. Drag and viscosity each damp the entire profile, but in particular, regions where $U'(Y) = 0$ are more prominently affected. For small values of λ and at steep gradients of the Jacobi-Elliptic profile the flux acts to further sharpen the mean flow.

We compare figures 2.6 and 2.7 to see how the two dissipative mechanisms act differently. For both profiles, λ tends to sharpen gradients more effectively than ν, although this is easier to observe with the $U(Y) = -\cos(y)$ mean flow. At the same time, the viscosity tends to effectively dissipate diffusive behaviour away from the origin (i.e. where the gradients of the mean flow are large), stopping it from sharpening the mean profile quite as strongly as the drag.

Another interesting feature that both frictional forces have in common is that they produce feedbacks which act to split the flat mean profile given in figures 2.6c and 2.7c via two smaller anti-diffusive spikes. Indeed, both seem to influence

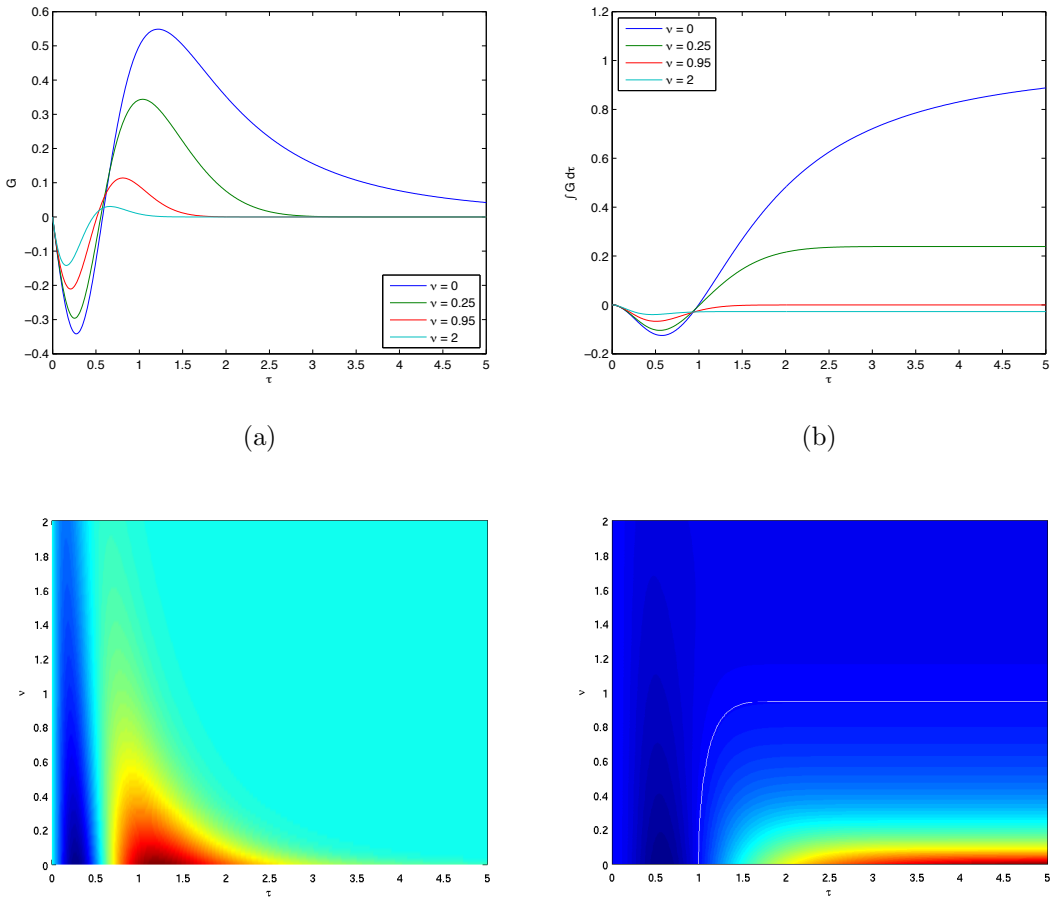

Figure 2.5: Graph of the reduced form of (a), (c) the flux, $G(\tau, \bar{\nu})$ and (b), (d) the integrated flux, $\mathcal{G}(\tau, \bar{\nu})$ found by calculating and numerically integrating equation (2.82). Plots (a) and (b) give simple line plots of their respective functions for different values of $\bar{\nu}$, whereas (c) and (d) are contour plots of the parameter space $(\tau, \bar{\nu})$, with the contour line $\mathcal{G} = 0$ overlayed in white. Note that ν in the figure corresponds to $\bar{\nu}$ in the text. The curve for $\bar{\nu} = 0$ is the same as found in (2.70) and plotted in figure 2.3.

the vertical length scales of system; even for drag, which has no preference for scale. This indicates that frictional forces may influence jet spacing, although we are unaware of any fully nonlinear results that support this.

The effect that both frictional forces have of sharpening the mean profile of a jet-like flow is one of the key results of this section. In addition, we emphasize the

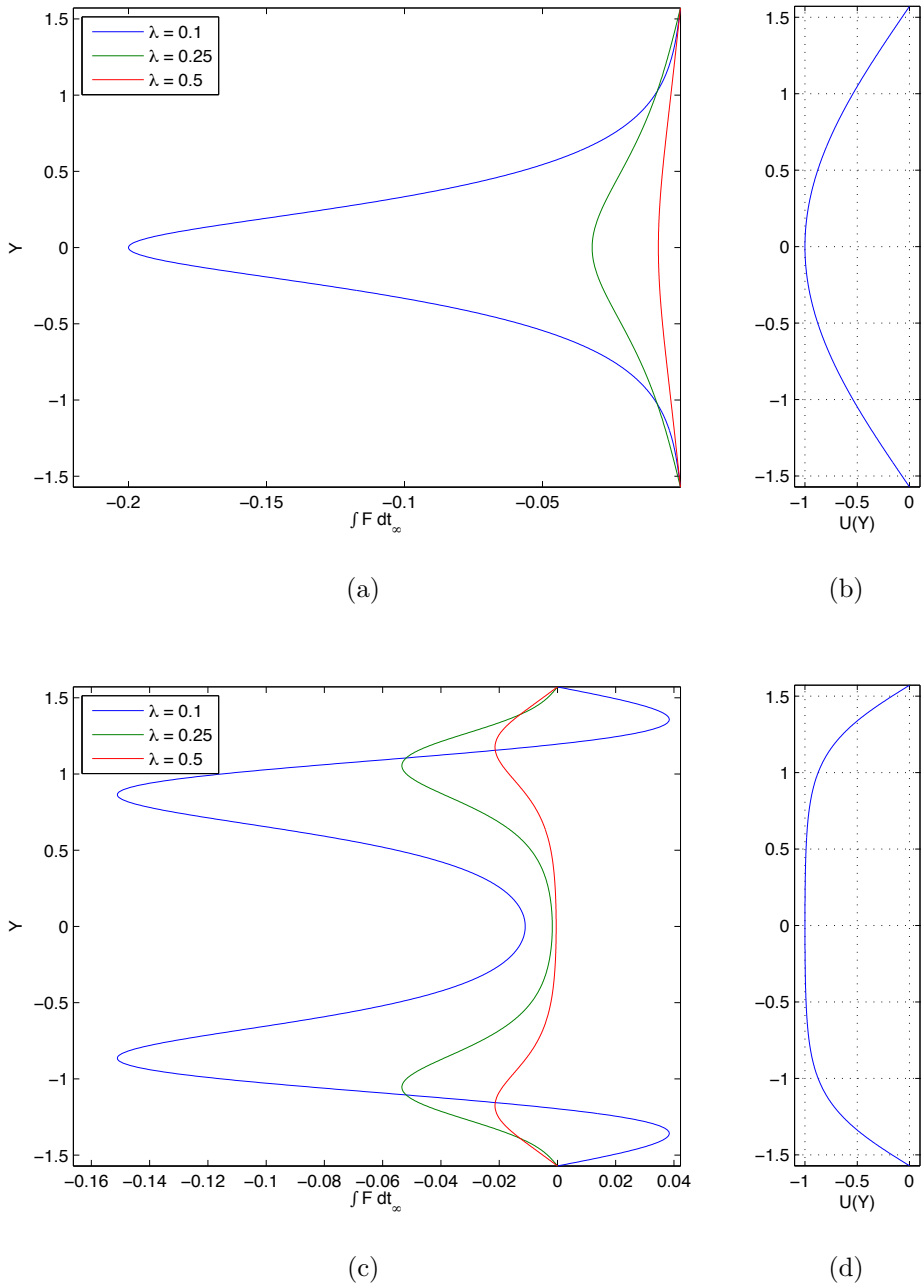

Figure 2.6: Graphs of the integrated flux, $\mathcal{F}_\infty(Y)$, obtained by integrating (2.71), for various values of λ. (a) uses a sinusoidal background flow (shown in (b)), whilst (c) uses a jet-like background flow (shown in (d)).

importance of frictional forces in damping waves before their diffusive feedback can take effect, promoting short time anti-diffusive behaviour in the flow.

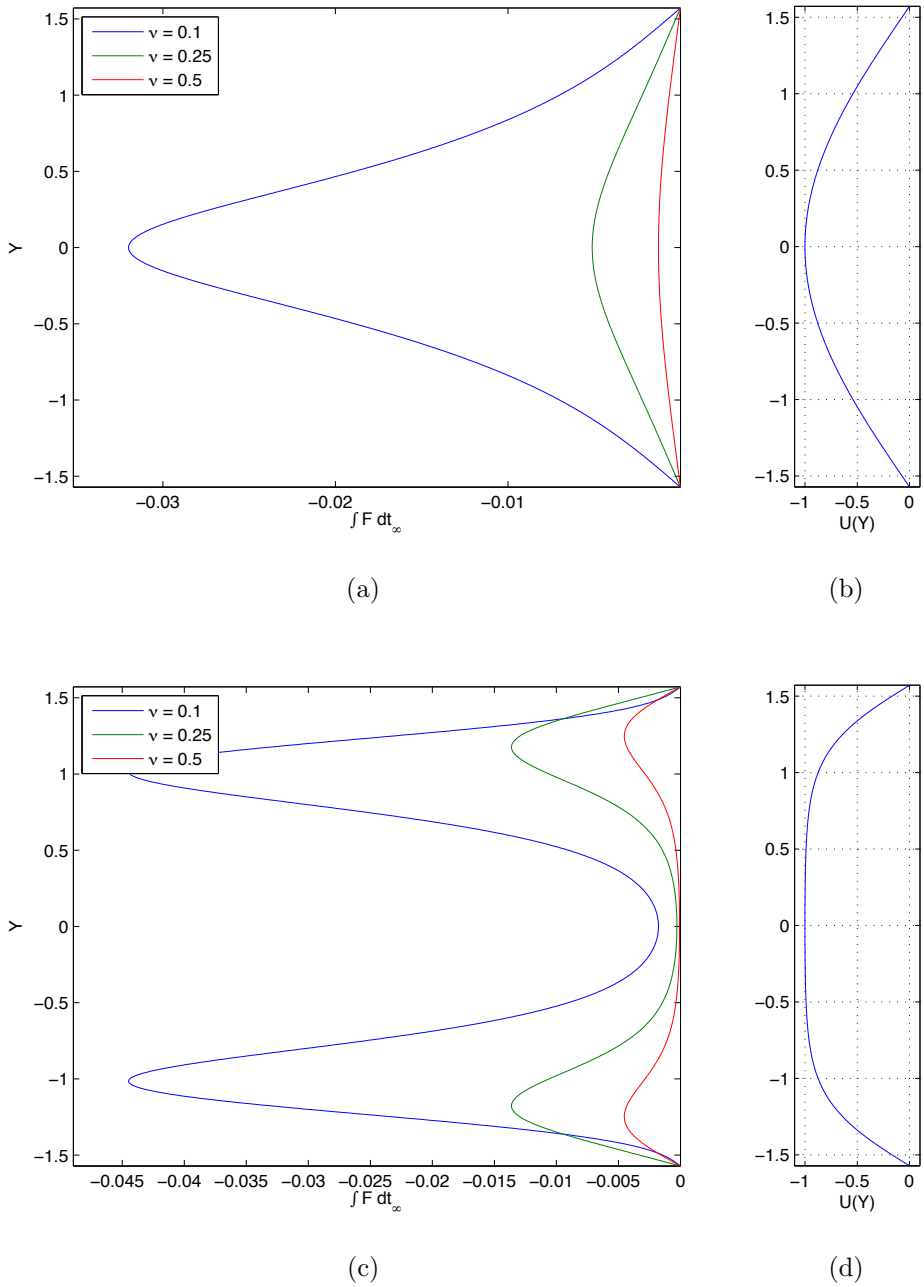

Figure 2.7: Graphs of the integrated flux, $\mathcal{F}_\infty(Y)$, obtained by integrating (2.79), for various values of ν. (a) uses a sinusoidal background flow (shown in (b)), whilst (c) uses a jet-like background flow (shown in (d)).

2.4.4 $\lambda = \nu = 0, \ \beta \neq 0$

As was the case for viscosity in section 2.4.3, to examine the effects of a background vorticity gradient on the flux, we need to introduce it at a relatively small

magnitude in order for our large-scale approximation to hold. Examining equation (2.47), it is clear that for β to have an effect on the $O(1)$ modified vorticity, we must take $\beta = O(\varepsilon)$. We set $\beta = \varepsilon\tilde{\beta}$, assuming $\tilde{\beta} = O(1)$, and solve (2.47) using (2.51) and our initial condition, $\zeta(Y, 0) = 1$, to obtain:

$$\zeta_0 = \exp\left(\frac{i\tilde{\beta}}{mU'}\tan^{-1}(U'T)\right). \tag{2.83}$$

Although $\tilde{\beta}$ has an effect on the vorticity at leading order, recalling equation (2.55), and noting that $|\zeta_0|^2 = 1$, it is clear that at the current scale $\tilde{\beta}$ has no effect on the $O(\varepsilon)$ flux (which remains as found in equation (2.61)).

From here there are two options in exploring β using the large-scale framework. The first is to introduce β at a larger magnitude. However, as previously mentioned, this results in the governing equations becoming disordered and unsolvable. The second option is to explore the flux in more detail, and in particular to calculate the flux to $O(\varepsilon^2)$ as given in equation (2.57). Using ζ_0 and (2.52), we find

$$\begin{aligned}\zeta_1 =&\frac{\tilde{\beta}U''}{m^2U'^4}[-\frac{1}{2}U'^2\ln(f) + f^2U'^2(1+2U'^2T^2)\\ &+\frac{i\tilde{\beta}}{4m}(\tan^{-1}(U'T) - f^2U'T(1-U'^2T^2))\\ &+\frac{\tilde{\beta}^2 f}{2m^2}(U'T-(1-U'^2T^2)\tan^{-1}(U'T)) + \frac{imU'^3}{\tilde{\beta}}\tan^{-1}(U'T)]\zeta_0,\end{aligned} \tag{2.84}$$

which gives the total flux to order ε^2 as

$$\begin{aligned}F =& -2m^{-2}f^3T[\varepsilon U''(1-3U'^2T^2) + \varepsilon^2\frac{\tilde{\beta}}{m^2U'^2}[U''f - 9U'^4U''^2T^4f\\ &-2U'^2U''^2T^2f^2 - 2U''^2f^2 - 24U'^4U''^2T^4f^2 + 4U'^3U'''T^2f - 8U'^2U''^2T^2f\\ &+2U'^2T(-2U''f(1-U'^2T^2) - 2U'U''' + 4U''^2)\tan^{-1}(U'T)]].\end{aligned} \tag{2.85}$$

The above equation is complicated. However, we observe that all of the $O(\varepsilon^2)$ terms have a common $\tilde{\beta}$ dependence, and that for $\tilde{\beta} = 0$ the flux has no other $O(\varepsilon^2)$ terms.

To more clearly see the effect of β, we numerically integrate the governing equations (2.47 – 2.49) and in figure 2.8 plot this and the integrated $O(\varepsilon^2)$ flux as given in equation (2.85). Direct comparison of the numerical results with figure

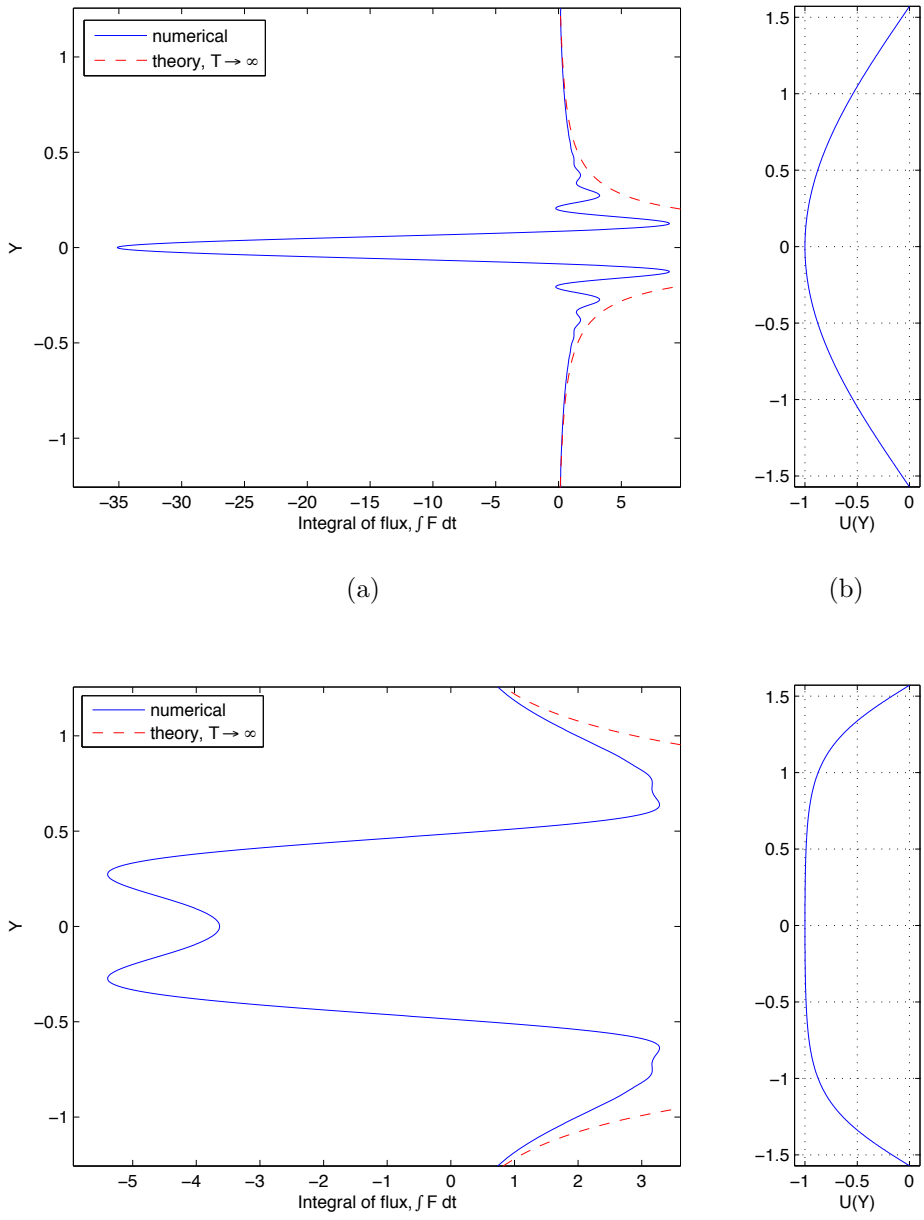

Figure 2.8: Graph of the profile of $\mathcal{F}(Y, T_0)$ for a numerical solution to equations (2.12) and (2.23) with $\lambda = \nu = 0, \beta = 0.1$, $T_0 = 10$ and prescribed mean flow: (a) $U(Y) = -\cos(Y)$ (as shown in (b)), and (c) $U(Y) = \mathrm{sn}(Y^\star)$ (as shown in (d)). Also shown is the $O(\varepsilon^2)$ approximation to the flux found by directly calculating (2.85) and the $O(\varepsilon)$ limit of $\mathcal{F}$ given by (2.65).

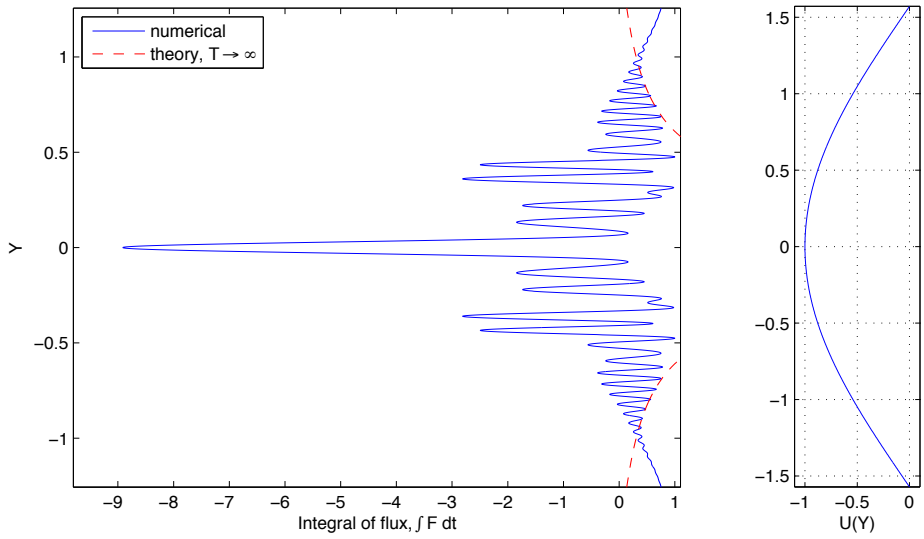

(a) (b)

Figure 2.9: Graph of the profile of $\mathcal{F}(Y, T_0)$ for a numerical solution to equations (2.12) and (2.23) with $\lambda = \nu = 0, \beta = 1$, $T_0 = 10$, and prescribed mean flow $U(Y) = -\cos(Y)$ (as shown in (b)). Also shown is the $O(\varepsilon)$ limit of $\mathcal{F}$ given by (2.65).

2.1 shows the effect β has of creating small-scale oscillations in the flux, which can be clearly seen in figure 2.8a. These also occur for the Jacobi-Elliptic profile, but are less pronounced. However, we find it difficult to match the small oscillations in 2.8c with any particular feature or region of the mean flow.

As β is increased, the frequency of these oscillations at a given time T_0 increases. This can be seen in figure 2.9, which is plotted from a solution using the same parameters as figure 2.8a, except for $\beta = 1$. The oscillations have roughly the same amplitude for the different values of β, although the maxima of the numerical solution in figure 2.9 are by no means as large as those in 2.8a. Over time, the length of the oscillations decreases, indicating a complicated relationship between the vertical length scale and β, T, and $U(Y)$.

One of the most important features of the flow is the anti-diffusive column protruding from $Y = 0$, a feature which remains in the results of this section.

For $\beta = 0.1$ this spike is actually larger in magnitude, which would suggest it amplifies jet-like features in the flow. However, as β is increased to 1, the column both decreases in strength and becomes narrower, decreasing the amount of anti-diffusive behaviour in the system.

So far we have only discussed the results of numerically solving equations (2.47 – 2.49). We now look at the integrated flux, extending it to include $O(\varepsilon^2)$ contributions. However, omitting the calculations due to length, we find that in the large T limit, the flux goes unchanged from its leading order form, i.e. it is the same as given in equation (2.65). As such, at second order (and we suppose higher orders also, although this is unchecked), β has no effect on the wholly diffusive nature of the flow that occurs when the flux persists for long enough times.

In summary, it has been difficult to quantify the behaviour of a flow with a background vorticity gradient using this large-scale expansion. It seems that β helps to create small-scale motions in the mean flow, which may correspond to jet-spacing and the Rhines scale. Yet at the same time, anti-diffusive regions of the flow are suppressed as β is increased (despite initially being strengthened by it). In order to explore this parameter in more detail, in section 2.6 we use a different type of expansion; one valid only for short times. However, first we look at the points in the mean flow where complicated behaviour has been observed by the large-scale expansion.

2.5 Turning Points in the Mean Flow

As discussed in the previous section, the solution to the large-scale expansion tends to break down in regions where $\partial_y U = 0$. In particular, the integrated flux in the limit of $T \to \infty$, which is given in equation (2.65), gives diffusive behaviour across the entire flow, regardless of additional effects bought in by parameters such as λ, ν and β. In equation (2.85) we saw that the second order terms in the flux were dependent on β. We expect the third order expansion to contain β^2 terms, etc, ultimately resulting in the $O(\varepsilon^n)$ flux being dependent on β^{n-1}. As such, the flux will become increasingly disordered as we increase β, due to lower terms in the

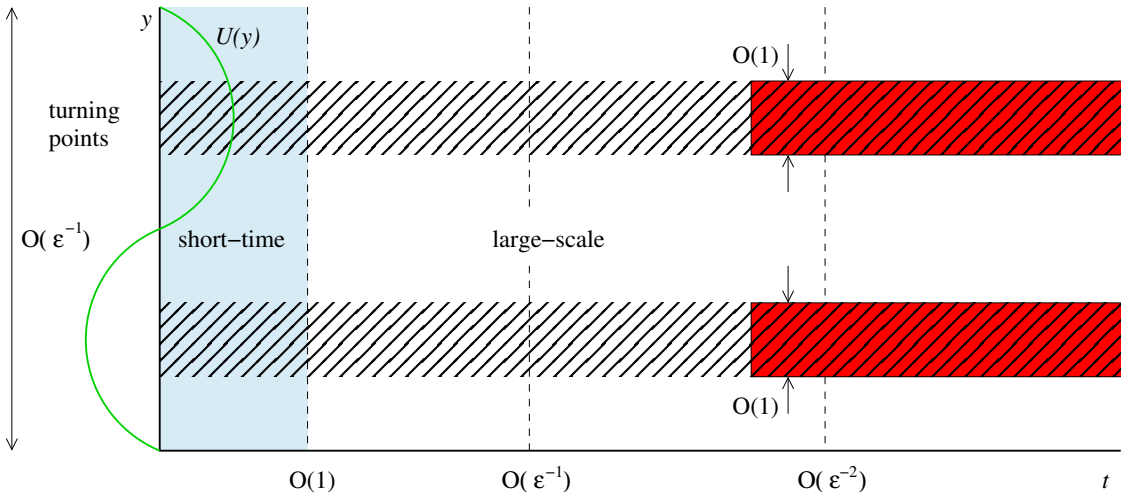

Figure 2.10: Schematic of the regions of validity for the different expansions used as part of the quasi-linear analysis discussed in this chapter. The large-scale expansion discussed in section 2.4 is valid everywhere except for where it breaks down at points $U'(y) = 0$ for large values of time. The material seen in this section is valid at those regions for all time, while a short-time expansion presented in section 2.6 is valid everywhere in y, but only for times of $O(1)$.

expansion increasing in magnitude and surpassing the leading order terms.

In the schematic given by figure 2.10, we draw the regions of validity for the different expansions used throughout this chapter. The large-scale expansion is valid for all regions and times apart from those discussed previously; areas close to $U' = 0$ at large values of t, given in red in the schematic. A short-time expansion, to be discussed in section 2.6, is valid for the light blue area. The diagonally shaded regions depict points around $U' = 0$, which will be the focus of our investigation in this current section: turning points in the mean flow.

To explore these regions in more detail, we note that any general turning point can be written in the form

$$U(y) = a_0 + \frac{1}{2}a_2\varepsilon^2 y^2 + ... \tag{2.86}$$

where a_n are arbitrary constants, and ε is a rescaling parameter with $\varepsilon \ll 1$. The constant a_0 represents a Galilean transformation in the y-direction, and so can be set to zero without loss of generality, whilst a_2 describes how steep the turning

point is. Substituting this into equation 2.12, with $\lambda = 0$ gives

$$\partial_t \omega + \frac{1}{2}\varepsilon^2 ima_2 y^2 \omega = im\left(\beta - \varepsilon^2 a_2\right)\psi - \nu\left(m^2 - \partial_y^2\right)\omega. \tag{2.87}$$

We proceed by looking at the long time-scale $\mathbb{T} = \varepsilon^2 t$, noting that this is an order of ε larger than the time-scale used previously in the large-scale expansion. Setting $\omega(y,t) = \omega^\dagger(y,\mathbb{T})$, etc, whilst taking the inviscid limit, $\nu = 0$, we have

$$\varepsilon^2 \partial_{\mathbb{T}} \omega^\dagger + \frac{1}{2}\varepsilon^2 ima_2 y^2 \omega^\dagger = im\left(\beta - \varepsilon^2 a_2\right)\psi^\dagger. \tag{2.88}$$

The above equation (and a rescaled equation (2.23)) can be written as a single parameter system via another suitable rescaling. We choose

$$\mathbb{T} = \frac{2m}{a_2}\tilde{\mathbb{T}},\ y = \frac{1}{m}\tilde{y},\ \omega^\dagger(y,\mathbb{T}) = \frac{2m}{a_2}\tilde{\omega}^\dagger(\tilde{y},\tilde{\mathbb{T}}), \tag{2.89}$$

$$\psi^\dagger(y,\mathbb{T}) = \frac{2}{ma_2}\tilde{\psi}^\dagger(\tilde{y},\tilde{\mathbb{T}}),\ \beta = \varepsilon^2 a_2\left(\frac{1}{2}\beta^\dagger + 1\right), \tag{2.90}$$

noting that $\beta = 0$ corresponds to $\beta^\dagger = -2$. Dropping the tildes and † in our notation (apart from $\beta^\dagger$, which we wish to compare with original β values), we obtain

$$\partial_{\mathbb{T}}\omega + iy^2\omega = i\beta^\dagger\psi, \tag{2.91}$$

$$\omega = \left(1 - \partial_y^2\right)\psi. \tag{2.92}$$

This is easily solved when $\beta^\dagger = 0$, which corresponds to the background vorticity gradient and the vorticity gradient introduced by the mean flow cancelling. Note that if we substitute (2.92) into (2.91) we find

$$\partial_{\mathbb{T}}\psi - \partial_{\mathbb{T}}\partial_y^2\psi = i(\beta^\dagger - y^2)\psi + iy^2\partial_y^2\psi. \tag{2.93}$$

This partial differential equation, while linear, is complicated and as such we refrain from exploring analytical solutions here.

Instead, we solve equations (2.91) and (2.92) using MATLAB's built in partial differential solver, `pdepe`, with the imposed boundary conditions $\omega(\pm 2\pi, t) = 0$. Note that these are not real physical boundary conditions, rather we have chosen arbitrary conditions at points far enough away from the centre of the flow that they should have no important effect on the dynamics at the turning points.

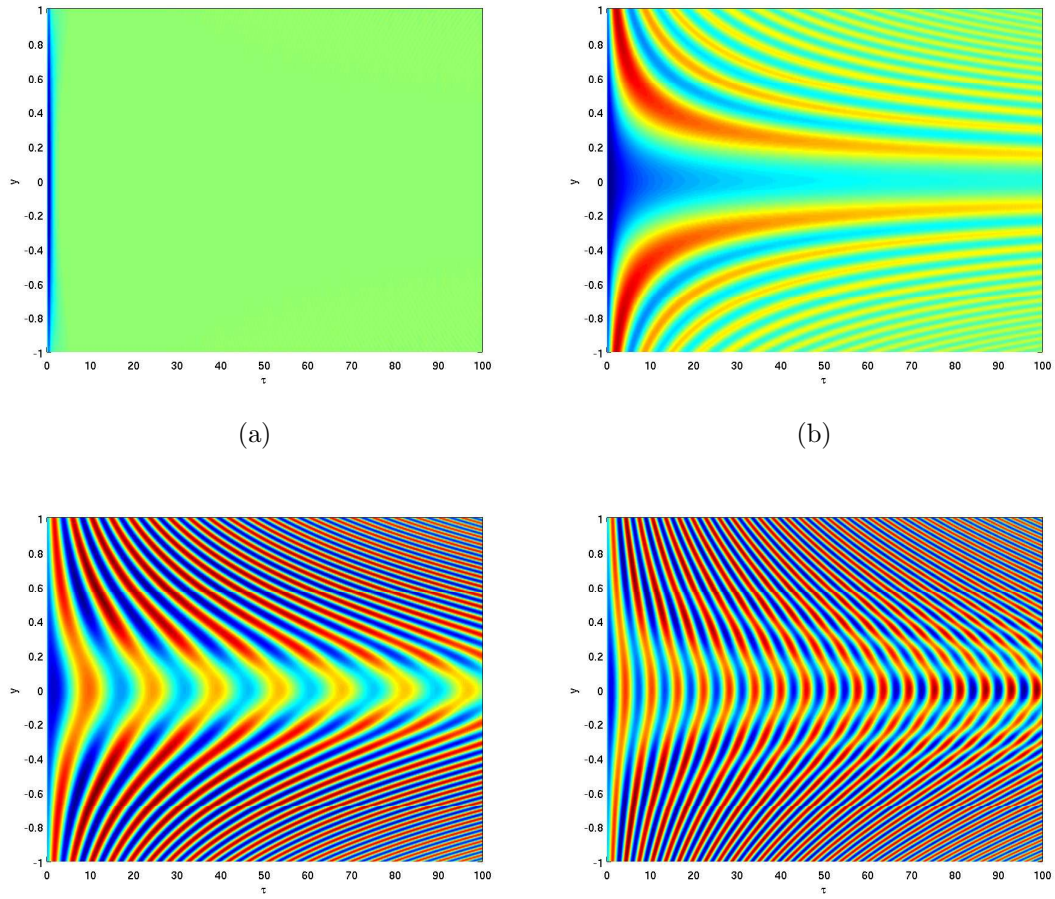

(a) (b)

(c) (d)

Figure 2.11: Shaded contour plots of the evolution of vorticity flux, $F(y)$, over the long time scale $\mathbb{T}$ for (a) $\beta^\dagger = -2$, (b) $\beta^\dagger = 0$, (c) $\beta^\dagger = 1$, (d) $\beta^\dagger = 2$. These are obtained by solving equations (2.91 – 2.92) numerically, and finding the flux via equation (2.34).

In figure 2.11 we give shaded contour plots of the vorticity flux profile, $F(y)$, over time for several values of $\beta^\dagger$. Note that the new variables introduced in this section have only been rescaled (without any transformations), and as such the equation for the flux in terms of these new variables is a rescaled version of (2.34), which we refrain from exploring here. For $\beta^\dagger = -2$, which corresponds to $\beta = 0$, the flow dissipates quickly to a homogenous state. Increasing $\beta^\dagger$ to 0 (corresponding to a balance in vorticity gradients), we observe zonal behaviour, with an increasing number of alternating flows occuring over time. Note however that these may be

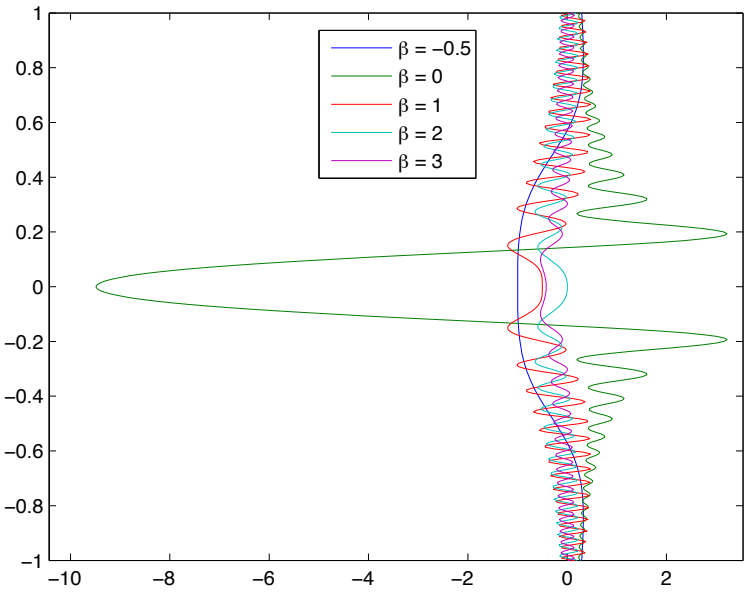

Figure 2.12: Graph of the profile of $\mathcal{F}_{T_0=100}(y)$ found by numerically integrating (2.91) and (2.92) for different values of $\beta^\dagger$, with boundary conditions set to $\omega(\pm 2\pi, t) = 0$, etc. Note that β in the figure refers to $\beta^\dagger$ in the text.

the result of the boundary conditions, and the key observation to make of figure 2.11b is the strongly anti-diffusive jet at $y = 0$. As can be seen, increasing $\beta^\dagger$ further seems to bring about an oscillating peak at $y = 0$, switching polarity with a mean value of zero. As $\beta^\dagger$ increases, the rate of oscillation also increases. The trail of filament-like structures either side of $y = 0$ is possibly a result of the boundary conditions, but may match to the flux for regions away from the turning point; again, the oscillating nature of the flow at $U' = 0$ for $\beta^\dagger > 0$ is the important observation here.

Different details are given in figure 2.12, which shows the flux integrated over time for different values of $\beta^\dagger$. For $\beta^\dagger < 0$, there are no oscillations, and the intensity of the peak at $y = 0$ seems to increase with $\beta^\dagger$ to a maximum at $\beta^\dagger = 0$. Beyond this point, the amplitude of the oscillations in the flow appears to be suppressed, with $\mathcal{F}(y) \to 0$ as $\beta^\dagger \to \infty$.

Although for $\beta^\dagger > 0$ the midpoint of the integrated flux is approximately zero,

we see negative peaks of flux at either side of it. These might represent a sharpening of the $U(y) = -y^2$ profile, however we cannot read too much into these results; it is quite possible that they are a consequence of artificial boundary conditions. However, they do correspond quite closely to the flux of the $U(Y) = \mathrm{sn}(Y)$ profile given in figure 2.8c.

To summarize, we have seen that the flow around turning points in the mean flow can be reduced to a one-dimensional linear system of PDEs governed by a single parameter, $\beta^\dagger$. The form of the feedback on the mean is dependent on this parameter, with both laminar and oscillatory solutions being supported. These appear to relate to certain cases of the large-scale quasi-linear system, although there is still work to be done in researching the reduced equations.

2.6 Short-time Expansion

Although our large-scale expansion has successfully given us a lot of information on the effect of the frictional parameters λ and ν, describing the β-effect has been more complicated. Analyzing the interactions of a vorticity gradient with the background flow over large periods of time is an inherently difficult problem, due to the scale separation introduced by having small-scale waves on a large-scale zonal flow.

In an attempt to shed more light on these interactions, we now implement a short-time expansion, i.e. we look at the immediate reaction of the fluid to the background flow. As we are not assuming any scale separation between the mean flow and the wave-like perturbations, we can explore any size difference between these two structures (through the parameter m). We can make comparisons with the large-scale expansion by looking at the limit of small-scale perturbations in this short-time expansion, noting that $\varepsilon \to 0$ corresponds to $m \to \infty$. We start with the full quasi-linear equations for a fluid with a mean flow, as derived in section 2.2:

$$\partial_t \omega + imU\omega = im\left(\beta - \partial_y^2 U\right)\psi - \lambda\omega - \nu\left(m^2 - \partial_y^2\right)\omega, \tag{2.94}$$

$$\omega = \left(m^2 - \partial_y^2\right)\psi, \tag{2.95}$$

with our definition of the vertical flux of vorticity

$$F(y,t) = \langle v\omega \rangle_x = im\left(\omega\psi^\star - \omega^\star\psi\right). \tag{2.96}$$

Again, we define the integrated flux to be

$$\mathcal{F}(y,t) = \int_0^t F(y,t)dt, \tag{2.97}$$

with $\mathcal{F}_\infty(y) = \mathcal{F}(y, t\to\infty)$.

Taking the transformation

$$\omega(y,t) = \zeta(y,t)e^{-imUt-\lambda t}, \tag{2.98}$$

$$\psi(y,t) = \phi(y,t)e^{-imUt-\lambda t}, \tag{2.99}$$

and taking $\lambda \neq 0$ and $\nu = 0$, we obtain

$$\partial_t\zeta = im(\beta - U'')\phi, \tag{2.100}$$

$$\zeta = m^2(1+U'^2t^2)\phi + imt\left(U''\phi + 2U'\partial_y\phi\right) - \partial_y^2\phi, \tag{2.101}$$

where $U' \equiv \partial_y U$ for this section. The flux becomes

$$F(y,t) = im\left(\zeta\phi^\star - \zeta^\star\phi\right)e^{-2\lambda t}. \tag{2.102}$$

To take a short-time approximation, we expand our variables as power series in terms of time, t:

$$\zeta = \zeta_0 + \zeta_1 t + \zeta_2 t^2 + ... \tag{2.103}$$

$$\phi = \phi_0 + \phi_1 t + \phi_2 t^2 + ... \tag{2.104}$$

where ζ_0, etc, here should not be confused with ζ_0, etc, from section 2.4. For large bottom drag, λ, we can similarly expand the non-exponential terms of the flux as

$$F = \left(F_0 + F_1 t + F_2 t^2 + ...\right)e^{-2\lambda t}. \tag{2.105}$$

Using Laplace transforms, we calculate the integrated flux in terms of the expanded components of the flux:

$$\begin{aligned}\mathcal{F}_\infty(y) &= \int \left(F_0 + F_1 t + F_2 t^2 + ...\right)e^{-2\lambda t}dt \\ &= \sum_{n=0}^{\infty} \frac{n!}{(2\lambda)^{n+1}}F_n \\ &= \frac{F_0}{2\lambda} + \frac{F_1}{(2\lambda)^2} + \frac{2F_2}{(2\lambda)^3} + ...\end{aligned} \tag{2.106}$$

For strong surface drag, $\lambda \gg 1$, the integral of flux should converge towards some value, allowing us to disregard higher order terms in the series. Note that we have essentially exchanged t for λ here; short time scale behaviour corresponds to the effect of frictionally dissipating the flow via the drag. Essentially, the limit of small t is equivalent to the limit of large λ.

Expanding equations (2.100) and (2.101) and equating like powers of t, we obtain

$$\zeta_1 = im\left(\beta - U''\right)\phi_0, \tag{2.107}$$

$$\zeta_2 = im\left(\beta - U''\right)\phi_1, \tag{2.108}$$

etc, and

$$\zeta_0 = m^2\phi_0 - \phi_0'', \tag{2.109}$$

$$\zeta_1 = m^2\phi_1 + im\left(U''\phi_0 + 2U'\phi_0'\right) - \phi_1'', \tag{2.110}$$

$$\zeta_2 = m^2\phi_2 + m^2U'^2\phi_0 + im\left(U''\phi_1 + 2U'\phi_1'\right) - \phi_2'', \tag{2.111}$$

etc. Likewise, the flux can be expanded as

$$F_0 = im\left(\zeta_0\phi_0^\star - \zeta_0^\star\phi_0\right), \tag{2.112}$$

$$F_1 = im\left(\zeta_0\phi_1^\star - \zeta_0^\star\phi_1 + \zeta_1\phi_0^\star - \zeta_1^\star\phi_0\right), \tag{2.113}$$

$$F_2 = im\left(\zeta_0\phi_2^\star - \zeta_0^\star\phi_2 + \zeta_1\phi_1^\star - \zeta_1^\star\phi_1 + \zeta_2\phi_0^\star - \zeta_2^\star\phi_0\right), \tag{2.114}$$

etc. Note that we can also write the total flux as

$$F = -2m\sum_{j=0}^{\infty}\sum_{k=0}^{\infty}\Im\{\zeta_j\phi_k^\star\}t^{j+k}, \tag{2.115}$$

where the function $\Im$ denotes the imaginary part of its inputs. Purely real initial conditions will result in $\zeta_0, \phi_0 \in \mathbb{R}$, which in turn results in $F_0 = 0$.

Looking at the next order in the equations (for ζ_1, etc), we observe that real ζ_0 and ϕ_0 also give purely imaginary ζ_1 and ϕ_1. This pattern continues for the whole expansion, resulting in

$$F_n \begin{cases} = 0 & \text{for even } n \\ \neq 0 & \text{for odd } n. \end{cases} \tag{2.116}$$

Starting with the initial condition $\zeta_0 = 1$, we can solve these equation successively. Despite the above simplification, the algebra becomes increasingly complicated when calculating higher order terms and so we employ the use of the symbolic mathematical engine Maple.

Taking $U(y) = -\cos(y)$, we calculate the first term which contributes to the flux as being

$$F_1 = -\frac{2(m^2-1)}{m^2(m^2+1)}\cos(y). \tag{2.117}$$

Using equation (2.106), this relatively simple result tells us that for short times, and at the leading order, the integrated flux has a sinusoidal profile across the y domain, with a pre-factor involving the parameters m and λ. In particular, we can see that β has no influence on the flux at leading order.

The next contributive term to the flux is F_3, which we write it in terms of powers of β:

$$\begin{aligned} F_3 = &\frac{(m^2-1)(m^2+9)(9m^2-8)\cos(y) - 9m^2(m^2-1)(m^2-3)\cos(3y)}{3(m^2+1)^2(m^2+4)(m^2+9)} \\ &- \frac{2(m^2-1)(5m^2+8)\cos(2y)}{3(m^2+1)^2(m^2+4)^2}\beta + \frac{(m^2-1)\cos(y)}{3m^4(m^2+1)^3}\beta^2. \end{aligned} \tag{2.118}$$

It is worth considering the effect individual terms in F_1 and F_3 will have on the mean flow. Terms proportional to $-\cos(y)$ will have an anti-diffusive effect across the entire y domain. This will lead to a growth in magnitude of the mean profile, confirmed by equation (2.21). Diffusive terms (proportional to $+\cos(y)$) will have the opposite effect, diminishing the mean flow. As such, for fluxes which contain only $\pm\cos(y)$ terms, anti-diffusive behaviour will encourage zonal flows on the same scale as the initial mean flow, $U(y) = -\cos(y)$, while diffusive behaviour will homogenize the flow. This type of behaviour is observed in the leading order flux, F_1, with the type of diffusivity depending on the value of m; for $m > 1$ there will be an anti-diffusive feedback and the mean flow will be amplified, with diffusive behaviour occuring otherwise.

When additional sinusoidal terms are introduced to the mean flow, simply labelling the flow diffusive/anti-diffusive no longer gives a sense as to the type of zonal behaviour being encouraged. As F/U'' will now vary in y, there will gener-

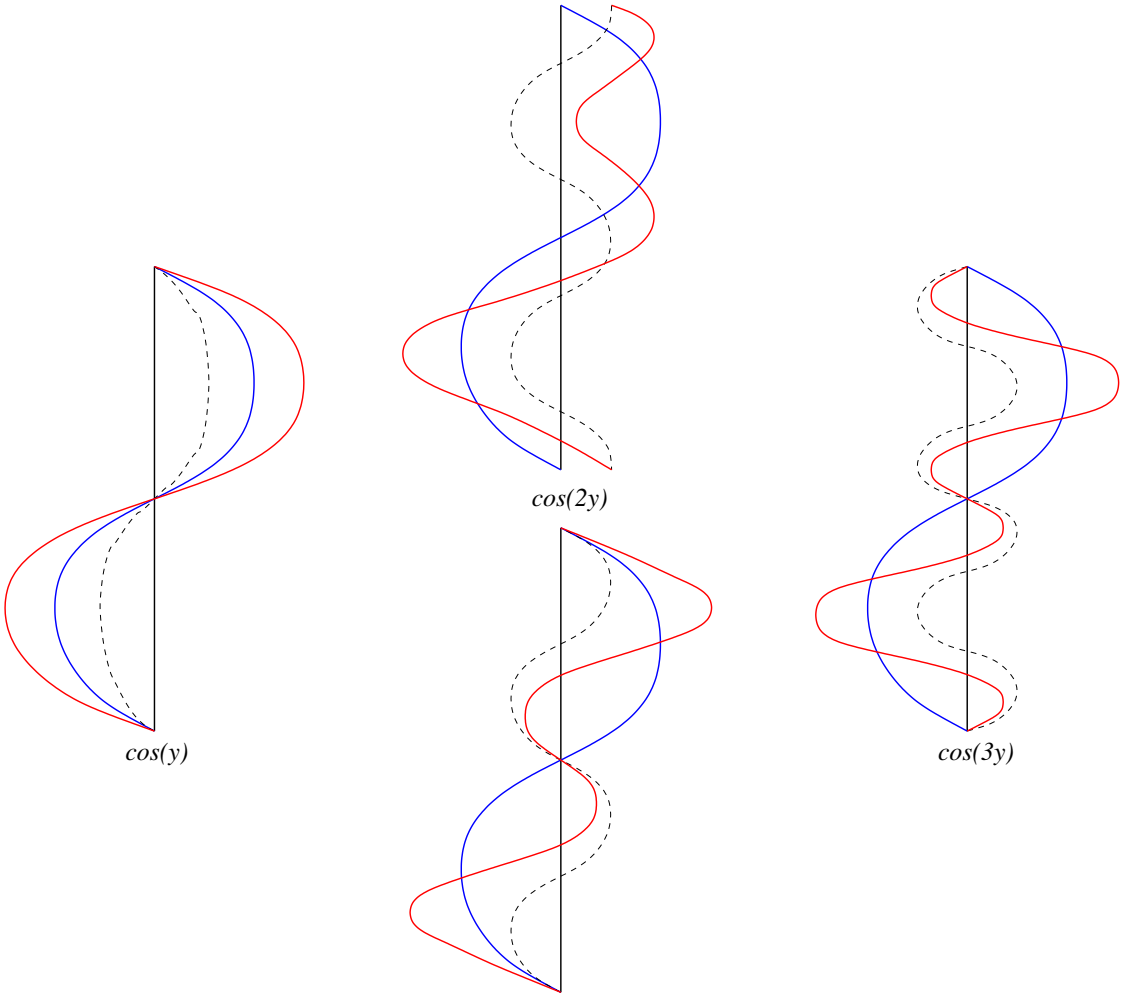

Figure 2.13: Schematic of the interactions between the mean flow and harmonic terms in the flux given by equations (2.117 – 2.118). The mean flow, $U(y)$, is given in blue, while the dotted profiles represent various cosine terms. The modifications to the mean flow, as given by equation (2.21), are plotted in red. Odd harmonics always maintain the rotational symmetry of the mean flow, while even harmonics may break it.

ally be regions in the flow of differing diffusivity. It is now more intuitive to look at the form of F, using equation (2.21) to determine how it will modify the mean flow. Odd harmonic terms, such as $\cos(3y)$ will amplify certain regions in the flow, promoting smaller length scales whilst retaining symmetry. Even harmonic terms, such as $\cos(2y)$ are more complicated; they can potentially break the symmetry of the mean flow, depending on the other terms making up the flux (note that in the

results of this thesis, we only observe symmetry breaking even harmonics). Each can have the effect of sharpening the gradients of $U(y)$, creating a more step-like structure commonly associated with β-plane jets. We plot each of these simplified types of behaviour in figure 2.13, noting that generally a combination of effects will take place for a moderate range of parameter values.

To make more sense of equation (2.118) we can look at the limits of several of the parameters. First turning our attention to β, we see that for a strong gradient of vorticity the last term in equation (2.118) will be dominant, which for our $U(y) = -\cos(y)$ profile will anti-diffusively reinforce the initial background mean flow when $m < 1$, and act diffusively otherwise. Indeed, for an individual point in y with constant $m \neq \pm 1$, equation (2.106) tells us that the integrated flux scales with β and λ as

$$\mathcal{F} \propto \frac{\beta^2}{\lambda^4}, \tag{2.119}$$

which is in agreement with results found by Srinivasan and Young (see [40], in particular page 9).

For a weak vorticity gradient, $\beta \ll 1$, the flux is instead dominated by the β^0 coefficient in (2.118), which contains a $\cos(3y)$ term. This will correspond to an additional harmonic in the flow profile, which, as it contains larger gradients, may lead to jet sharpening in zonal flows. Comparatively, the even harmonic introduced by the β^1 term in (2.118), will give bias to the direction of the flow (as seen in figure 2.13). Physically, this is to be expected; while the flow without external effects should be isotropic, the introduction of a gradient in the vorticity will affect the direction of the flow. We must be careful with all harmonics, as the feedback is given by F/U'', which will be complicated by the various cosine terms in (2.118).

Logically, we expect that for small-scale wave-like motions, $m \gg 1$, the entire flux will tend to dissipate as $m \to \infty$. This has been realised by the short-time expansion; both $F_1 \to 0$ and $F_3 \to 0$ as $m \to \infty$, and due to symmetry we expect further terms in the expansion to follow suit.

As for the behaviour of the flux in this small-scale limit, we find

$$F \simeq -\frac{2t}{m^2}\cos(y) + \frac{3t^3}{m^2}\left(\cos(y) - \cos(3y)\right). \tag{2.120}$$

For short times we see a generally anti-diffusive behaviour, which over time becomes a competition between diffusive behaviour and a tendency towards smaller scales. Notable, however, is the lack of β in equation (2.120). This, and the inclusion of the $\cos(3y)$ term, indicates that for very small-scale waves travelling across a large-scale background flow, the mechanism for sharpening the profile of the mean flow or pushing it to smaller scales is the feedback of the flow itself, rather than the β-effect.

This limit is of particular importance, as it relates directly to the approximations made in the large-scale expansion, investigated in section 2.4. In particular, we found that the β-effect had no influence on the flux at leading order. This is also the case for the short-time expansion; both the large-scale and short-time expansions have reassuringly similar forms, with both taking $F \sim -2tm^{-2}$ at leading order. The feedback for the $m \gg 1$ limit of the short-time case is simpler, with anti-diffusive behaviour across the entire profile, whereas more structure is given in equation (2.85) for the large-scale flux.

At higher orders of accuracy, equation (2.85) indicated that β would push the flux to smaller scales, but with the expansion for the flux becoming disordered for large β. For the corresponding short-time flux (at large values of t), β does not affect the feedback. In fact, if we look at the trend for where the dominant m terms in equations (2.117) and (2.118) occur, it becomes clear that the flux will never contain any β terms in this $m \gg 1$ limit, regardless of expansion in t. As such, we can conclude that for small waves on a large-scale flow, the vorticity gradient simply does not affect the mean flow on short time scales; this partially explains the difficulty in exploring the β-effect at higher orders of the large-scale expansion.

Interestingly, in the limit of large-scale motion, $m \ll 1$, which corresponds to the case of forcing the flow at a larger scale than that of the mean flow, we find the total flux to be

$$F \simeq \frac{2t}{m^2}\cos(y) - \frac{\beta^2 t^3}{3m^4}\cos(y). \tag{2.121}$$

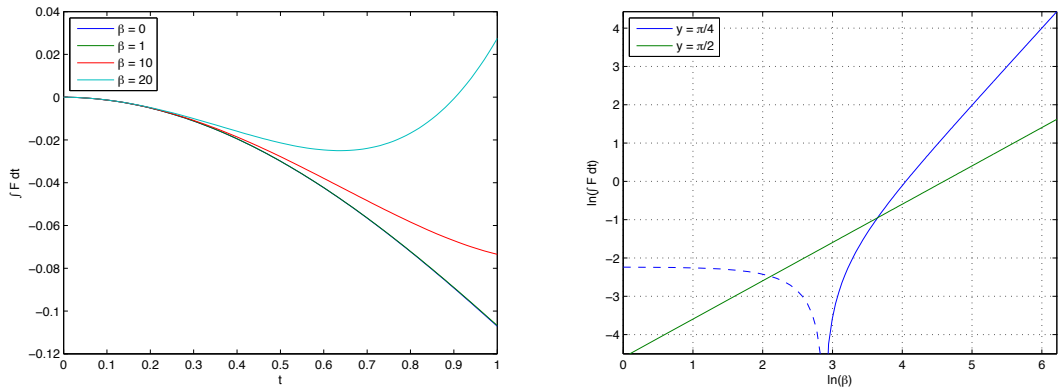

(a) (b)

Figure 2.14: The integrated flux, $\mathcal{F}$, found by taking the inviscid short-time expansion, up to and including $O(t^3)$ terms for: (a) a single point, $y_0 = \pi/4$ evolving over time (corresponding to a general $U(y) = -\cos(y) \neq 0$, and (b) the log-log scaling relationship of $\mathcal{F}$ to β for two points, the first for $U(y) \neq 0$, as in (a), and the second for $U(y) = 0$. Note that for points with $\mathcal{F} < 0$, the log of the real part of the integrated flux has been plotted by a dashed line. In both of these plots $m = \sqrt{5/2}$.

We can see that in this limit, due to the common $\cos(y)$ terms in F, the feedback on the mean flow will be homogeneous across y, with a diffusive effect at leading order (in contrast to the anti-diffusive feedback on small-scale waves). For large β the second order term grows and we see anti-diffusive behaviour as the flow evolves. However, we have to be cautious here as the expansion will quickly become disordered due to the size of β in the higher order terms.

We plot the full short-time expansion of the flux up to and including the $O(t^3)$ terms for several values of β and m, with $\lambda = 0$ in figures 2.14 and 2.15. In figure 2.14 we look at the integrated flux of a single point, $\mathcal{F}(y_0)$, while varying β and keeping a constant $m = \sqrt{5/2}$. In 2.14a, we see that increasing β will produce a diffusive effect, which will reduce the anti-diffusive behaviour of the leading order term. We confirm the relation given by equation (2.119) in figure 2.14b, where we plot the log-log graph of the dependence of $\mathcal{F}$ on β. Although we have only shown

this for a single point y_0 (as used in figure 2.14a), we have checked and confirmed this relation for a range of y. In particular, we observe a critical point at $\beta_c \approx e^3$, which separates totally anti-diffusive behaviour (for $\beta < \beta_c$) from totally diffusive behaviour for an integration time $t = 1$.

For points approaching $\cos(y) = 0$, the flux scales with β differently to the surrounding flow. Around these regions, $F_1 = 0$, while equation (2.118) gives

$$F_3 = \frac{2(m^2-1)(5m^2+8)}{3(m^2+1)^2(m^2+4)^2}\beta, \tag{2.122}$$

which in the large β limit results in the integrated flux becoming

$$\mathcal{F} \propto \frac{\beta}{\lambda^4}, \tag{2.123}$$

as can be seen in figure 2.14b. Note that the figure indicates that this scaling persists for all of β, which is to be expected, as the gradient of the flux given in the small β limit would be determined by the β^1 terms in (2.118). This is important: it implies different regions of the flow (corresponding to the appropriate points in the mean flow) will exhibit different levels of diffusivity, leading to a change in the profile of the mean flow.

We examine the evolution of the entire profile of integrated flux over time in figure 2.15. As the key point of interest here is the tendency of the jet towards diffusive or anti-diffusive behaviour, contours of $\mathcal{F} = 0$ have been plotted in black. Note, however, that $U''(y) = \cos(y)$ changes sign on the range of y we have given in these figures, and as such the behaviour may change at these points. As discussed previously, the flux exhibits a diffusive effect across the background flow in the large β limit, which occurs for $\beta > 50$. For mid-range values of β we see how harmonics influence the flux, with several additional 'jets' forming at $\beta = 20$. In the large β ranges, we observe the transition from a state with an anti-diffusive central column to a diffusive one, although, as previously noted, the expansion will become disordered at large times, meaning β will simply reduce the anti-diffusve effect of the leading order flux.

In summary, we have seen that a variety of diffusive and anti-diffusive feedbacks are possible under the short-time expansion of the quasi-linear equations for a

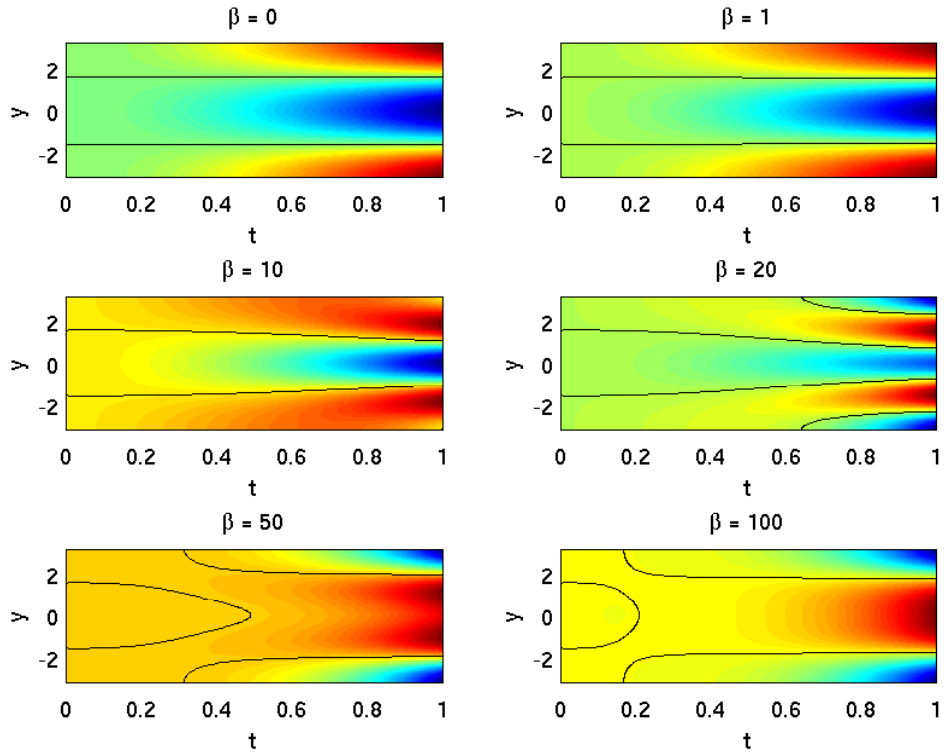

Figure 2.15: Shaded contour plot of the integrated flux, $\mathcal{F}(y,t)$, found by taking the inviscid short-time expansion, up to and including $O(t^3)$ terms for $U(y) = -\cos(y)$, $m = \sqrt{5/2}$ and several values of β as indicated in the figure. Contours of $\mathcal{F} = 0$ have been overlayed in black.

sinusoidal mean flow, $U(y) = -\cos(y)$. As the form of the flux is complicated, we have looked at the limit of several of the key parameters in the system. At certain wavenumbers, important changes to the flow take place, such as $m = \pm 1$ determining whether the flux is positive or negative at leading order. For large m (which corresponds to small-scale waves on a large background field, the focus of this investigation), the flux is anti-diffusive across the y-domain at leading order. For large β, the feedback has a competing diffusive effect, which will reduce the level of anti-diffusivity of the flow. For moderate parameter values complicated behaviour occurs, which includes indications that the vorticity gradient breaks the symmetries in the feedback, potentially leading to an anisotropic mean flow.

2.7 Conclusion

To briefly recap, we present the key results of this chapter in the following list:

- We have found and given a general formula for the flux of a quasi-linear flow in terms of the stream function of the waves launched on the mean flow (see equation (2.35). This can be used to find the flux from any equation (or approximation) governing the stream function.

- For a large-scale expansion of the governing equations, we found that regions of $U'(Y) = 0$ in the mean flow tend to correspond to strong anti-diffusive regions of flux. These will modify the mean flow, enabling transport and potentially leading to jet-like or self-narrowing (and hence zonal flow maintaining) behaviour.

- In these $U'(Y) = 0$ regions, the expansion used becomes disordered at large times and so an alternative approximation is required to explore them in more detail. We found that the behaviour of the flow at these points corresponds to a simplified single parameter linear partial differential equation, which we explored numerically.

- In our large-scale expansion we found that frictional forces, such as drag and viscosity, can 'cut off' the flux before it changes sign and becomes positive, resulting in a purely anti-diffusive feedback.

- We found that β has no leading order effect on the mean flow. This was the case for both the large-scale and short-time expansions. For the large-scale feedback, β tends to introduce small-scale oscillations in the mean flow, but is difficult to quantify otherwise. In the short-time flux, β introduces symmetry breaking terms, allowing for the flow to become anisotropic. However, in the limit of large β, it simply weakens the anti-diffusive nature of the leading order feedback.

In the following chapters we will discuss the MHD extension to this quasi-linear analysis (chapter 3), and look at numerical simulations of the full nonlinear

governing equations (chapters 4 – 7), making comparisons to these results in chapter 8.

Chapter 3

MHD Quasi-linear Analysis

3.1 Introduction

In this chapter we extend the quasi-linear approximation investigated in chapter 2 to include flows subject to a background magnetic field. Similarly to the purely hydrodynamical case, we separate mean flow and perturbations to it, and concentrate on the feedback on the mean from the waves. This feedback now also consists of a Lorentz force term, while an additional flux, the magnetic flux, determines the feedback on the magnetic field.

For the case of a linear shear there is no feedback on the mean flow (as in the HD case), while the magnetic flux is generally non-zero. In the absence of frictional or other external effects, the vorticity and magnetic field can each be described by a second order homogeneous ODE, although solutions to these cannot be found analytically. Taking a large-scale expansion by investigating small-scale perturbations on a large-scale background flow, we find that at leading order the equations reduce to the same form as the linear shear case. As such, without using numerical methods, this approximation does little to aid our investigation of the flow.

In order to try and establish analytical solutions to the quasi-linear equations, we again turn to the short-time expansion. Despite being complicated by the magnetic field, the short-time equations are solvable, and allow us to pull apart features of the flow. We look at several limits of the parameter regime, with a focus on the diffusive/anti-diffusive feedbacks of the magnetic field and flow.

3.2 Governing Equations

An incompressible, two-dimensional, viscously decaying, electrically conducting fluid on a β-plane, with frictional drag at its bottom surface can be described by the following equations:

$$\partial_t \Omega = J(\Psi, \Omega) + \beta \partial_x \Psi - \lambda \Omega + \nu \nabla^2 \Omega + J(A, \nabla^2 A), \tag{3.1}$$

$$\partial_t A = J(\Psi, A) + \eta \nabla^2 A, \tag{3.2}$$

where $\Omega(x, y, t)$ is the normal component of the fluid vorticity, $\Psi(x, y, t)$ is the corresponding stream function, β is the gradient of the Coriolis force, λ is the coefficient of drag and ν is the fluid viscosity, which can be thought of as an inverse Reynolds number [9]. Equation (3.2) is found by 'un-curling' the magnetic induction equation, where η is the magnetic resistivity and $A(x, y, t)$ is the magnetic potential, related to the magnetic field, $\mathbf{B}(x, y, t)$, by

$$\mathbf{B} = (\partial_y A, -\partial_x A)\,. \tag{3.3}$$

The determinant of the Jacobian of Ω and Ψ is given by

$$J(\Psi, \Omega) = (\partial_x \Psi)(\partial_y \Omega) - (\partial_y \Psi)(\partial_x \Omega)\,, \tag{3.4}$$

etc, and the vorticity is related to the stream function by

$$\Omega = -\nabla^2 \Psi = -\left(\partial_x^2 \Psi + \partial_y^2 \Psi\right). \tag{3.5}$$

The components of the fluid velocity are related to the stream function by

$$\mathbf{u} = (\partial_y \Psi, -\partial_x \Psi)\,. \tag{3.6}$$

Similarly to chapter 2, we aim to solve equations (3.1) and (3.2) with the stream function relation, equation (3.5), but this is difficult due to their nonlinearity. We take a quasi-linear approach by only looking at wave-wave and wave-eddy effects, ignoring eddy-eddy interactions.

We split the variables into separate parts; contributions from the mean flow and the perturbations about it:

$$\Omega(x, y, t) = \widetilde{\Omega}(x, y, t) + \bar{\Omega}(y, t) = \widetilde{\Omega}(x, y, t) - \partial_y U(y, t), \tag{3.7}$$

$$\partial_y \Psi(x, y, t) = \partial_y \widetilde{\Psi}(x, y, t) + \partial_y \bar{\Psi}(y, t) = \partial_y \widetilde{\Psi}(x, y, t) + U(y, t), \tag{3.8}$$

$$A(x, y, t) = \widetilde{A}(x, y, t) + \int B(y, t) dy, \tag{3.9}$$

where we define the barred quantities U and B to be the x-averaged profiles of their respective variables, for example

$$\bar{\Omega}(y, t) \equiv \langle \Omega(x, y, t) \rangle_x\,. \tag{3.10}$$

Likewise, the vorticity and stream function perturbations are related by $\widetilde{\Omega} = -\nabla^2\widetilde{\Psi}$, while the magnetic quantities are related by $\widetilde{\mathbf{B}} = (\partial_y\widetilde{A}, -\partial_x\widetilde{A})$. From now on, we choose to work with the variable $U(y,t)$, the mean profile of the velocity. The β-plane vorticity equation becomes

$$\partial_t\left(\widetilde{\Omega} - \partial_y U\right) = J\left(\widetilde{\Psi}, \widetilde{\Omega}\right) - \partial_y^2 U\partial_x\tilde{\Psi} - U\partial_x\widetilde{\Omega} + \beta\partial_x\widetilde{\Psi} - \lambda\left(\widetilde{\Omega} - \partial_y U\right) + \nu\nabla^2\widetilde{\Omega} - \nu\partial_y^3 U + J\left(\widetilde{A}, \nabla^2\widetilde{A}\right) - B\partial_x\nabla^2\widetilde{A} + \partial_y^2 B\partial_x\widetilde{A}, \tag{3.11}$$

with corresponding magnetic induction equation

$$\partial_t\left(\widetilde{A} + \mathcal{A}\right) = J\left(\widetilde{\Psi}, \widetilde{A}\right) + B\partial_x\widetilde{\Psi} - U\partial_x\widetilde{A} + \eta\nabla^2\left(\widetilde{A} + \mathcal{A}\right), \tag{3.12}$$

where $\mathcal{A} = \int B dy$, and the Jacobian term is defined as in equation (3.4).

Assuming wave-like solutions

$$\widetilde{\Omega}(x,y,t) = \omega(y,t)e^{imx} + c.c., \tag{3.13}$$

$$\widetilde{\Psi}(x,y,t) = \psi(y,t)e^{imx} + c.c., \tag{3.14}$$

$$\widetilde{A}(x,y,t) = a(y,t)e^{imx} + c.c., \tag{3.15}$$

where *c.c.* refers to the complex conjugate of the preceding terms, we equate powers of e^{imx}, neglecting the eddy-eddy contributions from e^{2imx} and the corresponding complex conjugate parts. The evolution of the mean flow and magnetic field is given by

$$\partial_t\partial_y U = -im\partial_y\left(\psi\omega^\star - \psi^\star\omega\right) - \lambda\partial_y U + \nu\partial_y^3 U - im\partial_y\left(a\nabla^2 a^\star - a^\star\nabla^2 a\right), \tag{3.16}$$

$$\partial_t\mathcal{A} = im\partial_y\left(\psi A^\star - \psi^\star A\right) + \eta\partial_y B, \tag{3.17}$$

where * represents the complex conjugate of the corresponding variable. The perturbation equations, obtained by equating the e^{imx} terms, are:

$$\partial_t\omega + imU\omega = im\left(\beta - \partial_y^2 U\right)\psi - \lambda\omega - \nu\left(m^2 - \partial_y^2\right)\omega + imB\left(m^2 - \partial_y^2\right)a + im\partial_y^2 Ba, \tag{3.18}$$

$$\partial_t a + imUa = imB\psi - \eta\left(m^2 - \partial_y^2\right)a. \tag{3.19}$$

As in the previous section, we can write the non-frictional parts of equation (3.16) in terms of a newly defined quantity, $F(y,t)$. However, with the addition of magnetic terms, we now write

$$F = F_K + F_L, \tag{3.20}$$

where

$$F_K(y,t) = im\left(\omega\psi^\star - \omega^\star\psi\right), \tag{3.21}$$

$$F_L(y,t) = im\left(a^\star\nabla^2 a - a\nabla^2 a^\star\right). \tag{3.22}$$

Previously, F was described as the x-averaged vertical vorticity flux; indeed this term still remains in (3.16) as the kinetic flux, F_K. However we also have the additional magnetic term, F_L (originating from the Lorentz force), which although not technically a flux, will be grouped in F for convenience.

The mean induction equation, (3.17), also contains the 'magnetic flux', F_M:

$$F_M(y,t) = im\left(a\psi^\star - a^\star\psi\right), \tag{3.23}$$

which is the x-averaged vertical magnetic potential flux. Note that these two quantities, F_K and F_M, come about due to the approximate material conservation of vorticity and magnetic field in the fluid (in the absence of forcing and dissipation):

$$D_t\boldsymbol{\Omega} = \partial_t\boldsymbol{\Omega} + \mathbf{u}\cdot\nabla\boldsymbol{\Omega} = 0, \tag{3.24}$$

$$D_t\mathbf{B} = \partial_t\mathbf{B} + \mathbf{u}\cdot\nabla\mathbf{B} = 0. \tag{3.25}$$

The mean equations, (3.11) and (3.12), in the absence of drag, viscosity and resistivity ($\lambda = \nu = \eta = 0$), are

$$-\partial_t\left(\partial_y U\right) + \partial_y F = 0, \tag{3.26}$$

$$\partial_t\mathcal{A} + \partial_y F_M = 0. \tag{3.27}$$

In the purely hydrodynamical case, we wrote the mean flow equation as a diffusivity equation, the form of which was determined by the kinetic flux. Similarly, here we have

$$\partial_t U' = \partial_y\left(\left(\frac{F_K}{U''}\right)U'' + F_L\right), \tag{3.28}$$

$$\partial_t\mathcal{A} = \partial_y\left(\left(-\frac{F_M}{B}\right)B\right), \tag{3.29}$$

where for simplicity of notation, we have set $U' \equiv \partial_y U$, etc. Note that we expect the factors U'' and B to appear in F_K and F_M respectively. We cannot make such predictions about the Lorentz flux, making its effect less clear.

However, in general we observe that the kinetic and magnetic fluxes will have the following feedback on their respective mean variables:

$$\begin{aligned} &\frac{F_K}{U''} \text{ or } -\frac{F_M}{B} > 0 \Rightarrow \text{diffusive}, \\ &\frac{F_K}{U''} \text{ or } -\frac{F_M}{B} < 0 \Rightarrow \text{anti-diffusive}. \end{aligned}$$

Alternatively, we can integrate (3.26) and (3.27) to obtain

$$U(y,t) = U(y,0) + \mathcal{F}(y,t), \tag{3.30}$$

$$B(y,t) = B(y,0) - \partial_y^2 \mathcal{F}_M(y,t), \tag{3.31}$$

where

$$\mathcal{F} = \mathcal{F}_K + \mathcal{F}_L = \int_0^t F_K dt + \int_0^t F_L dt, \tag{3.32}$$

$$\mathcal{F}_M = \int_0^t F_M dt. \tag{3.33}$$

As such, we can see the key role the fluxes (and their time-integrals) play in the evolution of both the mean flow and magnetic field. For future reference, we also define

$$\mathcal{F}_{K\infty}(y) \equiv \mathcal{F}_K(y, t \to \infty) = \int_0^\infty F_K(y,t) dt, \tag{3.34}$$

etc. If we prescribe the background mean flow to be constant in time, $U = U(y)$, equations (3.18) and (3.19), along with the stream function relation

$$\omega = \left(m^2 - \partial_y^2\right) \psi, \tag{3.35}$$

give us a system of three, spatially one-dimensional partial differential equations to solve.

We can look for solutions to a particularly simplified form of these equations and use these to remove the fast advection term from the main equations:

$$\omega(y,t) = \zeta(y,t) e^{-imUt}, \tag{3.36}$$

$$\psi(y,t) = \phi(y,t) e^{-imUt}, \tag{3.37}$$

$$a(y,t) = \chi(y,t) e^{-imUt}, \tag{3.38}$$

which is akin to taking a local Galilean transformation following the shear. Unlike the previous chapter, due to the coupled nature of the bottom drag in (3.18), we cannot factorize it out of the governing equations. As such, it will play a more complicated role when calculating the fluxes.

The derivatives of ω, ψ and a are given by

$$\partial_t \omega = \left[\partial_t \zeta - imUt\zeta\right] e^{-imUt}, \tag{3.39}$$

$$\partial_y \omega = [\partial_y \zeta - imU't\zeta] e^{-imUt}, \tag{3.40}$$

$$\partial_y^2 \omega = [\partial_y^2 \zeta - imt\left(2U'\partial_y \zeta + U''\zeta\right) - m^2 U'^2 t^2] e^{-imUt}, \tag{3.41}$$

etc. This gives the following system of equations:

$$\partial_t \zeta = im(\beta - U'')\phi - \lambda\zeta - \nu\mathcal{L}(\zeta) + imB\mathcal{L}(\chi) + imB''\chi, \tag{3.42}$$

$$\partial_t \chi = imB\phi - \eta\mathcal{L}(\chi), \tag{3.43}$$

$$\zeta = \mathcal{L}(\phi), \tag{3.44}$$

$$\mathcal{L}(\phi) \equiv m^2(1 + U'^2 t^2)\phi + imt\left(U''\phi + 2U'\partial_y \phi\right) - \partial_y^2 \phi. \tag{3.45}$$

Here, $\mathcal{L}$ corresponds to the Laplacian operator, taking into account the effect of the removal of the advection terms from the flow.

The fluxes can be written in terms of our new variables as:

$$F_K(y,t) = im\left(\zeta\phi^\star - \zeta^\star\phi\right), \tag{3.46}$$

$$F_L(y,t) = -im\left(\chi^\star\mathcal{L}(\chi) - \chi\mathcal{L}(\chi)^\star\right), \tag{3.47}$$

$$F_M(y,t) = im\left(\chi\phi^\star - \chi^\star\phi\right). \tag{3.48}$$

We see that fast-advection terms have no influence on the flux, and that unlike the purely hydrodynamical case, drag will come into play in determining the form of ζ, ϕ and χ.

Using the relationship between ζ and ϕ (as given in equation (3.44)), and χ and $\mathcal{L}(\chi)$, we can write the kinetic and Lorentz fluxes as:

$$F_K = -\left[2m^2 t\partial_y\left(U'|\phi|^2\right) + im\left(\phi^\star\partial_y^2\phi - \phi\partial_y^2\phi^\star\right)\right], \tag{3.49}$$

$$F_L = 2m^2 t\partial_y\left(U'|\chi|^2\right) + im\left(\chi^\star\partial_y^2\chi - \chi\partial_y^2\chi^\star\right). \tag{3.50}$$

These can be combined via an Elsasser-type approach (where typically one would investigate $U + B$ and $U - B$ as single quantities), and the total feedback on the mean flow written as

$$F = -2m\left[mt\partial_y\left(U'(|\phi|^2 - |\chi|^2)\right) - \Im\{\phi^\star\partial_y^2\phi - \chi\partial_y^2\chi^\star\}\right] \tag{3.51}$$

Further progress on the flux cannot be made without looking for solutions to the system of equations given by (3.42 – 3.45). In this chapter we aim to find these solutions by looking at various approximations to the governing equations.

3.3 Linear Shear

With a complicated and entangled system of partial differential equations to solve, it is helpful to first look at the simplest non-trivial case; $U(y) = \alpha y$ and $B(y) = B_0$, for constant α and B_0.

Given constant initial conditions, we expect a frictionless flow with no dissipation ($\lambda = \nu = \eta = 0$) to evolve identically at all points in the y-domain, with only a difference in phase which can be removed from the equations via a Galilean transformation. As such, we can assume that ζ, ϕ and χ are independent of vertical position:

$$\omega(y,t) = \zeta(t)e^{-im\alpha yt}, \tag{3.52}$$

$$\psi(y,t) = \phi(t)e^{-im\alpha yt}, \tag{3.53}$$

$$a(y,t) = \chi(t)e^{-im\alpha yt}. \tag{3.54}$$

On inspection of equations (3.49) and (3.50), it should be immediately clear that the total feedback on the mean flow, $F = F_K + F_L$, will be zero for a linear shear flow. However, the feedback on the mean magnetic field is not quite so obvious. To investigate this we start by writing our new system of equations:

$$\partial_t\zeta = im\beta\phi + imB_0\mathcal{L}(\chi), \tag{3.55}$$

$$\partial_t\chi = imB_0\phi, \tag{3.56}$$

$$\zeta = \mathcal{L}(\phi), \tag{3.57}$$

$$\mathcal{L}(\phi) = m^2(1 + \alpha^2t^2)\phi, \tag{3.58}$$

which, for no background vorticity gradient, $\beta = 0$, reduces to

$$\partial_t \zeta = im^3 B_0 (1 + \alpha^2 t^2) \chi, \tag{3.59}$$

$$\partial_t \chi = im^{-1} B_0 (1 + \alpha^2 t^2)^{-1} \zeta. \tag{3.60}$$

There is interesting symmetry in these two equations, which remains when separating variables to write as two second-order ODEs:

$$\frac{\partial^2 \zeta}{\partial t^2} - \frac{2\alpha^2 t}{1 + \alpha^2 t^2} \frac{\partial \zeta}{\partial t} + m^{-2} B_0^2 \zeta = 0, \tag{3.61}$$

$$\frac{\partial^2 \chi}{\partial t^2} + \frac{2\alpha^2 t}{1 + \alpha^2 t^2} \frac{\partial \chi}{\partial t} + m^2 B_0^2 \chi = 0. \tag{3.62}$$

Unfortunately, these two equations cannot be solved in terms of standard functions, only Heun functions, which tell us little about the structure of the two fields. It may be possible to rearrange these equations in such a way that more information about the variables or fluxes in the problem can be gained. Likewise, numerical methods can be used to integrate the equations, giving specific solutions for a choice of parameter values. However, we defer this to later research, and proceed to look at further approximations to the governing equations.

3.4 Large-scale Expansion

Similarly to section 2.4, we aim to use a large-scale expansion of the terms involved in equations (3.42 – 3.45) in order to explore the quasi-linear system in more detail. We rescale the entire problem by introducing the parameter ε:

$$Y = \varepsilon y, \ T = \varepsilon t,$$

$$\tilde{U}(Y) = U(y), \ \tilde{\zeta}(Y,T) = \zeta(y,t), \ \tilde{\phi}(Y,T) = \phi(y,t), \ \tilde{\chi}(Y,T) = \chi(y,t). \tag{3.63}$$

and now write $\partial_Y \left(\tilde{U}(Y,T) \right) \equiv \tilde{U}'$, etc. Omitting the tildes from the appropriate variables, equations (3.42 – 3.45) become

$$\varepsilon \partial_T \zeta = im(\beta - \varepsilon^2 U'') \phi - \lambda \zeta - \nu \mathcal{L}(\zeta) + imB \mathcal{L}(\chi) + im\varepsilon^2 B'' \chi, \tag{3.64}$$

$$\varepsilon \partial_T \chi = imB\phi - \eta \mathcal{L}(\chi), \tag{3.65}$$

$$\zeta = \mathcal{L}(\phi), \tag{3.66}$$

$$\mathcal{L}(\phi) \equiv m^2 (1 + U'^2 T^2) \phi + \varepsilon imT \left(U'' \phi + 2U' \phi' \right) - \varepsilon^2 \phi'', \tag{3.67}$$

where $\partial_Y \phi(Y,T) \equiv \phi'$, etc, and noting the change in the operator $\mathcal{L}$.

Like the HD case, no approximations (other than the initial quasi-linear approximation) have been made thus far, and the transformation given in (3.63) is exact.

We now choose for $U(Y)$ to be large in scale, that is $\varepsilon \ll 1$. On the assumption that there is good scale separation, we write

$$\zeta(Y,T) = \zeta_0(Y,T) + \varepsilon\zeta_1(Y,T) + \varepsilon^2\zeta_2(Y,T) + ..., \tag{3.68}$$

with similar expansions for ϕ and χ. This approximation is valid given $\zeta_0 \gg \varepsilon\zeta_1 \gg \varepsilon^2\zeta_2 \gg ...$, etc. We aim to solve the system of equations, (3.64 – 3.67) by equating powers of ε. In order for the system to be well ordered and solvable we need to make certain assumptions about the magnitude of the parameters involved. The largest β, λ, ν, B and η can be is $O(\varepsilon)$, leading us to take

$$\beta = \varepsilon\tilde{\beta},\ \lambda = \varepsilon\tilde{\lambda},\ \nu = \varepsilon\tilde{\nu},\ B = \varepsilon\tilde{B},\ \eta = \varepsilon\tilde{\eta}, \tag{3.69}$$

where we assume all tilde variables are $O(1)$. Note that for the parameters involved in the purely hydrodynamic investigation, these values are unchanged. Equating terms proportional to ε^0 in our expanded system of equations, we have

$$\partial_T\zeta_0 = im\tilde{\beta}\phi_0 - \tilde{\lambda}\zeta_0 - \tilde{\nu}m^2f^{-1}\zeta_0 + im^3f^{-1}\tilde{B}\chi_0, \tag{3.70}$$

$$\partial_T\chi_0 = im^{-1}f\tilde{B}\phi_0 - \tilde{\eta}m^2f^{-1}\chi_0, \tag{3.71}$$

$$\zeta_0 = m^2f^{-1}\phi_0, \tag{3.72}$$

where

$$f(Y,T) = (1 + U'^2T^2)^{-1}. \tag{3.73}$$

Unfortunately, it is impossible to give analytical solutions to equations (3.70 – 3.72) due to how tightly interwoven ζ_0, ϕ_0 and χ_0 are. Reducing all of the parameters other than $\tilde{B}$ to zero (noting that setting $\tilde{B} = 0$ simply reverts the equations to the HD case) and cancelling ϕ_0, we have

$$\partial_T\zeta_0 = im^3f^{-1}\tilde{B}\chi_0, \tag{3.74}$$

$$\partial_T\chi_0 = im^{-1}f\tilde{B}\phi_0. \tag{3.75}$$

The above equations are identical in form to equations (3.59 – 3.60) which govern the evolution of the waves on a linear shear flow. As such, we observe that our first order approximation is equivalent to assuming a linear background flow and constant B field. As in section 3.3, the only solutions to (3.59) and (3.60) are Heun functions which, without solving numerically, tell us little about the state of the flow and cannot be used to find meaningful values of the flux.

As such we are stuck; even at leading order with the simplest set of parameters to describe the MHD system, we cannot solve the large-scale quasi-linear equations analytically. One approach would be to integrate them numerically; this would allow us to investigate each parameter individually and find the general feedback on the mean, although we would not easily be able to tell at what order of magnitude the parameters take effect, or if the system is becoming disordered.

However, we choose not to look at this in the current thesis, and refer the reader to future work in which we resume this line of investigation. Instead, we look at the short-time expansion, as taken in the hydrodynamical case in section 2.6.

3.5 Short-time Expansion

Having gained little information from the linear shear flow and large-scale approximations, we aim to use a short-time expansion similar to that given in section 2.6. This makes no assumption about scale separation in the flow, instead it will only give information about very small time scale reactions to the perturbations of the mean flow.

Starting with the quasi-linear MHD equations derived earlier in this chapter, with the addition of artificial drag on the magnetic field:

$$\begin{aligned}\partial_t\omega + imU\omega = im\left(\beta - \partial_y^2 U\right)\psi - \lambda\omega - \nu\left(m^2 - \partial_y^2\right)\omega \\ + imB\left(m^2 - \partial_y^2\right)a + im\partial_y^2 Ba, \qquad (3.76)\end{aligned}$$

$$\partial_t a + imUa = imB\psi - \lambda a - \eta\left(m^2 - \partial_y^2\right)a, \qquad (3.77)$$

$$\omega = \left(m^2 - \partial_y^2\right)\psi. \qquad (3.78)$$

Although the magnetic drag term is not physical, its addition is necessary in order

to make good progress with the equations. Regardless of physical motivations, λ is not an integral part of our flow in this limit, and its effect is the equivalent to 'cutting off' the flow after an amount of time proportional to λ^{-1}. However, we will still attempt to gain some information regarding its scaling with the flux.

Taking the operator $\mathcal{L} \equiv (m^2 - \partial_y^2)$ to represent the negative Laplacian in our current configuration, the kinetic, Lorentz and magnetic fluxes are respectively defined as

$$F_K(y,t) = im\left(\omega\psi^\star - \omega^\star\psi\right), \tag{3.79}$$

$$F_L(y,t) = im\left(a\mathcal{L}a^\star - a^\star\mathcal{L}a\right), \tag{3.80}$$

$$F_M(y,t) = im\left(a\psi^\star - a^\star\psi\right), \tag{3.81}$$

with $F = F_K + F_L$, and

$$\mathcal{F}(y,t) = \int_0^t F(y,t)dt, \tag{3.82}$$

with $\mathcal{F}_\infty(y) = \mathcal{F}(y, t \to \infty)$.

Taking the transformation

$$\omega(y,t) = \zeta(y,t)e^{-imUt-\lambda t}, \tag{3.83}$$

$$\psi(y,t) = \phi(y,t)e^{-imUt-\lambda t}, \tag{3.84}$$

$$a(y,t) = \chi(y,t)e^{-imUt-\lambda t}, \tag{3.85}$$

and taking $\lambda \neq 0$ and $\nu = 0$, we obtain:

$$\begin{aligned}\partial_t\zeta &= im(\beta - U'')\phi \\ &\quad + imB\left[m^2(1+U'^2t^2)\chi + imt(U''\chi + 2U'\partial_y\chi) - \partial_y^2\chi\right] + imB''\chi,\end{aligned} \tag{3.86}$$

$$\partial_t\chi = imB\phi, \tag{3.87}$$

$$\zeta = m^2(1+U'^2t^2)\phi + imt\left(U''\phi + 2U'\partial_y\phi\right) - \partial_y^2\phi, \tag{3.88}$$

where $U' \equiv \partial_y U$ and $B' \equiv \partial_y B$ for this section. The fluxes become

$$F_K(y,t) = im\left(\zeta\phi^\star - \zeta^\star\phi\right)e^{-2\lambda t}, \tag{3.89}$$

$$F_L(y,t) = im\left(\chi\mathcal{L}\chi^\star - \chi^\star\mathcal{L}\chi\right)e^{-2\lambda t}, \tag{3.90}$$

$$F_M(y,t) = im\left(\chi\phi^\star - \chi^\star\phi\right)e^{-2\lambda t}, \tag{3.91}$$

where $\mathcal{L}$ (which still represents the Laplacian operator) has been redefined to follow the transformation:

$$\mathcal{L}(\chi) \equiv m^2(1 + U'^2t^2)\chi + imt\left(U''\chi + 2U'\partial_y\chi\right) - \partial_y^2\chi. \tag{3.92}$$

To take a short-time approximation, we expand our variables as power series in terms of time, t:

$$\zeta = \zeta_0 + \zeta_1 t + \zeta_2 t^2 + ... \tag{3.93}$$

$$\phi = \phi_0 + \phi_1 t + \phi_2 t^2 + ... \tag{3.94}$$

$$\chi = \chi_0 + \chi_1 t + \chi_2 t^2 + ... \tag{3.95}$$

For large bottom drag, λ, we can similarly expand the non-exponential terms of each of the fluxes:

$$F_K = \left(F_{K0} + F_{K1}t + F_{K2}t^2 + ...\right)e^{-2\lambda t}, \tag{3.96}$$

$$F_L = \left(F_{L0} + F_{L1}t + F_{L2}t^2 + ...\right)e^{-2\lambda t}, \tag{3.97}$$

$$F_M = \left(F_{M0} + F_{M1}t + F_{M2}t^2 + ...\right)e^{-2\lambda t}. \tag{3.98}$$

Using Laplace transforms, we calculate the integrated flux in terms of the expanded components of the flux:

$$\begin{aligned}\mathcal{F}_\infty(y) &= \int \left(F_0 + F_1 t + F_2 t^2 + ...\right)e^{-2\lambda t}dt \\ &= \sum_{n=0}^{\infty} \frac{n!}{(2\lambda)^{n+1}}F_n \\ &= \frac{F_0}{2\lambda} + \frac{F_1}{(2\lambda)^2} + \frac{2F_2}{(2\lambda)^3} + ...\end{aligned} \tag{3.99}$$

For strong surface drag, $\lambda \gg 1$, the integral of flux should converge towards some value, allowing us to disregard higher order terms in the series. Note that we have essentially exchanged t for λ here; short time scale behaviour corresponds to the effect of frictionally dissipating the flow via the drag. Essentially, the limit of small t is equivalent to the limit of large λ.

We use these results to expand our system of equations given by (3.86 – 3.88) and equate powers of t. We also make the assumption that the background mag-

netic field described by $B(y)$ is constant, $B(y) = B_0$. Equation (3.86) gives

$$\zeta_1 = im\left(\beta - U''\right)\phi_0 + imB_0\left(m^2\chi_0 - \chi_0''\right), \tag{3.100}$$

$$2\zeta_2 = im\left(\beta - U''\right)\phi_1 + imB_0\left(m^2\chi_1 + im(U''\chi_0 + 2U'\chi_0') - \chi_1''\right), \tag{3.101}$$

$$3\zeta_3 = im\left(\beta - U''\right)\phi_2 + imB_0\left(m^2\chi_2 + m^2U'^2\chi_0 + im(U''\chi_1 + 2U'\chi_1') - \chi_2''\right), \tag{3.102}$$

where $\chi'' = \partial_y^2\chi$, etc. Then, from equation (3.87) we obtain

$$\chi_1 = imB_0\phi_0, \tag{3.103}$$

$$2\chi_2 = imB_0\phi_1, \tag{3.104}$$

$$3\chi_3 = imB_0\phi_2. \tag{3.105}$$

For the stream function, we also need an equation to relate the initial condition to ϕ_0. Expanding equation (3.88) we have

$$\zeta_0 = m^2\phi_0 - \phi_0'', \tag{3.106}$$

$$\zeta_1 = m^2\phi_1 + im(U''\phi_0 + 2U'\phi_0') - \phi_1'', \tag{3.107}$$

$$\zeta_2 = m^2\phi_2 + m^2U'^2\phi_0 + im(U''\phi_1 + 2U'\phi_1') - \phi_2'', \tag{3.108}$$

$$\zeta_3 = m^2\phi_3 + m^2U'^2\phi_1 + im(U''\phi_2 + 2U'\phi_2') - \phi_3''. \tag{3.109}$$

Likewise, the kinetic flux can be expanded as

$$F_{K0} = im\left(\zeta_0\phi_0^\star - \zeta_0^\star\phi_0\right), \tag{3.110}$$

$$F_{K1} = im\left(\zeta_0\phi_1^\star - \zeta_0^\star\phi_1 + \zeta_1\phi_0^\star - \zeta_1^\star\phi_0\right), \tag{3.111}$$

$$F_{K2} = im\left(\zeta_0\phi_2^\star - \zeta_0^\star\phi_2 + \zeta_1\phi_1^\star - \zeta_1^\star\phi_1 + \zeta_2\phi_0^\star - \zeta_2^\star\phi_0\right), \tag{3.112}$$

with components of the Lorentz and magnetic fluxes being given similarly. We can also write each flux in total as

$$F_K = -2m\sum_{j=0}^{\infty}\sum_{k=0}^{\infty}\Im\{\zeta_j\phi_k^\star\}, \tag{3.113}$$

$$F_L = -2m\sum_{j=0}^{\infty}\sum_{k=0}^{\infty}\Im\{\chi_j\mathcal{L}\chi_k^\star\}, \tag{3.114}$$

$$F_M = -2m\sum_{j=0}^{\infty}\sum_{k=0}^{\infty}\Im\{\chi_j\phi_k^\star\}, \tag{3.115}$$

where the function $\Im$ denotes the imaginary part of a function. Purely real initial conditions will result in $\zeta_0, \chi_0, \phi_0, \in \mathbb{R}$, which in turn results in $F_{K0} = F_{L0} = F_{M0} = 0$.

Looking now at ζ_1, etc, we can see that real ζ_0, χ_0 and ϕ_0 also give purely imaginary ζ_1 and ϕ_1. This pattern continues for the whole expansion, resulting in

$$F_{Kn}, F_{Ln}, F_{Mn} \begin{cases} = 0 & \text{for even } n \\ \neq 0 & \text{for odd } n. \end{cases} \tag{3.116}$$

3.5.1 Mean Flow Feedback

Starting with the initial conditions $\zeta_0 = 1, \chi_0 = 0$, and prescribing $U(y) = -\cos(y)$, we can solve equations (3.100 – 3.109) successively in order to find the fluxes given by (3.113 – 3.115). Despite the above simplification, the algebra becomes increasingly complicated when calculating higher order terms and so we make use of the program Maple.

The first term in the expansion of the kinetic and Lorentz fluxes is calculated to be

$$F_{K1} = -\frac{2(m^2-1)}{m^2(m^2+1)}\cos(y), \tag{3.117}$$

$$F_{L1} = 0, \tag{3.118}$$

Here we can see that, to $O(t)$, the feedback on the mean flow, $F_1 = F_{K1} + F_{L1}$ is unchanged from the hydrodynamical case. In order to see how the magnetic field affects the feedback on the flow, we extend the expansion to t^3 terms:

$$\begin{aligned} F_{K3} = & \frac{(m^2-1)(m^2+9)(9m^2-8)\cos(y) - 9m^2(m^2-1)(m^2-3)\cos(3y)}{3(m^2+1)^2(m^2+4)(m^2+9)} \\ & - \frac{2(m^2-1)(5m^2+8)\cos(2y)}{3(m^2+1)^2(m^2+4)^2}\beta + \frac{(m^2-1)\cos(y)}{3m^4(m^2+1)^3}\beta^2 \\ & + \frac{2(3m^2-2)\cos(y)}{3(m^2+1)}B_0^2, \end{aligned} \tag{3.119}$$

$$F_{L3} = -\frac{2m^2\cos(y)}{m^2+1}B_0^2, \tag{3.120}$$

It is worth reminding ourselves of the simplified effect of individual terms in the flux on the mean flow. In general, an anti-diffusive feedback across y ($F \sim -\cos(y)$)

will promote the growth of the (magnitude of the) mean flow, while diffusive terms ($F \sim +\cos(y)$) will diminish it. Terms such as $\cos(2y)$, $\cos(3y)$, etc, are more complex, generally not giving a single diffusive/anti-diffusive feedback. For more complicated fluxes, it is often worth referring to equation (3.31), and considering the modification to $U(y)$ over time. For further discussion on this, please see section 2.6 and figure 2.13.

Equations (3.117 – 3.120) are reassuring due to their symmetry. As is well known, changing the polarity of the magnetic field has no effect on the flow of a plasma, as only the direction of the magnetic field lines will influence the feedback. As such, it is no surprise to find only even powers of B_0 in $F_3 = F_{K3} + F_{L3}$.

Likewise, we do not expect the magnetic field to show preference for any particular polarity of the flow. Hence, we should only see B_0 included with terms containing odd harmonics, as even harmonics will amplify peaks of the flow in one direction alone. This is clearly the case in the above equations, and we expect this to carry on throughout the expansion. Note that this is also the case for the flow's feedback on itself, as can be seen by the $\cos(3y)$ term in F_{K3}. On the other hand, β has no such restrictions on preference of direction, and so it is not surprising to observe the even harmonic $\cos(2y)$ in equation (3.120).

Due to the number of variables and complication of the above equations, we explore them in more detail by looking at different limits of key parameters. First we look at the $m \gg 1$ limit, which is the most applicable due to its crossover with the large-scale expansion, explored in detail for the hydrodynamic case in chapter 2. In this limit, we find the feedback on the mean flow to be

$$F \simeq -\frac{2t}{m^2}\cos(y) + \frac{t^3}{m^2}\left(3\left(\cos(y) - \cos(3y)\right) - \frac{4B_0^2}{3}\cos(y)\right), \tag{3.121}$$

where the $O(t^3)$ term results from the largest (in m) terms in F_K and F_L cancelling when combined. We can't definitively determine the diffusive/anti-diffusive behaviour from this, due to the $\cos(3y)$ term from the kinetic flux. However, the fact that there are only odd harmonics implies that the symmetry of the flow will remain the same, albeit with a push towards small-scale behaviour, and a possible sharpening of the mean profile. Our main observation of including a magnetic field

is that we will generally see $O(t^3)$ anti-diffusive effects coming into play (dependent on the size of B_0), reinforcing the leading order anti-diffusive effects.

Note also that in this limit the feedback has no β dependence, even at short times when F_{K1} is prevalent. This is an important result, as it very much confirms that β has no influence on transport of small-scale waves over short time periods; its effects must take place over long periods of time (even when a magnetic field is present).

Next in our investigation of different limits, we look at $B_0 \gg 1$ for general length-scale m. For the feedback on the mean-flow, B_0 has no effect at $O(t)$. As such, we look at the next largest term, noting that it will not be the dominant term in the general expansion:

$$F \simeq -\frac{4B_0^2 t^3}{3(m^2+1)}\cos(y). \tag{3.122}$$

Referring to the solution for F_{K1} found in (3.31), whilst noting $F_{L1} = 0$, we can see that for general $m > 1$, a strong magnetic field will encourage the already anti-diffusive behaviour of the flow. For small m, the field will compete with a diffusive F_{K1}.

Examining F for a general choice of parameters, the most important thing we learn about B_0 is that, in terms of its contribution to the feedback, it always affects the entire domain equally. For the flow's feedback on itself, it introduces odd harmonics, while β brings in additional even and odd harmonics. These lead to differing diffusive/anti-diffusive behaviour dependent on position relative to $U(y)$ with the flow maintaining symmetry, while β breaks it. The magnetic field, however, only contributes a $\cos(y)$ terms to the flux, and so when looking at the feedback, F/U'' will act homogeneously across the domain. In this sense, B_0 will always reinforce the original mean flow, potentially promoting jet-like motion (albeit without sharpening the jets). This is somewhat surprising, as we find that magnetic fields generally disrupt jets (see chapter 7). However, it may simply be the case that the short-time behaviour is weak in comparison to the long time action of the magnetic field.

In figure 3.1a we see how the integrated flux evolves over short periods of time,

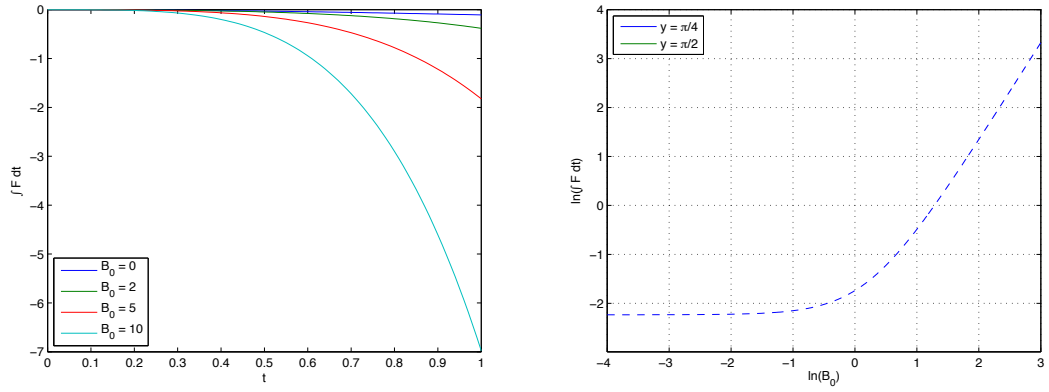

(a) (b)

Figure 3.1: The integrated flux, $\mathcal{F} = \mathcal{F}_K + \mathcal{F}_L$, found by taking the $O(t^3)$ short-time expansion given by equations (3.117 – 3.120) for: (a) a single point, $y_0 = \pi/4$ evolving over time (corresponding to a general $U(y) = -\cos(y) \neq 0$), and (b) the log-log scaling relationship of $\mathcal{F}$ to B_0 for two points, the first for $U(y) \neq 0$, as in (a), and the second for $U(y) = 0$. Note that for points with $\mathcal{F} < 0$, the real part of the log of the integrated flux has been plotted by a dashed line. In both of these plots $m = \sqrt{5/2}$ and $\beta = 0$.

with no additional β-effect. In particular, we can see that for this choice of m, y and β the integrated flux is negative regardless of the value of B_0, and continues to decrease as B_0 is increased.

In figure 3.1b, we see the relation of the integrated flux to the magnetic field at a final time $t = 1$. As suggested by equation (3.122), we have a $-B_0^2$ relation for large values of B_0, with a $-B_0^0$ trend for smaller values. We observe in this figure that for typical points such as $y = \pi/4$, the integrated flux is always anti-diffusive, whereas for points in the flow where $\cos(y) = 0$, there is a zero net contribution to the flux for $\beta = 0$ (hence the lack of a corresponding curve in the figure).

In figure 3.2 we can see more clearly the evolution of the integrated flux across the whole profile. Note that the color maps representing each subplot are assigned to different values, and so information regarding the magnitude of the flux is sacrificed for the sake of viewing the structure. In each case, the flux takes a

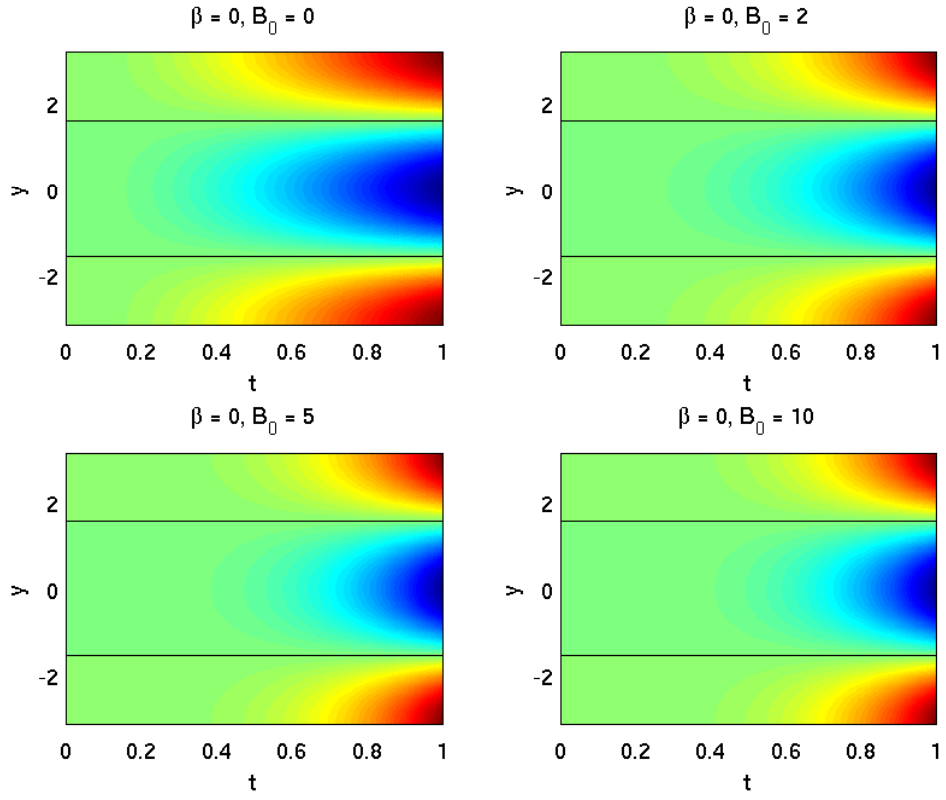

Figure 3.2: Shaded contour plot of the integrated flux, $\mathcal{F} = \mathcal{F}_K + \mathcal{F}_L$, found by integrating the $O(t^3)$ short-time expansion given by equations (3.117 – 3.120) for $U(y) = -\cos(y)$, $m = \sqrt{5/2}$, $\beta = 0$ and several values of B_0 as indicated in the figure. Contours of $\mathcal{F} = 0$ have been overlayed in black.

roughly $-\cos(y)$ profile, meaning that the feedback will be reinforcing the original $U(y) = -\cos(y)$ profile in some way. We observe that the points of $\mathcal{F} = 0$ remain constant at $y = \pi/2$ for all time across each profile. The magnitude of the flux is more evenly distributed in time for small values of B_0; the gradients leading to the maximum values of the profile (at $t = 1$) are sharper as B_0 increases. This is essentially displaying the dominance of the $B_0^2 t^3$ term in (3.119) and (3.120) for large values of B_0.

We now turn our attention to the additional effect β has on the two fluxes. Note that for smaller $O(1)$ values of β, there is very little change in the profile and structure of $\mathcal{F}$, and so we choose to look at a value of $\beta = 50$ throughout.

In figure 3.3a we again see the evolution of a typical point over time. Similar

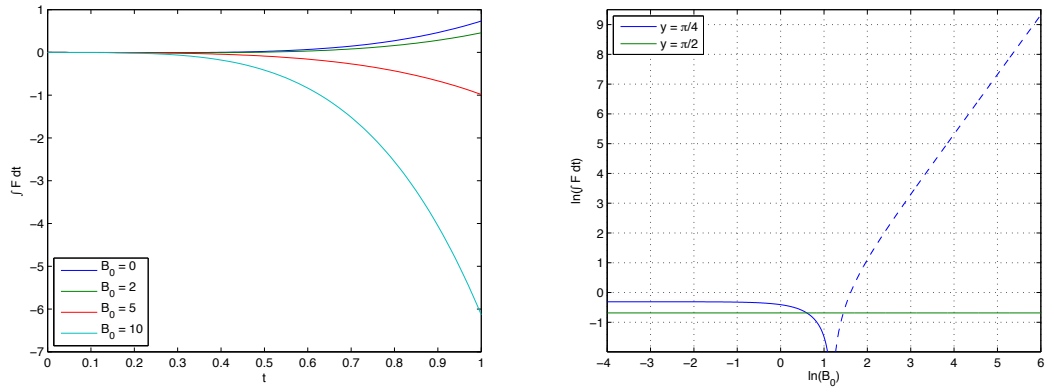

(a) (b)

Figure 3.3: The integrated flux, $\mathcal{F} = \mathcal{F}_K + \mathcal{F}_L$, found by taking the $O(t^3)$ short-time expansion given by equations (3.117 – 3.120) for: (a) a single point, $y_0 = \pi/4$ evolving over time (corresponding to a general $U(y) = -\cos(y) \neq 0$, and (b) the log-log scaling relationship of $\mathcal{F}$ to B_0 for two points, the first for $U(y) \neq 0$, as in (a), and the second for $U(y) = 0$. Note that for points with $\mathcal{F} < 0$, the log of the real part of the integrated flux has been plotted by a dashed line. In both of these plots $m = \sqrt{5/2}$ and $\beta = 50$.

to the $\beta = 0$ case, we stress that the form of the flux for small B_0 is dependent on the relevant parameters; m, y and in this case β. In figure 3.3a it is clear that for small values of B_0 we have a diffusive flux at our chosen point in y. However, for other points in y the feedback may be anti-diffusive, due to the change in the stucture of the flow bought about by the symmetry breaking β terms.

In figure 3.3b we see the flux tending towards the same $\mathcal{F} \sim -B_0^2$ scaling law in the large B_0 limit as seen previously. At small values, B_0 becomes negligible; to be expected when another larger parameter is introduced. For $y = \pi/4$, the flux produces a diffusive feedback until $B_0 = O(1)$, where it becomes anti-diffusive. Comparing to figure 3.4, we can see that this switch in behaviour corresponds to the extension of the central anti-diffusive jet of flux, taking place for $0 < B_0 < 5$.

Note that unlike the $\beta = 0$ case, the flux is no longer limited to being zero at points where $\cos(y) = 0$. As such, the flux at these points grows with t, and

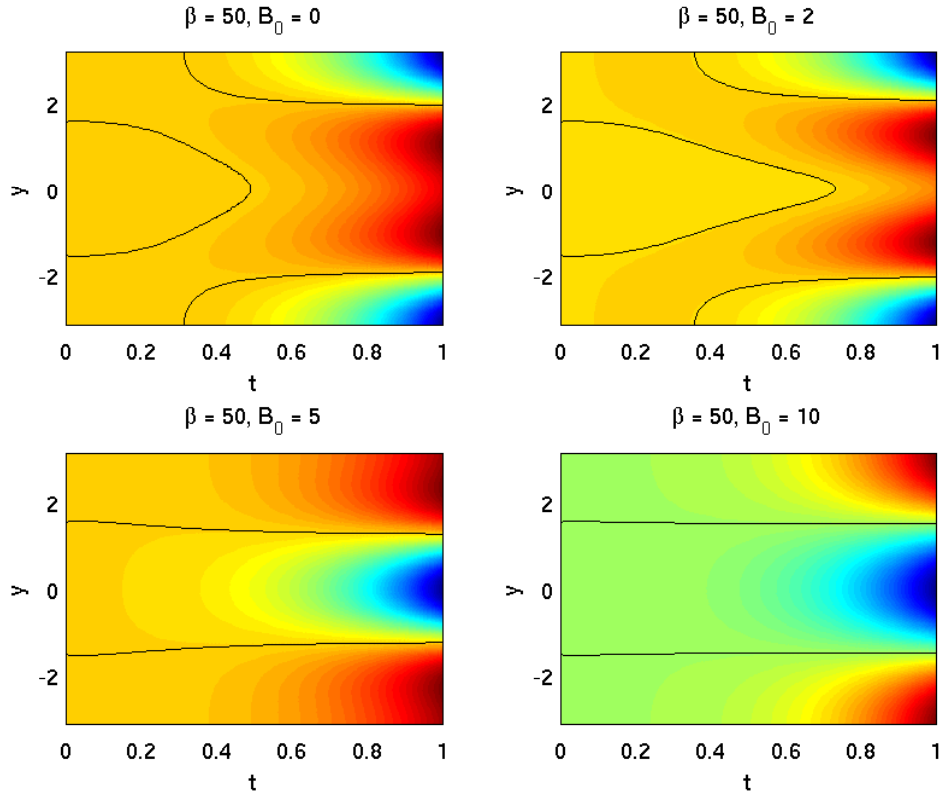

Figure 3.4: Shaded contour plot of the integrated flux, $\mathcal{F} = \mathcal{F}_K + \mathcal{F}_L$, found by integrating $O(t^3)$ short-time expansion given by equations (3.117 – 3.120) for $U(y) = -\cos(y)$, $m = \sqrt{5/2}$, $\beta = 50$ and several values of B_0 as indicated in the figure. Contours of $\mathcal{F} = 0$ have been overlayed in black.

doesn't change sign at any point:

$$F(y = \pi/2, t) = \frac{2(m^2-1)(5m^2+8)}{3(m^2+1)^2(m^2+4)^2}\beta t^3. \tag{3.123}$$

These points in the flux also lack B_0 dependence, hence the flat $y = \pi/2$ curve in figure 3.3b

We can compare figure 3.4 to figure 3.2 (with $\beta = 0$). We see that for the two larger B_0 cases, the structure of the profile is very much unchanged, with only slight differences in the position of the lines $\mathcal{F} = 0$. However, for small B_0, the flux takes quite a different form, with merging peaks in the flux leading to a more spread out positive peak of $\mathcal{F}$, which centres at $y = 0$ (in contrast to the $\beta = 0$ case). As B_0 increases, a narrow anti-diffusive jet emerges, splitting the positive peak, and

eventually returning the profile to its previous form. This process is particularly well represented by the $B_0 = 2$ case; we can see two distinct peaks, which unlike the $\beta = 0$ case, are not separated by a region of anti-diffusive behaviour.

In summary, the key result of this section is that the magnetic field has second order anti-diffusive effect across the entire domain, regardless of the scale of the waves relative to the mean. For small-scale waves, the magnetic field will reinforce the leading order anti-diffusive behaviour, potentially encouraging and maintaining zonal structures in the flow. For large-scale waves the magnetic field will make the leading order behaviour less diffusive, stopping the mean from dissipating as rapidly. Despite these results, we see that neither B_0 or β have leading order effects on the mean flow feedback in the MHD short-time expansion.

3.5.2 Magnetic Feedback

Casting our thoughts back to section 3.2 of this chapter, we found the relation between the fluxes and the mean flow/magnetic field in equations (3.26) and (3.27). Both of these equations implied that the evolution of the relevant background field was dependent on a y-derivative of the corresponding flux, with the magnetic field being governed by

$$\partial_t B = -\partial_y^2 F_M. \tag{3.124}$$

Unlike the kinetic and Lorentz fluxes, F_K and F_L, our current initial conditions ($\zeta_0 = 1, \chi_0 = 0$) make it possible for the magnetic flux, F_M, to contain constant terms, independent of y. This is due to the fact that we have taken a constant background magnetic field, $B(y) = B_0$, unlike the mean flow, $U(y)$. As such, we can omit the constant terms found in F_M.

Having considered the feedback on the mean flow in section 3.5.1, it is worth considering the behaviour of the magnetic feedback. Unlike the mean flow, the magnetic field is constant in y. Terms from F modify the mean flow, with wholly anti-diffusive feedbacks (across y) reinforcing the initial $U(y)$. In contrast, F_M will determine the structure of $B(y)$, due to the background profile being constant (see equation (3.31)). As such, for the magnetic field the terms 'diffusive' and

'anti-diffusive' do not by themselves indicate whether or not zonal flows might be supported. Rather, this is determined by the structure of $F_M(y)$. In ways, this makes the feedback on the magnetic field much simpler than that of the mean flow; it will take the shape of F_M, while B_0 simply scales it, i.e. determines how long it takes F_M to evolve via (3.31). Interesting interactions between different terms of F_M may still take place, as is highlighted later in this section.

The first term of the expansion of the magnetic flux is

$$F_{M1} = 0, \tag{3.125}$$

i.e. there is no leading order feedback on the magnetic field. This important result tells us that the magnetic field will generally go unchanged by the waves launched on it, with any perturbations to the initial field being very small in magnitude. Indeed, like the other fluxes, the next non-zero term in the expansion of the flux is the t^3 term:

$$F_{M3} = -\frac{8\cos(y)}{3(m^2+1)^2}\beta B_0 - \frac{4m^2(2m^2-7)\cos^2(y)}{3(m^2+4)(m^2+1)^2}B_0. \tag{3.126}$$

A lot of information about the magnetic field can be gained from equation (3.126). First we comment that, unlike the feedback on the mean flow (where only even powers of B_0 were found), we expect the magnetic feedback to be dependent on the polarity of the field. As such, it is no surprise to have B_0^1 in both terms of F_M.

However, a consequence of this is that when we look at the feedback, given by F_M/B_0 (see equation (3.29)), we find that it is independent of B_0. As such, the strength of the field plays no role in determining strength of the magnetic feedback. However, as mentioned previously, when considering equation (3.31), B_0 will influence the rate at which the profile of the field evolves.

When $m \gg 1$ (or $\beta = 0$), the flux is given by

$$F_M = -\frac{4m^2(2m^2-7)\cos^2(y)}{3(m^2+4)(m^2+1)^2}B_0 t^3, \tag{3.127}$$

with the feedback being largely dependent on a $\cos^2(y)$ term. As this term is positive, we can see that for $m > \sqrt{7/2}$ the flux will have a diffusive feedback on the field. However, unlike much of the behaviour seen previously, different

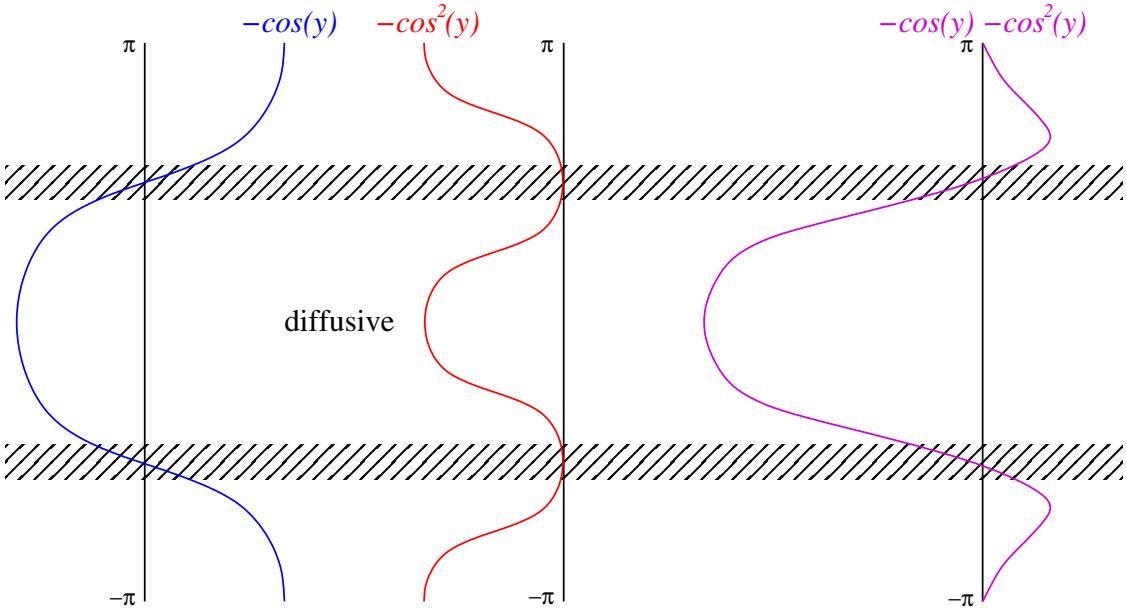

Figure 3.5: Schematic of the terms of the magnetic flux, F_M as given in equation (3.126). The red curve gives the form of the flux when $m \gg 1$ or $\beta = 0$, whereas the magenta curve represents an interaction between the two terms of F_M when they are of similar magnitude, which results in a strong diffusive region, with weak anti-diffusion when y approaches $|\pi|$.

regions will correspond to different levels of diffusivity, with points where $\cos(y) = 0$ having zero magnetic flux. The $\cos^2(y)$ term essentially comes from $|U|^2$, and implies that in general, regions with $|U'(y)| \to 0$ will correspond to diffusive areas of the magnetic field, while large $|U'(y)|$ will be less diffusive (without actively encouraging transport via anti-diffusion). For this particular choice of $U(y)$, the magnetic flux will establish a $\cos(2y)$ zonal feedback.

The effect of the feedback can be seen in the schematic given by figure 3.5. Here we plot $-\cos(y)$, which comes from the β term in equation (3.126), as well as $-\cos^2(y)$ which represents the feedback when $m \gg 1$ or $\beta = 0$. The feedback in this case is diffusive, although this is weak in the shaded regions. However, as mentioned previously, simply labelling the behaviour 'diffusive' or 'anti-diffusive' tells us little about the evolution of the mean field. More importantly, the $\cos^2(y)$ term introduces form to $B(y)$, developing smaller scales than those given by the mean flow.

In section 3.5.1 we found that B_0 always reinforces the mean flow. This is unexpected, as generally it has been observed that a magnetic field disrupts zonal jets. However, here we see that the magnetic field has a tendency to move to small scales (although not at leading order), which would then relay back to the mean flow feedback, potentially breaking the mean flow profile. It is still interesting that none of these effects come in at leading order, or that magnetic field suppresion does not appear in the mean flow feedback alone.

With non-zero β, competition will take place between the $\cos(y)$ and $\cos^2(y)$ terms in equation (3.126). When the two terms are comparable in magnitude, it is possible for strong diffusive jets to occur at $y = 2n\pi, n \in \mathbb{Z}$, due to the juxtaposition of the two profiles. These are similar to the jets introduced by β for for the mean flow, as seen in section 2.6, and may allow for the formation of zonal regions in the magnetic field. A representation of this can be seen in the magenta curve of figure 3.5, which gives $-\cos(y)-\cos^2(y)$. The strong diffusive jet has areas of weak anti-diffusive behaviour either side of it, which may promote mixing in the field.

However, more generally, for large β or small values of m, the $\cos(y)$ term will become dominant, which gives the profile of the feedback. This will result in a magnetic field similar in shape to the mean flow. However, we emphasize again that all of these effects come in at very small magnitudes, and that the leading order behaviour of the magnetic field remains homogeneous and constant across the domain.

3.6 Conclusion

We give a summary of the results of this chapter through the following points:

- We have established the various quantities (in the form of fluxes or similar) relating to the feedback on the mean flow and magnetic field. The general form of these equations is similar to that given in the hydrodynamical case (compare (2.35) and (3.49 – 3.50)).

- Unlike the HD case, a linear shear flow will have a feedback on the mean flow

(and magnetic field), but the equations governing this are complicated and unsolvable analytically.

- Similarly, at leading order the large-scale expansion takes the same form as the linear shear problem. As such, solutions can only be found by numerical methods, which we do not look at in this current investigation.

- A short-time expansion does produce analytical results. At leading order, the magnetic field has no effect on the feedback on the mean flow (with the Lorentz force not contributing to the feedback at all).

- At second order, the feedbacks become a lot more complicated, with scale separation, the vorticity gradient and magnetic field all bringing in competing effects. The magnetic field gives additional anti-diffusive effects across the entire domain of the mean flow. For small-scale waves, these act to reinforce the leading order anti-diffusive feedback, potentially encouraging the growth of zonal jets. For large-scale waves, the field reduces the level of diffusivity from the leading order feedback.

- Including β will bring in behaviour similar to that seen in the hydodynamical study. At large β, the mean flow feedback will revert to the HD case.

- We found that there was no feedback on the magnetic field at leading order for constant $B(y) = B_0$. Expanding our solution, we found that the feedback, while completely diffusive, fluctuated in magnitude across the profile at a scale shorter than that of the mean flow. This may indicate the mechanism by which the magnetic field disrupts jet-like profiles.

- Introducing β brings about a bias to the direction of the background field, which allows for a strong diffusive jet to occur. At larger values of β, the field takes on the same profile as the mean flow.

We will now look at numerical methods for investigating these types of flows, both hydrodynamical (chapters 4 – 5) and magnetohydrodynamical (chapters 6 – 7). We will present a comparative study of these results in chapter 8.

Chapter 4

Nonlinear Dynamics

4.1 Introduction

In this chapter we investigate the fully nonlinear system governing the evolution of a two-dimensional fluid under the effects of a vorticity gradient, background linear shear flow, viscosity and body force. We begin by deriving the sheared β-plane equations and then look at one of the important quantities describing the flow, the vorticity flux. After showing that the vorticity flux averages to zero across our sheared system, we look at the evolution and flux of a passive scalar field carried by the flow.

Following this, we investigate how a sheared system can be numerically modelled. We use a shearing box coordinate system to take a frame of reference which follows the mean shear, which we implement in Fourier space in order to make use of the effectiveness of spectral codes. We explore in some detail the different methods used to ensure our methods are accurate, and give a system of discretized equations to be integrated.

We then look at the means by which energy is put into the flow; the body force. We describe two different types of forcing typically used in unsheared systems, and give reasons for choosing the one we deem most suitable for our investigation. We then look at how this can be adapted for use with the shearing box coordinate system. Lastly we discuss the non-dimensionalization of the governing equations, although discussion of the relevant dimensionless numbers is deferred to later chapters.

In chapter 5 we look at the results of performing the simulations described in this current chapter. In particular, we look at the effects of varying the strength of the background shear flow and the coefficient of the vorticity gradient, and how these two parameters affect vertical transport in the flow. In later chapters, we explore the magnetohydrodynamic extension to this current investigation (see chapters 6 and 7).

4.2 Governing Equations

The Navier-Stokes equation describing the evolution of an incompressible flow is given by

$$\rho\left(\frac{\partial \mathbf{U}}{\partial t} + \mathbf{U}\cdot\nabla\mathbf{U}\right) = -\nabla p + \mu\nabla^2\mathbf{U} + \rho\mathbf{F}, \tag{4.1}$$

$$\nabla\cdot\mathbf{U} = 0, \tag{4.2}$$

where $\mathbf{U}$ describes the total flow velocity, ρ is the fluid density, p is the pressure, μ is the coefficient of dynamic viscosity and $\mathbf{F}$ is some external force [33]. We will use the following form of notation throughout this chapter:

$$\frac{\partial}{\partial t} \equiv \partial_t\,,\ \frac{\partial}{\partial x} \equiv \partial_x\,,\ \text{etc.} \tag{4.3}$$

This allows us to rewrite equation (4.1) as

$$\partial_t\mathbf{U} + \mathbf{U}\cdot\nabla\mathbf{U} = -\frac{1}{\rho}\nabla p + \nu\nabla^2\mathbf{U} + \mathbf{F}, \tag{4.4}$$

where $\nu = \mu/\rho$ is the kinematic viscosity.

Taking the curl of equation (4.4) leads to the vorticity equation

$$\partial_t\mathbf{\Omega} + \mathbf{U}\cdot\nabla\mathbf{\Omega} = \mathbf{\Omega}\cdot\nabla\mathbf{U} + \nu\nabla^2\mathbf{\Omega} + \mathbf{G}, \tag{4.5}$$

or

$$\partial_t\mathbf{\Omega} = \nabla\times(\mathbf{U}\times\mathbf{\Omega}) + \nu\nabla^2\mathbf{\Omega} + \mathbf{G}, \tag{4.6}$$

where $\mathbf{\Omega}$ is the total fluid vorticity and $\mathbf{G} = \nabla\times\mathbf{F}$ is some external force curl [1].

By imposing that the flow can be described in terms of a stream function, $\mathbf{U} = \nabla\times(\Psi\mathbf{k})$, we reduce (4.6) from a vector equation to one simply describing the scalar field Ω, where $\mathbf{\Omega} = (0, 0, \Omega)$:

$$\partial_t\Omega = J(\Psi,\Omega) + \nu\nabla^2\Omega + G, \tag{4.7}$$

where G is the $\mathbf{k}$-component of the forcing $\mathbf{G}$. The nonlinear terms are given by the determinant of the Jacobian,

$$J(\Psi,\Omega) = (\partial_x\Psi)(\partial_y\Omega) - (\partial_y\Psi)(\partial_x\Omega)\,. \tag{4.8}$$

We also note that the vorticity, Ω, is related to the stream function, Ψ, by

$$\Omega = -\nabla^2\Psi = -\left(\frac{\partial^2\Psi}{\partial x^2} + \frac{\partial^2\Psi}{\partial y^2}\right). \tag{4.9}$$

We now impose that there is a background vorticity gradient. There are two methods by which we can do this: the first is by directly adding a gradient of vorticity to the flow, and the second by introducing the additional physical effects of being on a β-plane. Adopting the former approach, we write the general solution of Ψ and Ω as

$$\Psi(x,y) = C_0 + C_1 y + C_2 y^2 + C_3 y^3 + \psi(x,y), \tag{4.10}$$

$$\Omega(x,y) = -2C_2 - 6C_3 y + \omega(x,y), \tag{4.11}$$

and

$$\omega = -\nabla^2\psi. \tag{4.12}$$

We set the gauge term, C_0 to zero, as it has no effect on the dynamics of the system. Likewise, any effect of C_1 can be described by a Galilean transformation, and so it can also be removed from (4.10) without consequence.

In order to impose a simple shear flow, we linearise the x-component of the fluid velocity about $y = 0$. This amounts to

$$U_x(x,y) = 2C_2 y + 3C_3 y^2 + u_x(x,y), \tag{4.13}$$

$$\simeq 2C_2 y + u_x(x,y), \tag{4.14}$$

which is valid given $y \ll C_2/C_3$. We intend to retain C_3 in the vorticity, due to it representing the background vorticity gradient of a β-plane approximation. This leaves the solution

$$\Psi(x,y) = C_2 y^2 + \psi(x,y), \tag{4.15}$$

$$\Omega(x,y) = -2C_2 - 6C_3 y + \omega(x,y). \tag{4.16}$$

Substituting these into our scalar vorticity equation, (4.7), results in

$$\partial_t\omega + 2C_2 y\partial_x\omega + 6C_3\partial_x\psi = J(\psi,\omega) + \nu\nabla^2\omega + G, \tag{4.17}$$

which we rewrite as

$$\partial_t \omega + \alpha y \partial_x \omega = J(\psi, \omega) + \beta \partial_x \psi + \nu \nabla^2 \omega + G, \tag{4.18}$$

where

$$\alpha = 2C_2, \quad \beta = -6C_3, \tag{4.19}$$

with the restriction

$$\left| \frac{\alpha}{\beta} \right| \gg y. \tag{4.20}$$

This restriction implies that for moderately sized planes of fluid, the strength of the shear needs to be relatively large compared to the vorticity gradient in order for our approximation to hold. However, we note that in the absence of shear, $C_2 = 0$ above, we no longer have the same restriction on β. Instead, we have a relation between the velocity perturbations and the vorticity gradient. Generally, when deriving the β-plane model, these terms are the result of taking the normal component of the Coriolis effect across the latitude of the sphere, and no such restrictions hold [45].

Equation (4.18) provides the sheared vorticity equation, which will be the primary subject of our investigation in this chapter. In the following sections we look at some of the quantities associated with this type of system, and the information they give us about the statistics of the flow.

4.3 Flux

The nonlinear system of equations given by (4.12) and (4.18) describes our sheared β-plane incompressible fluid, and will result in several interesting quantities worth investigating. In particular, we give attention to the flux, the transport (in a given direction) of a chosen quantity throughout the flow.

Much of this follows from the work of Moffatt, who showed that the flux could be directly related to a type of diffusive feedback on the fluid, labelled the effective diffusivity [25]. A flux that is averaged across each of the N directions spanned by the fluid gives the effective diffusivity as an $N \times N$ matrix. Each component

describes the preference for diffusive behaviour, from which directional bias in the flow can be read. As the flux changes with any given parameter, the effect of that parameter on the anisotropy of the flow should become apparent.

Given the preference for the y-direction in equation (4.18), we restrict this investigation to the downward (i.e. negative) vertical component of the flux of a variable h:

$$F(x,y) = -hv = h\partial_x\psi, \tag{4.21}$$

where v is the vertical component of the velocity perturbations, and noting that h can be represent any variable of the form $h(x,y)$ at a given time, t. Another important point is that the use of the flux here differs from that implemented in chapters 2 and 3, where we used the standard, upward vertical component of flux. As such, there is a change of sign when translating F from the previous chapters to F given in equation (4.21).

As mentioned previously, an average value of the flux can be related to the effective diffusivity of the flow. We take

$$F = \langle h\partial_x\psi \rangle_{x,y}\,, \tag{4.22}$$

where $\langle\cdot\rangle$ denotes a spatial average, in this particular case over the whole x and y domain. Unless otherwise stated, we will generally take the average over the whole spatial domain.

There are several variables which may produce an interesting and informative flux. The first that we willl look at is the vorticity, ω. Our flux can be related to the nonlinear parts of the flow (see equation (4.8)) by:

$$\begin{aligned} J(\psi,\omega) &= (\partial_x\psi)(\partial_y\omega) - (\partial_y\psi)(\partial_x\omega) \\ &= -\partial_x(\omega\partial_y\psi) - \partial_y(-\omega\partial_x\psi) \\ &= -\left[\partial_x(u\omega) + \partial_y(v\omega)\right], \end{aligned} \tag{4.23}$$

where the velocity is given by $\mathbf{u} = (u,v)$. One must be careful here; for F we measured the *downward* vertical flux, whilst equation (4.23) gives us the Jacobian in terms of the positive fluxes. We can write the Jacobian in the following vector

form:

$$J(\psi, \omega) = -\nabla \cdot \mathbf{F}_\omega, \tag{4.24}$$

where $\mathbf{F}_\omega = (u\omega, v\omega)$. Note that more generally, this relation to the Jacobian holds for the flux of any quantity h and $J(\psi, h)$:

$$J(\psi, h) = -\nabla \cdot \mathbf{F}_h, \tag{4.25}$$

where $\mathbf{F}_h = (uh, vh)$. This will be made use of when discussing magnetohydrodynamics. Note that our definition of F gives $F = -\hat{\mathbf{y}} \cdot \mathbf{F}$.

Restricting our view to the average of the vertical component of the vorticity flux, we explore further by considering the total stream function and vorticity:

$$\Psi(x, y) = \frac{1}{2}\alpha y^2 + \psi(x, y), \tag{4.26}$$

$$\Omega(x, y) = -\alpha + \beta y + \omega(x, y), \tag{4.27}$$

which have been obtained from equations (4.15 – 4.16) and (4.19). As such, our averaged flux can be written as

$$F = \langle \omega \partial_x \psi \rangle = \langle (\Omega + \alpha - \beta y) \partial_x \Psi \rangle \,. \tag{4.28}$$

Using standard techniques for manipulating averages, we can reduce this to

$$F = \langle \Omega \partial_x \Psi \rangle_{x,y} + \alpha \langle \partial_x \Psi \rangle_{x,y} - \beta \langle y \langle \partial_x \Psi \rangle_x \rangle_y \,. \tag{4.29}$$

For any bounded function $h(x)$,we have $\langle \partial_x h(x) \rangle_x = 0$. As such, both the α and β terms in equation (4.29) will be zero, leaving

$$F = \langle \Omega \partial_x \Psi \rangle_{x,y} \,. \tag{4.30}$$

This result is interesting as it shows that there is no difference between using the total vorticity Ω or vorticity perturbations ω when calculating the flux. Note that the equations providing the evolution of ω will of course involve both α and β given that they are non-zero.

If we restrict our flow further, to a case where we are on a doubly periodic plane (i.e. our variables are periodic in both the x and y directions), the remaining term

in the vorticity flux will also disappear. Although we won't show the method for this here, it simply follows from taking the average of the Fourier transform of Ω and $\partial_x \Psi$. In this case, we then have

$$F = 0. \tag{4.31}$$

This can also be shown using a shearing box coordinate system; a concept we shall introduce later in this chapter (see section 4.5). This proof will be given in appendix A. This result is effectively a consequence of the Orr mechanism, which is looked at in more detail in section 2.3. For cases where a background mean flow is present (rather than a linear shear flow), the vorticity flux is expected to describe the feedback of the mean flow on the rest of the fluid, and hence be non-zero.

As the vorticity flux provides us with no information regarding the effect of shear and rotation on the fluid under these circumstances, we instead investigate the flux of a passive scalar field.

4.4 Passive Scalar Fields

Equations (4.12) and (4.18) allow us to study the evolution of a vorticity field and its corresponding flow. Whilst all the characteristics of this flow may be calculated, it is of interest to study the transport of a passive scalar field subject to the flow. In particular, as indicated in the previous section, the flux of passive scalar across the flow gives us an effective diffusivity for the fluid. By measuring this, we aim to give a quantitative description of the effect of the parameters α and β on the flow.

The governing equation of a passive scalar, Θ, being carried by the total flow, $\mathbf{U}$, is

$$\partial_t \Theta + \mathbf{U} \cdot \nabla \Theta = \kappa \nabla^2 \Theta, \tag{4.32}$$

where κ is the diffusivity of the passive scalar field [19].

In keeping with the previous sections, in particular using equations (4.14) and (4.19), we write

$$\mathbf{U} = (\alpha y, 0) + \mathbf{u}, \tag{4.33}$$

where u_x from equation (4.14) is the x-component of $\mathbf{u}$. We proceed to rewrite equation (4.32) as

$$\partial_t \Theta + \alpha y \partial_x \Theta = J(\psi, \Theta) + \kappa \nabla^2 \Theta, \tag{4.34}$$

which is our sheared passive scalar equation. Equation (4.34) bears remarkable similarity to equation (4.18), the vorticity perturbation equation. Indeed, setting $\beta = 0$ and forgoing any driving force, the form of the equations is the same, except for the fact that the passive scalar has no feedback on the flow through equation (4.12) (hence *passive* scalar). This, and the diffusivity of the passive scalar field may take a different value from the viscosity of the flow.

We can examine the ratio of these two viscosities as a Prandtl number, which when set to unity brings about further symmetry in the two flows. Indeed, we expect the passive scalar to evolve in much the same way as the vorticity.

It is also interesting to impose a background gradient on the passive scalar field. Physically this could describe some distribution of temperature with a colder (or hotter) northern area relative to the southern area. We separate the perturbations of the passive scalar about this gradient by writing

$$\Theta = \iota y + \theta', \tag{4.35}$$

where ι is the strength of the gradient, and θ' is the departure of Θ from it. Substituted into equation (4.34), this results in

$$\partial_t \theta' + \alpha y \partial_x \theta' - \iota \partial_x \psi = J(\psi, \theta') + \kappa \nabla^2 \theta'. \tag{4.36}$$

Note that as θ' is a passive scalar and has no effect on the actual flow, we can divide by ι to factor it out:

$$\partial_t \theta + \alpha y \partial_x \theta = J(\psi, \theta) + \partial_x \psi + \kappa \nabla^2 \theta, \tag{4.37}$$

where $\theta = \theta'/\iota$ is our new passive scalar field.

The similarities between the vorticity equation and the passive scalar equation are clear; with $\nu/\kappa = \beta = 1$ (or $\iota = \beta$), the two equations are symmetric with regards to the gradients of their main variable. The difference between the two is that energy is put into the flow via a body force, whereas it is the flow itself which

drives the passive scalar. As such, the two equations will have different, albeit often similar solutions

Following from the previous section, we can consider the flux of passive scalar to be related to a type of diffusivity in the fluid [25]. For further discussion on diffusive feedbacks to the flow, please refer to section 2.2. Our averaged downward vertical flux is given by:

$$F = \langle \theta \partial_x \psi \rangle \,. \tag{4.38}$$

Expanding θ in a similar fashion to (4.26) and (4.27) we obtain

$$\Theta(x, y) = \iota(\theta(x, y) + y), \tag{4.39}$$

and use these to write the flux in terms of the total variables

$$\begin{aligned} F &= \left\langle \left(\frac{\Theta}{\iota} - y \right) \partial_x \Psi \right\rangle_{x,y} \\ &= \frac{1}{\iota} \langle \Theta \partial_x \Psi \rangle_{x,y} - \langle y \langle \partial_x \Psi \rangle_x \rangle_y \,. \end{aligned} \tag{4.40}$$

In our doubly periodic geometry (with regards to the fields ω, ψ and θ) we observe that the second term in (4.40), which is the result of the passive scalar gradient, is identically zero. However, we can make no further simplifications to the first term, which gives our resultant flux:

$$F = \frac{1}{\iota} \langle \Theta \partial_x \Psi \rangle \,. \tag{4.41}$$

As such, we can see that the gradient of passive scalar has no influence on the structure of the flux, but will scale θ appropriately when integrating equation (4.37).

Again, the fact that this flux is generally non-zero can also be shown simply by observing that the modified Fourier transform of the components of the flux no longer cancel (see appendix A). Using the established results of Moffatt, we use the average flux of the passive scalar field as a diagnostic describing the vertically diffusive nature of the flow [25]. In particular, in the presence of strong zonal jet-like structures which act as barriers to transport across the fluid, we expect this flux to be severely inhibited [14].

4.5 Numerical Methods: Shearing Box Coordinate System

As we will be referring to them repeatedly throughout the remainder of this chapter, we restate our sheared β-plane equations for an incompressible two-dimensional fluid as

$$\partial_t \omega + \alpha y \partial_x \omega = J(\psi, \omega) + \beta \partial_x \psi + \nu \nabla^2 \omega + G, \tag{4.42}$$

$$\omega = -\nabla^2 \psi, \tag{4.43}$$

where $\omega(x, y, t)$ and $\psi(x, y, t)$ represent the perturbations of vorticity and the stream function respectively. The parameters α, β and ν represent the strength of the shear, the vorticity gradient and the viscosity, whilst $G(x, y, t)$ is an external body force. The passive scalar field carried by such a flow can be described by

$$\partial_t \theta + \alpha y \partial_x \theta = J(\psi, \theta) + \partial_x \psi + \kappa \nabla^2 \theta, \tag{4.44}$$

where θ represents the passive scalar and κ gives its diffusivity.

Due to their speed and accuracy (when properly resolved), we aim to use spectral methods to solve the above equations in Fourier space [20]. Such techniques require our working variables to be doubly periodic across the (x, y) domain. Clearly, as can be seen from the α containing terms in (4.42) and (4.44), the above system is not periodic in the y-direction, and as such standard methods cannot be used. Instead, we adopt an approach commonly used in astrophysical simulations of accretion discs and other strongly sheared physical phenomena [21].

We consider a frame of reference in which we follow the perturbations of the flow about its sheared state. Such a coordinate system will be linearly dependent on time, and can be visualised as a standard Cartesian coordinate system being sheared horizontally with rate α (see figure 4.1). The variables representing our flow, ω and ψ, will be periodic relative to this system. In the x-direction we retain

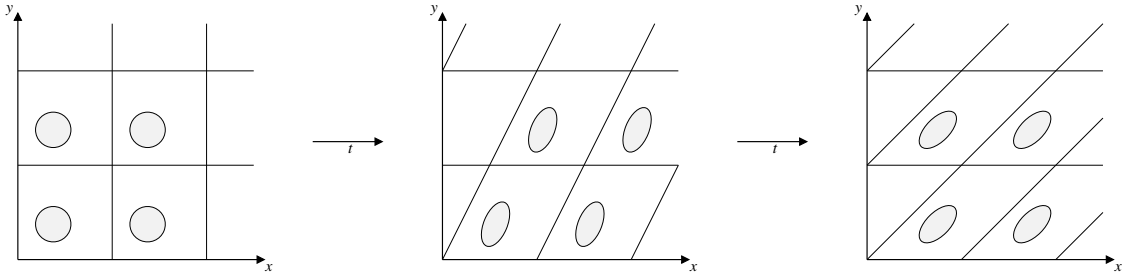

Figure 4.1: Schematic of the real space evolution of several boxes periodic about the shearing box coordinate system. An idealised blob of passive fluid has been included to show the effect of shear alone (with no frictional or body forces).

standard periodicity:

$$\psi(x + 2\pi k, y, t) = \psi(x, y, t), \tag{4.45}$$

$$\mathbf{u}(x + 2\pi k, y, t) = \mathbf{u}(x, y, t), \tag{4.46}$$

$$\omega(x + 2\pi k, y, t) = \omega(x, y, t), \tag{4.47}$$

for $k \in (Z)$. In y, the shearing box system give a slightly more complicated relation:

$$\psi(x, y + 2\pi k, t) = \psi(x, y, t) + 2\alpha\pi k y, \tag{4.48}$$

$$\mathbf{u}(x, y + 2\pi k, t) = \mathbf{u}(x, y, t) + (2\alpha\pi k, 0) \tag{4.49}$$

$$\omega(x, y + 2\pi k, t) = \omega(x, y, t). \tag{4.50}$$

The new coordinate system requires a modification to our standard Fourier transform in order to write the corresponding spectral space equations. This will be discussed in more detail in section 4.6. We will refer to this new operation as the Shearing Box Fourier Transform (SBFT) throughout the following chapters. It is given by

$$\omega(x, y, t) = \sum_{m,n} \hat{\omega}_{m,n}(t) e^{imx + i(n - \alpha m t)y}, \tag{4.51}$$

where (m, n) are components of our spectral domain and $\hat{\omega}_{m,n}(t)$ is the function corresponding to $\omega(x, y, t)$ in Fourier space [10]. Note that all 'hatted' variables in this thesis will refer to their Fourier or wave-like equivalents.

Using the SBFT we write the relation between the vorticity and stream function given in equation (4.43) in terms of Fourier components as

$$\hat{\omega} = \left(m^2 + (n - \alpha m t)^2\right) \hat{\psi}. \tag{4.52}$$

This relationship allows us to easily eliminate $\hat{\psi}$ from our spectral equation for the evolution of $\hat{\omega}$:

$$\partial_t \hat{\omega}_{m,n} = \hat{J}_{m,n} + \left[\frac{im\beta}{m^2 + (n - \alpha m t)^2} - \nu\left(m^2 + (n - \alpha m t)^2\right)\right] \hat{\omega}_{m,n} + \hat{G}_{m,n}. \tag{4.53}$$

The nonlinear Jacobian term is given by

$$\hat{J}_{m,n}(\hat{\psi}, \hat{\omega}) = \hat{J}_{m,n} = \left[\{im\hat{\psi}\}\{i(n - \alpha m t)\hat{\omega}\} - \{i(n - \alpha m t)\hat{\psi}\}\{im\hat{\omega}\}\right], \tag{4.54}$$

where each $\{\cdot\}$ in equation (4.54) represents the inner components being converted to real space using the SBFT, and the $[\cdot]$ represents the final conversion back to Fourier space; a standard practice when using spectral methods of this type.

For brevity, we will rewrite equation (4.53) as

$$\partial_t \hat{\omega}_{m,n} = \hat{J}_{m,n} + \hat{G}_{m,n} + r_{m,n}(t)\hat{\omega}_{m,n}, \tag{4.55}$$

where

$$r_{m,n}(t) = \frac{im\beta}{m^2 + (n - \alpha m t)^2} - \nu\left(m^2 + (n - \alpha m t)^2\right), \tag{4.56}$$

which contains all of the linear terms. Note that for $\alpha = 0$, the non-sheared case, r becomes a function of the wavenumbers m and n alone, and can be calculated once at the beginning of each numerical simulation.

Likewise, we find the Fourier space passive scalar equation, derived from equation (4.44) to be:

$$\partial_t \hat{\theta}_{m,n} = \hat{J}_{m,n}(\hat{\psi}, \hat{\theta}) + \frac{im\hat{\omega}_{m,n}}{m^2 + (n - \alpha m t)^2} - \kappa\left(m^2 + (n - \alpha m t)^2\right) \hat{\theta}_{m,n}, \tag{4.57}$$

Using similar methods to those described for equation (4.54), we give the above Jacobian term as

$$\hat{J}_{m,n}(\hat{\psi}, \hat{\theta}) = \left[\{im\hat{\psi}\}\{i(n - \alpha m t)\hat{\theta}\} - \{i(n - \alpha m t)\hat{\psi}\}\{im\hat{\theta}\}\right], \tag{4.58}$$

We then rewrite equation (4.57) as

$$\partial_t \hat{\theta}_{m,n} = \hat{J}_{m,n}(\hat{\psi}, \hat{\theta}) + \frac{im\hat{\omega}_{m,n}}{m^2 + (n - \alpha m t)^2} + s_{m,n}(t)\hat{\theta}_{m,n}, \tag{4.59}$$

where

$$s_{m,n} = -\kappa \left(m^2 + (n - \alpha m t)^2\right). \tag{4.60}$$

We aim to solve equations (4.55) and (4.59) using optimized numerical schemes. First, we discretize the above equations by setting $t = t_j$, where the integer j represents each step in the integration. The progression of time at each step is given by

$$t_{j+1} = t_j + \Delta t, \tag{4.61}$$

where the time difference, Δt is an important numerical parameter. We describe the Fourier component of the vorticity at (m, n) after j time steps by $\hat{\omega}^j_{m,n}$, with a similar form used for all other variables.

The first step of our integration is performed using the Forward Euler method, as given in the following equations for the vorticity and passive scalar fields respectively:

$$\hat{\omega}^{j+1}_{m,n} = \Delta t \left(\hat{J}^j_{m,n}(\hat{\psi}, \hat{\omega}) + \hat{G}^j_{m,n}\right) + \left(1 + r^j_{m,n}\Delta t\right)\hat{\omega}^j_{m,n}, \tag{4.62}$$

$$\hat{\theta}^{j+1}_{m,n} = \Delta t \left(\hat{J}^j_{m,n}(\hat{\psi}, \hat{\theta}) + \frac{im\hat{\omega}_{m,n}}{m^2 + (n - \alpha m t)^2}\right) + \left(1 + s^j_{m,n}\Delta t\right)\hat{\theta}^j_{m,n}. \tag{4.63}$$

Following this, we use an Integrating Factor method to find the exact solution to the linear parts of equations (4.55) and (4.57), and a second order Adams-Bashforth approach to the nonlinear Jacobian and body force terms [12]. The equation for the integration of vorticity is:

$$\begin{aligned}\hat{\omega}^{j+1}_{m,n} = &\left(\hat{\omega}^j_{m,n} + \frac{3\Delta t}{2}\left(\hat{J}^j_{m,n} + \hat{G}^j_{m,n}\right)\right)\exp\left\{R^{j+1}_{m,n} - R^j_{m,n}\right\} \\ &- \frac{\Delta t}{2}\left(\hat{J}^{j-1}_{m,n} + \hat{G}^{j-1}_{m,n}\right)\exp\left\{R^{j+1}_{m,n} - R^{j-1}_{m,n}\right\},\end{aligned} \tag{4.64}$$

where

$$\begin{aligned}R_{m,n}(t) &= \int r_{m,n}(t)dt \\ &= -\frac{1}{3}\nu t\left[m^2\left(\alpha^2 t^2 + 3\right) - 3\alpha m n t + 3n^2\right] \\ &\quad + \frac{i\beta}{\alpha m}\left[\tan^{-1}\left(\frac{n}{m}\right) - \tan^{-1}\left(\frac{n}{m} - \alpha t\right)\right],\end{aligned} \tag{4.65}$$

noting that $R^{j-1}_{m,n} = R_{m,n}(t - \Delta t)$.

When $\alpha = 0$ we have instead

$$R_{m,n}(t) = \left[\frac{im\beta}{m^2+n^2} - \nu\left(m^2+n^2\right)\right] t, \tag{4.66}$$

with further simplifications when $m = 0$.

The Integrating Factor-Adams Bashforth Method for integrating the passive scalar field is given by

$$\begin{aligned}\hat{\theta}^{j+1}_{m,n} = &\left(\hat{\theta}^{j}_{m,n} + \frac{3\Delta t}{2}\left(\hat{J}^{j}_{m,n}(\hat{\psi},\hat{\theta}) + \frac{im\hat{\omega}^{j}_{m,n}}{m^2+(n-\alpha mt)^2}\right)\right)\exp\left\{S^{j+1}_{m,n} - S^{j}_{m,n}\right\} \\ &- \frac{\Delta t}{2}\left(\hat{J}^{j-1}_{m,n}(\hat{\psi},\hat{\theta}) + \frac{im\hat{\omega}^{j-1}_{m,n}}{m^2+(n-\alpha mt)^2}\right)\exp\left\{S^{j+1}_{m,n} - S^{j-1}_{m,n}\right\},\end{aligned} \tag{4.67}$$

where

$$S_{m,n}(t) = \int s(t)dt = -\frac{1}{3}\kappa t\left[m^2\left(\alpha^2t^2+3\right) - 3\alpha mnt + 3n^2\right], \tag{4.68}$$

to be compared with $R(t)$ in (4.65).

Equations (4.64 – 4.68) give a closed discretized system that, given an appropriate input for the body force $\hat{G}^{j}_{m,n}$ (to be discussed in section 4.7), allow us to solve equations (4.42 – 4.44) directly via a computer. We have written an original program which performs these integrations, while recording key numerical data, using the Fortran 95 programming language.

How we have performed the Fourier transforms needed to represent a shearing box coordinate system is an important detail of our code. This will be discussed in the next section.

4.6 Implementing the shearing box coordinate system

For completeness, it is worth including a discussion on how our redefined Fast Fourier Transform (FFT), the Shearing Box Fourier Transform, is implemented numerically.

Performing an FFT without the aid of a highly optimized numerical library (such as FFTW) is incredibly inefficient, and as such writing our own routine to calculate the SBFT has been ruled out [18]. Instead, we use a 'mode resetting' algorithm to implement the effect of being in a shearing box coordinate system, while employing a double one-dimensional FFT method to translate the flow back to real unsheared space.

The basic principle behind our mode resetting algorithm is that horizontal shear in real space roughly translates to negative vertical shear in the spectral plane. This becomes clear if we write equation (4.51) in the form

$$\omega(x, y, t) = \sum_{m,p} \hat{\omega}_{m,n}(t) e^{imx+ipy}, \tag{4.69}$$

where $p = n - \alpha m t$. A schematic of the plane (m, p) relative to (m, n) is given in figure 4.2. In order to implement the shear, we 'reset' the modes whenever $\alpha t = 1$, that is, whenever the modes on (m, p) and (m, n) overlap. This is done by assigning the modes on (m, p) to their corresponding positions on (m, n), again displayed in figure 4.2. This also corresponds to the last part of figure 4.1, where the grid becomes periodic in unsheared real space, and so can be rearranged.

This method is not without its complications. As the modes are shifted down, we have to pad the modes with $n > -m + \frac{\mathrm{N}}{2}$ or $n < -m - \frac{\mathrm{N}}{2}$, where N is the length of our spectral grid. We make the assumption that the majority of the important dynamics take place in the small range of wavenumbers about the origin, and hence assign the padded modes to be zero. Our justification for this is that the large wavenumber modes are more rapidly damped by the viscosity, and hence these modes are supressed anyway.

Generally it is convenient to view the evolution of a flow from a fixed Cartesian geometry. Using mode resetting we can only do this when (m, p) and (m, n) align, i.e. when $t = \frac{k}{\alpha}, k \in \mathbb{N}$. This isn't an issue if we are only interested in the behaviour of the flow over many shear turnover times. However, to investigate behaviour that occurs on time scales shorter than this, we must use an additional approach to translate it to real space.

The 'double one-dimensional FFT' approach aims to directly implement the

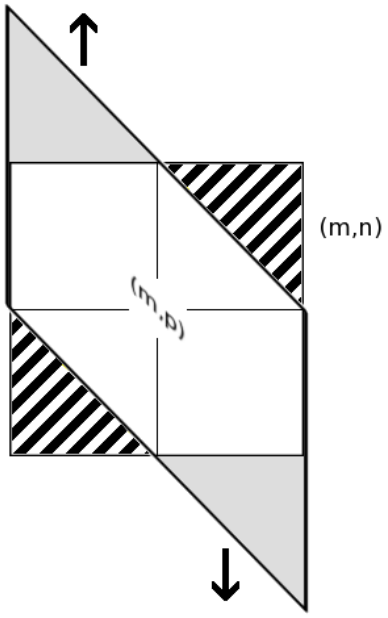

Figure 4.2: Schematic of the evolution of modes in the SBFT relative to standard Fourier space, at time roughly $t = \frac{1}{\alpha}$. The mode resetting method works by mapping our grid (which has been sheared into the state (m, p)) onto the square box (m, n). The striped areas are padded to zero as no data is available from (m, p) due to it being sheared down, whilst the grey areas are discarded.

SBFT as defined in equation (4.51). To do this we split the transform into a series of smaller operations [6]. We rewrite the SBFT and its reverse operation as

$$\omega(x, y, t) = \sum_m \left(\left(\sum_n \hat{\omega}_{m,n}(t) e^{iny} \right) e^{-im\alpha ty} \right) e^{imx}, \tag{4.70}$$

$$\hat{\omega}_{m,n}(t) = \sum_y \left(\left(\sum_x \omega_{m,n}(t) e^{-imx} \right) e^{im\alpha ty} \right) e^{-iny}. \tag{4.71}$$

To perform the SBFT we use one-dimensional Fourier transforms to produce an 'in between' state of ω which is partially in real space (in the y-direction) and partially in Fourier space (in the m-wavenumbers). We then multiply this by the $e^{\pm im\alpha ty}$ term, and complete the process by taking a Fourier transform in the remaining direction. In the above equations we can visualize this algorithm as the execution of each operation in a parenthesis; from innermost to outermost.

Again, there are issues in performing this, in particular regarding computational

restrictions. Over time the sheared grid of Fourier modes produced by the SBFT becomes increasingly skewed. This poses no issue to an infinite grid, as the data can always be retrieved from the corresponding Fourier mode. However, when working with a finite grid, data may become lost or truncated as the grid becomes more distorted.

As such, we combine the double one-dimensional FFT with the mode resetting technique in order to make our simulation more effective; we use mode resetting to keep track of the data (noting that we use $t = t_e$, an elapsed time since the last mode reset), whilst using the series of one-dimensional Fourier transforms to find, plot and diagnose our real data while it isn't available between mode resetting times. This will ensure that the spectral grid is never too skewed to return accurate results, as the grid will never exceed the amount of shear shown in figure 4.2. Note also that one has to be careful when implementing any of these methods with FFTW due to its handling of complex arrays and implementation of Hermitian symmetry.

4.7 Body Force

A key component of equation (4.42) that we wish to explore is the body force term, $G(x, y, t)$. This term represents the injection of energy into our system by external elements. Physically, this generalised forcing could be the result of convection stimulating the atmospheric fluid, the motion of different layers of material above or below the fluid, or the effect of a surface below the fluid [38]. Such phenomena may be rigorously integrated into a system with the aim of realistically recreating their effects. This may involve many different length and time-scales, and strong dependence on other parameters [13]. Despite this, little is know about these processes [36], and as is common practice when investigating our type of idealised system, we include a relatively simple body force which will hopefully allow us to better understand the key features of the equations themselves.

As such, our aim is this: to utilize a forcing with a single length scale, a single time scale and a rate of energy injection (which in turn will have an impact on

the typical velocities of the fluid). The latter of these three can be described by a parameter defining the magnitude of $G(x, y, t)$, and shall be discussed later in this chapter.

Deciding how to effectively implement a length and time scale in the force is more complicated. In order to have a realistic, non-trivial system to explore, we rely on some kind of randomization in each simulation we explore. This is made manifest in our force term, and for this particular case, we randomize some element of the spatial characteristics of the force. In this current section we will discuss two types of body force that fall into this category; the first we shall call a *renewing forcing*, and the second a *ring forcing*.

Initially, we will consider the benefits and drawbacks of each body force in a standard Cartesian coordinate system, with the flow unaffected by any mean shear. Following this, we consider the implications of using a body force in a shearing box coordinate system.

4.7.1 Renewing Force

We will use the term 'renewing force' to refer to the group of body forces which select a single Fourier mode in spectral space, and for a given amount of time (which we will refer to as our forcing correlation time scale, T_c), injects energy into the system. The choice of Fourier component is made by randomly selecting a single mode (and its phase) in a predefined region of Fourier space, such as to roughly match our desired length scale:

$$\hat{G}_{m,n}(t) = \begin{cases} e^{2i\pi\phi_3(t)} & \text{if } (m,n) = (\phi_1(t), \phi_2(t)) \\ 0 & \text{otherwise,} \end{cases} \tag{4.72}$$

where $\phi_i(t)$ are independent uniformly distributed random variables with the following properties:

$$m_{low} \leq |\phi_1| \leq m_{high}, \quad \phi_1 \in \mathbb{Z}, \tag{4.73}$$

$$n_{low} \leq |\phi_2| \leq n_{high}, \quad \phi_2 \in \mathbb{Z}, \tag{4.74}$$

$$0 \leq \phi_3 \leq 1, \quad \phi_3 \in \mathbb{R}, \tag{4.75}$$

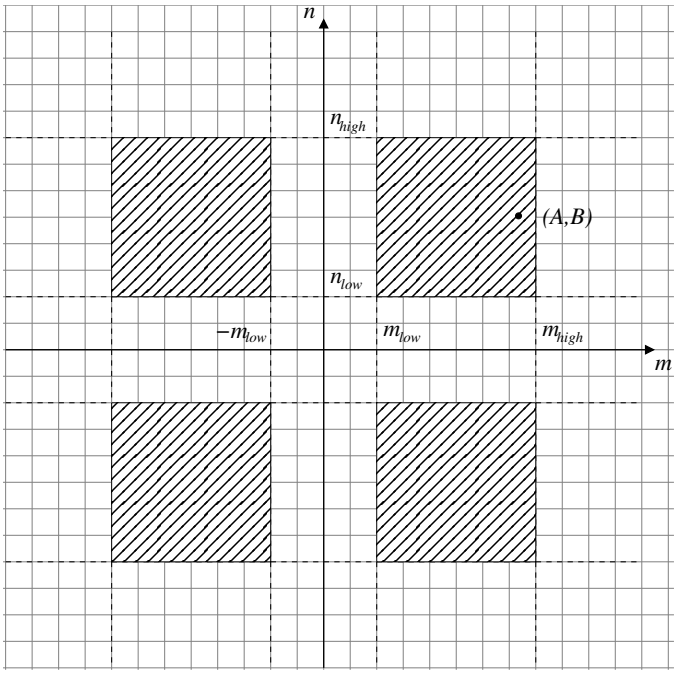

Figure 4.3: Schematic of the region of possible Fourier modes to excite when using the renewing forcing described by equations (4.73 – 4.76), in the absence of shear. Energy is put into single mode at any given point in time, with a new mode (and phase) chosen whenever the time, t, coincides with the forcing correlation time, T_c.

$$\phi_i(t) = \begin{cases} \text{randomly chosen as above} & \text{if } t = kT_c,\ k \in \mathbb{N} \\ \phi_i(kT_c) & \text{if } kT_c < t < (k+1)T_c. \end{cases} \tag{4.76}$$

Clearly the forcing correlation time, T_c, will correspond to the time scale of the above body force. The length scales will be determined by our choice of the range of modes excited, i.e. the values of m_{low}, m_{high}, n_{low} and n_{high}. This can be seen in figure 4.3, which displays the region of Fourier modes available to excite.

A consequence of this implementation of the body force is that there will be a range of length scales forced (rather than a single one). Even for a relatively small band of possible forced modes (small $m_{high} - m_{low}$ and $n_{high} - n_{low}$), unless our range only allows for a single forced mode, there will be a difference in scale between modes at (m_{high}, n_{high}) and (m_{low}, n_{low}). This can make estimating an appropriate length scale for analytical purposes a challenge.

Additionally, the smaller the range of modes we excite, the fewer modes are

available in our random selection. As we only force a single mode at a time, we rely on the interaction of several modes in order to produce dynamically interesting fluid states. As such, generally we require $m_{high} - m_{low}$ and $n_{high} - n_{low}$ to be relatively large, increasing the number of scales involved in the forcing.

4.7.2 Ring Force

The ring, or narrow band forcing continuously excites the group of modes forming a ring about the origin [40]. We write

$$\hat{G}_{m,n}(t) = \begin{cases} e^{2i\pi\phi_{m,n}(t)} & \text{if } K - \delta K \leq \sqrt{m^2+n^2} \leq K + \delta K \\ 0 & \text{otherwise,} \end{cases} \tag{4.77}$$

where $\phi_{m,n}(t)$ is the array of random variables with the following properties:

$$0 \leq \phi_{m,n} \leq 1, \quad \phi_{m,n} \in \mathbb{R}, \tag{4.78}$$

$$\phi_{m,n}(t) = \begin{cases} \text{randomly chosen as above} & \text{if } t = kT_c,\ k \in \mathbb{N} \\ \phi_{m,n}(kT_c) & \text{if } kT_c < t < (k+1)T_c. \end{cases} \tag{4.79}$$

Similarly to the renewing forcing, the time scale of the ring forcing is given by assigning random values to certain variables at an interval of time, T_c. Here we change the value of the phase of each mode contained in the ring group, emphasizing that every mode in the group is continuously forced with the same amplitude for all time.

The range of modes, K, of this body force is given by the radius of the ring group. Fourier modes falling into a narrow band around the ring, $K \pm \delta K$, are continuously 'on' and δK typically takes small values (we use $\delta K = \frac{K}{10}$). This can be seen in figure 4.4. Given this consistent value of K and relatively small variation from it, we can assume that the ring force promotes a single length scale proportional to K^{-1}, making it useful when comparing with analytical methods [35]. In the absence of shear, the Fourier space equation is

$$\partial_t \hat{\omega}_{m,n} = \hat{J}_{m,n} + \left[\frac{im\beta}{m^2+n^2} - \nu\left(m^2+n^2\right)\right]\hat{\omega}_{m,n} + \hat{G}_{m,n}. \tag{4.80}$$

Given that the primary length scale in the system will be represented by the constant $K = \sqrt{m^2+n^2}$, we can use this when analyzing the form of equation (4.80).

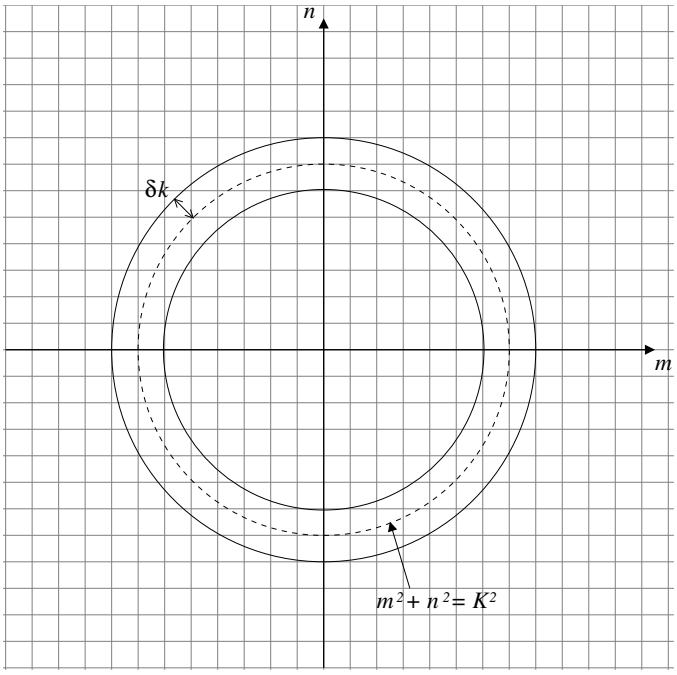

Figure 4.4: Schematic of the choice of Fourier modes made when implementing the ring forcing described by equations (4.77 – 4.79), in the absence of shear. The group of modes contained by the ring are excited continuously, with a new phase for each mode chosen whenever the time, t, coincides with the forcing correlation time, T_c.

This has been made use of in chapters 2 and 3, which discuss the quasi-linear approximation to the flow.

In comparison to the renewing force, a less drastic change takes place at the correlation time, T_c. In the renewing forcing, a new length scale would often be selected at this time, whereas here the phases of modes in the ring are randomized. As such, a renewing force will strongly promote T_c as a prominent time scale in the system. This is at the cost of putting energy into a range of length scales. As we aim to investigate systems with few forced length scales (ideally a single one), the ring forcing is more suitable than the renewing forcing for our purposes.

4.7.3 Forcings in a Shearing Box Coordinate System

Working with a time dependent coordinate system provides additional challenges when deciding on an optimal body force. In this section we will consider how the body force interacts with the shear, and what effects might come about from this interaction. First it is worth considering the nature of the sheared coordinate system in Fourier space. A stationary mode with constant magnitude and phase positioned in standard Fourier space at (A, B) (with additional mode $(-A, -B)$ in keeping with Hermitian symmetry) corresponds to the real function $f(x, y) = \cos(Ax + By)$. Taking the SBFT defined in equation (4.51), we have

$$\begin{aligned}\hat{f}_{m,n} &= \sum_{x,y} \cos(Ax + By) e^{-imx - i(n - \alpha mt)y} \\ &= \sum_{x,y} \exp\left\{i(A - m)x + i(B - (n - \alpha mt))y\right\} + c.c.\end{aligned}$$

$$\hat{f}_{m,n} = \begin{cases} 1 & \text{if } (m, n) = \pm(A, B + \alpha At) \\ 0 & \text{otherwise,} \end{cases} \tag{4.81}$$

Our stationary mode will correspond to a mode travelling away from the m-axis in shearing box Fourier space at $(A, B + \alpha At)$ (and $(-A, -B - \alpha At)$ by Hermitian symmetry).

This has important consequences for our choice of body force. On an ideal, infinitely populated grid of Fourier components, this poses no issue, as we can continuously track the stationary points relative to the sheared frame of reference. However, on a computational grid of finite size, the stationary modes can only be accurately represented when $(A, B + \alpha At)$ coincides with integer valued grid points. The practical effect of this is that modes 'stationary' with regards to the numerical grid are actually sheared relative to the physical Fourier space, before being snapped back into their original unsheared positions when the numerical and physical grids points align (see last stage of figure 4.1).

As such, it is impractical to use a body force that does not follow the background shear flow. Such a force would introduce additional time scales (including the computational 'snap back' time), but also would not give a single length scale for

the sheared system. As is clear from equation (4.53), introducing shear into our system gives a generally time dependent range of modes:

$$K(t) = \sqrt{m^2 + (n - \alpha m t)^2}. \tag{4.82}$$

Unlike K defined in the previous section, $K(t)$ as defined in equation (4.82) cannot be constant for all times t unless m or n are also time dependent. In order to achieve this, we introduce a body force which excites modes whose positions evolve over time, in order to 'follow' the shear:

$$\hat{G}_{m,n}(t) = \begin{cases} e^{2i\pi\phi_{m,n}(t)} & \text{if } K - \delta K \leq \sqrt{m^2 + (n - \alpha m t)^2} \leq K + \delta K \\ 0 & \text{otherwise,} \end{cases} \tag{4.83}$$

where $\phi_{m,n}(t)$ is the array of random variables determining the phase of each mode in the ring, as defined in equation (4.79).

Clearly, $K(t)$ as given in (4.82) will be an estimate for the length scale of this body force; this can be seen in figure 4.5. This is achieved by allowing the wavenumber n to be dependent on time, such that $n - \alpha m t$ is constant. As before, the time scale will be determined by the interval at which the phase of each mode is calculated, T_c. This body force will also incorporate the shearing turnover time as an additional time scale, however this can be considered a natural scale of such a system.

Physically, a body force that follows the shear will correspond to energy input from sources following the fluid. This includes the variety of convective forces observed in physical phenomena. However, we stress that the implementation of our body force is intentionally highly simplified.

In section 4.6 we discussed the computational implementation of the shearing box coordinate system. Equation (4.83) describes the sheared ring force in its ideal form, relative to standard Fourier space; we modify this slightly in order to accommodate the implementation of the shearing box coordinate system. Relative to sheared Fourier space (our numerical grid), (m, p), we define

$$\hat{G}_{m,p}(t) = \begin{cases} e^{2i\pi\phi_{m,p}(t)} & \text{if } K - \delta K \leq \sqrt{m^2 + \left(p - \frac{1}{2}\alpha m T_c\right)^2} \leq K + \delta K \\ 0 & \text{otherwise.} \end{cases} \tag{4.84}$$

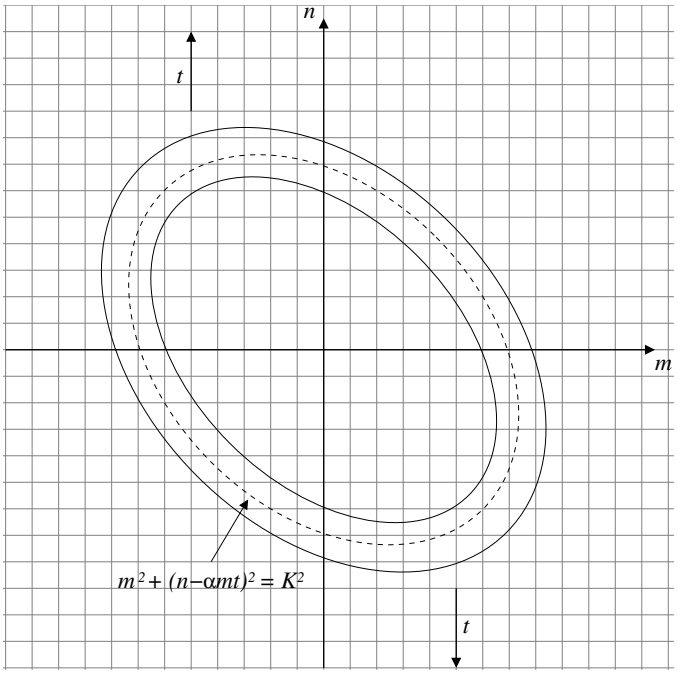

Figure 4.5: Schematic of the choice of Fourier modes made when implementing the sheared ring forcing described by equations (4.79) and (4.83). The group of standard Fourier modes contained by the ring changes as it is sheared. In the shearing box coordinate system, this group of modes is stationary, due to the system itself following the shear. A new phase for each mode is chosen whenever the time, t, coincides with a multiple of the forcing correlation time, T_c.

The above body force is stationary on our numerical grid, and hence follows the shear. The additional T_c term in equation (4.84) is present in order to ensure that the average position of the ring over each forcing correlation time is $(m, n - \alpha mt)$ in physical Fourier space. We track the force using the same methods used to follow other variables in the shearing box system; a mode reset is performed at the appropriate time in order to correctly align the grid, while the SBFT is used to convert it to/from Fourier space whenever necessary.

Although a qualitative comparison of the different types of body force discussed in this section will not be given, we have performed extensive testing of a variety of forcings across several parameters. As should be clear from the relative smoothness of the results in this chapter, we conclude that a carefully defined ring forcing

following the shearing box is the most appropriate choice of body force for our investigation.

4.8 Non-dimensionalization

Non-dimensionalization is an important technique in the mathematical study of physical phenomena. In fluid dynamics, many key characteristics of the flow can be described by a select set of non-dimensional numbers [33]. This allows us to make comparisons between flows which may have completely different physical scales, but offer a resemblance to each other. Examples of non-dimensional numbers include the Reynolds number, which desribes the turbulent properties of the flow, and the Prandtl number, which gives a ratio of diffusivities (such as the viscosity to the passive scalar diffusivity) [4].

By the use of non-dimensionalization we can often restrict our search of the parameter regime by eliminating unimportant variables. As per the Buckingham π theorem, we can reduce the number of parameters in the system by the number of dimensions spanned by our physical quantity [7]. With a body force, G defined as in equations (4.79) and (4.83) in the previous section, we have the following characteristic scales:

$$G = G\left(\frac{x}{L}, \frac{y}{L}, \frac{t}{T}\right), \tag{4.85}$$

where L is the length scale and T the correlation time of the body force (previously labelled T_c).

Each of the components and operations of equation (4.42) can be written in their non-dimensional forms as

$$\begin{gathered} x = \mathfrak{L}x^\star, \quad y = \mathfrak{L}y^\star, \quad t = \mathfrak{T}t^\star, \quad \omega = \frac{1}{\mathfrak{T}}\omega^\star, \quad \psi = \frac{\mathfrak{L}^2}{\mathfrak{T}}\psi^\star, \quad u = \frac{\mathfrak{L}}{\mathfrak{T}}u^\star, \\ \partial_x \equiv \frac{1}{\mathfrak{L}}\partial_x^\star, \quad \partial_t \equiv \frac{1}{\mathfrak{T}}\partial_t^\star, \end{gathered} \tag{4.86}$$

where $\mathfrak{L}$ and $\mathfrak{T}$ are respectively our dimensional length and time scales, and ' $\star$ ' denotes the dimensionless form of the variable/operation. Note also that we write

our force as

$$G = \delta G^\star \left(\frac{\mathfrak{L}x^\star}{L}, \frac{\mathfrak{L}y^\star}{L}, \frac{\mathfrak{T}t^\star}{T} \right), \tag{4.87}$$

where δ (which is not dimensionless) represents the strength of the forcing. As mentioned earlier in the chapter, the amount of energy applied to the system via the body force will have a direct impact on the typical velocities that occur. Hence δ will have a direct impact on the turbulent features of our flow. Also, we observe that

$$J(\psi, \omega) = \frac{1}{\mathfrak{T}^2} J(\psi^\star, \omega^\star) = \frac{1}{\mathfrak{T}^2} J^\star \tag{4.88}$$

By substituting the above into equation (4.42) and multiplying by $\mathfrak{T}^2$, we obtain

$$\partial_t^\star \omega^\star + \mathfrak{T}\alpha y^\star \partial_x^\star \omega^\star = J^\star + \mathfrak{L}\mathfrak{T}\beta \partial_x^\star \psi^\star + \frac{\mathfrak{T}}{\mathfrak{L}^2} \nu \nabla^{2\star} \omega^\star + \mathfrak{T}^2 \delta G^\star. \tag{4.89}$$

Hence our dimensionless parameters are

$$\alpha = \frac{1}{\mathfrak{T}} \alpha^\star, \quad \beta = \frac{1}{\mathfrak{L}\mathfrak{T}} \beta^\star, \quad \nu = \frac{\mathfrak{L}^2}{\mathfrak{T}} \nu^\star, \quad \delta = \frac{1}{\mathfrak{T}^2} \delta^\star, \tag{4.90}$$

resulting in the fully non-dimensional equation

$$\partial_t^\star \omega^\star + \alpha^\star y^\star \partial_x^\star \omega^\star = J^\star + \beta^\star \partial_x^\star \psi^\star + \nu^\star \nabla^{2\star} \omega^\star + \delta^\star G^\star. \tag{4.91}$$

Although this bears little difference to our starting equation, (4.42), the relation between the non-dimensional parameters and their dimensional equivalents forms a basis on which we can eliminate two parameters. This does not equate to simply ignoring the chosen parameters; we can observe the relative change in these parameters compared to those remaining in order to relate our non-dimensional investigations to a fully dimensional case.

Generally, it is in our interests to preserve parameters that we consider key to the investigation at hand, as it avoids having to calculate these parameters from others in the system. For example, we could fix our dimensionless $\alpha^\star$ and $\beta^\star$, giving

$$\partial_t^\star \omega^\star + y^\star \partial_x^\star \omega^\star = J^\star + \partial_x^\star \psi^\star + \nu^\star \nabla^{2\star} \omega^\star + \delta^\star G^\star, \tag{4.92}$$

a somewhat simplified equation. However, if we then want to calculate the effective dimensional values of α and β, we would need to estimate $\mathfrak{T}$ and $\mathfrak{L}$ in order to find

$$\alpha = \frac{1}{\mathfrak{T}}, \quad \beta = \frac{1}{\mathfrak{L}\mathfrak{T}}. \tag{4.93}$$

Additionally, should we wish to investigate the case where either α or β were zero, we would have to take the limit $\mathfrak{T} \to \infty$. This would be both computationally difficult and awkward for analysis.

As we consider these two parameters to be vital to our investigation, this would be an unwise choice. Instead, we opt to fix the length and time scales of the body force, $L^\star = L/\mathfrak{L} = 1$ and $T^\star = T/\mathfrak{T} = 1$. As a result, our non-dimensional equation (after removing asterisks), takes the same form as equation (4.42)

$$\partial_t \omega + \alpha y \partial_x \omega = J(\psi, \omega) + \beta \partial_x \psi + \nu \nabla^2 \omega + \delta G, \tag{4.94}$$

where the body force is now simply

$$G = G(x, y, t), \tag{4.95}$$

and the dimensional length and time scales of body force set the length and time scales of our system; a simple yet practical choice:

$$L = \mathfrak{L}, \quad T = \mathfrak{T}. \tag{4.96}$$

Although we have fixed these two non-dimensional parameters in the above analysis, it is clear that we are assessing a system of equations with a large number of parameters, many of which we could have chosen to set to unity. Due to the complex nature of this system we limit our degrees of freedom further by fixing other parameters; this will be discussed in the next chapter.

Chapter 5

Direct Numerical Simulations

5.1 Numerical Considerations

In chapter 4 we derived the system of equations, (4.42 – 4.44), describing a two-dimensional nonlinear flow on a β-plane, under the influence of a background shear flow. We discussed some of the key quantities describing transport in the flow (see sections 4.3 – 4.4), and gave numerical methods with which to numerically simulate the system (see section 4.6). We also explored the different possible ways of putting energy into the system (section 4.7), and looked at a non-dimensionalization scheme for the governing equations (section 4.8). As has been discussed previously, the system contains a number of parameters to explore; seven to be exact: α, β, ν, δ, L, T and κ (from the passive scalar equation). Two of these can be considered dependent on the remaining parameters by use of the aforementioned non-dimensionalization, where we have chosen the length and time scales of our body force, L and T. Note also that in our simulations, although we set T to unity, we fix the length scale, L, at a non-unity value, as given in table 5.1.

However, $(\alpha, \beta, \nu, \delta, \kappa)$ still leaves a large parameter space to explore. As such, we only vary the two parameters we consider to be key to our current investigation: α and β. In the subsequent chapters of this thesis we will explore the magnetohydrodynamic (MHD) equivalent to this problem, which will introduce several more parameters for investigation (see chapters 6 and 7).

Although we will not vary them, ν and δ still have important roles to play in our system. The fluid viscosity, ν, can be related to an inverse Grashof number, and plays a large role in determining the laminar or turbulent behaviour of the fluid. Likewise, the strength of the body foce, δ, will decide the rate of energy input in the system, and hence will determine the typical velocities of the flow. As such, it too will have a significant bearing on the turbulent properties of the flow.

The passive scalar viscosity, κ, on the other hand, has no feedback on the dynamics of the system. However, it will have an effect on the evolution of the passive scalar field, and as such, the value of the passive scalar flux (see equation (4.38)). When the fluid and passive scalar diffusivities are equal, i.e. the Prandtl number $P_r = \nu/\kappa = 1$, equations (4.42) and (4.44) take a similar form, particularly

Description	Parameter	Typical value
Strength of background shear	α	$0 \leq \alpha \leq 1$
Coefficient of vorticity gradient	β	$0 \leq \beta \leq 1$
Viscosity	ν	10^{-3}
Strength of body force	δ	0.5
Forcing length scale	L	$\frac{5}{2\pi} \pm 10\%$
Forcing time scale	T	1
Passive scalar diffusivity	κ	10^{-3}
Time step	Δt	10^{-2}
Box length (x)	L_x	2π
Box length (y)	L_y	2π
Number of grid points	N	$64^2 \leq N \leq 128^2$ *

Table 5.1: A list of parameters involved in finding numerical solutions to equations (4.42 – 4.44) using our shearing box coordinate system and associated methods. Typical values/ranges of each of these parameters are given in the third column. *The size of the numerical grid, N, is decided on a case by case basis, and is generally dependent on the parameters α and β. We have been careful to ensure that each simulation is fully resolved on a sufficiently fine grid.

when $\beta = 1$. The input of energy from $G(x, y, t)$ into the vorticity equation drives the passive scalar (although it may have a different initial state to ω). More detail on similarities resulting from $P_r = 1$ will be discussed in the MHD chapter. In regards to physical motivations for the parameter choice, this value is also at the correct order of magnitude for many atmospheric gases [48].

Although not a parameter as such, it has been observed that the form of the body force, G, has little effect on the occurance of zonal jets in β-plane systems. In other words, the structure and implementation of G can be considered unimportant when triggering the instability which leads to jet formation (although the energy injection rate determined by δ may have an important effect). However, we have

been careful to choose a body force which fits naturally with the shear flow; for more information please see section 4.7.

We fix the parameters at values at which we expect to see relatively turbulent, inviscid behaviour, but with the restriction of requiring relatively short computational times. Turbulence generally involves the interaction of widely varying scales in a single fluid system. Typically, the more turbulent a flow is, the larger the ratio of largest to smallest length scales. This poses a problem when numerically simulating turbulent fluids, as the difference in scales makes the integration harder to resolve. The turbulent flows we observe in nature (including those motivating this research) typically have Reynolds numbers many orders of magnitude larger than can currently be achieved on the most powerful supercomputers. Rather than attempting to push our simulations in order to get as close to these realistic Reynolds numbers as possible, we use our resources to gain a solid knowledge of a moderately turbulent regime. As such, we can integrate many individual systems simultaneously in order to obtain ensemble averages which establish trends between the change in parameters and dynamics.

We avoid using any non-physical techniques to remove energy from the system. Often, this is achieved by implementing hyper-viscosity, which replaces the Laplacian in the viscous term with an operator of the form $\nabla^{2k}, k \in \mathbb{N}$ [36]. Alternatively, one may include additional damping terms [40] or artificially remove energy from individual or groups of modes [30]. When damping small-scale modes, this equates to the use of hyper-viscosity, which rapidly removes energy from Fourier components far from the origin. This is often done with the aim of implementing large Reynolds number flows, as the suppression of small-scale behaviour allows for less fine computational grids. Whether or not this truly captures the behaviour (and scale separation) of turbulent flow is a matter for discussion that we will avoid here.

We also have several purely numerical parameters to take into account, such as the time step and the number of grid points used to represent the domain. The optimal values of these parameters will depend on our choice of physical parameters, and the type of dynamics produced. As such, we have considered each of these for

different regions of the parameter space, and have been careful to make sure our simulations are properly resolved in each case. Below we will discuss typical values and dependencies for each numerical parameter.

First we consider the time step, Δt, as discussed while outlining the schemes used to integrate our system of equations. Generally, the faster the dynamics of our system, the smaller Δt will need to be in order for the system to be properly resolved. The rate of energy input, δ, and the rate of energy dissipation, largely controlled by ν, will have an impact on our choice of time step. As we have fixed these parameters across all of our simulations, we have found no need to change Δt, as can be seen in table 5.1.

Working in periodic geometry, it is natural to use a box of size $(2\pi)^2$. We then discretize this space by taking a finite sized array representing specific points of this continuous plane. The Reynolds number typically has a large impact on the necessary number of grid points, and so viscosity is key to determining the value of N. As one would expect, α and β have an impact on the type of behaviour in our system, and also strongly affect the required grid size. For the majority of our experiments we use 128^2 grid points, noting that this is adapted depending on the parameter choice.

The majority of the operations performed throughout each simulation are done in spectral space. The Fourier transform we utilize (discussed in section 4.6) makes use of Hermitian symmetry in order to reduce the number of grid points required in Fourier space. As such, our spectral grid is roughly half the size of the real space grid. For example, 128^2 real grid points would correspond to 128×65 spectral grid points. Fourier components contain both real and imaginary amplitudes, so the actual number of operations performed is not reduced by the smaller spectral grid. The efficiency of working in Fourier space comes from the ease with which spectral forms of derivatives can be found, with the differential operation reducing to a multiplication of each Fourier component. For this reason, finding the stream function via the inverse Laplacian of vorticity is also greatly simplified.

We note here that, although a $(2\pi)^2$ box is natural for a doubly periodic plane,

the anisotropic nature of the zonal jets arising from the Coriolis force actually provides some motivation to extend the size of the box in the vertical y-direction. The Rhines scale, given by

$$L_{Rh} = \sqrt{\frac{U_{jet}}{\beta}}, \tag{5.1}$$

determines the spacing between each alternating jet, with U_{jet} representing a typical velocity in the jet [34]. For small values of β we expect the Rhines scale to be relatively large, and as such the spacing of the jets will be restricted by the size of the box; this has been demonstrated in our results, where we have typically used a square, $(2\pi)^2$ box. However, we have also implemented rectangular $2\pi \times 4\pi$ and larger boxes in order to fully accommodate the Rhines length scale. In doing so, we increase the real space grid size to 128×256 or larger.

5.2 Classic β-plane Jets, $\alpha = 0, \beta \neq 0$

As we begin to explore the relevant parameters involved in the shearing box simulations, we start by looking at a β-plane system in the absence of background shear, $\alpha = 0$. As mentioned previously, we will avoid varying non-essential parameters, and focus on observing the effect of changing β in this section.

With $\alpha = 0$, $\beta = 1$ and the rest of our parameters at their standard values (see table 5.1), we observe the formation of zonal jets. In figure 5.1 we plot the x-averaged mean profile of velocity over 10^4 units of time. Two alternating jets have filled the domain, and seem to be stable throughout the plotting time, with small deviations from a constant position. The maximum velocity in the jets is approximately $O(1)$, whilst the mean jet speed is typically $O(10^{-1})$. Given $T_c = 1$, the time scale for which the jets are stable is clearly separated from the forcing correlation time.

However, if we look at the full evolution of the fluid, it is clear that the position of the jets is time-dependent, despite their spatial separation staying relatively constant. In figure 5.2 we again plot the mean profile of velocity, now for the full simulation (from which figure 5.1 is taken). Here we can see that over very long

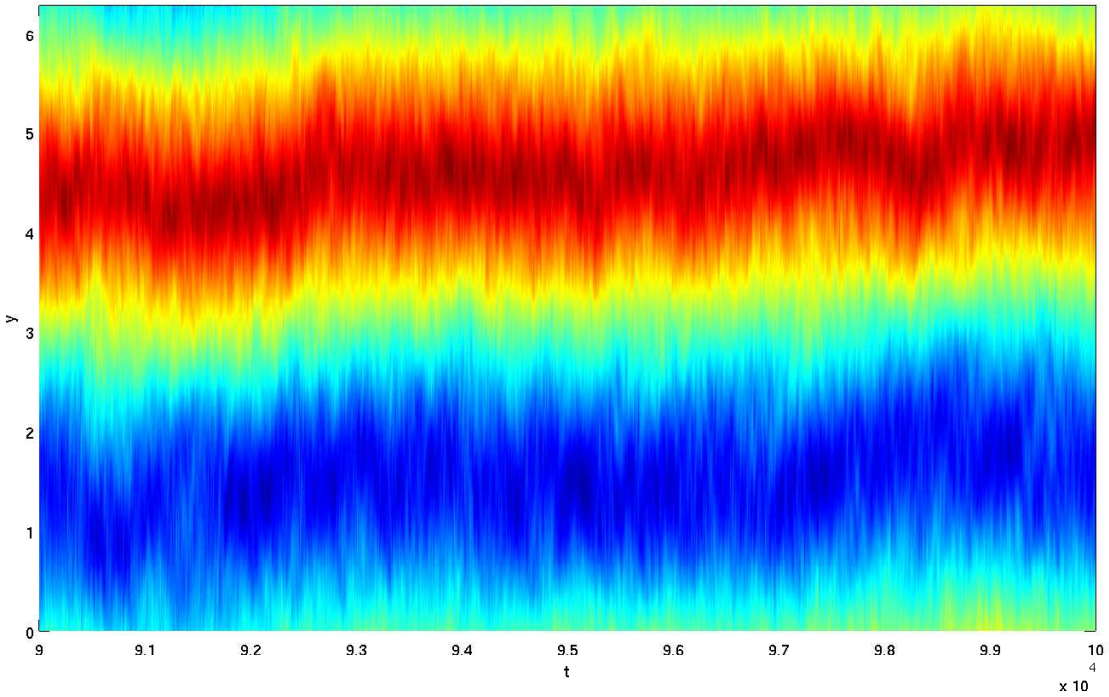

Figure 5.1: Contour plot of the evolution of the mean (x-averaged) profile of velocity over 10^4 units of time, starting at $t = 9 \times 10^4$, with $(\alpha, \beta) = (0, 1)$ and all other parameters defined as in table 5.1. Produced from the data used to make figure 5.2.

periods of time the jets, although distinct, wander across the y-domain. Sometimes the jet seems to 'walk' relatively smoothly over an extended period of time, such as can be seen in the vertical motion from $t \sim 5 \times 10^4$ to $t \sim 6 \times 10^4$. Alternatively, the jets will make occasional sharp 'jumps' in vertical position, as can be seen most prominently at $t \sim 4 \times 10^4$.

Why does this happen? The vertical movement of a jet over time can be seen in some of the physical phenomena motiving our model, such as ocean currents and some (but not all) spherical systems [42]. In figure 5.3 it appears (at initial observation) that over the course of a year, Jupiter's zonal jets undergo an observable change. However, while the appearance of the jets may have changed, their latitudinal position is actually quite stable, despite a large period of time passing.

This is emphasized further by figure 5.4, which shows the average latitudinal

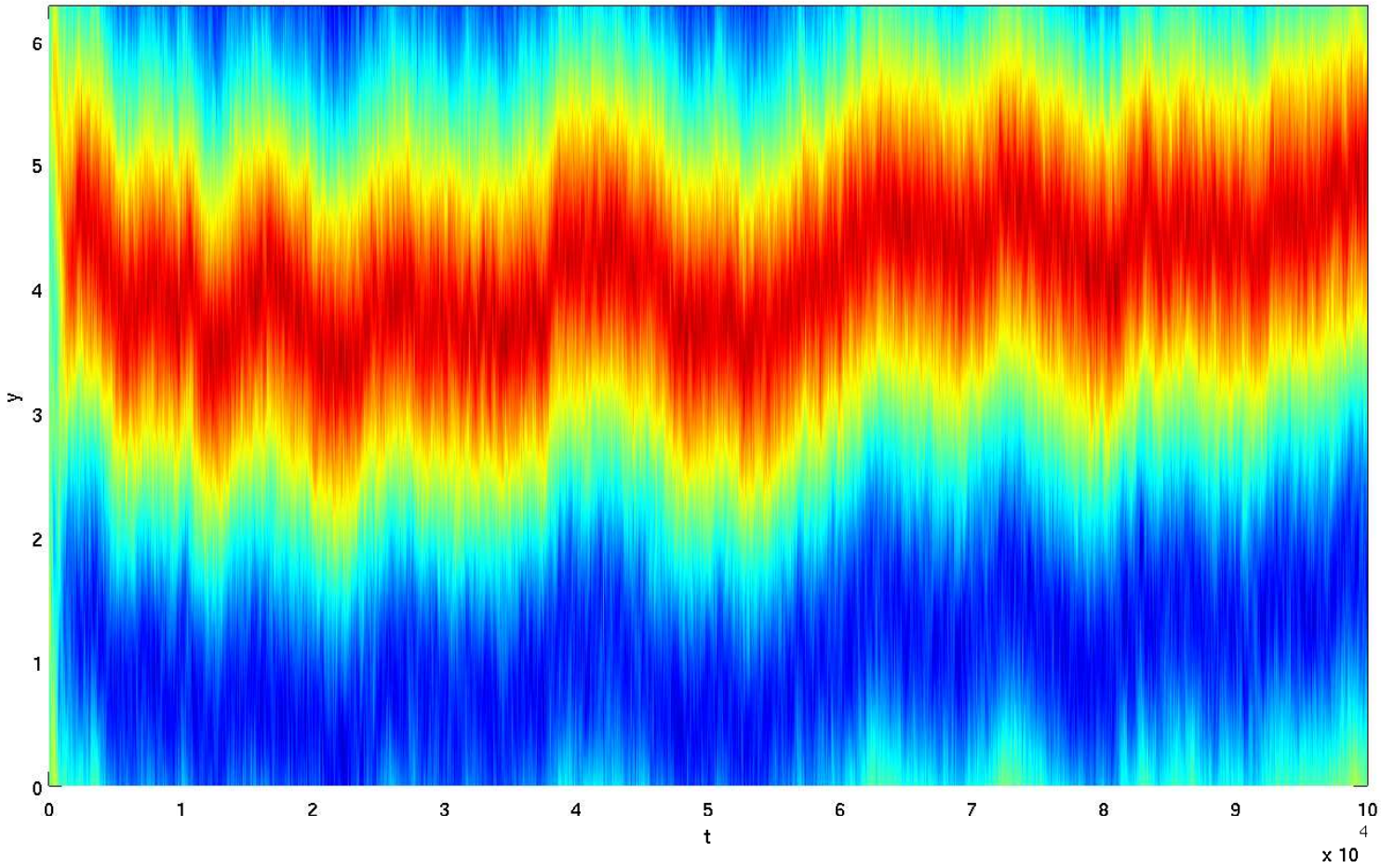

Figure 5.2: Contour plot of the evolution of the mean (x-averaged) profile of velocity over 10^5 units of time, with $(\alpha, \beta) = (0, 1)$ and all other parameters defined as in table 5.1.

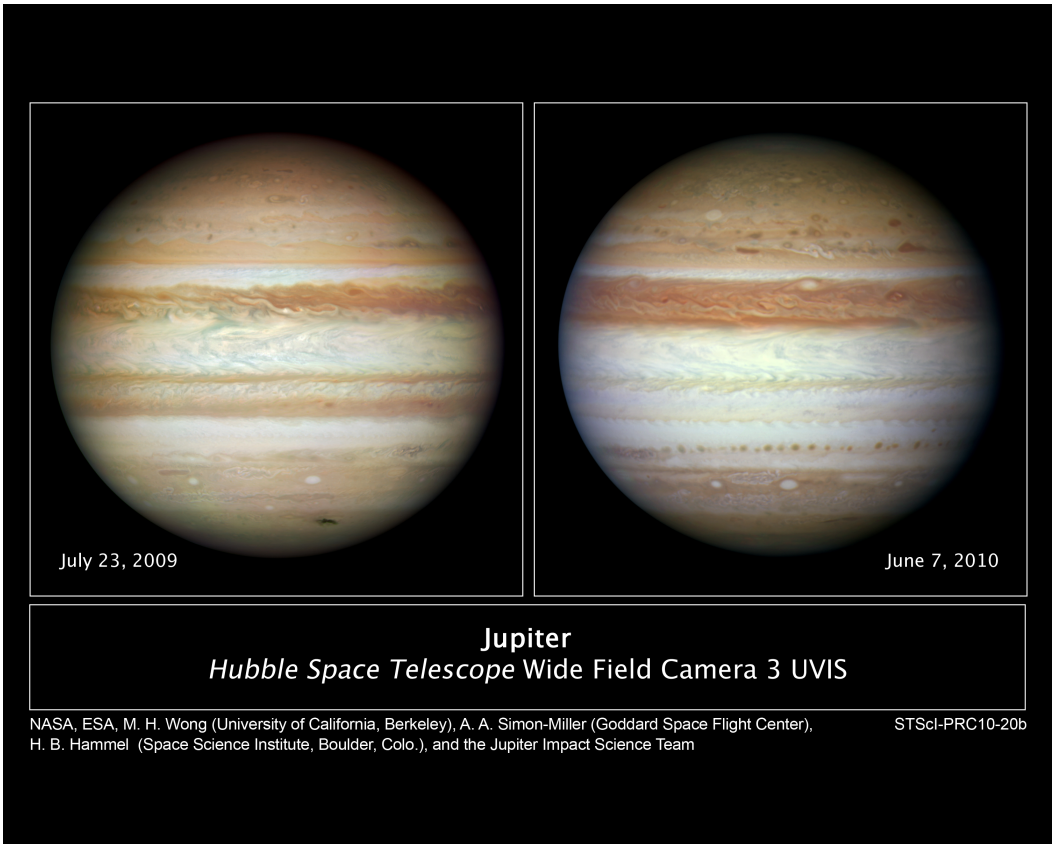

Figure 5.3: Portraits of Jupiter, as taken by NASA's Hubble Space Telescope [27].

wind speed on Jupiter as observed by the Voyager 2 (1979–1980) and Cassini (2000) probes. In the 20 year period between these two missions, there is very little vertical variance in the position of the jets. While this feature is not captured by our model, results regarding the transport properties of such flows should still have a general impact on the nature of rotating fluids. However, our results may have more relevance to the aforementioned oceanic jets. To prevent the drift in our model we would need to modify it in such a way as to break the Galilean symmetry in y (see section 4.2).

The reason for the jets meandering in our numerical simulations is a direct consequence of the model we are using. The ideal, two-dimensional β-plane equation has no mechanism tethering the jets to a particular position. The physics taking place on a giant planet such as Jupiter involve the Coriolis term as a function of latitude, giving preference to certain features dependent on their distance from the

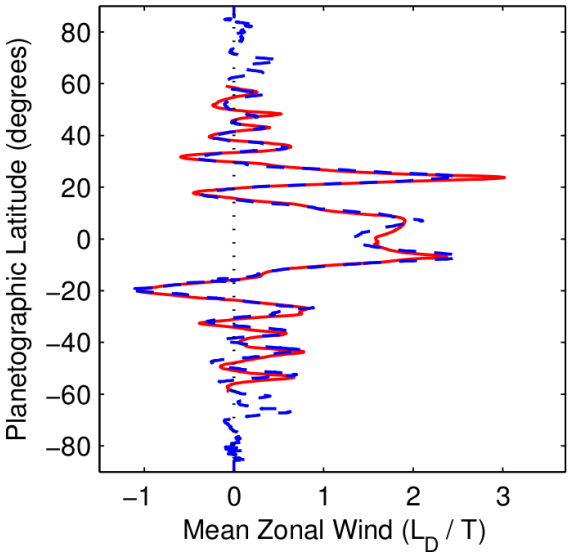

Figure 5.4: Mean zonal wind as a function of latitude as observed on Jupiter, from Warneford and Dellar, 2014 [47]. The red line represents data gathered by the Voyager 2 probe (1979 – 1980), whilst the blue dashed line is from Cassini (2000).

equator/poles. By making a β-plane approximation, we assume that the gradient of the Coriolis force is constant across the y-domain, with the general latitude and strength of the force implied by β alone. Simply put, there is nothing anchoring the jets to a particular position in y.

Although in figures 5.1 and 5.2 the zonal flows seem to be meandering about a line of roughly constant y, this level of consistency is not common across our current parameter choice, as can be seen in figure 5.5, another simulation with a different randomized initial state (and body force). Here we see that the jets are displaced vertically by approximately π over 10^5 units of time. Overall, we do not expect there to be any preference to the vertical displacement of the jets; this is determined by the body force over many forcing correlation times.

Despite the limitations of our model, the flow remains stable for long periods of time, and exibits a distinct spatial distribution such that we can confidently make comparisons with zonal jets observed in physical systems.

Figures 5.2 and 5.5, while displaying the long term behaviour of the zonal flow, do not give a clear representation of how jet formation takes place. In figure 5.6 we

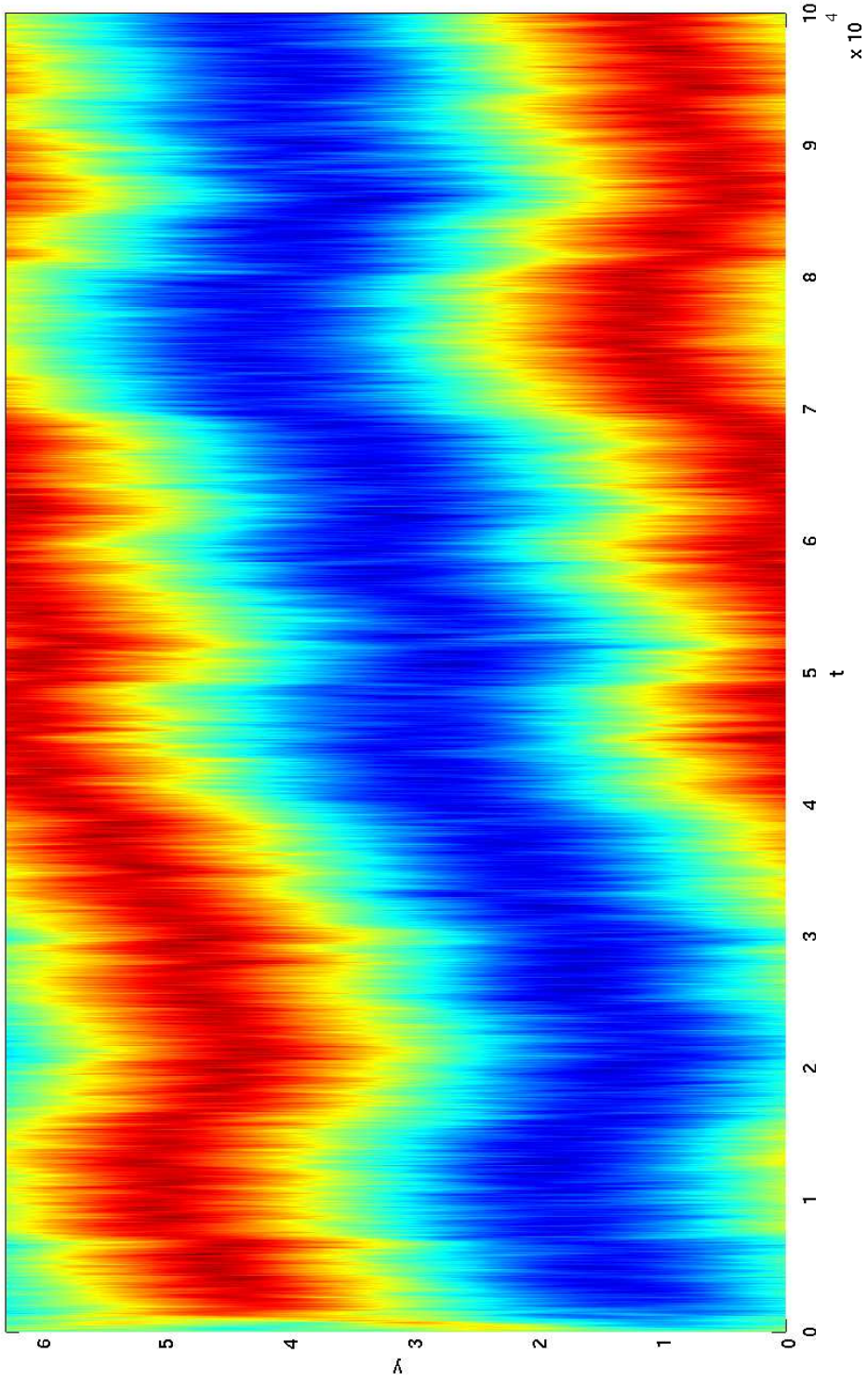

Figure 5.5: Contour plot of the evolution of the mean (x-averaged) profile of velocity over 10^5 units of time, with $(\alpha, \beta) = (0, 1)$ and all other parameters defined as in table 5.1. Note that although this figure has been produced using the same parameters as the simulation used to produce figures 5.1 and 5.2, the randomized initial state and body force have taken different values.

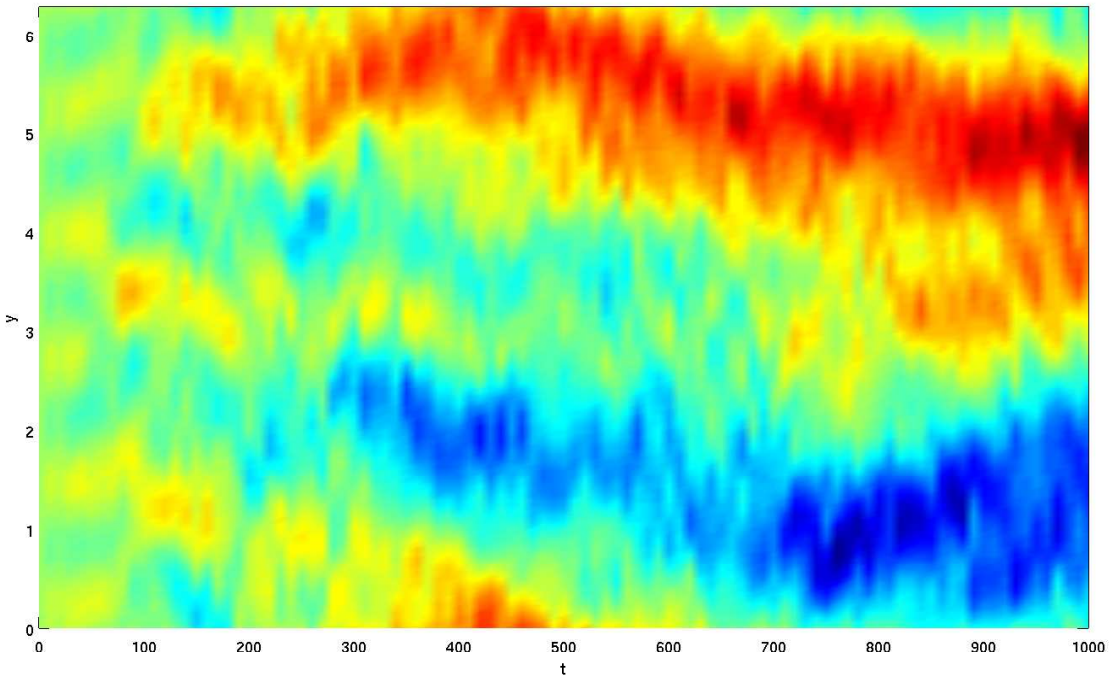

Figure 5.6: Contour plot of the evolution of the mean (x-averaged) profile of velocity over 10^3 units of time, with $(\alpha, \beta) = (0, 1)$ and all other parameters defined as in table 5.1. Produced from the data used to make figure 5.2.

plot the zonal velocity of the simulation shown in figure 5.2 for the first 10^3 units of time. For early times ($t < 50$), there are roughly five sets of weak alternating zonal jets. These merge into three distinct pairs, which persist until $t \sim 200$, at which point the flow begins the steady transformation into the two alternating jets which dominate the behaviour of the system for a long period of time (see figure 5.2). This process of jet merging is not unique to this individual simulation; the inverse cascade driven by the vorticity gradient pushes energy into increasingly large scales until reaching the limiting distance between jets as given by the Rhines scale.

However, we note that although the Rhines scale governs the physical length of the jets, there are also computational restrictions on jet spacing. The size of the box of the fluid will influence this length scale; the maximum distance between the centres of equally sized alternating jets can only ever be $L_y/2$. When the Rhines scale exceeds this value, we observe that the jets reach an equilibria about the

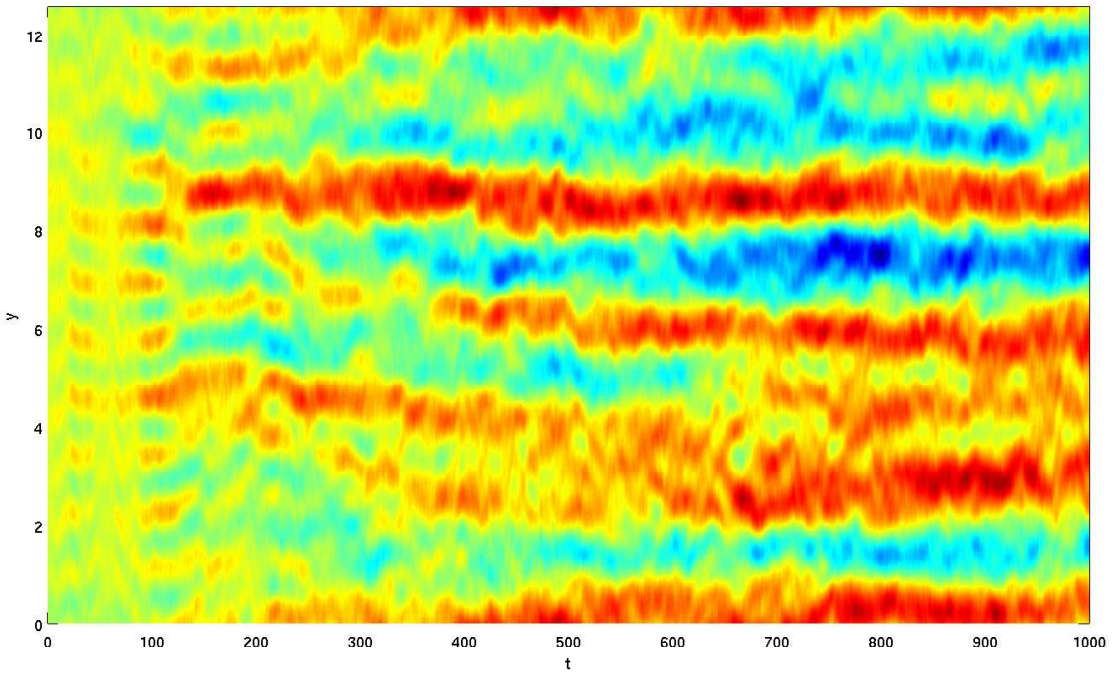

Figure 5.7: Contour plot of the evolution of the mean (x-averaged) profile of velocity over 10^3 units of time, with $(\alpha, \beta) = (0, 1)$ and all other parameters defined as in table 5.1, except for $L_y = 4\pi$. Produced from the data used to make figure 5.8.

largest possible state they can occupy in the box, i.e. with spacing $L_y/2$.

As mentioned in the introduction of this chapter, our code accomodates the simulation of rectangular domains of a fluid, allowing for larger vertical length scales without having to expand the horizontal range. Note that due to our implementation of the Fast Fourier Transform, simulations on a square domain with $2^{2k}, k \in \mathbb{N}$ gridpoints are slightly more efficient [18].

In figure 5.7 we plot the mean profile of velocity for a fluid with the same parameters as the others figures given in this section so far, but with $L_y = 4\pi$ (twice the vertical box length). Comparing to figure 5.6, we observe how, with many jets merging in the early stages of the fluid's evolution, a more complicated state is reached by $t = 1000$, despite having roughly the same spacing between jets.

As the fluid continues to evolve, it settles to a state with four alternating jets, as seen in figure 5.8. This reassures us that the vertical length scales given by

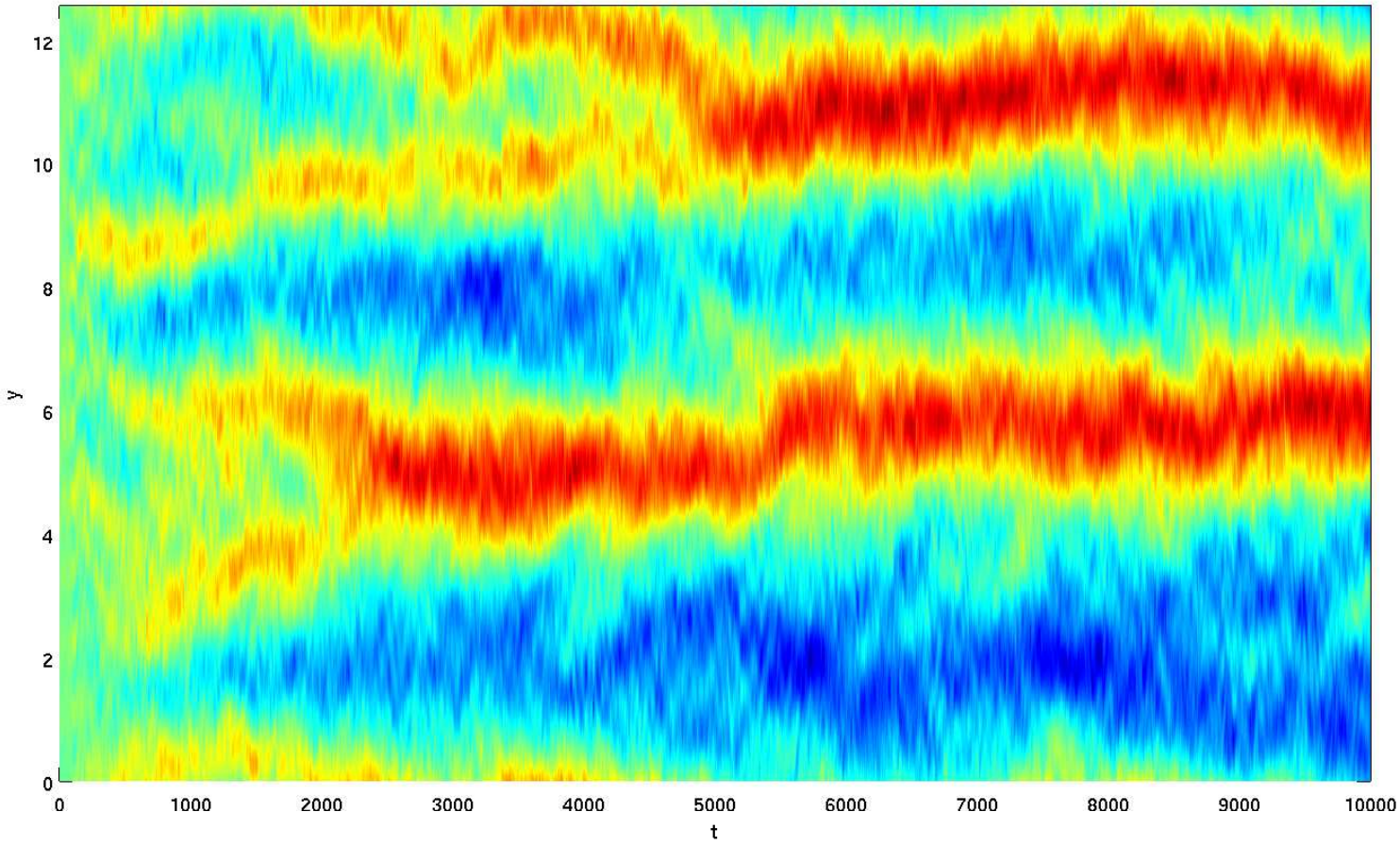

Figure 5.8: Contour plot of the evolution of the mean (x-averaged) profile of velocity over 10^4 units of time, with $(\alpha, \beta) = (0, 1)$ and all other parameters defined as in table 5.1, except for $L_y = 4\pi$ (with grid size adjusted appropriately).

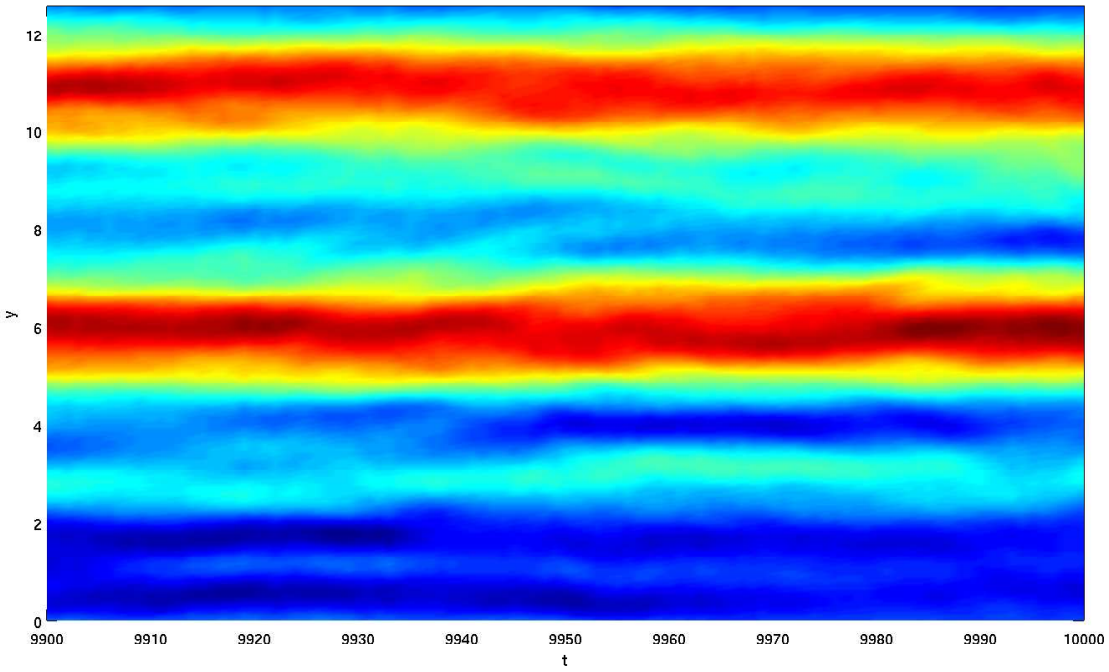

Figure 5.9: Contour plot of the evolution of the mean (x-averaged) profile of velocity over 100 units of time, starting at $t = 9.9 \times 10^3$, with $(\alpha, \beta) = (0, 1)$ and all other parameters defined as in table 5.1, except for $L_y = 4\pi$. Produced from the data used to make figure 5.8.

the $(2\pi)^2$ periodic box are not restricted. However, interestingly we note that the spacing between jets in figure 5.8 is not regular; at $t = 10^4$ jets appear to be centred at approximately $y = 2, 6, 8.5, 11$. This can be seen more clearly in figure 5.9. Although the length of the jets has been preserved between the smaller and larger box simulations, the lack of symmetry in the y-direction shown here is a feature that cannot be observed in boxes that only allow for one pair of alternating jets. We must also consider that over incredibly long time scales (beyond those accessible to us), the spacing could evolve further.

For a long time, stable system with multiple jets, the spacing between each jet on the domain tends to be equal when averaged over many simulations. Generally, the variations in jet spacing between two pairs of zonal flows do not exceed that seen in figures 5.8 and 5.9 (in the absence of background shear and magnetic fields).

However, this is a feature of the flow we will not go into detail about in this thesis.

As mentioned previously, the characteristic vertical length scale in a β-plane system is the Rhines scale, given by

$$L_{Rh} = \sqrt{\frac{U_{jet}}{\beta}}, \tag{5.2}$$

where U_{jet} is a typical jet velocity. Due to its dependence on the velocity field, the Rhines scale is calculated as a diagnostic of each simulation. Calculating U_{jet} is not a particularly trivial exercise. Systematically defining and calculating the position of each jet in a rigorous manner can be difficult and prone to error. As such, following the literature we take a simplified U_{jet} to be

$$U_{jet} = U_{max} - U_{min}, \tag{5.3}$$

where U_{min} and U_{max} are respectively the minimum and maximum values of the horizontal component of the magnitude of velocity [15]. For idealised jets, with no mixing occuring at the boundary between the alternating flows, this value of U_{jet} tells us the difference in velocity between the fastest moving particles (generally at the centre of the jet), and the slowest moving (at the boundary). As such, it could be considered a relative maximum velocity of the jet. Realistically, due to mixing occuring between the jets, it is likely that U_{min} will be close to zero at some point across the fluid domain, and as such $U_{jet} \approx U_{max}$. As such, this quantity is more indicative of the fastest horizontal velocity of the strongest jet than a typical jet velocity. We note that another measure of the jet velocity used in the literature is the root mean square of the velocity field, U_{rms}.

Nevertheless, without considerable time and effort dedicated to it, there is no better method for accurately calculating U_{jet}. As such, we refer to the following results with some caution, noting that we will not make much use of the Rhines scale elsewhere in this thesis.

In figure 5.10 we plot the Rhines scale, calculated for the flow shown in figure 5.8, with $\beta = 1$ and all other parameters set as given in table 5.1. Despite the large variance between calculated values (typically $\pm 10\%$), it is clear that the average value of the Rhines scale is relatively stable over long periods of time, with

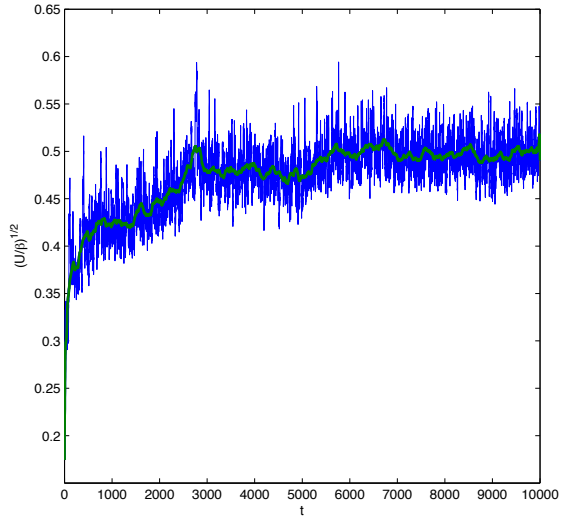

Figure 5.10: Rhines scale plotted as a function of time, with U_{jet} calculated as in equation (5.3). Produced from the data used to make figure 5.8.

$L_{Rh} = 0.5$ for the last 4×10^3 units of time. This doesn't match the spacing between jets exactly, but it is of the same order of magnitude.

Comparing with figure 5.8, which gives an overview of the evolution of the flow, we can see how merging events roughly correspond with different regions in figure 5.10. Three 'states' of the flow are divided by the two events occuring at roughly $t = 2.5, 5 \times 10^3$, and correspond to the initially unstable state of L_{Rh}, a stable period with $L_{Rh} \approx 0.475$, and the final stable region with $L_{Rh} \approx 0.5$. The initial dynamically unstable state features the merging of many weak jet-like structures, and is defined by a (mostly) increasing Rhines scale. Following this, we have a period of time in which there are three distinct jets, during which L_{Rh} seems to plateau. As the two weaker jets merge we enter the third and final stage of the flow's evolution.

So far we have discussed the general statistics of the flow without looking at the structure of the fluid at any particular time. In figure 5.11 we plot the vorticity field of the flow corresponding to figure 5.8 for several values of t. On initial observation, the system appears to be dominated by vortex-like behaviour, in complete contrast to the jet-like features of the mean velocity field. However, as the flow evolves, the

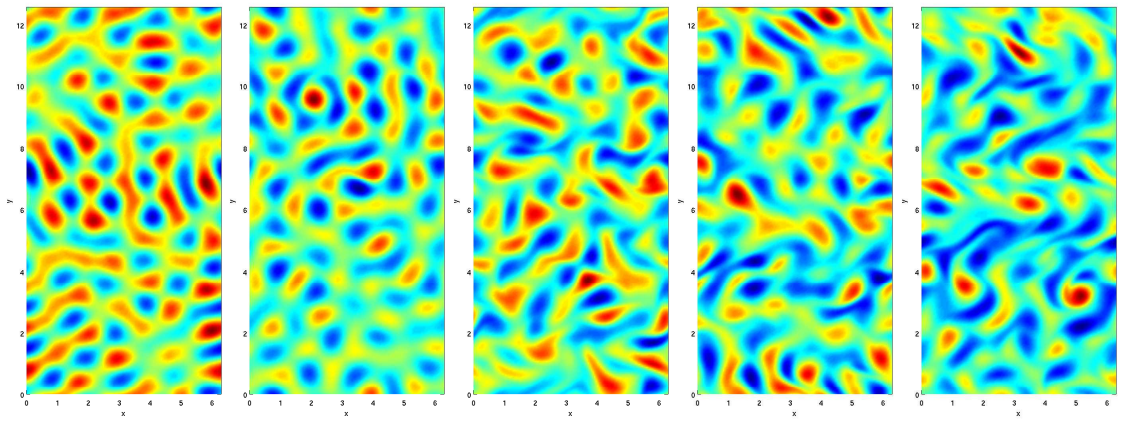

(a) (b) (c) (d) (e)

Figure 5.11: Contour plot of the perturbations of the vorticity field at (a) $t = 10$, (b) $t = 100$, (c) $t = 10^3$, (d) $t = 5 \times 10^3$, (e) $t = 10^4$. $(\alpha, \beta) = (0, 1)$ and all other parameters defined as in table 5.1, except for $L_y = 4\pi$. Produced from the data used to make figure 5.8.

background gradient of vorticity (removed from these plots) acts to organise the vortices, with a preference for the horizontal direction. Note that the vortices here are roughly on the scale of the body force. For much smaller values of L, we would expect the vortices to be smoothed by the upscale energy cascade before forming zonal features, making the forcing correlation time less important. By $t = 5 \times 10^3$ the fluid has adopted a preference for the location of positive and negative parcels of vorticity in the y-direction, which remains similar for the rest of the simulation.

This becomes clear from the mean, x-averaged profile of vorticity, as displayed in figure 5.12. While the jets in the vorticity profile appear less consistent than their velocity profile counterparts, they are still persistent features of the β-plane system. Note that strong (positive or negative) zonal regions of vorticity denote regions of mixing in the flow, with jets (in regards to the velocity) occuring in between these regions (compare figure 5.8). This comes about due to the relationship between the vorticity and velocity, with $\omega \approx -\partial_y u_x$ for a horizontally dominant flow.

Of interest is the passive scalar field acted on by the fluid. As discussed in the previous chapter, we impose a background gradient on the passive scalar, the

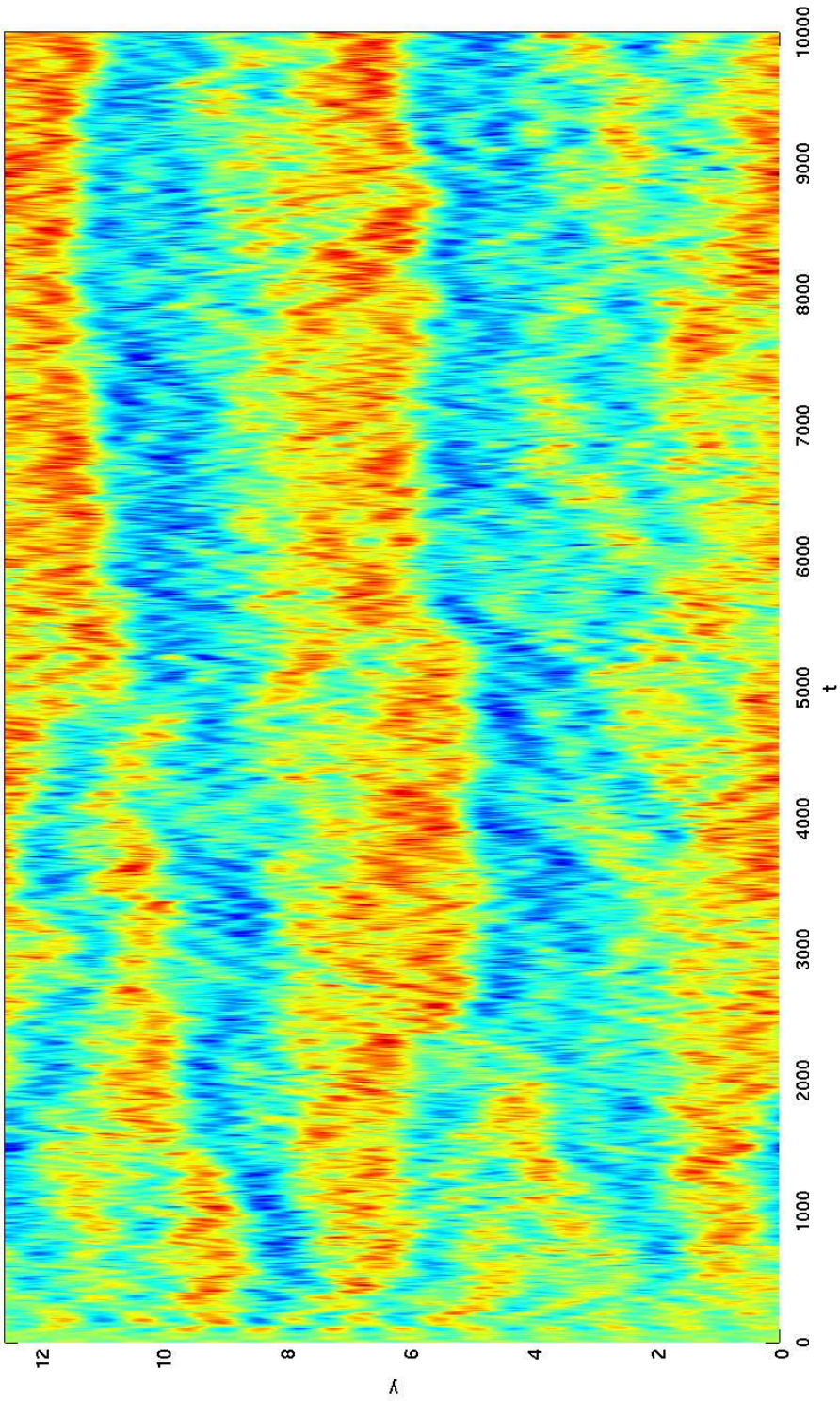

Figure 5.12: Contour plot of the evolution of the mean (x-averaged) profile of vorticity over 10^4 units of time, with $(\alpha, \beta) = (0, 1)$ and all other parameters defined as in table 5.1, except for $L_y = 4\pi$. Produced from the data used to make figure 5.8.

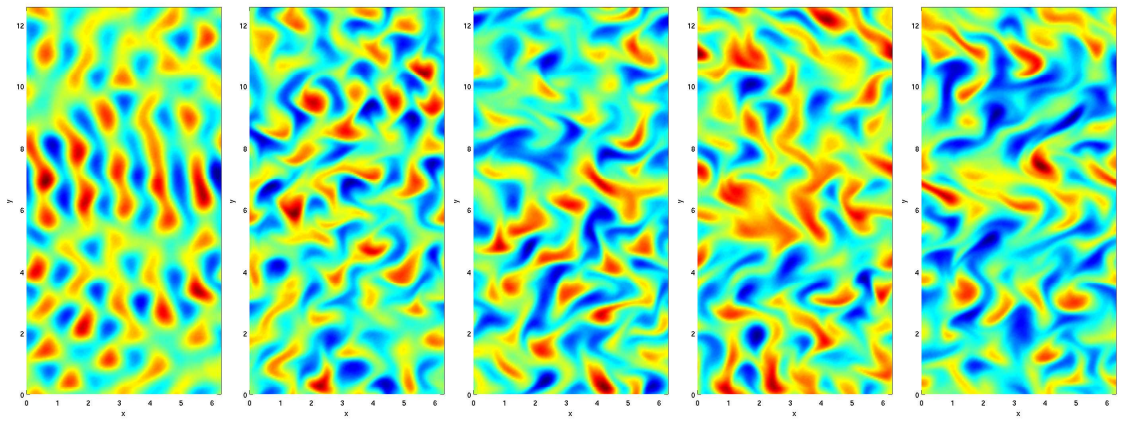

(a) (b) (c) (d) (e)

Figure 5.13: Contour plot of the perturbations of the passive scalar field at (a) $t = 10$, (b) $t = 100$, (c) $t = 10^3$, (d) $t = 5 \times 10^3$, (e) $t = 10^4$. $(\alpha, \beta) = (0, 1)$ and all other parameters defined as in table 5.1, except for $L_y = 4\pi$. Produced from the data used to make figure 5.8.

strength of which affects only the magnitude of the field (not its structure), which we consequently set to unity. The Prandtl number giving the ratio of dynamic viscosity to passive scalar diffusivity is also set to unity (i.e. $\kappa = \nu$). With $\beta = 1$, this leaves us with two similarly governed quantities; the differences being that the vorticity is driven by the random body force G, while the passive scalar is driven by the vorticity itself.

As such, it should be of little surprise that the passive scalar fields plotted in figure 5.13 bear a striking resemblence to the vorticity fields of figure 5.11. The latter tends to maintain tight, regularly shaped vortices, whilst the passive scalar appears a little more distorted and stretched; this may be a result of the rigid structure of the body force being relaxed through the vorticity before it is passed on to the passive scalar field. Transport of the passive scalar across the fluid is key to our investigation of the flux, which we will discuss later in this section.

Having explored the occurence of jets and other related phenomena for a single value of β, it is interesting to investigate when these features occur in regards to the strength of the vorticity gradient. For $\beta = 0$, we certainly expect no stable

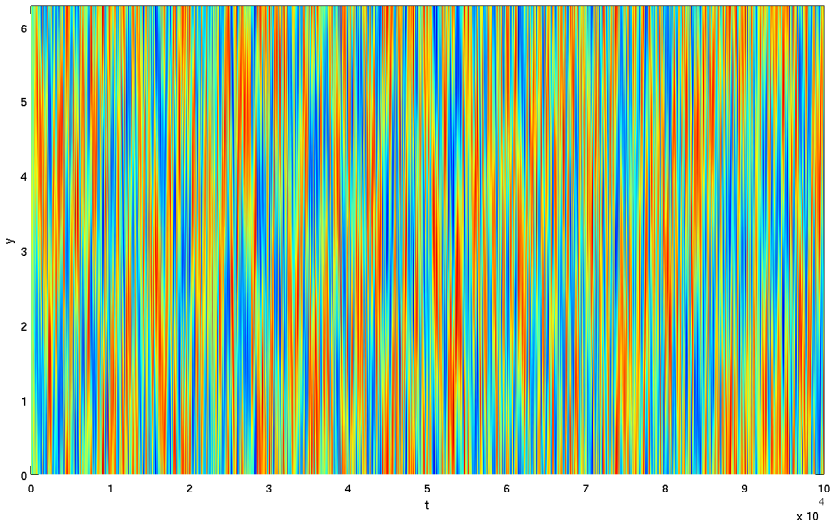

(a)

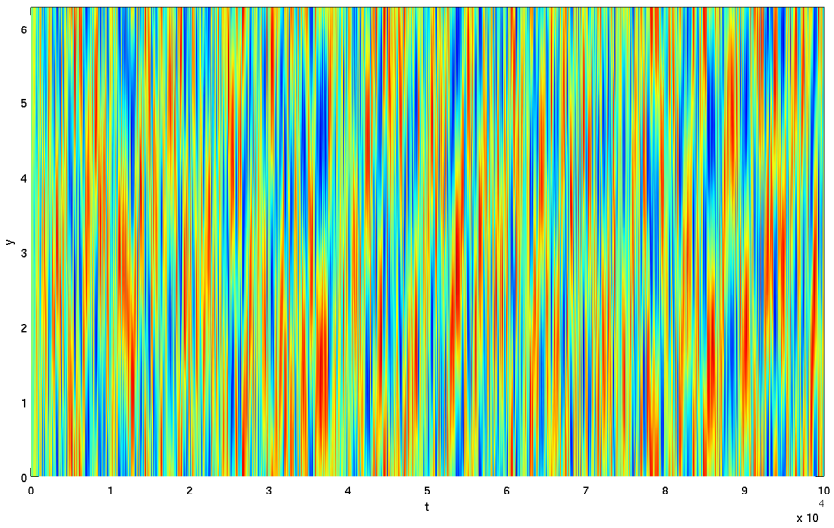

(b)

Figure 5.14: Contour plot of the evolution of the mean (x-averaged) profile of velocity over 10^5 units of time, for (a) $(\alpha, \beta) = (0, 0.01)$, (b) $(\alpha, \beta) = (0, 0.1)$, and all other parameters defined as in table 5.1.

jets to be present in the flow, although very short-time zonal behaviour may be observed (as discussed in section 5.3).

In figures 5.14 and 5.15 we plot the x-averaged profiles of velocity for flows with $\beta = 0.01, 0.1, 0.2$. Figures 5.14a and 5.14b appear to display little to no organized vertical structure. While the simulation with $\beta = 0.2$ does seem to have

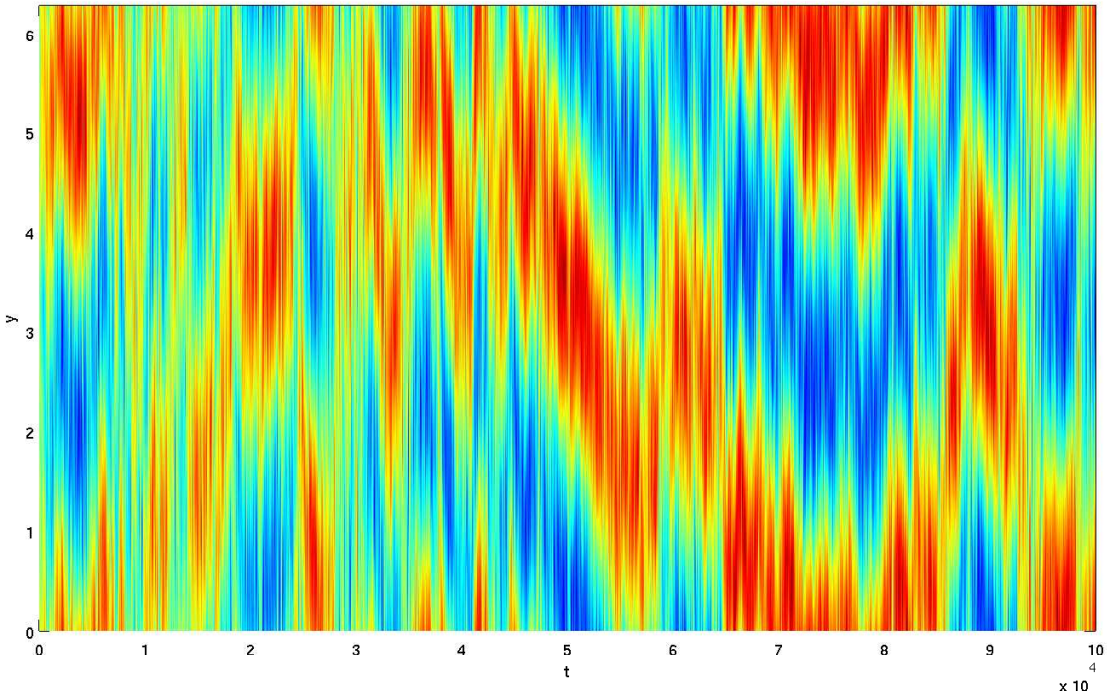

Figure 5.15: Contour plot of the evolution of the mean (x-averaged) profile of velocity over 10^5 units of time, with $(\alpha, \beta) = (0, 0.2)$ and all other parameters defined as in table 5.1.

some prominent jet-like features, these are relatively unstable when compared with figure 5.2 for $\beta = 1$. Again, we emphasize that our system lacks the physical mechanism which anchors the jets to any particular lattitude, and as β decreases the jet-like features in the flow tend to drift in y increasingly rapidly.

As such, precisely defining the term 'zonal jet' is necessary before we can investigate their occurrence. Arguably, even small β flows such as those shown in figures 5.14a and 5.14b have jet-like structures over very small times; indeed, a snapshot of the mean velocity profile for the last 10^3 units of time for each figure will reveal a relatively stable jet-like flow. However, at some point (in β, as it decreases) the mechanism which organizes the flow may switch from being the vorticity gradient to the body force. Finding a diagnostic which indicates this transition in behaviour is not a trivial exercise.

A quantity we use in our attempt to investigate this is the passive scalar flux;

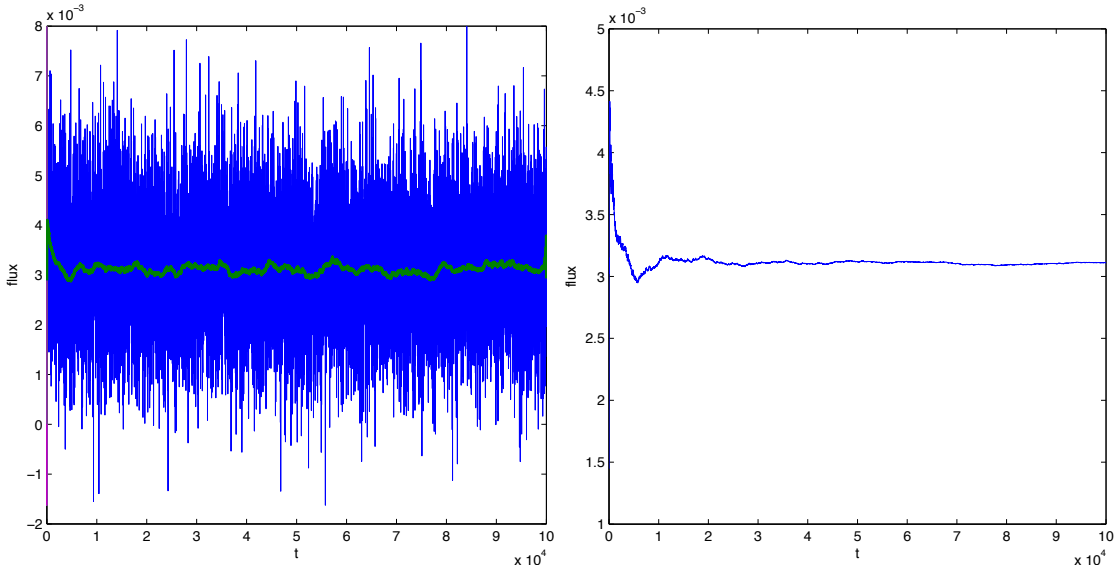

(a) (b)

Figure 5.16: Spatially averaged passive scalar flux plotted as a function of time $(\alpha, \beta) = (0, 1)$. (a) gives the flux in blue and a smoothed average in green, whilst for (b) the average of the flux over the previous 50% of the simulation is calculated and plotted for each point in time. Produced from the data used to make figure 5.2.

the downward vertical transport of the passive scalar field throughout the system:

$$F(x, y, t) = -v\theta. \tag{5.4}$$

More details on this quantity can be found in the previous chapter. For figure 5.16a, we average F spatially and plot against t for $\beta = 1$ (as shown in figure 5.2). As can be seen, the variance is very large and although most of the transport is downward, i.e. $F > 0$ (as to be expected due to the passive scalar gradient), there are numerous points where this is not the case. However, in general when averaging over time the flux does take a consistent value. This can be seen in figure 5.16b, where at each point in time we calculate the flux averaged temporally over the latter half of the simulation. This helps eliminate transient data, and leads to a stable value of F; approximately 3.1×10^{-3} here.

It should be noted that in the above figures, the passive scalar flux settles to a

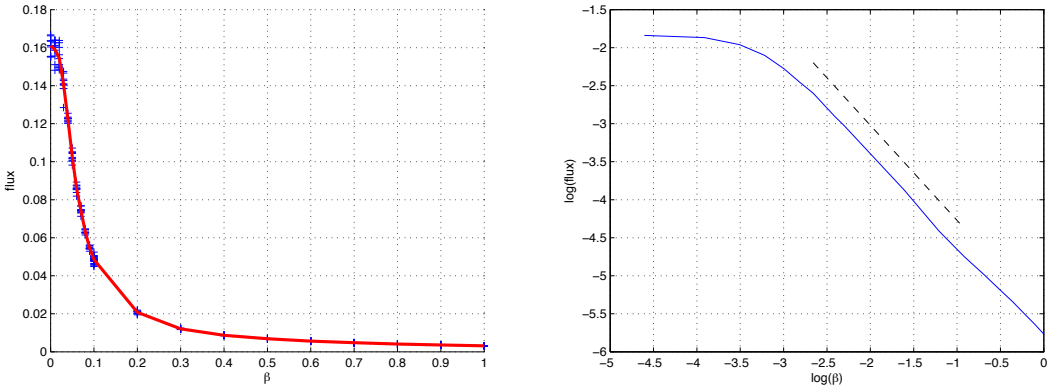

(a) (b)

Figure 5.17: Spatially and temporally averaged passive scalar flux plotted as a function of β. Time-averaging is performed by taking the mean of the flux over the previous 50% of the simulation. This is averaged over a number of randomized simulations, each represented in (a) by a blue cross. The ensemble average is plotted in red in (a), while the natural log-log relationship of this line is given in (b), with $\beta^{-5/4}$ given by the dashed line. A denser selection of points is used for $\beta \leq 0.1$ in order to properly establish the relationship between β and the flux. Note that some individual points lie directly beneath the average line in (a).

stable value after roughly 10^4 units of time. How quickly an appropriate value of F is found is dependent on the parameter regime of the system. Generally, flows tend to stabilize faster when α, β or B_0 are large relative to the forcing correlation time. We have been careful to make sure that the values of F used in our data have come from properly resolved simulations, and will comment when this is not the case (in particular, see section 5.3).

The single value of a spatially and temporally averaged flux of a simulated fluid gives a very rough idea as to how much vertical mixing takes place in the final (possibly stable) state of the flow. Building up a collection of these values across a range of β allows us investigate the dependency of the vertical transport on the vorticity gradient.

In figure 5.17 we plot F for the range of $0 \leq \beta \leq 1$. We can see how the flux

rapidly drops for $\beta < 0.1$, before more slowly levelling out. It is interesting to compare this to our mean velocity profiles in figure 5.14. In particular, we can see how the 'quick drop' region in figure 5.17a produces flows without stable jet-like features, whilst as we reach the 'levelled off' region at $\beta = 0.2$, we start to observe increasingly steady zonal flows.

Figure 5.17b shows the log-log relationship between the flux and β. For small β, the flow has no dependence on the parameter; the body force appears to be the sole determining feature of the system. As β increases, we develop an approximately $F \propto \beta^{-5/4}$ relationship, which is maintained as β grows. We have been unable to find reference to this power law elsewhere in the literature.

Note that as β tends to zero, the time average of the flux starts to converge poorly (as the flux never tends to a constant value; an issue we will discuss in the next section 5.3). However, we are confident that the results presented in the current section are fully resolved for values as small as $\beta = 3 \times 10^{-2}$.

In summary, we have mapped out the form of the flow across a range of moderate values of β, having confirmed observations previously made of the spontaneous formation of large-scale zonal jets. Scaling laws relating the vertical transport and the effective diffusivity of the flow have been given for this range of β, with a power law of $F \propto \beta^{-5/4}$ becoming apparent for stronger vorticity gradients.

We have found that the threshold for the occurence of jets is difficult to measure, as to do so requires some quantification of what a 'jet' consists of. This will be explored in more detail in the next section, where we look at the statistics of the flow over long time periods for very small values of β.

5.3 The Small β Limit, $\alpha = 0, \beta \to 0$

Having discussed the effect of varying β in section 5.2, we have noted how the passive scalar flux requires an increasingly large amount of time to settle to a fixed value in the small β limit. In this subsection we briefly investigate the cause of this, as well as the case of forced isotropic two-dimensional turbulence ($\beta = 0$).

The passive scalar flux, F, a diagnostic of the vertical transport properties of

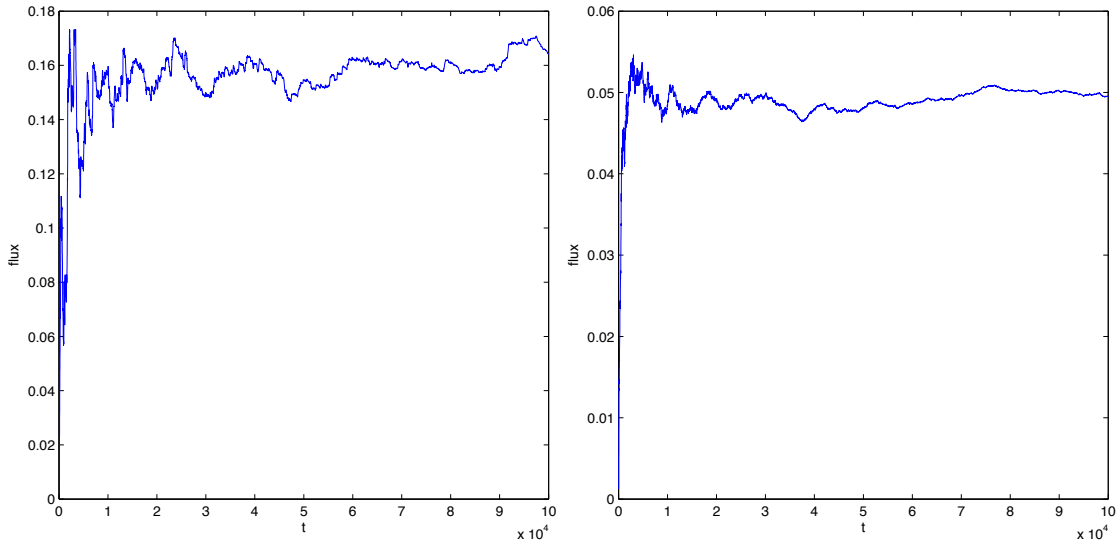

(a) (b)

Figure 5.18: Spatially averaged passive scalar flux plotted as a function of time for (a) $(\alpha, \beta) = (0, 0.01)$, (b) $(\alpha, \beta) = (0, 0.1)$. The average of the flux over the previous 50% of the simulation is calculated and plotted for each point in time. Note that (a) and (b) are produced from the data used to make figures 5.14a and 5.14b respectively.

our fluid flow, has been shown to converge to a single average value (despite a sometimes large variance) for moderate values of β. For any flow which reaches an equilibrium or displays regular periodic behaviour it can be expected that the transport of a passive scalar will, when averaged over time or space, similarly settle down. For $\beta = 1$, we saw that as the flow reached an increasingly stable, jet-like state, F quickly reached a constant value of approximately 3×10^{-3} (see figure 5.16).

As β decreases, so does the stability of the zonal jets and the time scales over which they exist. Likewise, the time required for the flux to reach an equilibrated value is increased. This can be seen in figure 5.18, where the smallest values of β have not allowed F to settle by $t = 10^5$.

The means by which the flux increases as β decreases is clear; as the vorticity gradient becomes weaker, the organization of the flow into well regulated vertical

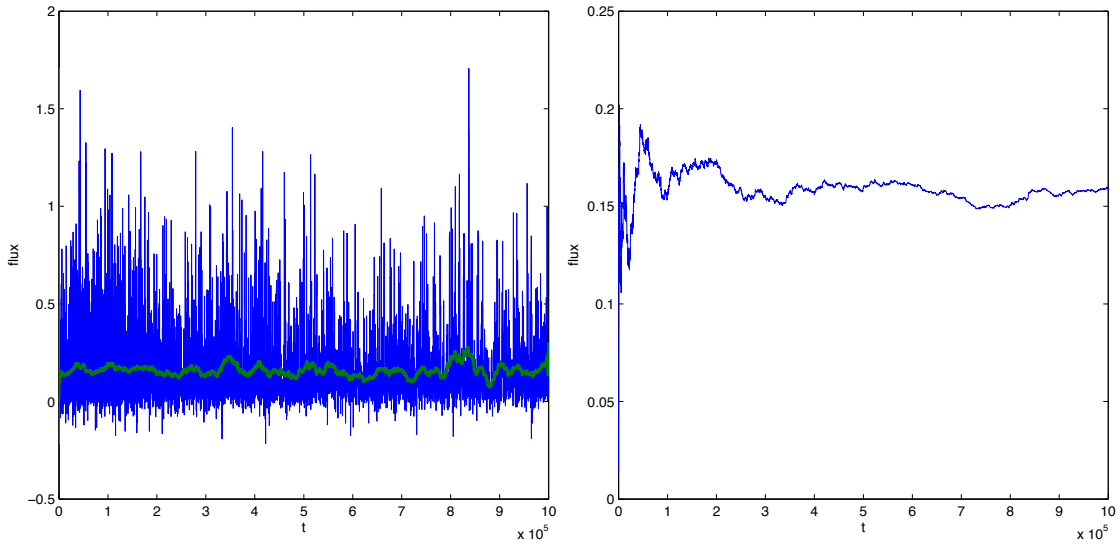

(a) (b)

Figure 5.19: Spatially averaged passive scalar flux plotted as a function of time for $(\alpha, \beta) = (0, 0)$. (a) gives the flux in blue and a smoothed average in green, whilst for (b) the average of the flux over the previous 50% of the simulation is calculated and plotted for each point in time. Produced from the data used to make figure 5.21. Note that generally $F > 0$ due to its definition, (4.38).

sections becomes less coherent, and vertical transport becomes intensified. The mechanism which governs how long it takes for the flux to settle is more subtle. As β tends towards zero, the flow becomes increasingly determined by the body force, G. Due to the random nature of G, when there are no other parameters influencing the flow, the flux will require a much longer averaging time to reach a value of the same accuracy as when β (or α, etc) are present.

However, this still leaves questions regarding the behaviour of the flux in the small β limit. Does the time required for F to stabilize, t_F, take a fixed value, t_G, as β tends to zero? Or is there a cut off point at which β becomes negligible when compared to G, and the flux requires the same amount of time to settle as when $\beta = 0$ (that is, $t_F = t_G$ for $\beta \neq 0$)? These two types of behaviour are represented in figure 5.20, where we give a schematic of the flux stability time against β. Figure 5.20a represents the former, while 5.20b gives a region of 'forcing

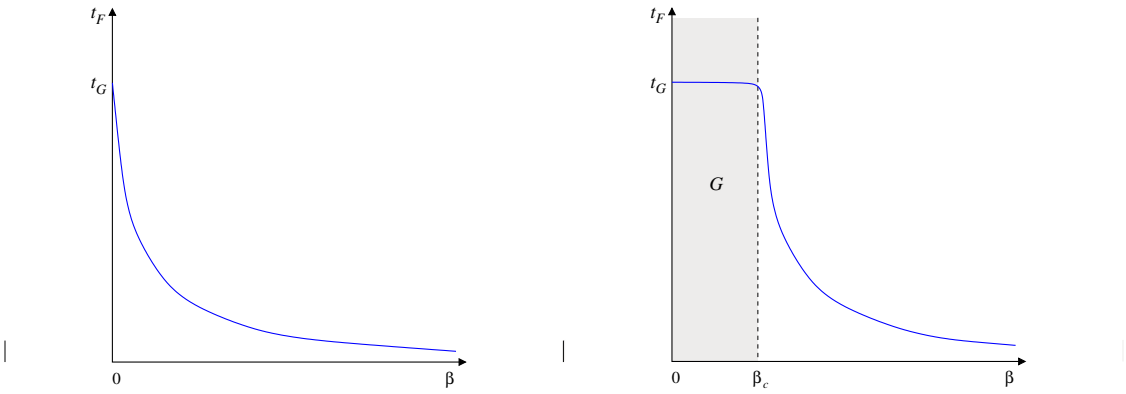

Figure 5.20: Schematic of the relationship between the flux stability time, t_F, and β in the limit of $\beta \ll 1$. Two possible behaviours occur; in the first, $t_F \to t_G$ as $\beta \to 0$, whilst in the second, t_F becomes independent of β for $\beta < \beta_c$ due to the body force, G, dominating the flow.

dominance', requiring $t_F = t_G$ integration times for flux stability when $\beta < \beta_c$.

At first glance, figure 5.17b suggests the latter to be the case, as it indicates that the flux becomes independent of β in its small limit, leaving F to depend on G alone. This raises the issue of the validity of our simulations at small β. Although the simulations are well resolved over the integration time, it brings into question how long we need to run small β simulations.

It is possible that the $F \propto \beta^0$ trend for small β in figure 5.17 comes about due to limitations in integration time (or possibly domain size), rather than physical effects. On closer inspection, this appears to be the case; the variance in values of F for small β is much larger than that in the rest of the parameter space. This indicates that the individual runs have not reached a stable point by the end of our integration time. The question now becomes one of how time scales with flux stability. Due to the huge computational demands in running such long-time simulations, checking this extends past the scope of this project. Further research into this would require looking at the probability density functions of the flux in this limit.

It is hard to be certain which of the behaviours given in figure 5.20 are phyical;

other parameters such as the viscosity may also have an effect on these scalings. Assuming that the behaviour is determined as in figure 5.20a, the power law given in figure 5.17b should extend across the range of β given suitably long integration times. If figure 5.20b gives the physical representation, then the accuracy of our results depend on the value of the cut off point β_c. We note that analytical results performed by Srinivasan and Young may infer the latter... see notes.

We turn our attention to the structure of the flow when under the effect of the body force alone. In figure 5.21 we plot the x-averaged velocity profile over the course of the simulation, noting that we have integrated over 10^6 units of time, much longer than the previous velocity diagrams. The distribution of velocity is clearly irregular, with no large time scale flows forming. Similarities can be drawn to the $\beta = 0.01$ case, displayed in figure 5.14a. Arguably, for $\beta = 0$ there is even less structure in the flow, although distinguishing between the two is difficult.

As mentioned in the previous section, it might be conceived that extremely short time zonal behaviour takes place even for small (or no) vorticity gradient. In fact, this is a consequence of the body force; the random ring force implemented in our simulations will naturally (on occasion) create regions with a higher concentration of positive/negative vorticity. When similar vertical regions of the flow are stimulated for consecutive forcing correlation times, the x-averaged variables describing the flow will display a zonal state, albeit one with no connection to a vorticity gradient or β-caused instability. As the forcing is isotropic, the same effect would be expected when measuring the y-averaged vorticity.

Figure 5.22 gives the vorticity field for several points in time throughout the evolution of a flow with no vorticity gradient. In 5.22a we can see that there is no indication of an organized zonal flow after 100 units of time. Figures 5.22b and 5.22c suggest that some kind of organized behaviour may be taking place, although a vertical flow appears likely in the former, whilst both horizontal and vertical structures may occur in 5.22c. These, in the context of other snapshots of the vorticity, confirm that over the current length of the integration there is no particular vertical or horizontal long-time structure in these types of flows; the

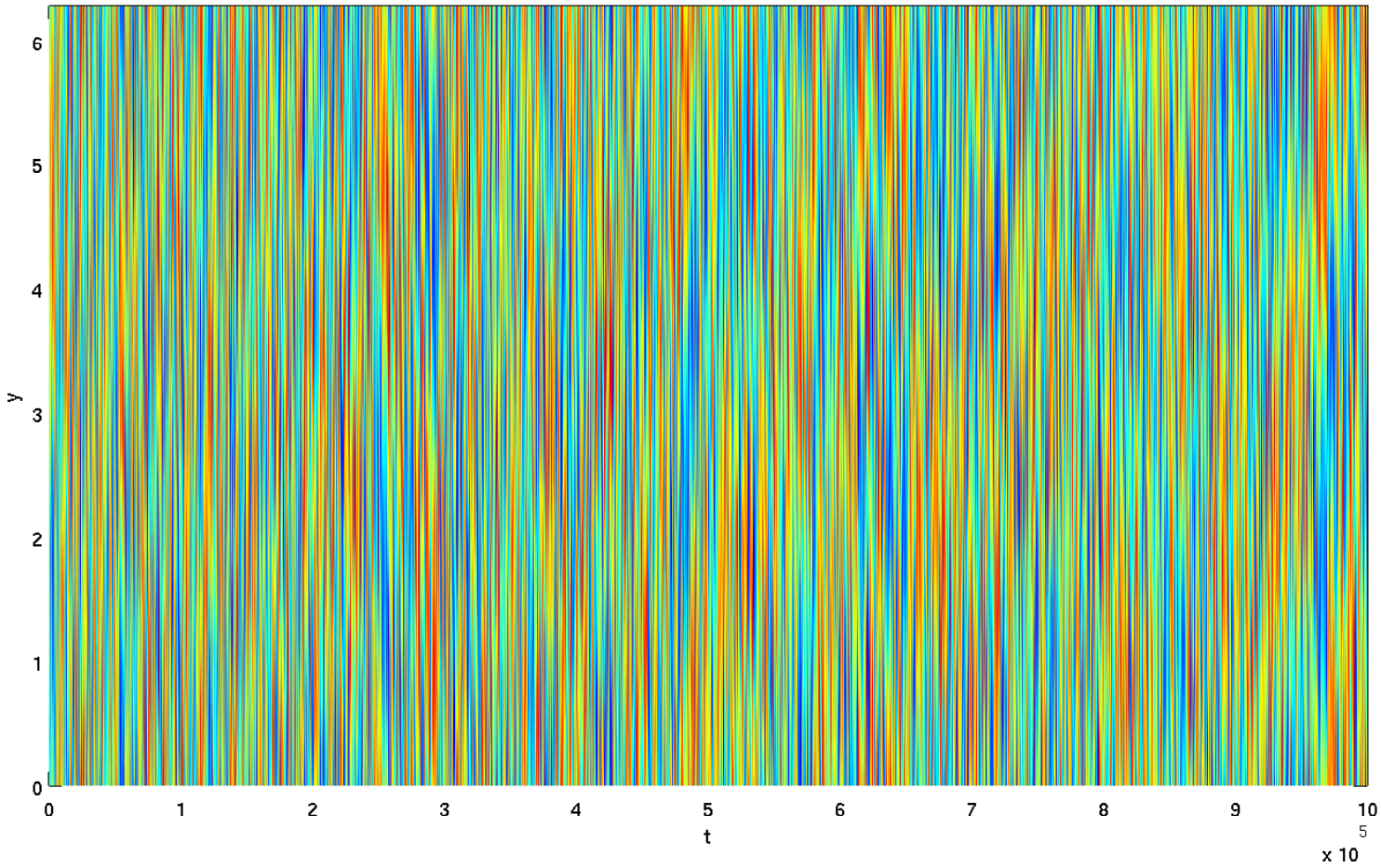

Figure 5.21: Contour plot of the evolution of the mean (x-averaged) profile of velocity over 10^6 units of time, with $(\alpha, \beta) = (0, 0)$ and all other parameters defined as in table 5.1.

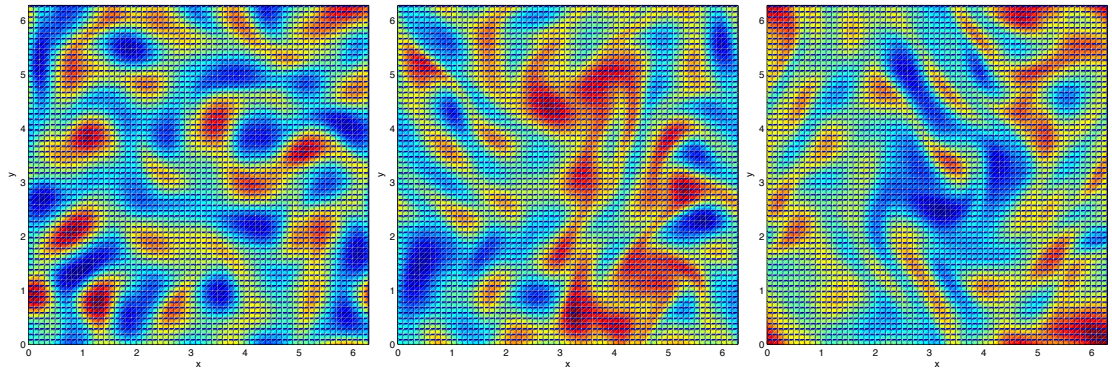

(a) (b) (c)

Figure 5.22: Contour plot of the perturbations of the vorticity field at (a) $t = 10^2$, (b) $t = 10^5$, (c) $t = 10^6$. $(\alpha, \beta) = (0, 0)$ and all other parameters defined as in table 5.1. Produced from the data used to make figure 5.21.

randomized body force remains the dominant aspect of the system.

To summarize, we have seen that distinguishing between vorticity gradient and body force as the primary mechanisms for zonal behaviour can be difficult, with the time scale of the jet-like structures being a deciding factor. One would expect that either a smooth transition over β would occur, with jet time scale being a continuous function of β, or that a cut off point would be reached where the effects of the vorticity gradient are negligible. We suggest that the former is the case, although this is difficult to confirm due to the long integration times required.

5.4 Sheared Turbulence, $\alpha \neq 0, \beta = 0$

Having investigated a general β-plane system and the effects of the body force, we now introduce a background shear flow. In this section we look at how the shear alters the dynamics of the flow as the strength of the shear, α, is increased. We postpone looking at the competition between α and β until section 5.5.

Using a shearing box coordinate system, we simulate a two-dimensional plane of fluid under the effects of a linear background shear and randomized body force by numerically integrating the governing equations, (4.42 – 4.44), using the methods

discussed in chapter 4. The body force injects energy into the system, while a shear-diffuse mechanism removes it. The force acts in such a way that it 'follows' the shear over time (and then resets); this has been discussed at length in the previous chapter.

We start by introducing a low level of shear to the system, $\alpha = 0.01$. In the case of the vorticity gradient, for small values of β the form of the flow is practically indistinguishable from that of $\beta = 0$. Likewise, we see in figure 5.23 how small values of α give an x-averaged velocity similar to that of the non-sheared case (see figure 5.21).

Similarly to $\beta = 0.01$ (see figure 5.14a), in figure 5.24 we observe that there are structures which are arguably long-lived, although not particularly steady, zonal features (given the large range of t covered by the plot). This can be seen more clearly in figure 5.24, which zooms into the last 10^3 units of time of figure 5.23. Here we can see regions of the flow taking a similar form over several hundred of units of time, before very suddenly becoming disrupted. Despite the time scale of this behaviour being much larger than the forcing correlation time ($T_c = 1$), we note that similar phenomena occurs for $(\alpha, \beta) = (0, 0)$. This is largely due to the nature of the ring forcing and the regions of flow that it excites.

However, differences in statistics regarding α and β are made much more obvious when looking at the passive scalar flux. For $\alpha = 0.01$ the flux rounds to a value of $F \approx 0.1$ (see figure 5.25), almost half the value of F at the equivalent value of β. In general, for equivalent values of α and β, the time-averaged flux tends to reach a constant value slightly faster for the shear (compare figures 5.18a and 5.25b).

The sharp drop in vertical transport associated with the shear is clearly depicted in the plot of F against α given in figure 5.26. We can see how the flux drops sharply as α is increased, tending to zero as α tends to infinity. In figure 5.26b we see that for larger values of α there is a roughly $F \propto \alpha^{-5/3}$ relationship. For weaker shear flows, this falls to approximately $F \propto \alpha^{-1/3}$ for $0.01 < \alpha < 0.1$, although it appears likely that as α tends to zero the flux will tend towards becoming independent of the shear. As discussed in section 5.3, this may be the result of flux stability

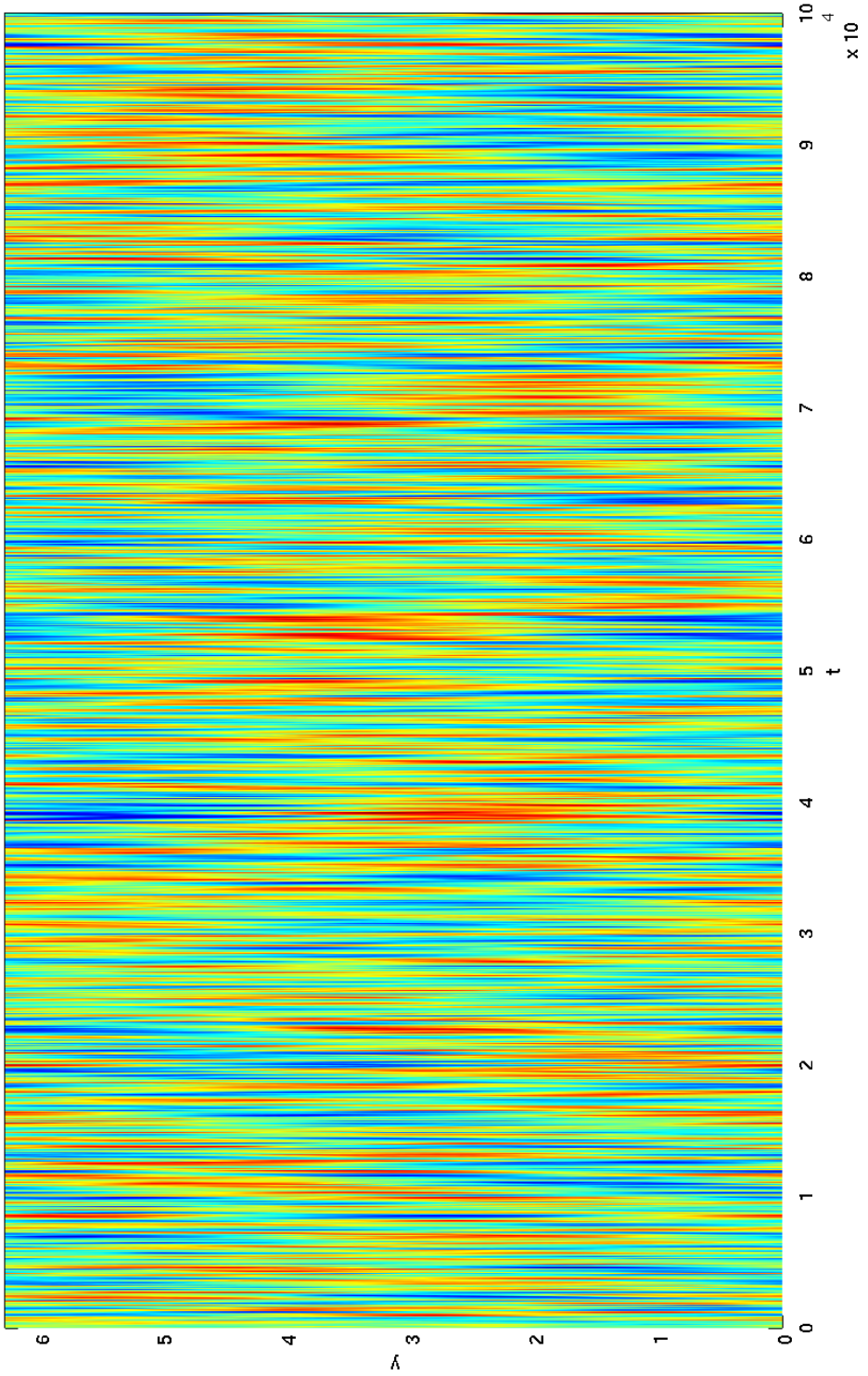

Figure 5.23: Contour plot of the evolution of the mean (x-averaged) profile of velocity over 10^5 units of time, with $(\alpha, \beta) = (0.01, 0)$ and all other parameters defined as in table 5.1.

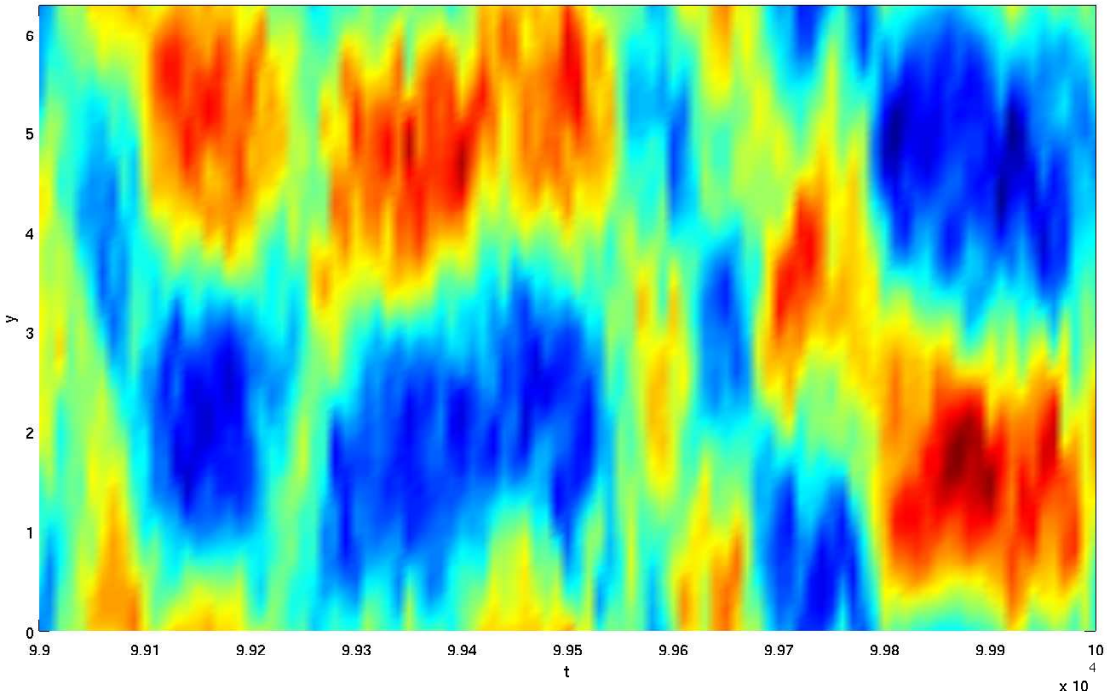

Figure 5.24: Contour plot of the evolution of the mean (x-averaged) profile of velocity over 10^3 units of time, starting at $t = 9.9 \times 10^4$, with $(\alpha, \beta) = (0.01, 0)$ and all other parameters defined as in table 5.1. Produced from the data used to make figure 5.23.

requiring long integration times at small parameter values.

Comparing the flux-shear relationship with that between the flux and the vorticity gradient (see figure 5.17), the main distinction between α and β (other than the difference in scaling laws) are their behaviour at small values. For small α, we observe an immediate drop in flux from $\alpha = 0$, whereas there appears to be a buffer zone in β before vertical transport is supressed. However, we have already noted in the previous section that this small-β region in figure 5.17a may be the artifical result of the long flux stablization times required by small values of β. The shear, however, tends to stabilise the flux earlier; we can be slightly more sure of the results given in figure 5.26 than those given for β in figure 5.17. Given longer integration times, the small-β case might show more resemblance to the trend given in the α-flux diagram.

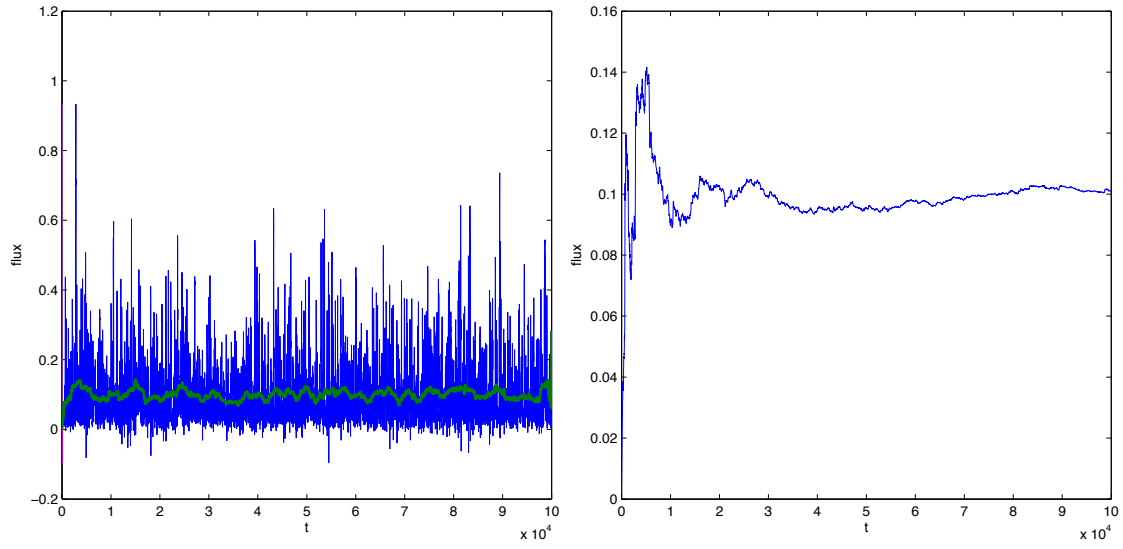

(a) (b)

Figure 5.25: Spatially averaged passive scalar flux plotted as a function of time for $(\alpha, \beta) = (0.01, 0)$. (a) gives the flux in blue and a smoothed average in green, whilst for (b) the average of the flux over the previous 50% of the simulation is calculated and plotted for each point in time. Produced from the data used to make figure 5.23.

We see that in terms of vertical transport suppression, α and β play similar roles (at least for values away from the $(\alpha, \beta) = (0, 0)$ point in the parameter space). By comparing the rate at which the flux decreases, shear can be seen as the more severe of the parameters, with $F \propto \alpha^{-5/3}$, while $F \propto \beta^{-5/4}$. But what does this mean in terms of the dynamics of the flow? In figures 5.27a and 5.27b we plot the x-averaged velocity profiles for $\alpha = 0.1$ and $\alpha = 1$ respectively. It is clear that, unlike figures 5.2 and 5.5 for example, there seems to be no long-time organization of the flow. However, each simulation is still quite distinct from each other, and from the $(\alpha, \beta) = (0, 0)$ case given in figure 5.21. For $\alpha = 0.1$ the flow is characterized by sporadic regions with large vertical length scale motion, separated by areas of comparatively weak flow. This is quite unlike the $\alpha = 0$ case, where the motions of the fluid were roughly equal in magnitude for the entire simulation. Increasing the shear to $\alpha = 1$, we have a similar result to the $\alpha = 0.1$

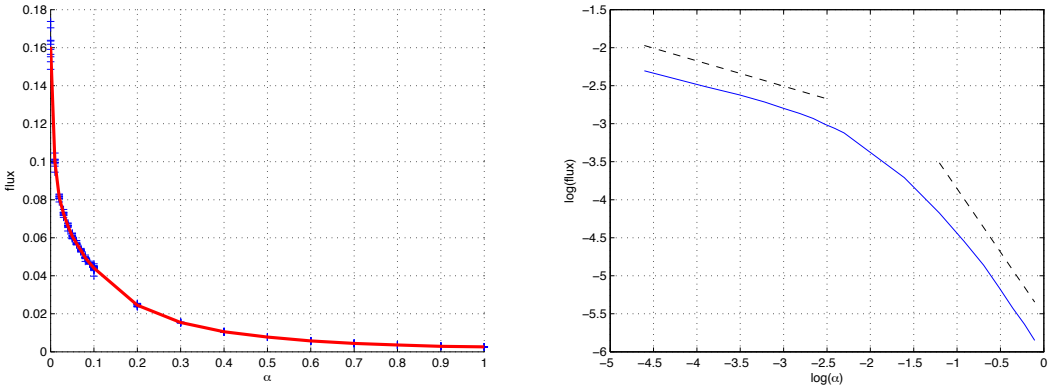

(a) (b)

Figure 5.26: Spatially and temporally averaged passive scalar flux plotted as a function of α. Time-averaging is performed by taking the mean of the flux over the previous 50% of the simulation. This is averaged over a number of randomized simulations, each represented in (a) by a blue cross. The ensemble average is plotted in red in (a), while the log-log relationship of this line is given in (b), with $\alpha^{-1/3}$ and $\alpha^{-5/3}$ given by the dashed lines. A denser selection of points is used for $\alpha \leq 0.1$ in order to properly establish the relationship between α and the flux.

case, but where the time and length scales of the stronger regions of flow have been decreased; the vertical structures in the flow are both smaller and shorter lived.

To more effectively display these phenomena, in figure 5.28 we zoom in to the last 10^3 units of time of each of the aforementioned simulations. For $\alpha = 0.1$ we observe that weakly persistent zonal flows occur; these form as vorticies created by the body force are organized into position by the shear, albeit very loosely. As the shear is increased, the strength with which these vortices are stretched is intensified, often splitting single large vortices into banded horizontal structures. This decreases the vertical length scale of these flows. These regions are easily disrupted by the body force, and so only survive for relatively short periods of time. As α is increased further, both the length and time scales continue to decrease, from which scaling laws for each may be established (e.g. compare Rhines scale for β), although we shall not investigate this quantitively here. Such scalings, however,

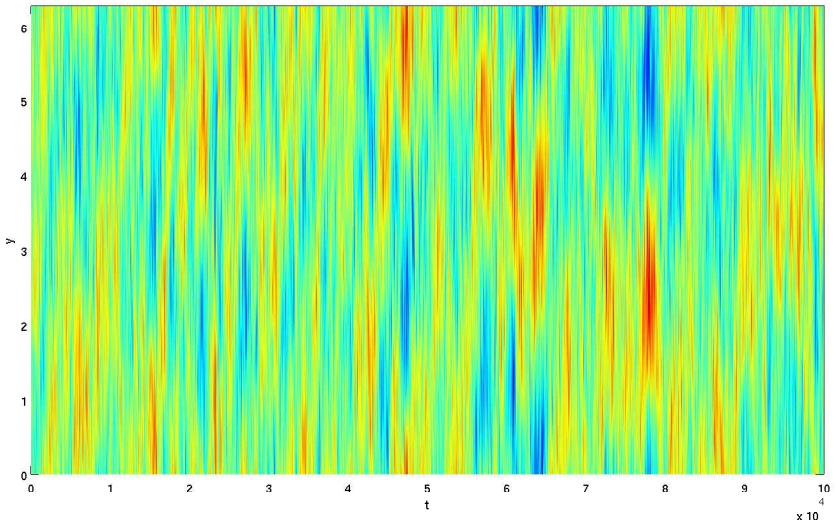

(a)

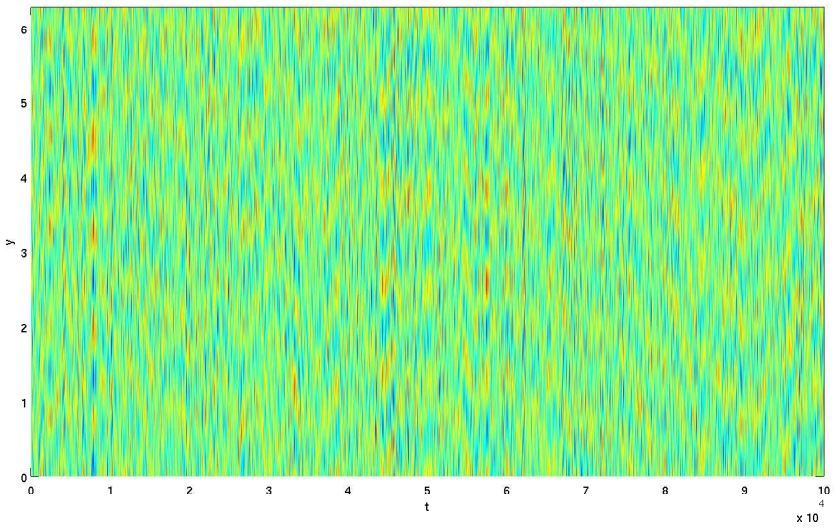

(b)

Figure 5.27: Contour plot of the evolution of the mean (x-averaged) profile of velocity over 10^5 units of time, with (a) $(\alpha, \beta) = (0.1, 0)$, (b) $(\alpha, \beta) = (1, 0)$, and all other parameters defined as in table 5.1.

may be dependent on the implementation of the body force.

The type of flows that these mean profiles represent can be seen in figure 5.29. Here we take a snapshot of the vorticity field late in the simulation for several values of α. The effect of the shear can be seen clearly; tipping over and stretching vortices. For very large values of α, as given in figure 5.29d, the flow forms zonal

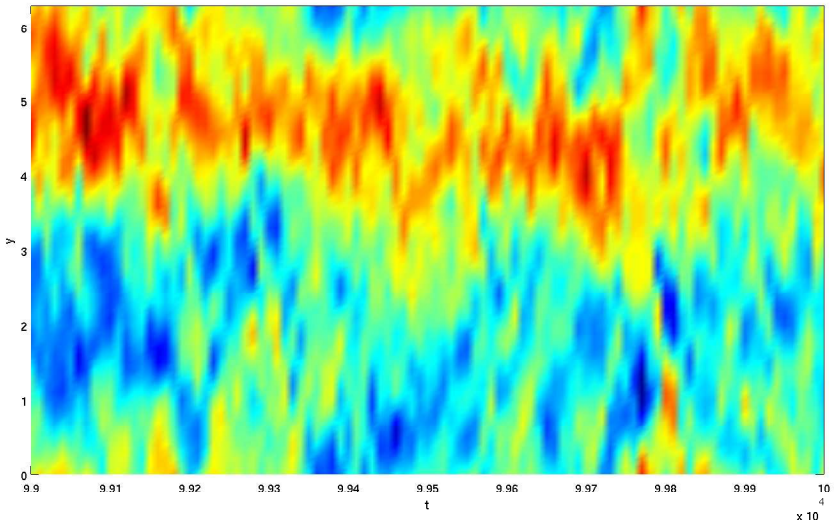

(a)

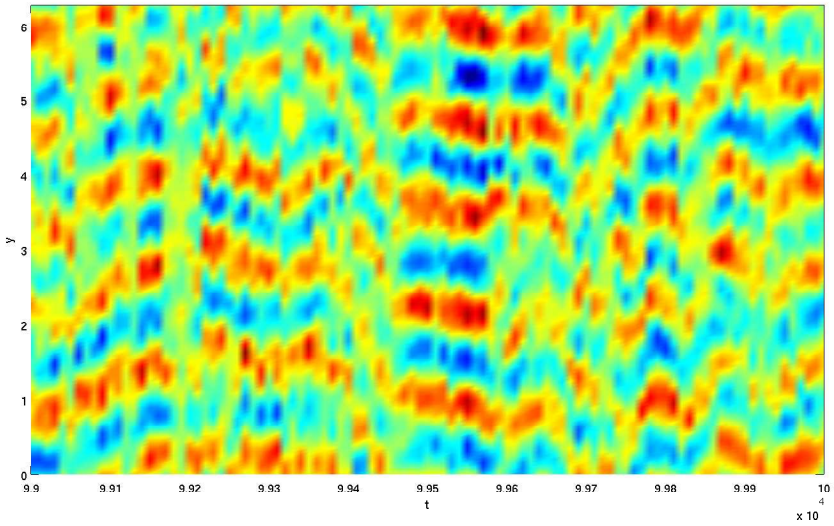

(b)

Figure 5.28: Contour plot of the evolution of the mean (x-averaged) profile of velocity over 10^3 units of time, starting at $t = 9.9 \times 10^4$, with (a) $(\alpha, \beta) = (0.1, 0)$, (b) $(\alpha, \beta) = (1, 0)$, and all other parameters defined as in table 5.1. Note that (a) and (b) are produced from the data used to make figures 5.27a and 5.27b respectively.

structures, which at first seem not dissimilar to the zonal jets of β-plane systems. As previouly noted, however, these structures occur for very short times and are dynamically quite different from jets. For example, β-plane jets tend to be strongest

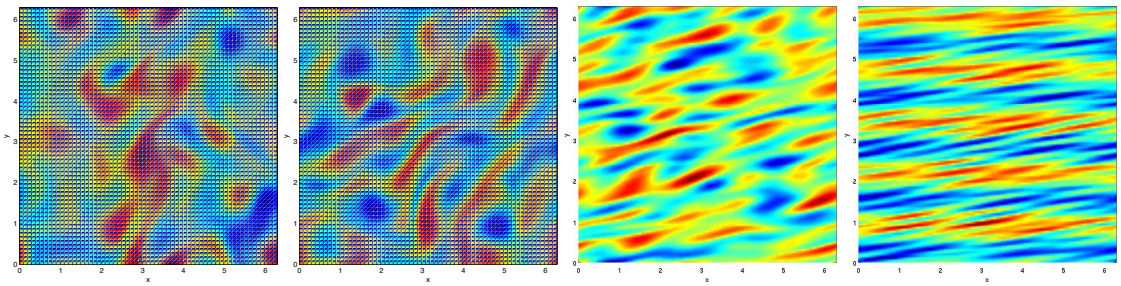

(a) (b) (c) (d)

Figure 5.29: Contour plot of the perturbations of the vorticity field at $t = 10^5$ for (a) $(\alpha, \beta) = (0.01, 0)$, (b) $(\alpha, \beta) = (0.1, 0)$, (c) $(\alpha, \beta) = (1, 0)$, (d) $(\alpha, \beta) = (10, 0)$, with all other parameters defined as in table 5.1. Note that (a), (b) and (c) are produced from the data used to make figures 5.23, 5.27a and 5.27b respectively.

at the centre of the jet, where little vertical mixing takes place. However, 'shear jets' are strongest at the top of the jet, where the shear has the strongest effect.

In closing, we emphasize the differences between α and β as mechanisms of transport regulation in the flow. At small values the shear seems to always have some impact on transport, even for very small α, whereas the effect of β is harder to quantify. At larger values, the shear was found to have an $F \propto \alpha^{-5/3}$ relationship with the flux, making it more effective at quelling mixing than β. Both the vorticity gradient and linear shear can create zonal structures, however the form of these 'jets' is inherently different, as are their length and time scales.

5.5 Jet Disruption, $\alpha \neq 0, \beta \neq 0$

Having investigated the individual effects of shear and a vorticity gradient on a two-dimensional fluid, we now look at how these features interact when both are present. We limit the parameter space by setting $\beta = 1$ and only varying α, with all other parameters defined as in table 5.1. As such, we are only investigating a slice of the parameter-plane given by (α, β). There may be many interesting phenomena which come about when also varying β, however due to our results from sections 5.2 – 5.4 we assume that the results found in the current section are

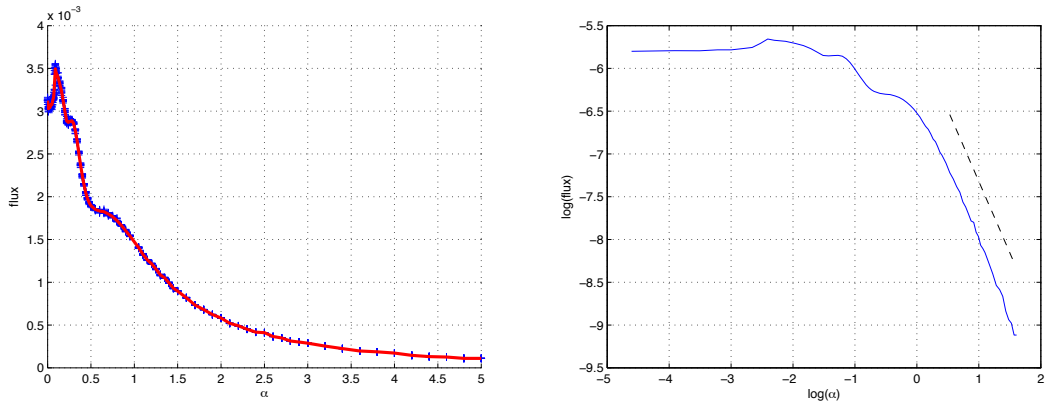

(a) (b)

Figure 5.30: Spatially and temporally averaged passive scalar flux plotted as a function of α, with $\beta = 1$. Time-averaging is performed by taking the mean of the flux over the previous 50% of the simulation. This is averaged over a number of randomized simulations, each represented in (a) by a blue cross. The ensemble average is plotted in red in (a), while the log-log relationship of this line is given in (b), with $\alpha^{-5/3}$ given by the dashed line. A denser selection of points is used for smaller values of α in order to properly establish the relationship between α and the flux. Note that a larger range of α has been plotted here (compared to figure 5.26), in order to display the limit of the flux as $\alpha \to \infty$.

typical of other values of β.

We start by looking at the relationship between the passive scalar flux and α, with $\beta = 1$, as plotted in figure 5.30. We will refer also to figures 5.17 and 5.26, the flux diagrams for α and β respectively, although we note that the scale of F in figure 5.30 is a lot smaller, starting in a region of the parameter space where the flow is jet-like and the flux is limited to small values. Likewise, the range of α over which we have plotted F is larger, as is required in order to capture the scaling of the flux with shear as it breaks out of the β-dominated regime.

Interesting behaviour occurs when varying α with a constant background vorticity gradient, as can be seen in figure 5.30a. For $\alpha > 1$ there is a regular power law decay toward zero. This decay appears to have roughly the same scaling as in

the $\beta = 0$ case, with $F \propto \alpha^{-5/3}$. Note that the reading for this relationship depends on where exactly we measure the gradient of each curve, and that arguably the $\beta = 1$ case may have a slightly steeper drop off in flux.

In the $0 \leq \alpha \leq 1$ region we observe an initial increase in the flux; the disruption to the formation of β-plane jets via shear actually stimulates vertical mixing in the fluid for small α. This sharp increase peaks at $\alpha \approx 0.1$ before dropping again as the shear helps regulate the flux. However, this transition between regimes of the flow is not without complications; rather than immediately forming the steady $\alpha^{-5/3}$ relationship which dominates the large-shear system, two 'disrupting' events take place. In each, the drop off in flux with α is temporarily delayed, bringing about a short $F \sim \alpha^0$ relationship. The first occurs at $\alpha \approx 0.2$, where $F = 2.8 \times 10^{-3}$, approximately the same value as when $\alpha = 0$. The second occurs less severely at $0.5 < \alpha < 0.75$. Unlike the initial increase in flux, the mechanisms behind these later events are difficult to pin down due to the complex nature of the flow in this regime.

We investigate the initial rise in flux by plotting x-averaged velocity for small values of α in figure 5.31. For $\alpha = 0.01$, the profile is comparably similar to the $(\alpha, \beta) = (0, 1)$ case, plotted in figure 5.2. However, as we increase α by a small amount to 0.05, we see a drastic change in the structure of the flow. While the fluid maintains a single pair of alternating jet-like structures at any given time, the jets appear to travel vertically over time, at a roughly constant rate. This uniform vertical movement corresponds to the increase in flux between $0 \leq \alpha \leq 0.1$.

As we increase α further towards 0.1, the flow begins to shift towards a form more similar to the profiles given in the $\alpha \neq 0, \beta = 0$ section (section 5.4). In figure 5.32a we see a disrupted flow, albeit with familiar vertical streaks of strong, but short lived zonal behaviour occuring at $t = 0.5, 2.5, 5 \times 10^4$. Setting $\alpha = 0.2$ in figure 5.32b, we observe completely shear dominated behaviour. Despite this being in the range of α at which the first 'flux plateau' takes place, we find it difficult to distinguish between the behaviour of the fluid at these points and those just outside these regions, with the dynamics of the flow giving little information as to

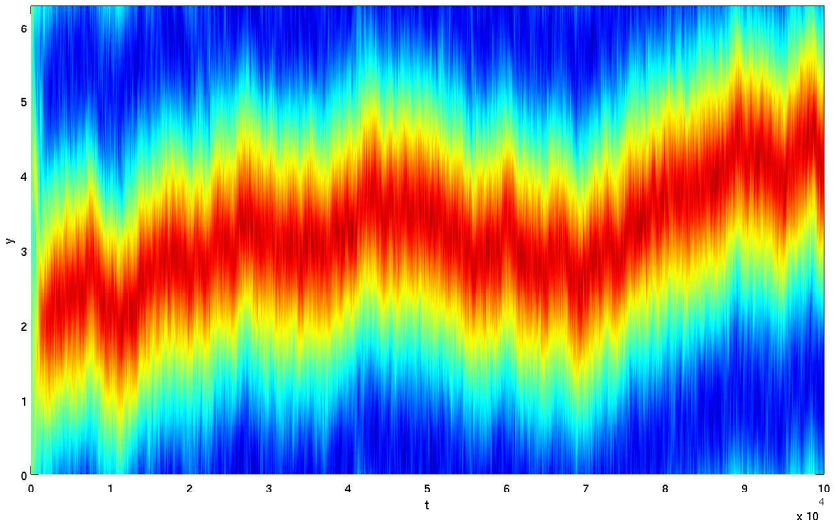

(a)

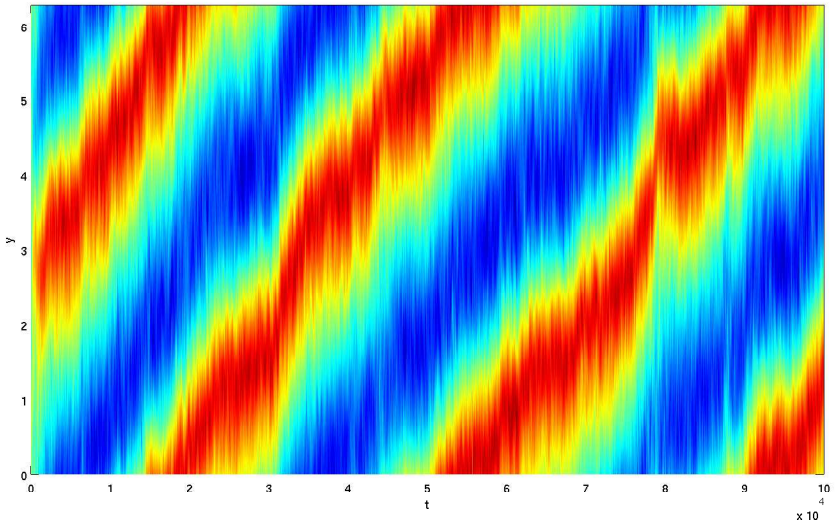

(b)

Figure 5.31: Contour plot of the evolution of the mean (x-averaged) profile of velocity over 10^5 units of time, with (a) $(\alpha, \beta) = (0.01, 1)$, (b) $(\alpha, \beta) = (0.05, 1)$, and all other parameters defined as in table 5.1.

why the flux levels out in such a way.

Plotting the flow over shorter time periods, as in figure 5.33, shows how the system transitions from a zonal state to a more turbulent flow (albeit with horizontal features) as α is increased. In figure 5.33b we see the short time jet-like structures being a prominent feature for $\alpha = 0.05$, despite being gradually shifted vertically

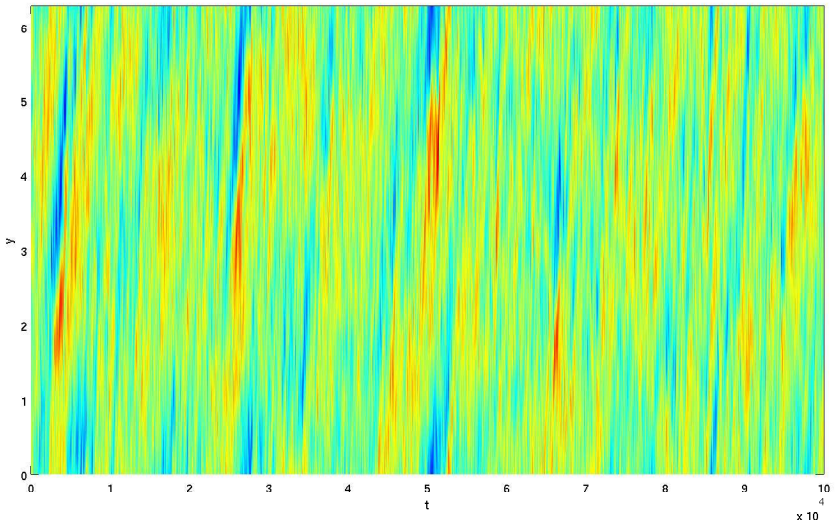

(a)

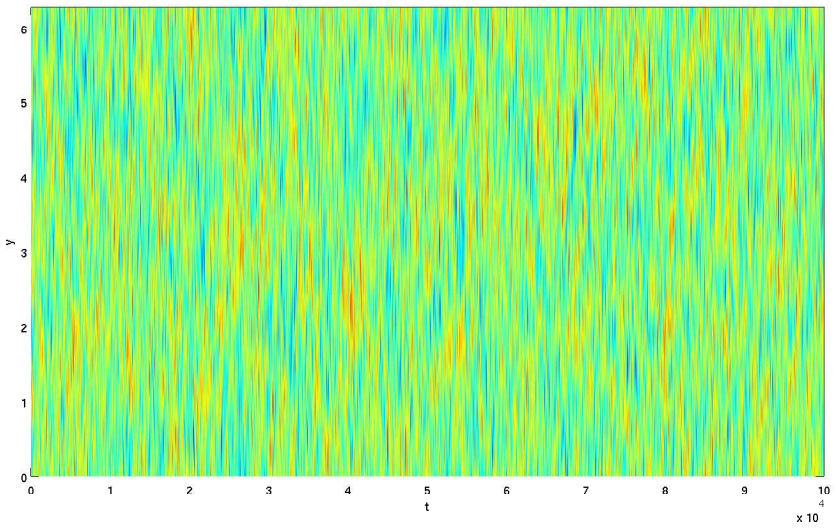

(b)

Figure 5.32: Contour plot of the evolution of the mean (x-averaged) profile of velocity over 10^5 units of time, with (a) $(\alpha, \beta) = (0.1, 1)$, (b) $(\alpha, \beta) = (0.2, 1)$, and all other parameters defined as in table 5.1.

over longer periods of time. Most interesting is the comparison between figures 5.33a and 5.33d; each flow gives an almost identical value of the passive scalar flux, despite being completely different in terms of structure. These figures illuminate the key difference in flux regulation between α and β; α dissipates vertical motion through the shear-diffuse mechanism, horizontally slicing vertical structures, with

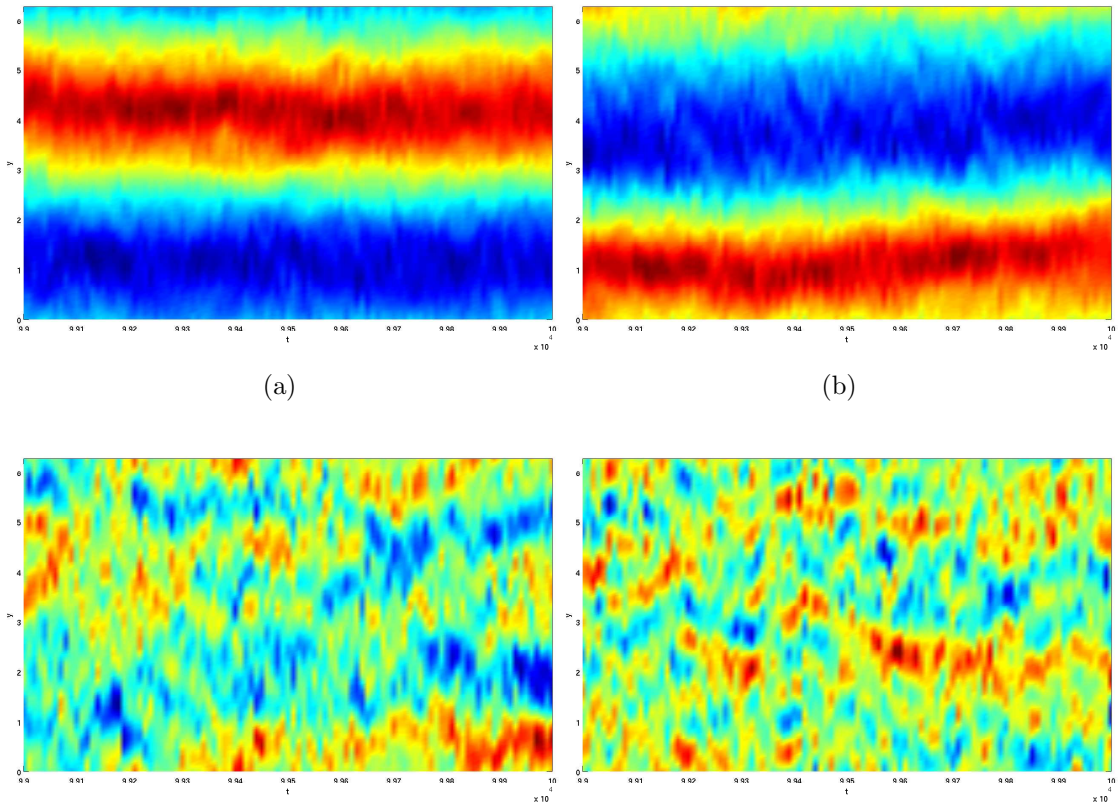

(a) (b)

(c) (d)

Figure 5.33: Contour plot of the evolution of the mean (x-averaged) profile of velocity over 10^3 units of time, starting at 9.9×10^4, with (a) $(\alpha, \beta) = (0.01, 1)$, (b) $(\alpha, \beta) = (0.05, 1)$, (c) $(\alpha, \beta) = (0.1, 1)$, (d) $(\alpha, \beta) = (0.2, 1)$, and all other parameters defined as in table 5.1. Note that (a), (b), (c) and (d) are produced from the data used to make figures 5.31a, 5.31b, 5.32a and 5.32b respectively.

no need for large time or length scale motions, while β introduces a persistent, organized flow, with little vertical mixing occuring between alternating jets.

In figure 5.34 we include a plot of the x-averaged velocity profile for the $(\alpha, \beta) = (1, 1)$ case. Comparing with figure 5.27b, we can see little difference between the two plots. This result, in conjunction with the scaling present in figure 5.30b, indicates that the system is in a fully shear dominated regime when $\alpha = 1$.

The transition towards this sheared system can be seen in more detail by examining the snapshots of vorticity for different values of α in figure 5.35. For 5.35a and 5.35b the zonal flow is very pronounced, as can be seen when comparing with

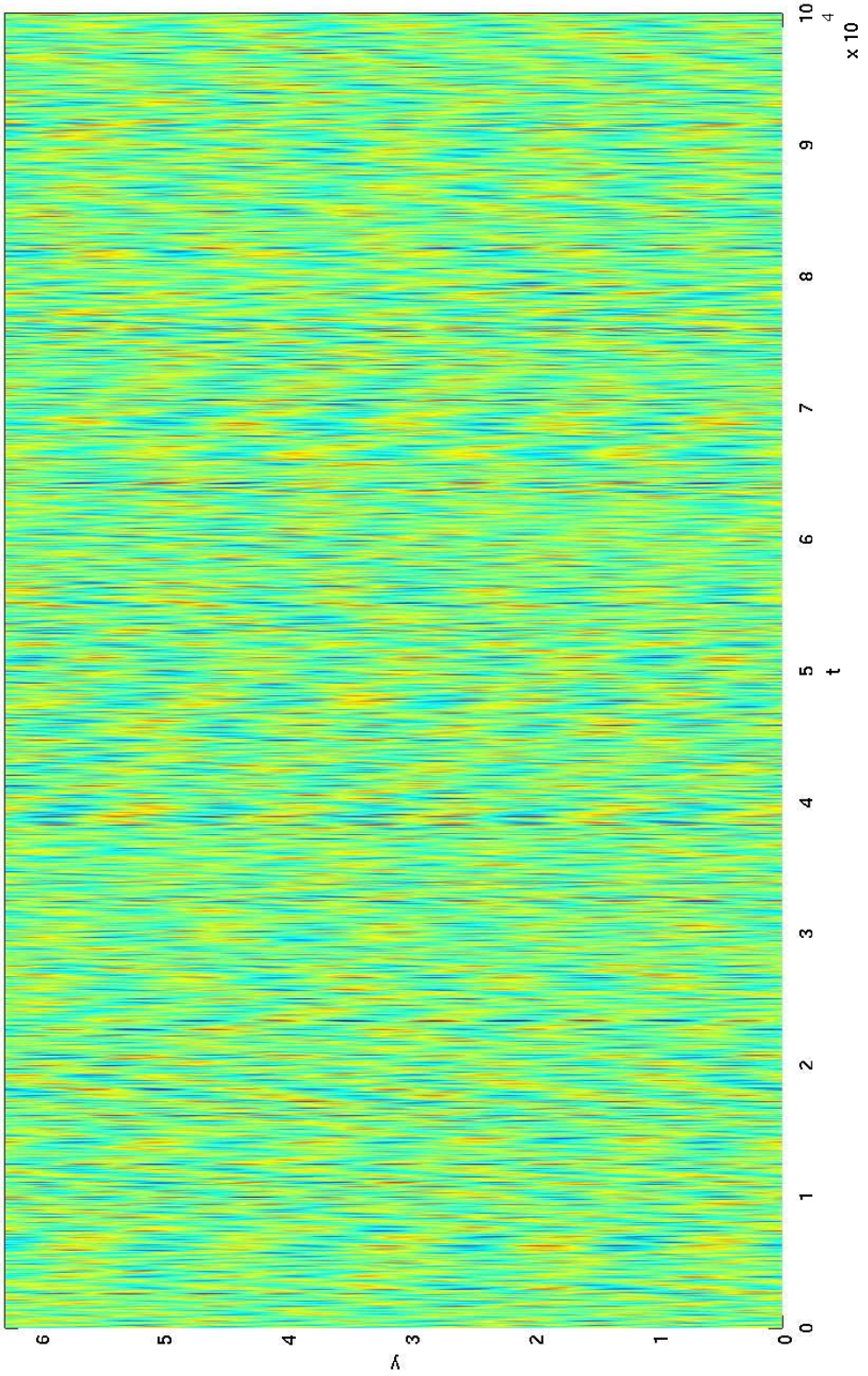

Figure 5.34: Contour plot of the evolution of the mean (x-averaged) profile of velocity over 10^5 units of time, with $(\alpha, \beta) = (1, 1)$ and all other parameters defined as in table 5.1.

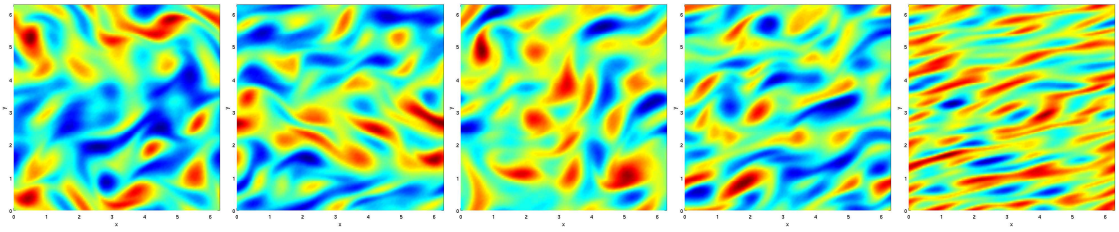

(a) (b) (c) (d) (e)

Figure 5.35: Contour plot of the perturbations of the vorticity field at $t = 10^5$ for (a) $(\alpha, \beta) = (0.01, 0)$, (b) $(\alpha, \beta) = (0.1, 0)$, (c) $(\alpha, \beta) = (1, 0)$, (d) $(\alpha, \beta) = (10, 0)$, with all other parameters defined as in table 5.1. Note that (a), (b), (c), (d) and (e) are produced from the data used to make figures 5.31a, 5.31b, 5.32a, 5.32b and 5.34 respectively.

figures 5.33a and 5.33b. As α is increased to 0.1 in 5.35c, the zonal flow has clearly been disrupted. However, it is still difficult to observe the effect of the shear directly; indeed both parameters are in direct competition here. In figures 5.35d and 5.35e shear becomes the dominant factor in the structure of the flow, making it comparable to figure 5.29c.

In summary, we have seen that for small amounts of shear, the zonal jets associated with β-plane flows are disrupted and vertical mixing is increased. However, as α increases further, its own mechanisms begin to supress the flux, and the original $\beta = 0$ scaling is obtained, $F \propto \alpha^{-5/3}$. Before this is reached, however, complicated interactions between the two effects lead to regions of the parameter space where the flux goes unchanged. The behaviour here is hard to pin down, due to the complicated dynamics of the flow.

5.6 Conclusion

In our direct numerical simulations of a two-dimensional sheared β-plane system, we have seen a variety of different types of behaviour in the flow. Our results include the following:

- We have confirmed the occurence of β-plane jets in the non-sheared system. The coefficient of viscosity and the length scale of our body force were both relatively large compared to typical values seen in the literature, although this has allowed us to obtain ensemble average results across a large number of individual simulations.

- As β decreases, jets become weaker and persist over shorter time scales. However, determining what is and is not a jet becomes difficult. As β becomes very small, it appears to reach a non-zero point, β_c, where the flux is independent of the vorticity gradient, i.e. there is effectively no β-related zonal behaviour. However, it is difficult to determine the exact behaviour of the flow in this limit due to the long time scales involved, and there is a strong possibility that an effect due to β could be seen if the integration is resolved for very long times (i.e. $\beta_c = 0$).

- For moderate values of β we found that the parameter is related to the flux of a passive scalar by the scaling law $F \propto \beta^{-5/4}$. This relates to the effective diffusivity of the flow, indicating the rate at which vertical transport is suppressed.

- The shear gives an $F \propto \alpha^{-5/3}$ scaling law for moderate values of α. Unlike β, shear suppresses transport by tipping over and stretching out vertical structures, dissipating energy by a shear-diffuse mechanism. It also appears to create short time jet-like structures, however these are the results of the shearing of the vortices created by the body force, and should not be confused with β-plane jets.

- Small values of α continuously dissipate vertical mixing, with no regime being solely determined by the body force. However, the statistics of the small shear results require shorter integration times to be fully resolved, making them more reliable than those for β (which may be spurious).

- For a β-plane system, the shear acts to disrupt the formation and stability of zonal jets. For small values of α this actually increases mixing as the jets are

broken down. However, as α is increased further, the shear-diffuse mechanism becomes dominant, and the $F \propto \alpha^{-5/3}$ scaling law is regained.

- Before this scaling law is reached, complicated interactions between α and β result in regions of 'flux plateaus' which cannot be easily explained. These may arise for several reasons, including an interaction between the forcing and the parameters (possibly due to the implementation of the body force).

In the next two chapters we will look at the magnetohydrodynamic extension to this current system. We make comparisons to this purely hydrodynamic flow, which will be summarized in chapter 8.

Chapter 6

MHD Nonlinear Dynamics

6.1 Introduction

In chapter 4 we investigated the nonlinear system of equations governing a two-dimensional sheared flow on a β-plane, as well as its associated passive scalar field. We now extend this investigation to include electrically conducting fluids which are influenced by a constant background magnetic field. We look at several new flux-like quantities which describe transport in the flow, and find that fluxes associated with the evolution of the vorticity field average to zero. However, there is a non-zero flux of magnetic potential (which we will refer to as *magnetic flux*), which is closely related to the flux of a passive scalar field.

Having implemented a shearing box coordinate system, we give a numerical scheme for finding solutions to our governing equations. As details regarding the coordinate system were given in chapter 4, we refrain from repeating them in the current chapter. We do similarly for the implementation of the body force, which remains the same as in the purely hydrodynamical case. Lastly we look at the non-dimensionalization of the governing equations. Our scheme goes unchanged, with the strength of the magnetic field and diffusivity being added to our parameter space.

In chapter 7 we examine the results of the numerical simulations performed by solving the discretized system of equations given in this current chapter. We look at the effect of varying the strength of the background field when holding other parameters at fixed values. We aim to establish the relationship between vertical transport and the magnetic field, and investigate how this changes when the flow is subjected to additional effects, including a background vorticity gradient and shear flow.

6.2 Governing Equations

The governing equations describing the nature of an incompressible electrically conducting fluid are given by

$$\rho\left(\frac{\partial \mathbf{U}}{\partial t} + \mathbf{U}\cdot\nabla\mathbf{U}\right) = -\nabla p + \mathbf{J}\times\mathbf{B} + \mu\nabla^2\mathbf{U} + \rho\mathbf{F}, \tag{6.1}$$

$$\nabla\cdot\mathbf{U} = 0, \tag{6.2}$$

where $\mathbf{U}$ is the total flow velocity, ρ is the fluid density, p is the pressure, μ is the coefficient of dynamic viscosity and $\mathbf{F}$ is an external force [33]. The $\mathbf{J}\times\mathbf{B}$ term gives the effect of a magnetic field, $\mathbf{B}$, on the fluid, with the evolution of the field carried by the flow given by

$$\frac{\partial \mathbf{B}}{\partial t} + (\mathbf{U}\cdot\nabla)\,\mathbf{B} = (\mathbf{B}\cdot\nabla)\,\mathbf{U} + \eta\nabla^2\mathbf{B}, \tag{6.3}$$

$$\nabla\cdot\mathbf{B} = 0, \tag{6.4}$$

where η is the magnetic diffusivity, and the current, J, is defined as

$$\mathbf{J} = \frac{1}{\rho}\nabla\times\mathbf{B}. \tag{6.5}$$

We will use the following notation throughout this chapter:

$$\frac{\partial}{\partial t} \equiv \partial_t\,,\ \frac{\partial}{\partial x} \equiv \partial_x\,,\ \text{etc.} \tag{6.6}$$

This allows us to rewrite equation (6.1) as

$$\partial_t\mathbf{U} + \mathbf{U}\cdot\nabla\mathbf{U} = -\frac{1}{\rho}\nabla p + \mathbf{J}\times\mathbf{B} + \nu\nabla^2\mathbf{U} + \mathbf{F}, \tag{6.7}$$

where $\nu = \mu/\rho$ is the kinematic viscosity.

Taking the curl of equation (6.7) leads to the following system of equations

$$\partial_t\boldsymbol{\Omega} + \mathbf{U}\cdot\nabla\boldsymbol{\Omega} = \boldsymbol{\Omega}\cdot\nabla\mathbf{U} + \nu\nabla^2\boldsymbol{\Omega} + \mathbf{G}, \tag{6.8}$$

$$\partial_t\mathbf{B} + \mathbf{U}\cdot\nabla\mathbf{B} = \mathbf{B}\cdot\nabla\mathbf{U} + \eta\nabla^2\mathbf{B}, \tag{6.9}$$

$$\nabla\cdot\mathbf{U} = \nabla\cdot\mathbf{B} = 0, \tag{6.10}$$

where $\boldsymbol{\Omega}$ is the total fluid vorticity and $\mathbf{G} = \nabla\times\mathbf{F}$ is some external torque forcing the vorticity [1]. Equations (6.8) and (6.9) appear similar; the nonlinear and diffusive terms take similar forms, while energy is put into the system via the body force

in the vorticity equation. Of course, the vorticity directly determines the velocity, whereas the mean field's relationship to the velocity is indirect, making it similar to (albeit not the same as) a passive scalar.

By imposing that the flow can be described in terms of a stream function, $\mathbf{U} = \nabla \times (\Psi \mathbf{k})$, and that the magnetic field can be given in similar terms with a mean horizontal part, $\mathbf{B} = B_0 \mathbf{i} + \nabla \times (A\mathbf{k})$, we can reduce our system of equations to a scalar form:

$$\partial_t \Omega = J(\Psi, \Omega) + J(A, \nabla^2 A) - B_0 \partial_x (\nabla^2 A) + \nu \nabla^2 \Omega + G, \tag{6.11}$$

$$\partial_t A = J(\Psi, A) + B_0 \partial_x \Psi + \eta \nabla^2 A, \tag{6.12}$$

where $\mathbf{\Omega} = (0, 0, \Omega)$, G is the $\mathbf{k}$-component of the forcing $\mathbf{G}$, and the nonlinear terms are given by the determinant of the Jacobian,

$$J(\Psi, \Omega) = (\partial_x \Psi)(\partial_y \Omega) - (\partial_y \Psi)(\partial_x \Omega), \tag{6.13}$$

$$J(A, \nabla^2 A) = (\partial_x A)\left(\partial_y \nabla^2 A\right) - (\partial_y A)\left(\partial_x \nabla^2 A\right), \tag{6.14}$$

$$J(\Psi, A) = (\partial_x \Psi)(\partial_y A) - (\partial_y \Psi)(\partial_x A). \tag{6.15}$$

We also note that the vorticity, Ω, is related to the stream function, Ψ, by

$$\Omega = -\nabla^2 \Psi = -\left(\frac{\partial^2 \Psi}{\partial x^2} + \frac{\partial^2 \Psi}{\partial y^2}\right). \tag{6.16}$$

We now impose that there is some background vorticity gradient. Directly adding a gradient of vorticity to the flow, we can write the general solution of Ψ and Ω as

$$\Psi(x, y) = C_0 + C_1 y + C_2 y^2 + C_3 y^3 + \psi(x, y), \tag{6.17}$$

$$\Omega(x, y) = -2C_2 - 6C_3 y + \omega(x, y), \tag{6.18}$$

and

$$\omega = -\nabla^2 \psi. \tag{6.19}$$

We set the gauge term, C_0 to zero, as it has no effect on the dynamics of the system. Likewise, any effect of C_1 can be described by a Galilean transformation, and so it will also be removed from (6.17) without consequence.

In order to impose a simple shear flow, we linearise the x-component of the fluid velocity about $y = 0$. This amounts to setting $C_3 = 0$ in the expansion of

the stream function, while retaining it for the vorticity. Substituting the resulting terms into our system of equations results in

$$\partial_t \omega + \alpha y \partial_x \omega = J(\psi, \omega) + \beta \partial_x \psi + J(A, \nabla^2 A) - B_0 \partial_x (\nabla^2 A) + \nu \nabla^2 \omega + G, \quad (6.20)$$

$$\partial_t A + \alpha y \partial_x A = J(\psi, A) + B_0 \partial_x \psi + \eta \nabla^2 A, \quad (6.21)$$

where we have set

$$\alpha = 2C_2, \quad \beta = -6C_3. \quad (6.22)$$

Equations (6.13 – 6.21) provide the full sheared vorticity equation problem for a electrically conducting fluid, which will be the primary subject of our investigation in this chapter.

6.3 Flux

Similarly to the purely hydrodynamic case, the nonlinear system of equations given by (6.19) and (6.20 – 6.21) describing our sheared β-plane incompressible plasma, and will result in several quantities worth investigating. Again, we give attention to the flux, the transport in a given direction, of several different quantities throughout this thesis.

Following the work of Moffatt [25], who showed that the flux could be directly related to a type of diffusive feedback on the fluid (the effective diffusivity), we restrict this investigation to the downward (i.e. negative) vertical component of the flux of a variable h:

$$F(x, y) = -hv = h\partial_x \psi, \quad (6.23)$$

where v is the vertical component of the velocity perturbations, and h can represent any variable of the form $h(x, y)$ at a given time, t.

As mentioned previously, an averaged value of the flux can be related to the effective diffusivity of the flow. We take

$$F = \langle h \partial_x \psi \rangle_{x,y}, \quad (6.24)$$

where $\langle \cdot \rangle$ denotes a spatial average, in this particular case over the whole x and y

domain. Unless otherwise stated, we will generally take the average as being over the whole spatial domain.

There are several variables which may produce an interesting flux. In the section discussing the purely hydrodynamical flux, we showed that

$$J(\psi, h) = -\nabla \cdot \mathbf{F}_h, \tag{6.25}$$

where $\mathbf{F}_h = (uh, vh)$, for any function $h(x, y)$, and $F_h = -\hat{\mathbf{y}} \cdot \mathbf{F}_h$. As such, it is logical to investigate the flux of functions involved in the jacobians found in equations (6.20 – 6.21).

Having already discussed the flux of vorticity in the previous chapter, we note that as the relationship between ω and ψ is unchanged in this MHD formulation (see equation (6.19), and appendix A), the spatially averaged vorticity flux is identically zero:

$$F_\omega = \langle \omega \partial_x \psi \rangle_{x,y} = 0. \tag{6.26}$$

Drawing from the nonlinear terms in equations (6.20 – 6.21), another flux of interest to us is that of the magnetic potential, A, given by

$$F_A = \langle A \partial_x \psi \rangle_{x,y}, \tag{6.27}$$

which gives the effective vertical diffusivity of the magnetic induction equation, (6.21).

Unlike the vorticity flux, there are no non-trivial situations at which the A-flux, which we will refer to as the *magnetic flux*, reduces to zero. Whereas the relationship between ω and ψ allows for a simple cancellation in F_ω, A and ψ are connected by equations (6.19) and (6.20 – 6.21), a complicated relationship which cannot be easily simplified.

Another quantity to examine is the Jacobian containing the magnetic potential and its Laplacian, $J(A, \nabla^2 A)$, as found in equation (6.20). Like the other Jacobians we have looked at, this can be written in terms of the divergence of a vector. However, unlike the other cases this quantity is not a flux, as it does not contain a velocity term. Instead, we write

$$J(A, \nabla^2 A) = -\nabla \cdot \mathbf{F}_L, \tag{6.28}$$

where $\mathbf{F}_L = (\nabla^2 A \partial_y A, -\nabla^2 A \partial_x A)$ is a flux-like quantity representing the Lorentz force. Taking into account the relationship between ω and ψ given in equation (6.19), $\mathbf{F}_L$ is similar in form to $\mathbf{F}_\omega$, despite an overall change in sign when writing the latter in terms of ψ alone.

The spatial average of the downward (negative, for consistency) vertical component of $\mathbf{F}_L$ is given by:

$$F_L = \left\langle \nabla^2 A \partial_x A \right\rangle_{x,y}. \tag{6.29}$$

Similarly to the vorticity flux, F_ω, the Laplacian relationship between the variables in F_L lead to it taking the value of zero whenever A is bounded:

$$F_L = 0. \tag{6.30}$$

For a full proof of this, see appendix A.

As such, both fluxes related to equation (6.20) are zero when averaged over a bounded domain. Note that these fluxes may still play important roles locally in the fluid, but will not give any statistical data about the diffusivity of the entire system. For that, we again turn to the flux of a passive scalar field.

6.4 Passive Scalar Fields

As we have found in the previous section, the flux-like quantities related to the nonlinear terms in equation (6.20) equate to zero when averaged across the (x, y) plane. In keeping with the purely hydrodynamical section of this thesis, we turn to the flux of a passive scalar field under the influence of the fluid flow.

The governing equation of a passive scalar Θ being carried by the total flow $\mathbf{U}$ is

$$\partial_t \Theta + \mathbf{U} \cdot \nabla \Theta = \kappa \nabla^2 \Theta, \tag{6.31}$$

where κ is the diffusivity of the passive scalar field [19].

In keeping with the previous sections, in particular using equations (4.14) and (6.22), we write

$$\mathbf{U} = (\alpha y, 0) + \mathbf{u}, \tag{6.32}$$

where u_x from equation (4.14) is the x-component of $\mathbf{u}$. We separate the perturbations of the passive scalar about a background gradient by writing

$$\Theta = \iota y + \theta', \tag{6.33}$$

where ι is the strength of the gradient, and θ' is the departure of Θ from it. Substituted into equation (6.31), and rescaling to eliminate ι, this results in:

$$\partial_t \theta + \alpha y \partial_x \theta = J(\psi, \theta) + \partial_x \psi + \kappa \nabla^2 \theta, \tag{6.34}$$

where $\theta = \theta'/\iota$ is our new passive scalar field. For a more detailed approach to the derivation of equation (6.34), please see chapter 4.

In the absence of a magnetic field, the passive scalar equation appears similar to the vorticity equation, albeit lacking a body force; the passive scalar is instead driven by the flow itself. Likewise, the passive scalar is not directly influenced by a background magnetic field when the field is present. Rather, the field will influence the flow, as seen in equation (6.20), which in turn determines the passive scalar evolution. For certain parameter choices, the magnetic field and resulting passive scalar field will take similar forms, despite scaling differently (when $\iota \neq B_0$).

Following from the previous section, we can consider the flux of passive scalar to be related to a type of diffusivity in the fluid [25]. For further discussion on this, see the chapter 4 where we discuss the purely hydrodynamical, as well as chapter 3. The averaged downward vertical flux is given by:

$$F = \langle \theta \partial_x \psi \rangle_{x,y}. \tag{6.35}$$

The fact that this flux is generally non-zero can also be shown by observing that the modified Fourier transform of the components of the flux no longer cancel (see Appendix A). Using the established results of Moffatt [25], we use the average flux of the passive scalar field as a diagnostic describing the vertically diffusive nature of the flow. In particular, in the presence of strong zonal jet-like structures which act as barriers to transport across the fluid [14], we expect this flux to be severely inhibited.

6.5 Numerical Methods

As we will be referring to them repeatedly over the next chapter, we restate the sheared β-plane MHD equations for an incompressible two-dimensional plasma as

$$\partial_t \omega + \alpha y \partial_x \omega = J(\psi, \omega) + \beta \partial_x \psi + J(A, \nabla^2 A) - B_0 \partial_x (\nabla^2 A) + \nu \nabla^2 \omega + G, \quad (6.36)$$

$$\partial_t A + \alpha y \partial_x A = J(\psi, A) + B_0 \partial_x \psi + \eta \nabla^2 A, \quad (6.37)$$

$$\omega = -\nabla^2 \psi, \quad (6.38)$$

where $\omega(x, y, t)$, $\psi(x, y, t)$ and $A(x, y, t)$ represent the perturbations of the vorticity, stream function and magnetic potential respectively. The parameters α, β, ν, B_0 and η respectively represent the strength of the shear, the vorticity gradient, the viscosity, the magnitude of the background magnetic field and the magnetic diffusivity, whilst $G(x, y, t)$ is an external body force. The passive scalar field carried by such a flow can be described by

$$\partial_t \theta + \alpha y \partial_x \theta = J(\psi, \theta) + \partial_x \psi + \kappa \nabla^2 \theta, \quad (6.39)$$

where θ represents the passive scalar field and κ gives its diffusivity.

In order to solve the above equations in Fourier space (noting that they are not periodic in (x, y)), we consider a frame of reference in which we follow the perturbations of the flow about its sheared state. This coordinate system will be linearly dependent on time, and can be visualised as a standard Cartesian coordinate system being sheared horizontally with rate α. The variables representing the flow, ω, ψ and A, will be periodic relative to such a system. In the x direction we retain standard periodicity:

$$\psi(x + 2\pi k, y, t) = \psi(x, y, t), \quad (6.40)$$

$$\mathbf{u}(x + 2\pi k, y, t) = \mathbf{u}(x, y, t), \quad (6.41)$$

$$\omega(x + 2\pi k, y, t) = \omega(x, y, t), \quad (6.42)$$

$$A(x + 2\pi k, y, t) = A(x, y, t), \quad (6.43)$$

for $k \in (Z)$. In y, the shearing box system gives a slightly more complicated

relation:

$$\psi(x, y + 2\pi k, t) = \psi(x, y, t) + 2\alpha\pi k y, \tag{6.44}$$

$$\mathbf{u}(x, y + 2\pi k, t) = \mathbf{u}(x, y, t) + (2\alpha\pi k, 0) \tag{6.45}$$

$$\omega(x, y + 2\pi k, t) = \omega(x, y, t), \tag{6.46}$$

$$A(x, y + 2\pi k, t) = A(x, y, t). \tag{6.47}$$

The new coordinate system requires a modified Fourier transform which we will refer to as the Shearing Box Fourier Transform (SBFT):

$$\omega(x, y, t) = \sum_{m,n} \hat{\omega}_{m,n}(t) e^{imx + i(n - \alpha m t)y}, \tag{6.48}$$

where (m, n) are components of our spectral domain and $\hat{\omega}_{m,n}(t)$ is the function corresponding to $\omega(x, y, t)$ in Fourier space [10]. Note that all 'hatted' variables in this thesis will refer to their Fourier or wave-like equivalents.

Using the SBFT we write the relation between the vorticity and stream function given in equation (6.38) in terms of Fourier components as

$$\hat{\omega}_{m,n} = \left(m^2 + (n - \alpha m t)^2\right) \hat{\psi}_{m,n}. \tag{6.49}$$

This relationship allows us to eliminate $\hat{\psi}$ as a variable from the spectral equations for the evolution of ω and A:

$$\begin{aligned} \partial_t \hat{\omega}_{m,n} = \hat{J}_{m,n}(\hat{\psi}, \hat{\omega}) + \left[\frac{im\beta}{m^2 + (n - \alpha m t)^2} - \nu \left(m^2 + (n - \alpha m t)^2\right) \right] \hat{\omega}_{m,n} \\ + \hat{J}_{m,n}(\hat{A}, \hat{\nabla^2} A) - imB_0 (\hat{\nabla^2} A)_{m,n} + \hat{G}_{m,n}, \end{aligned} \tag{6.50}$$

$$\partial_t \hat{A}_{m,n} = \hat{J}_{m,n}(\hat{\psi}, \hat{A}) + \frac{imB_0}{m^2 + (n - \alpha m t)^2} \hat{\omega}_{m,n} + \eta (\hat{\nabla^2} A)_{m,n}. \tag{6.51}$$

Note that the complex function corresponding to the Laplacian of the magnetic potential is calculated by:

$$(\hat{\nabla^2} A)_{m,n} = -\left(m^2 + (n - \alpha m t)^2\right) \hat{A}_{m,n}, \tag{6.52}$$

with $\hat{A}$ being found using the SBFT given in equation (6.48). The nonlinear Jaco-

bian terms are given by

$$\hat{J}(\hat{\psi},\hat{\omega}) = \left[\{im\hat{\psi}\}\{i(n-\alpha mt)\hat{\omega}\} - \{i(n-\alpha mt)\hat{\psi}\}\{im\hat{\omega}\}\right], \tag{6.53}$$

$$\hat{J}(\hat{A},\hat{\nabla^2}A) = \left[\{im\hat{A}\}\{i(n-\alpha mt)\hat{\nabla^2}A\} - \{i(n-\alpha mt)\hat{A}\}\{im\hat{\nabla^2}A\}\right], \tag{6.54}$$

$$\hat{J}(\hat{\psi},\hat{A}) = \left[\{im\hat{\psi}\}\{i(n-\alpha mt)\hat{A}\} - \{i(n-\alpha mt)\hat{\psi}\}\{im\hat{A}\}\right], \tag{6.55}$$

$$\tag{6.56}$$

where each $\{\cdot\}$ in equations (6.53 – 6.55) represents the inner components being converted to real space using the SBFT, while the $[\cdot]$ represents the final conversion back to Fourier space.

For brevity, we will rewrite equations (6.50 – 6.51) as

$$\partial_t\hat{\omega}_{m,n} = \hat{J}_{m,n}(\hat{\psi},\hat{\omega}) + \hat{J}_{m,n}(\hat{A},\hat{\nabla^2}A) - imB_0(\hat{\nabla^2}A)_{m,n} + \hat{G}_{m,n} + r_{m,n}(t)\hat{\omega}_{m,n}, \tag{6.57}$$

$$\partial_t\hat{A}_{m,n} = \hat{J}_{m,n}(\hat{\psi},\hat{A}) + \frac{imB_0}{m^2+(n-\alpha mt)^2}\hat{\omega}_{m,n} + \eta(\hat{\nabla^2}A)_{m,n}. \tag{6.58}$$

where

$$r_{m,n}(t) = \frac{im\beta}{m^2+(n-\alpha mt)^2} - \nu\left(m^2+(n-\alpha mt)^2\right), \tag{6.59}$$

which contains all of the linear terms. Note that for $\alpha = 0$, the non-sheared case, r becomes a function of the wavenumbers m and n alone, and can be calculated once at the beginning of each simulation.

We find the Fourier space passive scalar equation, derived from equation (4.44) to be

$$\partial_t\hat{\theta}_{m,n} = \hat{J}_{m,n}(\hat{\psi},\hat{\theta}) + \frac{im}{m^2+(n-\alpha mt)^2}\hat{\omega}_{m,n} + s_{m,n}(t)\hat{\theta}_{m,n}, \tag{6.60}$$

where

$$s_{m,n}(t) = -\kappa\left(m^2+(n-\alpha mt)^2\right). \tag{6.61}$$

Using similar methods to those described above, we give the Jacobian term as

$$\hat{J}(\hat{\psi},\hat{\theta}) = \left[\{im\hat{\psi}\}\{i(n-\alpha mt)\hat{\theta}\} - \{i(n-\alpha mt)\hat{\psi}\}\{im\hat{\theta}\}\right], \tag{6.62}$$

We aim to solve the above equations using optimized numerical schemes. First, we discretize each equation by setting $t = t_j$, where the integer j represents each step

in our equations. The progression of time at each step is given by

$$t_{j+1} = t_j + \Delta t, \tag{6.63}$$

where the time difference, Δt is an important numerical parameter, to be discussed in the next chapter (see section 7.1). We describe the Fourier component of the vorticity at (m, n) after j time steps by $\hat{\omega}^j_{m,n}$, with a similar form used for all other variables.

The first step of our integration is performed using the Forward Euler method, as given in the following equations for the vorticity, magnetic potential and passive scalar fields respectively:

$$\begin{aligned}\hat{\omega}^{j+1}_{m,n} = {} & \Delta t \left(\hat{J}^j_{m,n}(\hat{\psi}, \hat{\omega}) + \hat{J}^j_{m,n}(\hat{A}, \nabla^{\hat{2}} A) - imB_0 (\nabla^{\hat{2}} A)^j_{m,n} + \hat{G}^j_{m,n} \right) \\ & + \left(1 + r^j_{m,n} \Delta t\right) \hat{\omega}^j_{m,n},\end{aligned} \tag{6.64}$$

$$\hat{A}^{j+1}_{m,n} = \Delta t \left(\hat{J}^j_{m,n}(\hat{\psi}, \hat{A}) + \frac{imB_0}{m^2 + (n - \alpha m t_j)^2} \hat{\omega}^j_{m,n} + \eta (\nabla^{\hat{2}} A)^j_{m,n} \right) + \hat{A}^j_{m,n}, \tag{6.65}$$

$$\hat{\theta}^{j+1}_{m,n} = \Delta t \left(\hat{J}^j_{m,n}(\hat{\psi}, \hat{\theta}) + \frac{im\hat{\omega}_{m,n}}{m^2 + (n - \alpha m t_j)^2} \right) + \left(1 + s^j_{m,n} \Delta t\right) \hat{\theta}^j_{m,n}. \tag{6.66}$$

Following this, we use an Integrating Factor method to find the exact solution to the linear parts of equations (6.57) and (6.58), and a second order Adams-Bashforth approach to the nonlinear Jacobian and body force terms [12]. The equation for the integration of vorticity is:

$$\begin{aligned}\hat{\omega}^{j+1}_{m,n} = {} & \left(\hat{\omega}^j_{m,n} + \frac{3\Delta t}{2} \left(\hat{J}^j_{m,n}(\hat{\psi}, \hat{\omega}) + \hat{J}^j_{m,n}(\hat{A}, \nabla^{\hat{2}} A) - imB_0 (\nabla^{\hat{2}} A)^j_{m,n} + \hat{G}^j_{m,n} \right) \right) \\ & \times \exp\left\{ R^{j+1}_{m,n} - R^j_{m,n} \right\} \\ & - \frac{\Delta t}{2} \left(\hat{J}^{j-1}_{m,n}(\hat{\psi}, \hat{\omega}) + \hat{J}^{j-1}_{m,n}(\hat{A}, \nabla^{\hat{2}} A) - imB_0 (\nabla^{\hat{2}} A)^{j-1}_{m,n} + \hat{G}^{j-1}_{m,n} \right) \\ & \times \exp\left\{ R^{j+1}_{m,n} - R^{j-1}_{m,n} \right\},\end{aligned} \tag{6.67}$$

where

$$\begin{aligned}R_{m,n}(t) = {} & \int r_{m,n}(t) dt \\ = {} & -\frac{1}{3} \nu t \left[m^2 \left(\alpha^2 t^2 + 3 \right) - 3\alpha mnt + 3n^2 \right] \\ & + \frac{i\beta}{\alpha m} \left[\tan^{-1}\left(\frac{n}{m} \right) - \tan^{-1}\left(\frac{n}{m} - \alpha t \right) \right],\end{aligned} \tag{6.68}$$

noting that $R^{j-1}_{m,n} = R_{m,n}(t - \Delta t)$. When $\alpha = 0$ we have instead

$$R_{m,n}(t) = \int r(t)dt = r(t=0)t = \left[\frac{im\beta}{m^2+n^2} - \nu\left(m^2+n^2\right)\right]t, \tag{6.69}$$

with further simplifications when $m = 0$. Note also that in general

$$(\hat{\nabla^2}A)^j_{m,n} = -\left(m^2 + (n - \alpha m t_j)^2\right)\hat{A}^j_{m,n}, \tag{6.70}$$

with $(\hat{\nabla^2}A)^{j-1}_{m,n}$ referring to the variable evaluated at $t - \Delta t$.

Following this, the corresponding equation for integrating the magnetic potential is:

$$\begin{aligned}\hat{A}^{j+1}_{m,n} = &\left(\hat{A}^j_{m,n} + \frac{3\Delta t}{2}\left(\hat{J}^j_{m,n}(\hat{\psi},\hat{A}) + \frac{imB_0}{m^2+(n-\alpha m t_j)^2}\hat{\omega}^j_{m,n}\right)\right) \\ &\times \exp\left\{P(t)^j_{m,n} - P(t)^{j+1}_{m,n}\right\} \qquad (6.71)\\ &- \frac{\Delta t}{2}\left(\hat{J}^{j-1}_{m,n}(\hat{\psi},\hat{A}) + \frac{imB_0}{m^2+(n-\alpha m t_{j-1})^2}\hat{\omega}^{j-1}_{m,n}\right) \\ &\times \exp\left\{P(t)^{j-1}_{m,n} - P(t)^{j+1}_{m,n},\right\} \qquad (6.72)\end{aligned}$$

where

$$P_{m,n}(t) = -\frac{1}{3}\eta t\left[m^2\left(\alpha^2t^2+3\right) - 3\alpha mnt + 3n^2\right], \tag{6.73}$$

to be compared with $R(t)$ in (6.68).

The Integrating Factor-Adams Bashforth Method for integrating the passive scalar field is given by

$$\begin{aligned}\hat{\theta}^{j+1}_{m,n} = &\left(\hat{\theta}^j_{m,n} + \frac{3\Delta t}{2}\left(\hat{J}^j_{m,n}(\hat{\psi},\hat{\theta}) + \frac{im\hat{\omega}^j_{m,n}}{m^2+(n-\alpha mt)^2}\right)\right)\exp\left\{S^{j+1}_{m,n} - S^j_{m,n}\right\} \\ &- \frac{\Delta t}{2}\left(\hat{J}^{j-1}_{m,n}(\hat{\psi},\hat{\theta}) + \frac{im\hat{\omega}^{j-1}_{m,n}}{m^2+(n-\alpha mt)^2}\right)\exp\left\{S^{j+1}_{m,n} - S^{j-1}_{m,n}\right\}, \qquad (6.74)\end{aligned}$$

where

$$S_{m,n}(t) = \int s(t)dt = -\frac{1}{3}\kappa t\left[m^2\left(\alpha^2t^2+3\right) - 3\alpha mnt + 3n^2\right], \tag{6.75}$$

to be compared with $R(t)$ and $P(t)$ in (6.68) and (6.73).

Equations (6.67 – 6.75) give a closed discretized system that, given an appropriate input for the body force $\hat{G}^j_{m,n}$ (to be given in section 6.6), allow us to solve

equations (6.36 – 6.39) directly via a computer. We have written an original program which performs these integrations, while recording key numerical data, using the Fortran 95 programming language.

We have omitted details of how the shearing box coordinate system is implemented in the MHD simulations as the methods are identical to those described in section 4.6 for the purely hydrodynamical system.

6.6 Body Force

When working in a time-dependent coordinate system, we have several choices on how implement a body force. In order for the force to interact as little as possible with the background shear flow, we introduce a body force which excites modes whose positions evolve over time, in order to 'follow' the shear:

$$\hat{G}_{m,n}(t) = \begin{cases} e^{2i\pi\phi_{m,n}(t)} & \text{if } K - \delta K \leq \sqrt{m^2 + (n - \alpha m t)^2} \leq K + \delta K \\ 0 & \text{otherwise,} \end{cases} \tag{6.76}$$

where $\phi_{m,n}(t)$ is the array of random variables determining the phase of each mode in the ring, with the following properties:

$$0 \leq \phi_{m,n} \leq 1, \quad \phi_{m,n} \in \mathbb{R}, \tag{6.77}$$

$$\phi_{m,n}(t) = \begin{cases} \text{randomly chosen as above} & \text{if } t = kT_c,\ k \in \mathbb{N} \\ \phi_{m,n}(kT_c) & \text{if } kT_c < t < (k+1)T_c. \end{cases} \tag{6.78}$$

Equation (6.76) describes the sheared ring force in its ideal form, relative to standard Fourier space; we modify this slightly in order to accommodate the implementation of the shearing box coordinate system. Relative to sheared Fourier space (our numerical grid), (m, p), we define

$$\hat{G}_{m,p}(t) = \begin{cases} e^{2i\pi\phi_{m,p}(t)} & \text{if } K - \delta K \leq \sqrt{m^2 + \left(p - \frac{1}{2}\alpha m T_c\right)^2} \leq K + \delta K \\ 0 & \text{otherwise.} \end{cases} \tag{6.79}$$

The above body force is stationary on our numerical grid, and hence follows the shear. The additional T_c term in equation (6.79) is present in order to ensure that

the average position of the ring over each forcing correlation time is $(m, n - \alpha mt)$. The force is subject to the same methods used to track other variables in the shearing box system; a mode reset is performed at the appropriate time in order to correctly align the grid, while the SBFT is used to convert it to/from Fourier space whenever necessary.

Note that there is no difference between the forcing used for the purely hydrodynamical and magnetohydrodynamical simulations. For a full discussion on the body force, we refer the reader to section 4.7.

6.7 Non-dimensionalization

Following the methods used in section 4.8, we can restrict our search of the parameter regime by eliminating unimportant variables. With a body force, G defined as in equations (6.78) and (6.76) in the previous section, we have the following characteristic scales:

$$G = G\left(\frac{x}{L}, \frac{y}{L}, \frac{t}{T}\right), \tag{6.80}$$

where L is the length scale and T the correlation time of the body force.

Each of the components and operations of equation (6.36 – 6.38) can be written in their non-dimensional forms as

$$\begin{aligned} x = \mathfrak{L}x^\star, \quad y = \mathfrak{L}y^\star, \quad t = \mathfrak{T}t^\star, \quad \omega = &\frac{1}{\mathfrak{T}}\omega^\star, \quad \psi = \frac{\mathfrak{L}^2}{\mathfrak{T}}\psi^\star, \quad u = \frac{\mathfrak{L}}{\mathfrak{T}}u^\star, \\ A = \frac{\mathfrak{L}^2}{\mathfrak{T}}A^\star, \quad \nabla^2 A = \frac{1}{\mathfrak{T}}\nabla^{2\star}A^\star, \quad &\partial_x \equiv \frac{1}{\mathfrak{L}}\partial_x^\star, \quad \partial_t \equiv \frac{1}{\mathfrak{T}}\partial_t^\star, \end{aligned} \tag{6.81}$$

where $\mathfrak{L}$ and $\mathfrak{T}$ are respectively our dimensional length and time scales, and ' $\star$ ' denotes the dimensionless form of the variable/operation. Note also that we write our force as

$$G = \delta G^\star = \delta G^\star\left(\frac{\mathfrak{L}x^\star}{L}, \frac{\mathfrak{L}y^\star}{L}, \frac{\mathfrak{T}t^\star}{T}\right), \tag{6.82}$$

where δ (which is not dimensionless) represents the strength of the forcing. Also,

we observe that

$$J\left(\psi,\omega\right)=\frac{1}{\mathfrak{T}^2}J^\star\left(\psi^\star,\omega^\star\right), \tag{6.83}$$

$$J\left(A,\nabla^2 A\right)=\frac{1}{\mathfrak{T}^2}J^\star\left(A^\star,\nabla^{2\star}A^\star\right), \tag{6.84}$$

$$J\left(\psi,A\right)=\frac{\mathfrak{L}^2}{\mathfrak{T}^2}J^\star\left(\psi^\star,A^\star\right), \tag{6.85}$$

where

$$J^\star\left(\psi^\star,\omega^\star\right)=\left(\partial_x^\star\psi^\star\right)\left(\partial_y^\star\omega^\star\right)-\left(\partial_y^\star\psi^\star\right)\left(\partial_x^\star\omega^\star\right), \tag{6.86}$$

etc. For brevity, we take $J(\psi,\omega)^\star\equiv J^\star\left(\psi^\star,\omega^\star\right)$, etc. By substituting the above into equation (6.36) and (6.37) and multiplying by the appropriate dimensional time/length scales, we obtain

$$\begin{aligned}\partial_t^\star\omega^\star+\mathfrak{T}\alpha y^\star\partial_x^\star\omega^\star&=J(\psi,\omega)^\star+\mathfrak{L}\mathfrak{T}\beta\partial_x^\star\psi^\star+J(A,\nabla^2A)^\star\\&\quad-\frac{\mathfrak{T}}{\mathfrak{L}}B_0\partial_x^\star\nabla^{2\star}A^\star+\frac{\mathfrak{T}}{\mathfrak{L}^2}\nu\nabla^{2\star}\omega^\star+\mathfrak{T}^2\delta G^\star,\end{aligned} \tag{6.87}$$

$$\partial_t^\star A^\star+\mathfrak{T}\alpha y^\star\partial_x^\star A^\star=J(\psi,A)^\star+\frac{\mathfrak{T}}{\mathfrak{L}}B_0\partial_x^\star\psi^\star+\frac{\mathfrak{T}}{\mathfrak{L}^2}\eta\nabla^{2\star}A^\star. \tag{6.88}$$

Hence our dimensionless parameters are

$$\alpha=\frac{1}{\mathfrak{T}}\alpha^\star,\quad \beta=\frac{1}{\mathfrak{L}\mathfrak{T}}\beta^\star,\quad \nu=\frac{\mathfrak{L}^2}{\mathfrak{T}}\nu^\star,\quad \delta=\frac{1}{\mathfrak{T}^2}\delta^\star,\quad B_0=\frac{\mathfrak{L}}{\mathfrak{T}}B_0^\star,\quad \eta=\frac{\mathfrak{L}^2}{\mathfrak{T}}\eta^\star, \tag{6.89}$$

resulting in the following fully non-dimensional system of equations

$$\begin{aligned}\partial_t^\star\omega^\star+\alpha^\star y^\star\partial_x^\star\omega^\star&=J(\psi,\omega)^\star+\beta^\star\partial_x^\star\psi^\star+J(A,\nabla^2A)^\star\\&\quad-B_0^\star\partial_x^\star\nabla^{2\star}A^\star+\nu^\star\nabla^{2\star}\omega^\star+\delta^\star G^\star,\end{aligned} \tag{6.90}$$

$$\partial_t^\star A^\star+\alpha^\star y^\star\partial_x^\star A^\star=J(\psi,A)^\star+B_0^\star\partial_x^\star\psi^\star+\eta^\star\nabla^{2\star}A^\star. \tag{6.91}$$

Although this bears little difference to our original system of equations, (6.36 – 6.37), the relation between the non-dimensional parameters and their dimensional equivalents forms a basis on which we can eliminate two parameters. This does not equate to simply ignoring the chosen parameters; we can observe the relative change in these parameters compared to those remaining in order to relate our non-dimensional investigations to a fully dimensional case.

We choose to fix the length and time scales of the body force, $L^\star = L/\mathfrak{L} = 1$ and $T^\star = T/\mathfrak{T} = 1$. As a result, our non-dimensional equation (after removing asterisks), take the same form as equations (6.36) and (6.37):

$$\partial_t \omega + \alpha y \partial_x \omega = J(\psi, \omega) + \beta \partial_x \psi + J(A, \nabla^2 A) - B_0 \partial_x (\nabla^2 A) + \nu \nabla^2 \omega + \delta G, \tag{6.92}$$

$$\partial_t A + \alpha y \partial_x A = J(\psi, A) + B_0 \partial_x \psi + \eta \nabla^2 A, \tag{6.93}$$

where the body force is now simply

$$G = G(x, y, t), \tag{6.94}$$

and the dimensional length and time scales of body force set the length and time scales of our system:

$$L = \mathfrak{L}, \quad T = \mathfrak{T}. \tag{6.95}$$

We note that this choice of set parameters is unchanged from our original hydrodynamical choice. Indeed, the only difference in our MHD non-dimensionalization scheme is the addition of two new parameters, B_0 and η. This increases the size of our parameter space, requiring us to fix certain parameters during our numerical experiments; this will be discussed further in chapter 7.

Chapter 7

MHD Direct Numerical Simulations

7.1 Numerical Considerations

In the following chapter we discuss the results of the MHD extension to the two-dimensional β-plane shearing box system presented in chapters 4 and 5. Having already discussed the assorted variables and parameters occuring in the purely hydrodynamical system, we now focus solely on the new or changed aspects of the flow due to the magnetic field.

As has been discussed in the section 6.7 on the topic of of non-dimensionalization, we have a number of parameters to investigate in our system; the addition of a magnetic field has introduced B_0 and η, bringing the total number of parameters to nine. We eliminate two of these by the Buckingham π theorem [7], choosing the length and time scales of our body force, L and T. Of the remaining parameters (see table 7.1), we have already discussed the effects of varying α and β in chapter 5. In the current chapter we choose to vary B_0, the strength of the background magnetic field.

Another important parameter introduced with the magnetic field is the magnetic diffusivity, η. The ratio of the fluid viscosity, ν, to η produces the non-dimensional magnetic Prandtl number, P_m. We set $\eta = \nu = 10^{-3}$ in order to have $P_m = 1$. Physically, this value can be motivated by accretion disc formation (see chapter 1 for more information), where a range of magnetic Prandtl numbers can be found (including $P_m = 1$), representing different types of stellar behaviour [3]. Having η take this value also means that the Prandtl number giving the ratio of magnetic to passive scalar diffusivities is also one. As such, the passive scalar equation (6.39) and magnetic induction equation (6.37) are identical in form. Of course, the magnetic potential feeds back on the flow, while the passive scalar does not. However, with our current parameter choices for the MHD system, the passive scalar takes the same form as A, (albeit scaling differently) and as such we tend to refer to one or the other rather than both variables. The most significant result of this is that the passive scalar and magnetic fluxes given in the previous chapter are proportional:

$$F_A =< A\partial_x\psi >=< B_0\theta\partial_x\psi >= B_0F. \tag{7.1}$$

Description	Parameter	Typical value
Strength of background shear	α	0 or 0.1
Coefficient of vorticity gradient	β	0 or 1
Strength of background magnetic field	B_0	$0 \leq B_0 \leq 0.02$
Viscosity	ν	10^{-3}
Magnetic diffusivity	η	10^{-3}
Strength of body force	δ	0.5
Forcing length scale	L	$\frac{5}{2\pi} \pm 10\%$
Forcing time scale	T	1
Passive scalar diffusivity	κ	10^{-3}
Time step	Δt	10^{-2}
Box length (x)	L_x	2π
Box length (y)	L_y	2π
Number of grid points	N	$64^2 \leq N \leq 256^2$ *

Table 7.1: A list of parameters involved in finding numerical solutions to equations (6.36 – 6.39) using our shearing box coordinate system and associated methods. Typical values/ranges of each of these parameters are given in the third column. *The size of our numerical grid, N, is decided on a case by case basis, and is generally dependent on the varied parameters α, β and B_0. We have been careful to ensure that each simulation is fully resolved on a sufficiently fine grid.

To keep in line with the HD investigation, we only look at the passive scalar flux, F, throughout this chapter, while taking note that it also can be used to find the effective diffusivity of the magnetic field.

We aim to keep the purely numerical parameters of our system at much the same values as in chapter 5. We found previously that as our 'main' parameters α and β tend towards zero, the length of time required for the passive scalar flux to settle to a constant value increases dramatically. As will be discussed in this chapter, we find similar results for B_0. Later in the chapter we find that increasing

the strength of the background field requires an increase of the number of points used on our numerical grid. As such, we are restricted as to the magnitude of the magnetic field that we can explore; we defer investigating particularly strong magnetic fields to later research focused on more powerful simulations. As before, we aim to run a large number of simulations over a range of the parameter space in order to investigate the relationship between the vertical transport properties of the flow (manifested through the passive scalar flux) and, in this chapter, B_0.

7.2 MHD Turbulence, $\alpha = 0, \beta = 0, B_0 \neq 0$

We start with a system free of any shear or vorticity gradient, as discussed in section 5.3 in the HD chapter of this thesis. From here we add a weak background magnetic field; it should be noted that the magnitude of the field does not need to be particularly large for it to have a prominent effect on the flow. This is already well known to the scientific community [9], and the topic of MHD turbulence has already been thoroughly investigated (see e.g. [37], [8], [2], etc).

In figure 7.1 we plot the x-averaged profile of velocity over a large period of time for $B_0 = 10^{-4}$. As can be seen, the velocity bears much similarity to the unstructured state of the $(\alpha, \beta) = (0, 0)$ case, as plotted in figure 5.21. Indeed, as was discussed at length in chapter 5, as we decrease the values of the key parameters α, β and B_0 towards zero, the flow becomes indistinguishable from one in which they are not present. We reiterate that this may be because of the increased time-scales over which associated behaviour is observed, rather than their complete absence from the flow (see section 5.3). In order to gain as much insight as we can given the scope of this project, we have run our simulations for as long as possible for a relatively small scale computational investigation.

However, we observe that all aspects of the flow are practically indistinguishable when comparing the results from the $B_0 = 10^{-4}$ case with those for smaller values of B_0 (for the reasons discussed above). This will be expanded on later in this section.

The flow depicted in figure 7.1 appears to be unstructured, with no tendency

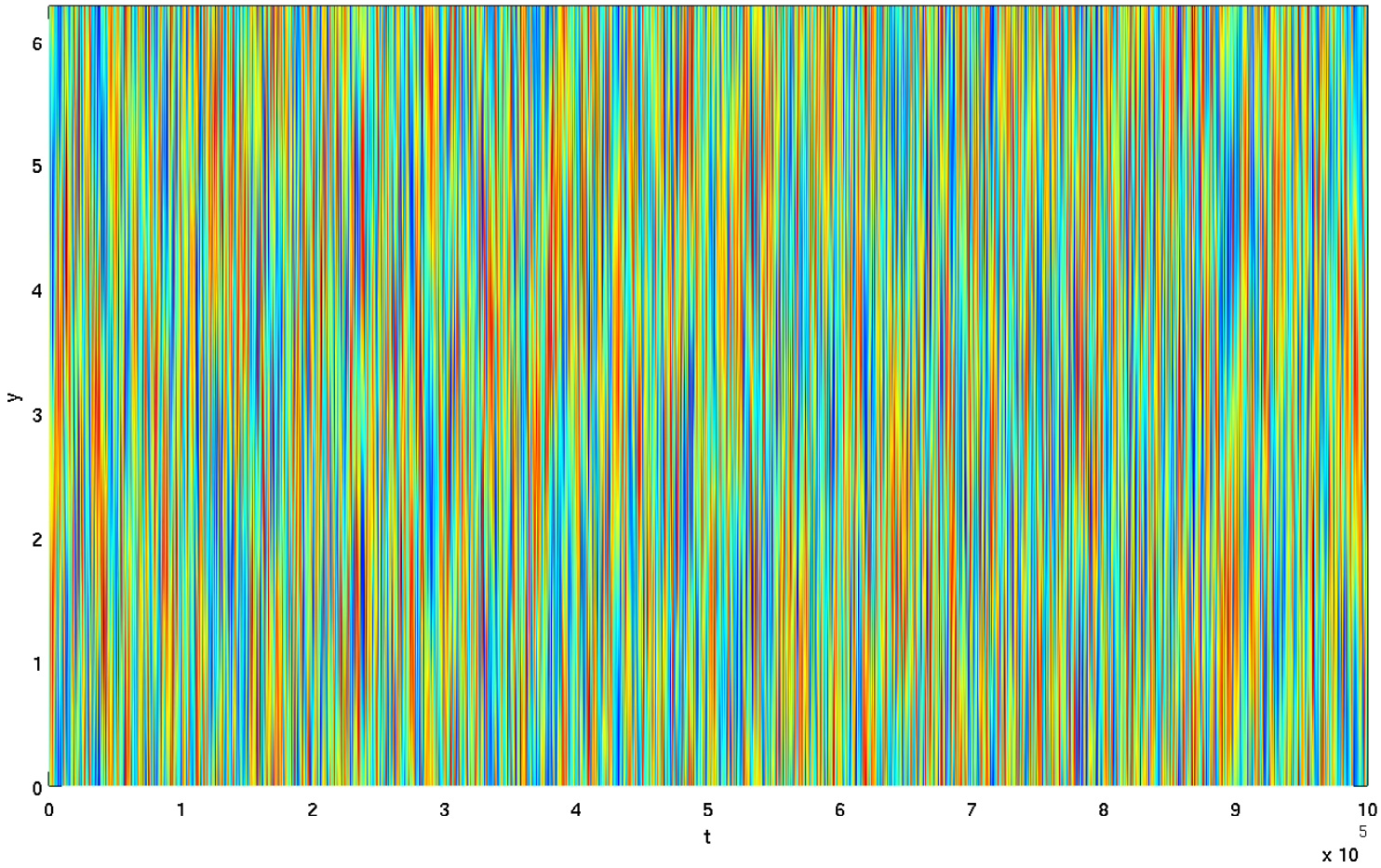

Figure 7.1: Contour plot of the evolution of the mean (x-averaged) profile of velocity over 10^6 units of time, with $(\alpha, \beta, B_0) = (0, 0, 10^{-4})$ and all other parameters defined as in table 7.1.

towards zonal motion and with very short time strong regions of motion. These regions can be attributed directly to the body force, and are positioned somewhat randomly throughout the flow (see section 5.3). Even when looking at a shorter period of this mean profile, as show in figure 7.2a, there is no consistent time scale of these structures.

As we increase B_0 to 10^{-3} as displayed in figure 7.2b, there is no immediate indication as to any particular change in the system. However, we note that although the same unstructured flow persists, there seems to be a larger region of 'weak' flow for the $B_0 = 10^{-3}$ case as opposed to $B_0 = 10^{-4}$. That isn't to say that the the flow is weaker, rather that the regions of relatively strong flow are spread more sparsely and are perhaps slightly shorter in length scale; the flow appears to be slightly more homogeneous. This will be elaborated on at the end of this section.

Despite the resemblance of the velocity profiles, other characteristics of the $B_0 = 10^{-4}$ and $B_0 = 10^{-3}$ systems are not so similar. In figure 7.3 we plot the time averaged passive scalar flux for various values of B_0, taking note of the differing scales presented by each figure. The first two plots, 7.3a and 7.3b contain similarities, however as we increase B_0 further the amount of time required for F to settle to a constant value decreases dramatically. As with the shear and the vorticity gradient, the horizontal magnetic field acts to suppress vertical transport in the flow. The stronger the field, the faster the flux is regulated. We would expect that the time it takes for the averaged flux to reach a constant value would be proportional to the largest time scale phenomena contained by the system.

Aside from the difference in the time scales shown in figure 7.3, another point of observation is that the value of F decreases slightly from 7.3b to 7.3c, with the flux dropping significantly for the $B_0 = 10^{-2}$ case. This leads naturally to our ensemble average of fluxes used to create figure 7.4. Here we have taken the time-averaged flux of 150 different randomized simulations to create a coherent map of the vertical transport's dependence on the parameter B_0. As can be seen, for very small values of B_0 the flux is approximately constant. This is represented in figure 7.4b by the

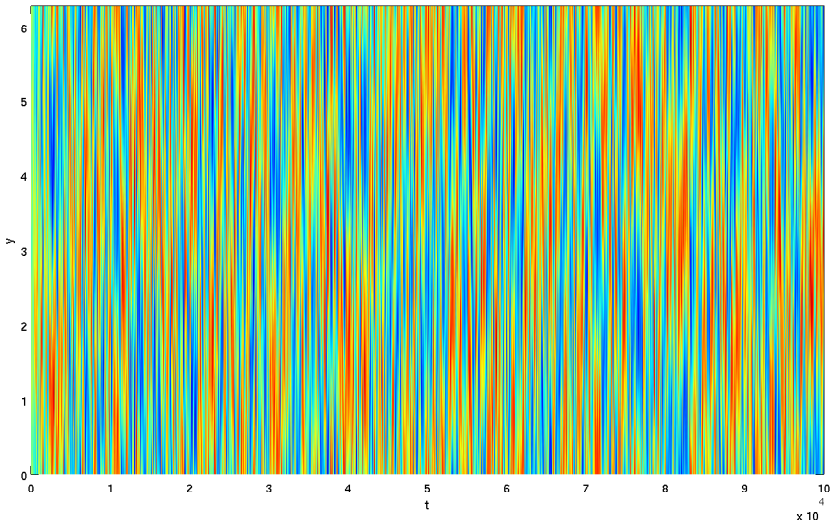

(a)

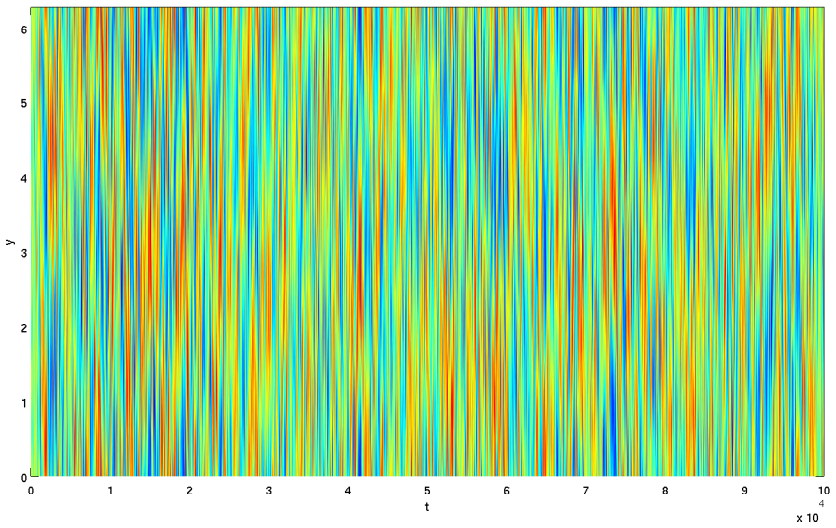

(b)

Figure 7.2: Contour plot of the evolution of the mean (x-averaged) profile of velocity over 10^5 units of time, for (a) $(\alpha, \beta, B_0) = (0, 0, 10^{-4})$, (b) $(\alpha, \beta, B_0) = (0, 0, 10^{-3})$, and all other parameters defined as in table 7.1. Note that (a) is produced from the data used to make figure 7.1.

flat gradient occupying $B_0 \leq e^{-7} \approx 10^{-4}$. Our prior observation, that there was little difference in the flow for values smaller than $B_0 = 10^{-4}$, is backed up by this B_0 independence.

As B_0 increases the flux drops sharply, with a power law relation given clearly

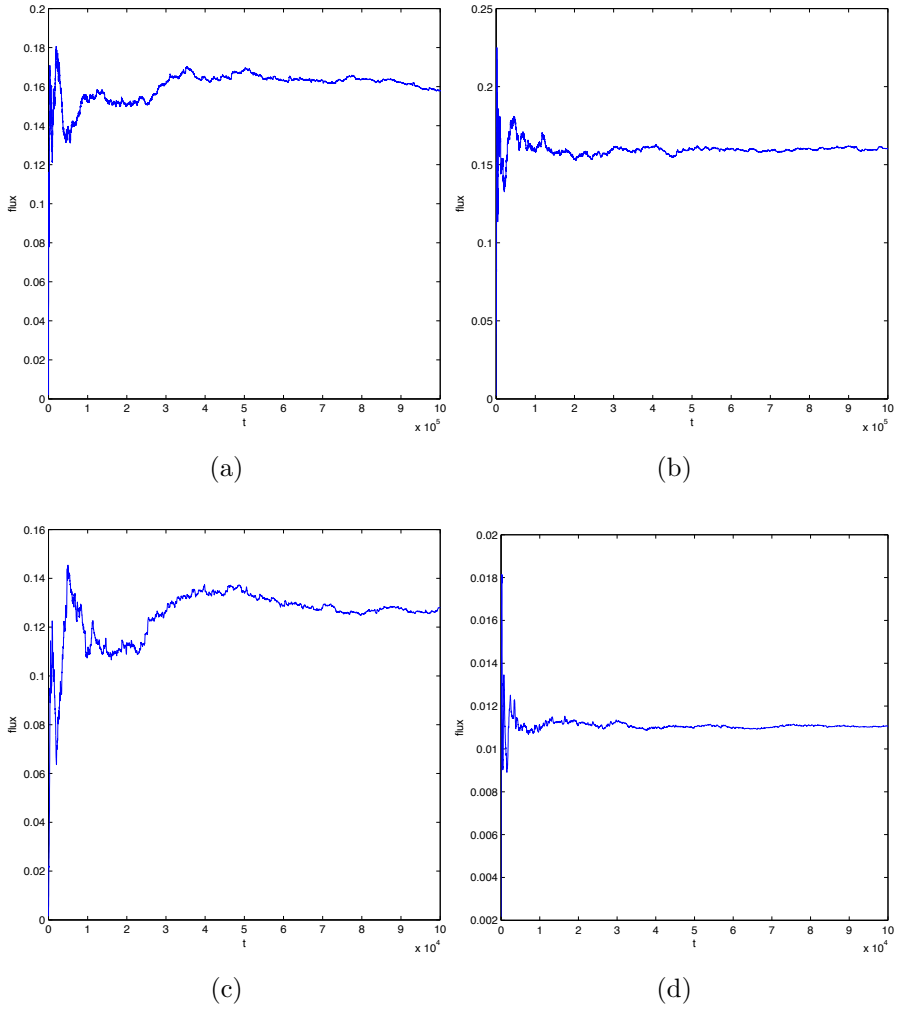

Figure 7.3: Spatially averaged passive scalar flux plotted as a function of time for (a) $(\alpha, \beta, B_0) = (0, 0, 10^{-5})$, (b) $(\alpha, \beta, B_0) = (0, 0, 10^{-4})$, (c) $(\alpha, \beta, B_0) = (0, 0, 10^{-3})$, (d) $(\alpha, \beta, B_0) = (0, 0, 10^{-2})$. The average of the flux over the previous 50% of the simulation is calculated and plotted for each point in time. Figures (a) and (b) are plotted over 10^6 units of time, while (c) and (d) cover 10^5. Note that (b), (c), and (d) are produced from the data used to make figures 7.1, 7.2b and 7.5 respectively.

by figure 7.4b. We measure this to be approximately $F \propto B_0^{-1}$, although the exact value might be either side of this. Note also that for larger values of B_0 there is a slight 'wobble' in this relationship (seen more clearly in the log-log graph); perhaps a precursor to a change in behaviour as B_0 increases. However, at this time we

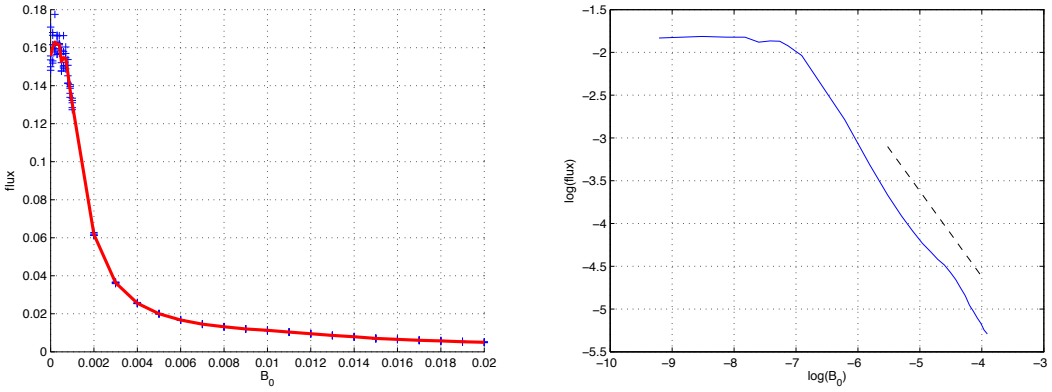

(a) (b)

Figure 7.4: Spatially and temporally averaged passive scalar flux plotted as a function of B_0. Time-averaging is performed by taking the mean of the flux over the previous 50% of the simulation. This is averaged over a number of randomized simulations, each represented in (a) by a blue cross. The ensemble average is plotted in red in (a), while the log-log relationship of this line is given in (b) with B_0^{-1} given by the dashed line. A denser selection of points is used for $B_0 \leq 10^{-3}$ in order to properly establish the relationship between B_0 and the flux.

do not run simulations with values of B_0 greater than 0.02, due to the large strain on our computations caused by the fast, turbulent flows associated with strong magnetic fields. As such, establishing that the above power law relation holds for large B_0 is a task left for later research.

One aspect of the flux diagram we draw attention to is the large variance in values of the flux for small B_0. As mentioned in section 5.3, this is to be expected due to the large times required for the flux to settle down to a constant value when the controlling parameters are small. We acknowledge that, given long enough integration times, the flux may eventually settle to a constant value, with the time required to achieve this tending towards infinity as $B_0 \to 0$. Regardless, the values of the flux are clearly in good agreement by $B_0 = 10^{-3}$, if not earlier (in the parameter space).

There is little change in the value of the flux between $B_0 = 10^{-4}$ and $B_0 = 10^{-3}$,

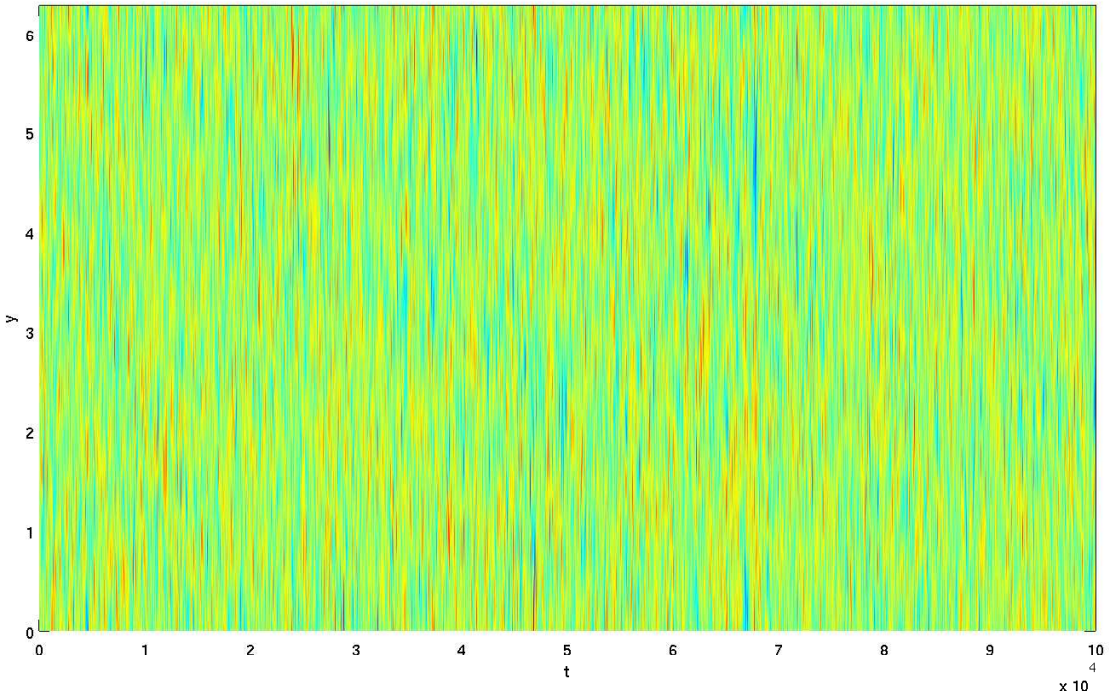

(a)

Figure 7.5: Contour plot of the evolution of the mean (x-averaged) profile of velocity over 10^5 units of time, for $(\alpha, \beta, B_0) = (0, 0, 10^{-2})$, and all other parameters defined as in table 7.1.

despite the change in power law regime. However, as we increase the strength of the magnetic field further to $B_0 = 10^{-2}$, there is a large drop in the flux, to approximately one tenth of its previous values. As such, we expect a substantial change to the structure of the flow in this range of B_0.

This change in the flow can be seen in figure 7.5, where we plot the x-averaged velocity for $B_0 = 10^{-2}$. Compared with the smaller values of B_0, as plotted in figure 7.7a, the velocity here is more homogenous, with fewer strong regions of motion. Generally, the length scales of the system appear to be shorter, although this is quite hard to measure from figure 7.5 alone.

To better understand what is happening at each of these values of B_0, we plot the velocity profiles of the flow for a shorter span of time in figures 7.6 and 7.7. The $B_0 = 10^{-4}$ and $B_0 = 10^{-3}$ cases appear somewhat similar (as expected), with

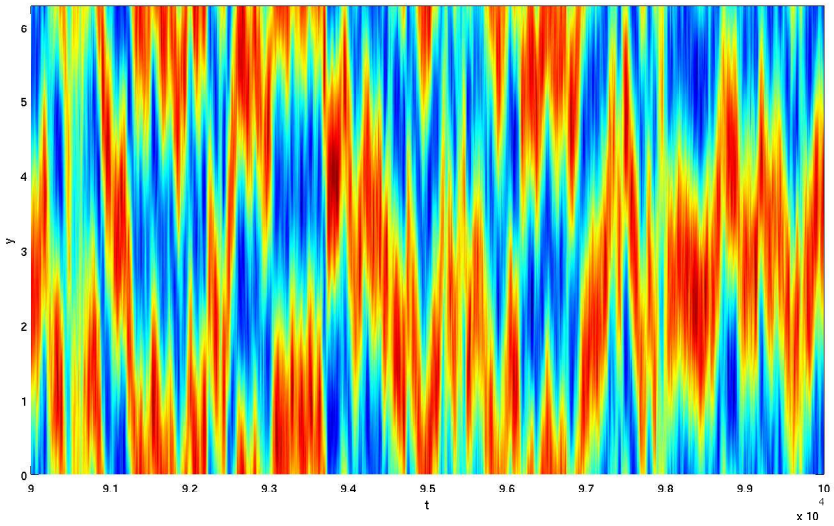

(a)

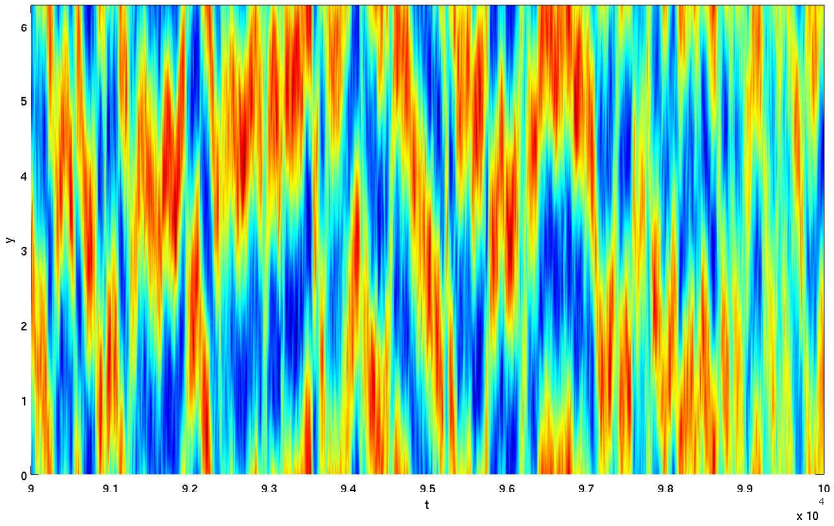

(b)

Figure 7.6: Contour plot of the evolution of the mean (x-averaged) profile of velocity over 10^4 units of time starting at $t = 9 \times 10^4$, for (a) $(\alpha, \beta, B_0) = (0, 0, 10^{-4})$, (b) $(\alpha, \beta, B_0) = (0, 0, 10^{-3})$, and all other parameters defined as in table 7.1. Note that (a) and (b) are produced from the data used to make figures 7.1 and 7.2b respectively.

very short time zonal structures forming, similarly to the small α and β cases (see figures 5.14 and 5.24). The time scales of these structures seem to be roughly the same in each figure, and as mentioned previously, the length scales appear to

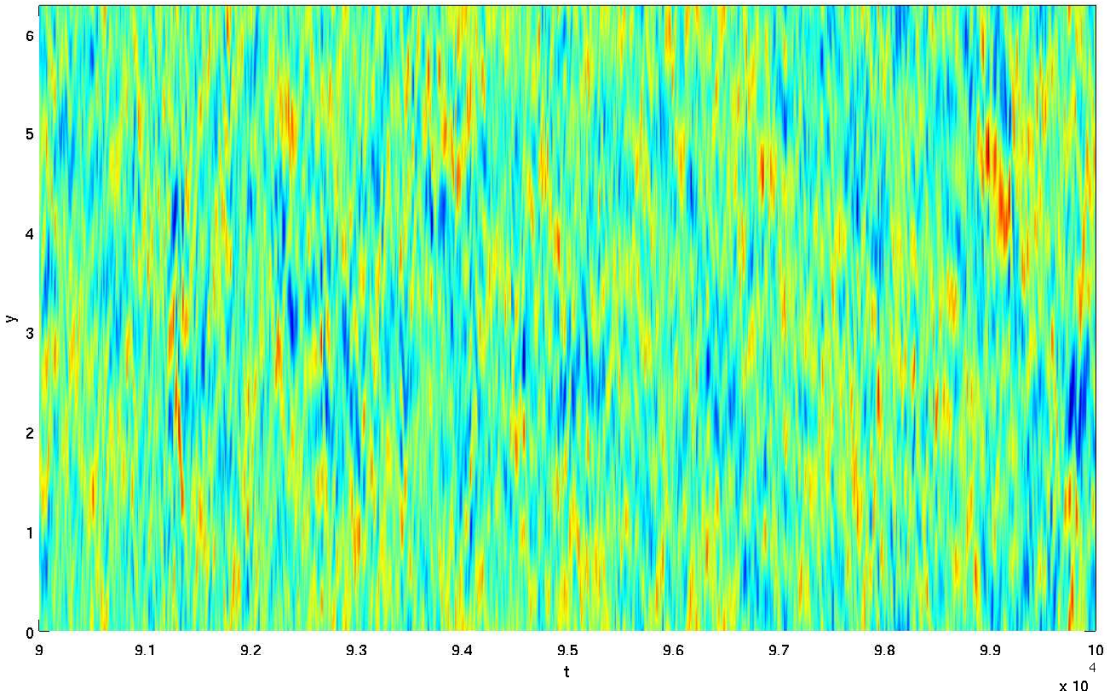

(a)

Figure 7.7: Contour plot of the evolution of the mean (x-averaged) profile of velocity over 10^4 units of time starting at $t = 9 \times 10^4$, for $(\alpha, \beta, B_0) = (0, 0, 10^{-2})$, and all other parameters defined as in table 7.1. Produced from the data used to make figure 7.5.

be slightly larger in 7.6a. However, on closer inspection, we note that the length scales of the two cases are actually the same; each has a pair of alternating zonal structures filling the y-domain. The $B_0 = 10^{-3}$ flow appears different due to the fact that the 'jets' are not as strong; the centre of the jet is thinner in comparison to the $B_0 = 10^{-4}$ case.

As we increase B_0, the structure of the flow changes to match the results displayed in figure 7.5. Both the length and time scales of the system appear to decrease as the magnetic field acts to disrupt any structure in the flow. As the flow carries and mixes the background field, the field behaves like a restoring force, elastically pushing and stretching the flow. The stretching out of the vortices created by the body force is what breaks down the flow into smaller scale, turbulent

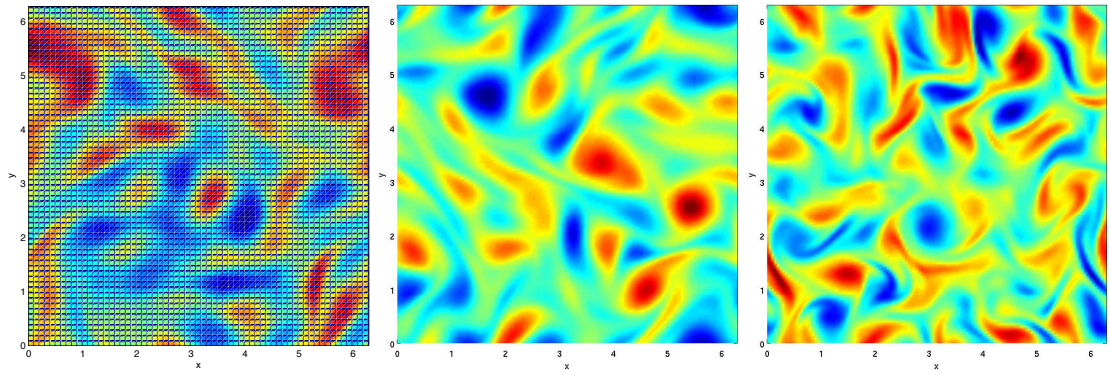

(a) (b) (c)

Figure 7.8: Contour plot of the perturbations of the vorticity field at $t = 10^5$ for (a) $(\alpha, \beta, B_0) = (0, 0, 10^{-4})$, (b) $(\alpha, \beta, B_0) = (0, 0, 10^{-3})$, (c) $(\alpha, \beta, B_0) = (0, 0, 10^{-2})$, with all other parameters defined as in table 7.1. Note that (a), (b) and (c) are produced from the data used to make figures 7.1, 7.2b and 7.5 respectively.

motions.

This phenomena can be seen more clearly in figure 7.8, where we plot the vorticity field at $t = 10^5$ for three different values of B_0. The first two, 7.8a and 7.8b, show typical velocity fields for systems with weak controlling parameters; vortex like motion appears dominant, with 'positive' and 'negative' vortices gathering at different regions of the flow, creating a vertically structured appearance seen in the mean velocity profiles of figure 7.6. Meanwhile, in figure 7.8c, we see how the magnetic field stretches the vortices, creating thin filament-like structures, often wrapped around the remaing vortices.

Computationally, this creation of short scale motion makes it challenging to accurately simulate flows under the influence of a strong magnetic field. As the strength of the field is increased, the filaments are stretched out faster and become thinner, requiring the fluid to be mapped on to large numerical grids in order to be properly resolved. Limiting our simulations to a grid size of 256^2, we are only able to resolve runs of $B_0 = 0.02$ when $(\alpha, \beta) = (0, 0)$, with the upper limit of B_0 changing as α and/or β are increased.

We look now at the magnetic potential, A, by plotting the x-averaged profile for

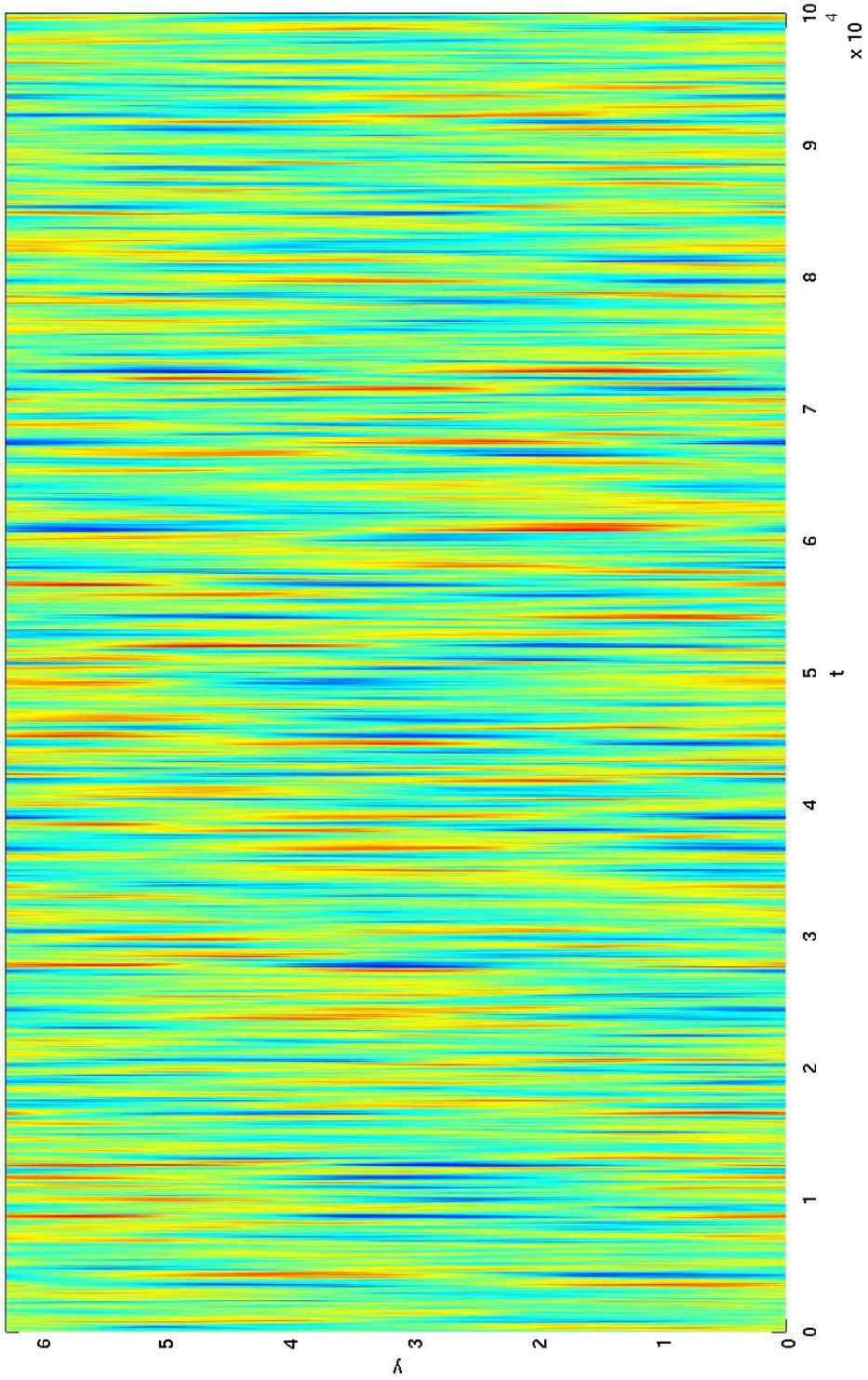

Figure 7.9: Contour plot of the evolution of the mean (x-averaged) profile of magnetic potential over 10^5 units of time, with $(\alpha, \beta, B_0) = (0, 0, 10^{-2})$ and all other parameters defined as in table 7.1. Note that this plot corresponds to the flow displayed in figure 7.5.

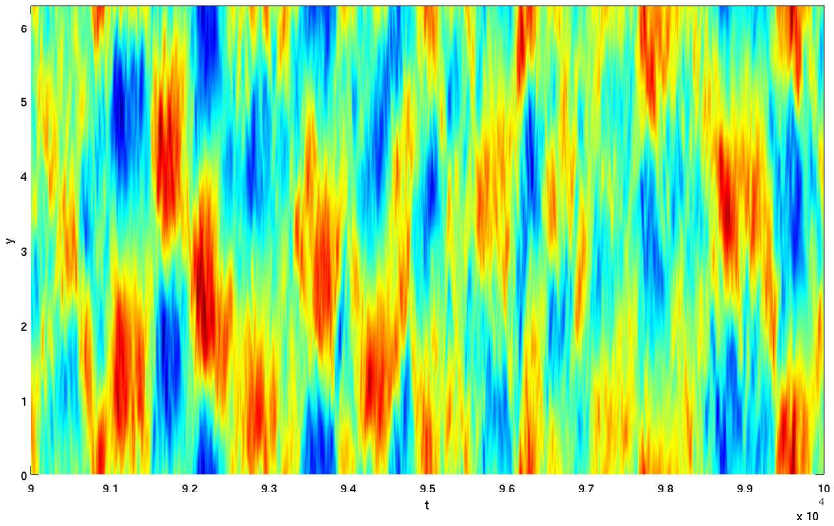

(a)

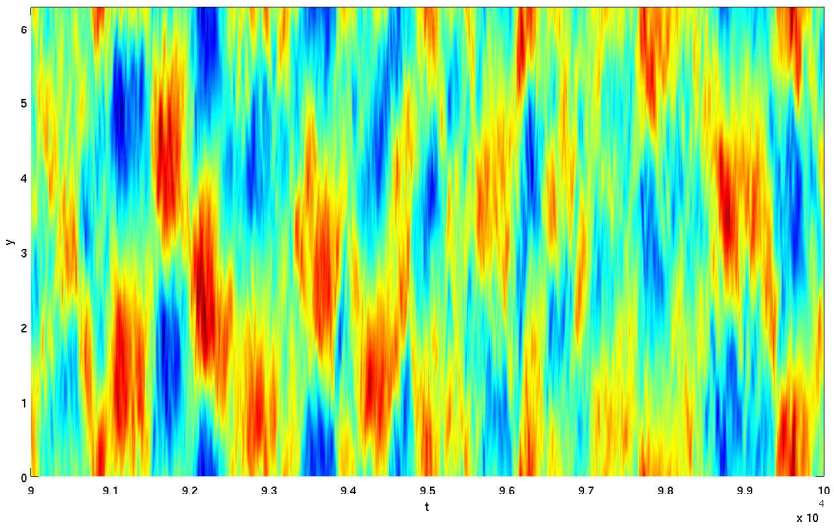

(b)

Figure 7.10: Contour plot of the evolution of the mean (x-averaged) profile of (a) magnetic potential and (b) passive scalar over 10^4 units of time. $(\alpha, \beta, B_0) = (0, 0, 10^{-2})$, and all other parameters are defined as in table 7.1. Note that this plot corresponds to the flow displayed in figure 7.5.

$B_0 = 10^{-2}$ in figure 7.9. In comparison with the corresponding velocity profile, as given in figure 7.5, the magnetic field appears to be less homogenous, with stronger events occuring at seemingly random points in its evolution.

Looking at the short time profile of an already evolved magnetic field given in

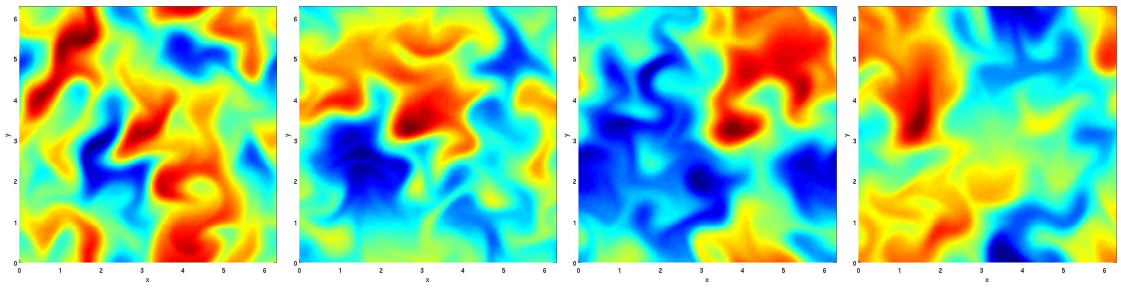

(a) (b) (c) (d)

Figure 7.11: Contour plot of the perturbations of the passive scalar field at (a) $t = 10^2$, (b) $t = 10^3$, (c) $t = 10^4$, (d) $t = 10^5$. $(\alpha, \beta, B_0) = (0, 0, 10^{-2})$ and all other parameters defined as in table 5.1. Note that this has been produced from the data used to make figure 7.9.

figure 7.10a, we see that the field exhibits much longer time scale behaviour than the flow (see figure 7.6a), with zonal structures forming for approximately 500 units of time. These structures also seem to have a rather consistent length scale, with alternating pairs filling the y-domain. However, we note that their scale may be limited by the size of the box of fluid that we are simulating (see table 7.1).

The fact that a strong magnetic field shows relatively large time and length scale behaviour when compared to the actual flow indicates that these scales have little influence on the flow itself. As discussed in chapter 3, the feedback on the mean flow from the magnetic field comes from vorticity flux and Lorentz force terms. Our results indicate that for these small values of B_0, the Lorentz force feedback is relatively small, making the magnetic field have little effect on the mean behaviour of the flow, despite being well structured itself.

Figure 7.11 gives snapshots of the magnetic potential at several values of t for $B_0 = 10^{-2}$. As can be seen in the mean profile plot (see figure 7.10), there is little change to the form of A throughout its evolution, with a generally wave-like behaviour dominating the inhomogeneous field.

We have included a plot of the mean profile of the passive scalar field in figure 7.10b, to be compared with the magnetic potential in figure 7.10a. As has been previously mentioned, due to the similarity of equations (6.39) and (6.37), as well

as our choice of parameters (with $P_r = P_m = 1$), we expect the form of the passive scalar and magnetic potential fields to evolve in the same way. This has been confirmed by figure 7.10. A result of this is that the passive scalar flux also describes the diffusive nature of the magnetic induction equation (see (7.1)), and so the $F \propto B_0^{-1}$ scaling seen in figure 7.4 directly gives a $F \propto B_0^0$ scaling of magnetic flux to B_0. As such, the Alfvén waves dominating the flow do not increase the amount of transport of magnetic potential, a result which can be expected. The results of both of these fluxes can easily be found using linear analysis.

In summary, having investigated the effect that a background magnetic field has on a two-dimensional turbulent flow, we have observed the field disrupting vertical transport in the flow, and established a power law of $F \propto B_0^{-1}$. Like the parameters α and β, for small values of B_0 the flux requires increasingly large averaging times to reach a stable value, due to the time scale of its 'controlling' behaviour increasing. For the small values of B_0 that we have investigated, we have found that the mean magnetic field has a much different structure to that of the mean flow, with coherent structures persisting for moderate time scales. We note that, although we have not looked at it here, it would be interesting to investigate the scaling of the magnetic Reynolds number, R_m, in relation to the passive scalar flux.

7.3 Sheared Magnetic Fields, $\alpha = 0.1, \beta = 0, B_0 \neq 0$

Having discussed the effects of adding an increasingly strong magnetic field to a forced electrically conducting fluid, we now investigate the interaction between the field and a system under the influence of a linear background shear flow. We refer the reader to section 4.4 where we discussed the purely hydrodynamical case, and in particular to figures 5.23 – 5.29. We also note that in the HD system, α had the effect of inhibiting vertical transport across the flow by shearing out the vortices created by the body force. Over short periods of time, these sheared vortices created small-scale zonal structures in the velocity profile, not dissimilar to weak jets.

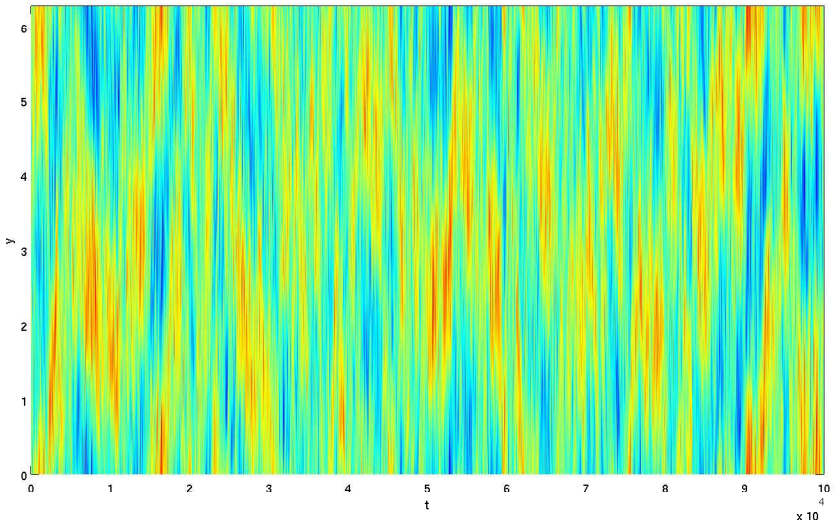

(a)

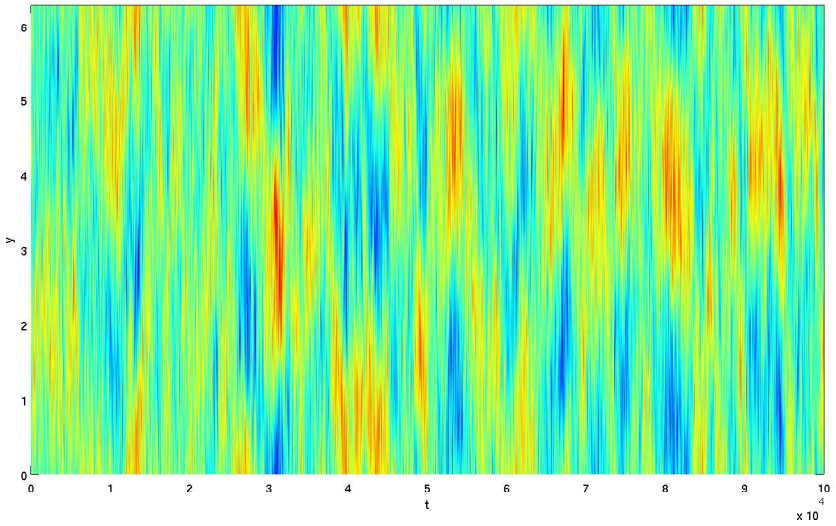

(b)

Figure 7.12: Contour plot of the evolution of the mean (x-averaged) profile of velocity over 10^5 units of time, for (a) $(\alpha, \beta, B_0) = (0.1, 0, 10^{-4})$, (b) $(\alpha, \beta, B_0) = (0.1, 0, 10^{-3})$, and all other parameters defined as in table 7.1.

In section 5.3 (and more recently, section 7.3), we found that when introducing a 'controlling' parameter, i.e. a parameter which leads to long time regularity in the flow, there seems to be a threshold below which the structure of the flow is uninfluenced by changes to the parameter. We suggested that this lack of change may be due to the increased time scales over which regular behaviour takes place

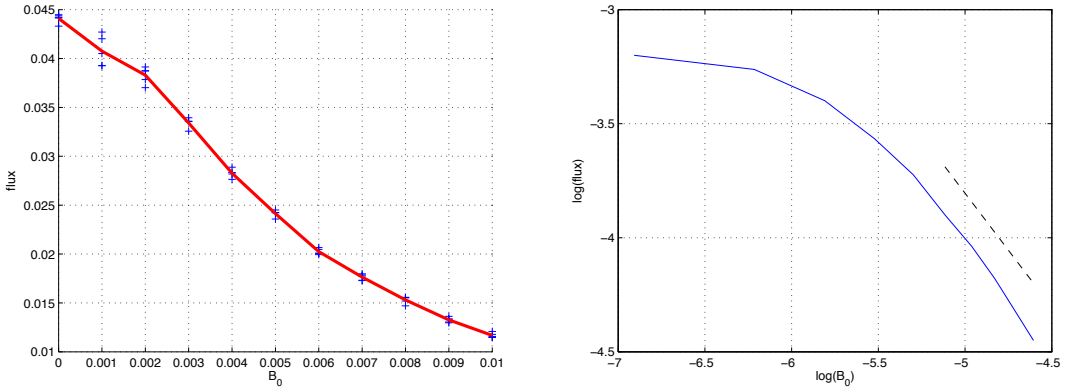

(a) (b)

Figure 7.13: Spatially and temporally averaged passive scalar flux plotted as a function of B_0 with $(\alpha, \beta) = (0.1, 0)$. Time-averaging is performed by taking the mean of the flux over the previous 50% of the simulation. This is averaged over a number of randomized simulations, each represented in (a) by a blue cross. The ensemble average is plotted in red in (a), while the log-log relationship of this line is given in (b), with B_0^{-1} given by the dashed line. Note that the variance of F for points at $B_0 = 0$ is small in comparison to small $B_0 \neq 0$ due to the use of a longer integration time for the former simulations (ten times longer for $B_0 = 0$).

when the controlling parameter is very small. We start now with a system where $\alpha = 0.1$, and begin to introduce a magnetic field. Unlike the previous section where long time scales became an issue, we now have a parameter regulating the flow, and as such we can expect a region of the parameter space where B_0 is negligible in comparison with α, and has no overall effect on the flow.

We find that in general, values of B_0 less than approximately 10^{-3} give no apparent change in the characteristics of the flow. To show this, we plot the mean velocity profiles of a flow with $B_0 = 10^{-4}$ and $B_0 = 10^{-3}$ in figure 7.12. There appears to be no particular difference between either figure, each giving the type of velocity profile typical of a system under moderate shear (e.g. figure 5.27a).

To explain this similarity we turn to the flux diagram given in figure 7.13. This figure gives a promisingly simple relationship between B_0 and F; after a region of

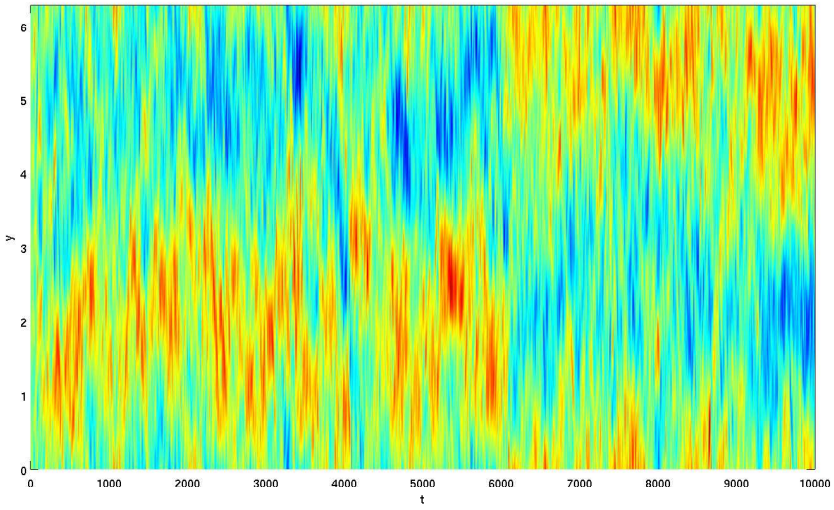

(a)

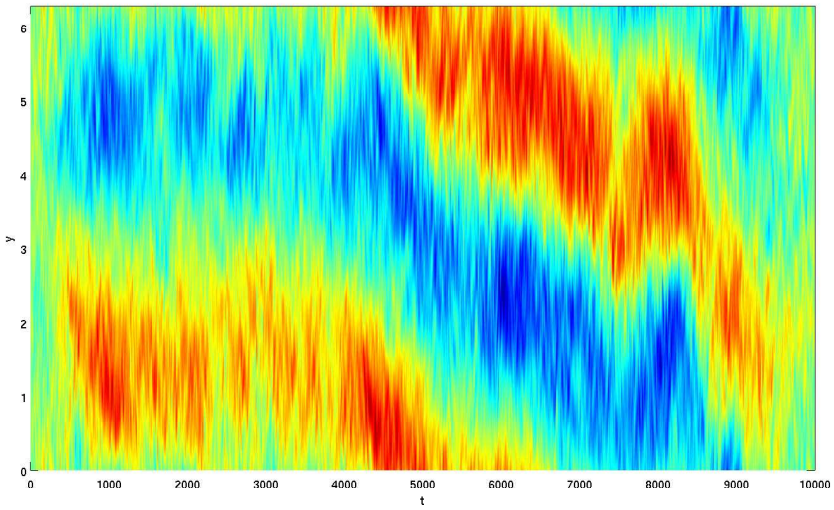

(b)

Figure 7.14: Contour plot of the evolution of the mean (x-averaged) profile of velocity over 10^4 units of time, for (a) $(\alpha, \beta, B_0) = (0.1, 0, 10^{-3})$, (b) $(\alpha, \beta, B_0) = (0.1, 0, 10^{-2})$, and all other parameters defined as in table 7.1. Note that (a) is produced from the data used to make figure 7.12b.

approximately linear dependence for small B_0, the curve makes a smooth transition to a standard power law. At the largest limit of B_0 given here, the power law seems to correspond to the $F \propto B_0^{-1}$ relationship found for $(\alpha, \beta) = (0, 0)$ in the previous section.

While we cannot be certain that the curve shown in figure 7.13b converges to this particular power law, it seems logical that, in the limit of strong B_0 to α, the $F \propto B_0^{-1}$ power law would be retained. Although we would like to check to make sure this is the case, we are faced with very strong turbulent flows at these current parameter values. Indeed, the interaction between the shear and the magnetic field creates a flow that requires high numerical resolution to accurately simulate. In comparison to the previous section where the limits to our current numerical simulations were met at $B_0 = 0.02$, the addition of $\alpha = 0.1$ effectively halves the value of B_0 that we can resolve on a 256^2 grid.

Returning to our original point, we note that the region of parameter space at which the flux is linearly dependent on B_0 seems to cover approximately $B_0 < 2 \times 10^{-3}$, indicating that our initial observation of an unvarying flow for $B_0 \leq 10^{-3}$ would be logical. Due to the smooth change between power laws as we increase B_0, we would expect the behaviour of systems with a small difference in parameters to be similar and regular in transition. As such, for the rest of this section, we focus on just two values of B_0; one from the 'independent' region, $B_0 = 10^{-3}$, and one from the standard power law region, $B_0 = 10^{-2}$.

In figure 7.14 we look at the velocity profiles of these two systems over 10^4 units of time. While both show zonal features, it is clear that the structures associated with $B_0 = 10^{-2}$ are both stronger and more prominent. While the structures move vertically at time scales much shorter than those observed in the classic β-plane case, they are comparable in terms of consistency and length scale. Meanwhile, the structures seen in figure 7.14a are relatively weak; this is demonstrated by the fact that they completely reverse in polarity over a very small period of time at $t \approx 6 \times 10^3$.

The fact that a large-scale zonal flow can be observed for a relatively large value of our parameters is somewhat surprising. Previously we found that as B_0 was increased, any jet-like structures present in the flow were broken down into small-scale, short lived motions. Likewise, for $\alpha = 0.1$, we have a relatively unstructured flow, with no particularly large length scales present. How these two parameters

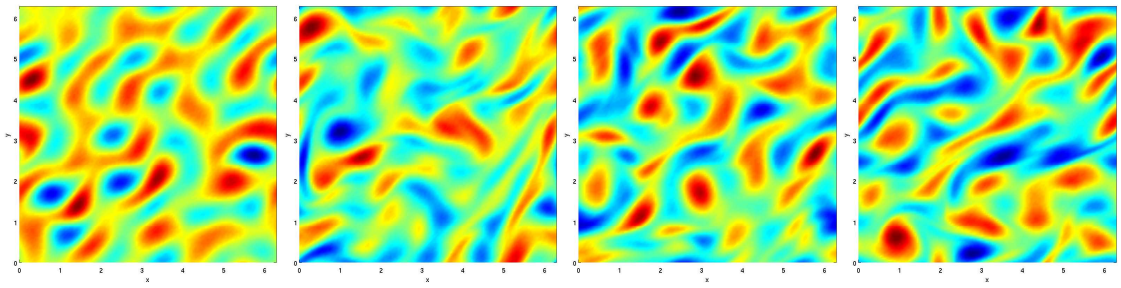

(a) (b) (c) (d)

Figure 7.15: Contour plot of the perturbations of the vorticity field at (a) $t = 10$, (b) $t = 10^2$, (c) $t = 10^3$, (d) $t = 10^4$. $(\alpha, \beta, B_0) = (0.1, 0, 10^{-3})$ and all other parameters defined as in table 7.1. Produced from the data used to make figure 7.12b.

somehow resonate to create such a large-scale, well ordered system is unknown to us.

To explore this phenomena further, we compare plots of the vorticity field taken at various points in time for the two values of B_0. In figure 7.15 we see that for small B_0 the stretching effect of the magnetic field on the vortices is negligible compared to the rate at which they are sheared out by the background flow. Similarly to the purely hydrodynamical case, we can see how the shear organises the vortices into roughly horizontal strips across the periodic domain.

In figure 7.16 we see the two forces working together to modify the vortices created by the body force. The magnetic field tears the vortices into thin filaments, while the shear tips these filaments over, creating a preference for horizontal alignment. Despite this, the snapshots depicted in figures 7.16a – 7.16d show little resemblance to the apparently well structured mean profile of horizontal velocity given in figure 7.14b. As such, it seems that the organisation of the system into ordered regions of alternating flow must originate from a more subtle mechanism than those discussed so far.

One possible influence on the structure of the flow for large values of B_0 is the magnetic field itself. In the previous section we found that the length and time scales observed in the magnetic potential did not seem to match those of the

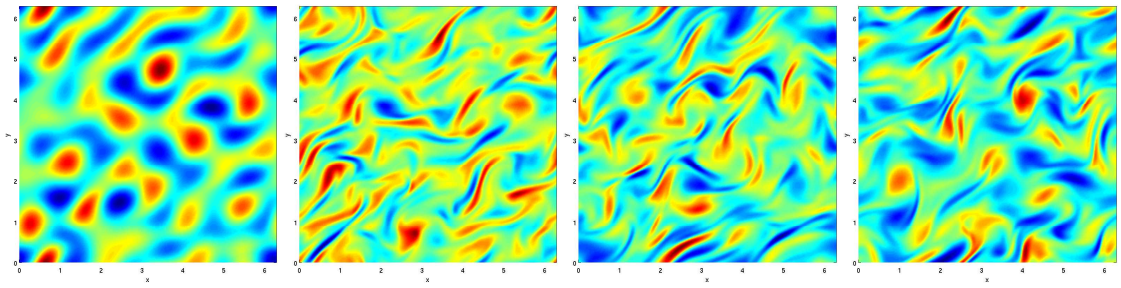

(a) (b) (c) (d)

Figure 7.16: Contour plot of the perturbations of the vorticity field at (a) $t = 10$, (b) $t = 10^2$, (c) $t = 10^3$, (d) $t = 10^4$. $(\alpha, \beta, B_0) = (0.1, 0, 10^{-2})$ and all other parameters defined as in table 5.1. Produced from the data used to make figure 7.14b.

actual flow. Indeed, in figure 7.17a we find this again to be the case, albeit now with the magnetic field displaying much shorter time and length scales than the flow (contrary to the $\alpha = 0$ case). We note that introducing a strong field brings Alfvén waves into the system, which introduce new timescales which are linked to the strength of B_0. As B_0 is increased to 10^{-2} we find that the magnetic potential closely matches the mean velocity profile, with positive regions of A corresponding to negative regions of v and vice-versa.

This similarity in mean profiles suggests that the magnetic terms in equation (6.36) begin to have significant effect. However, the fact that this type of behaviour does not occur for large B_0 when $\alpha = 0$ also indicates that the shear itself somehow facilitates this transfer of dominance from the flow to the magnetic field.

In conclusion, we have found interesting behaviour as the flow moves from an α dominated regime to one affected by the magnetic field. Despite simple behaviour in terms of flux suppresion (with the $F \propto B_0^{-1}$ scaling law being regained for large B_0), interactions between B_0 and α appear to cause long time zonal behaviour for larger values of B_0. Unfortunately, we have been unable to establish whether these features persist as we increase B_0 further (or if the flow returns to the $\alpha = 0$ regime) due to the large amount of computing power needed to resolve each simulation. A proposed mechanism for this zonal behaviour is the combined 'stretch and shear'

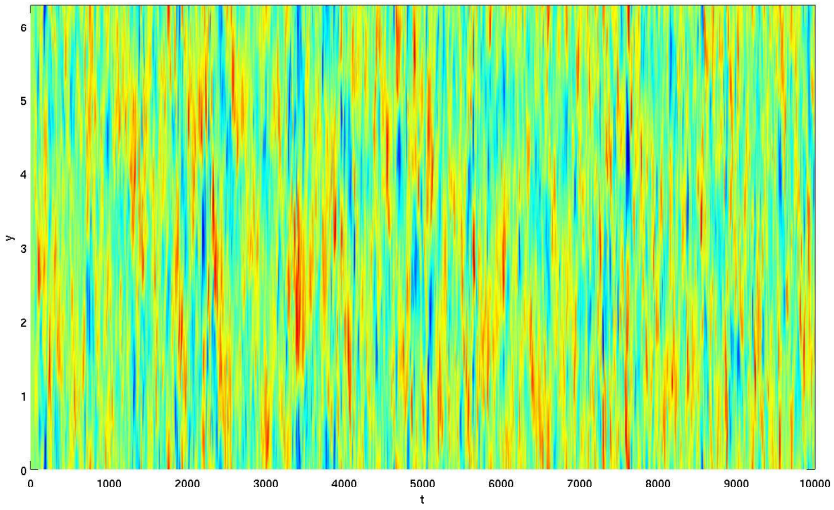

(a)

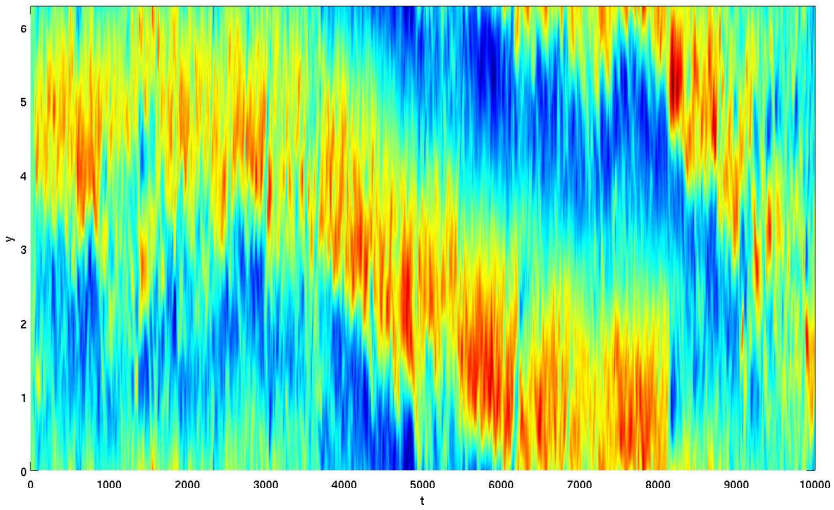

(b)

Figure 7.17: Contour plot of the evolution of the mean (x-averaged) profile of magnetic potential over 10^5 units of time, for (a) $(\alpha, \beta, B_0) = (0.1, 0, 10^{-3})$, (b) $(\alpha, \beta, B_0) = (0.1, 0, 10^{-2})$, and all other parameters defined as in table 7.1. Note that (a) and (b) correspond to figures 7.14a and 7.14b respectively.

effect the magnetic field and mean flow have on vortices produced by the body force, however we might expect vertical length scales similar to that of the forcing if this is indeed the case, which has not been observed.

7.4 Magnetized Jets, $\alpha = 0, \beta = 1, B_0 \neq 0$

We now discuss the effect of increasing the strength of a magnetic field on a system with a background gradient of vorticity. For the physical systems these two effects simultaneously occur in, e.g. the solar tachocline [24], the non-dimensional numbers characterizing the flow can reach extreme values, particularly R_e and R_m, the Reynolds and magnetic Reynolds numbers, while the magnetic Prandtl number, P_m is typically $O(10^{-2})$. As previously discussed, we use moderate values for each of our parameters in order to better understand the region of parameter space we can afford to simulate using a reasonable amount of computing power.

In this section we set the strength of the vorticity gradient, β, to unity; a value at which we see persistent, well structured zonal jets occuring in the purely hydrodynamical system. While these jets were not anchored to any particular vertical position, we observed that large-scale movement of the jet tended to take place over relatively long periods of time, if at all. At these parameter values, the jets themselves consisted of clustered regions of equal parity vortices, rather than strong homogeneous flows. We also found that a single, fully evolved jet has a vertical length scale of approximately $L_y = \pi$, allowing for an alternating pair of jets in a standard $(2\pi)^2$ simulation. For a full discussion of the hydrodynamical results, please see chapter 5.

We begin by introducing a weak background magnetic field with $B_0 = 10^{-4}$ to our β-plane system. For reference, the case of $(\alpha, \beta, B_0) = (0, 1, 0)$ can be found in section 5.2, particularly figures 5.2 and 5.5. In comparison, figure 7.18a gives no particular difference between the HD and weakly magnetic cases. The slowly meandering jet-like profiles persist over long periods of time, taking on the same vertical length scale as the $B_0 = 0$ system. Increasing B_0 further to 10^{-3} does little to change this; the two plots in figure 7.18 are indistinguishable from each other and figure 5.2.

Clearly, at the current range of B_0, the dominant parameter in the system is β. As we discuss the passive scalar flux and its relation to B_0 later in this section, the limit at which B_0 begins to take effect will become clear.

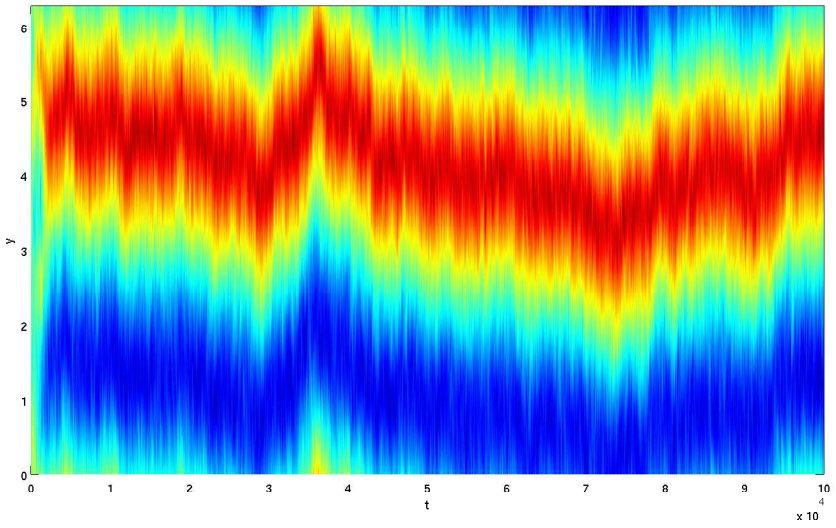

(a)

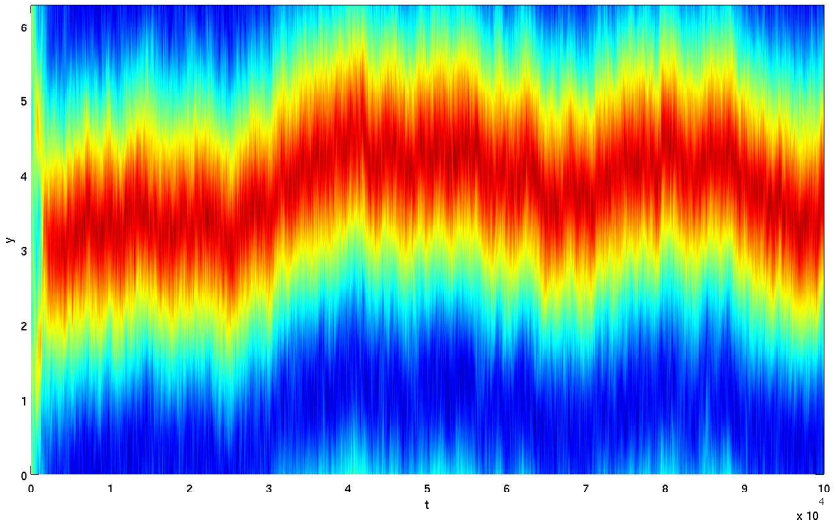

(b)

Figure 7.18: Contour plot of the evolution of the mean (x-averaged) profile of velocity over 10^5 units of time, for (a) $(\alpha, \beta, B_0) = (0, 1, 10^{-4})$, (b) $(\alpha, \beta, B_0) = (0, 1, 10^{-3})$, and all other parameters defined as in table 7.1.

Increasing B_0 by a factor of 10 dramatically changes the mean velocity profile, as can be seen in figure 7.19b. The long-time structure of the zonal jets has been broken down, leaving sporadic, briefly occuring structures of shorter length scale and apparently random verical position. Clearly some important dynamical changes have taken place on the range $10^{-3} < B_0 < 10^{-2}$. As we increase B_0 again

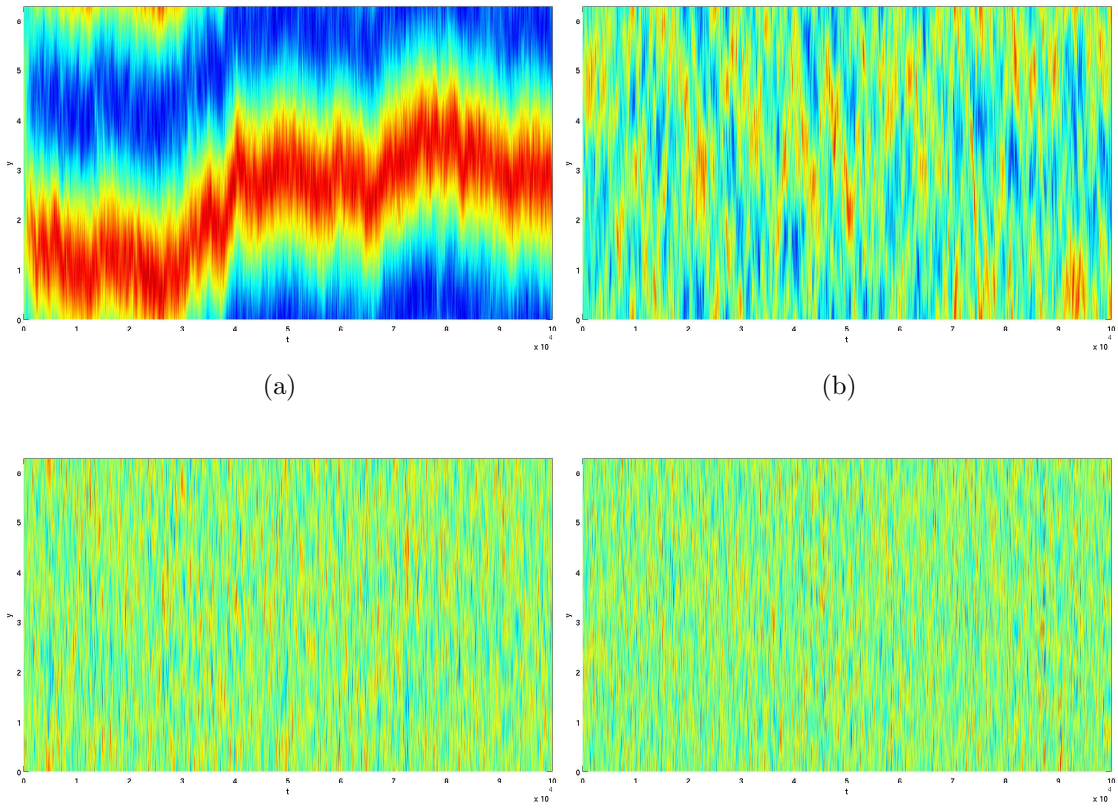

(a) (b)

(c) (d)

Figure 7.19: Contour plot of the evolution of the mean (x-averaged) profile of velocity over 10^5 units of time, for (a) $(\alpha, \beta, B_0) = (0, 1, 7 \times 10^{-3})$, (b) $(\alpha, \beta, B_0) = (0, 1, 10^{-2})$, (c) $(\alpha, \beta, B_0) = (0, 1, 1.5 \times 10^{-2})$, (d) $(\alpha, \beta, B_0) = (0, 1, 2 \times 10^{-2})$, and all other parameters defined as in table 7.1.

to 1.5×10^{-2} and 2×10^{-2} in figures 7.19c and 7.19d respectively, the zonal features of the flow are broken down further to smaller time and length scales, making the vertical profile increasingly homogeneous.

Looking at the value of B_0 required to suppress jet-like motion, we find that at $B_0 = 10^{-2}$ there is arguably little to no zonal structure to the flow, whereas at $B_0 = 7 \times 10^{-3}$ (see figure 7.19a) there are clear, persistent vertical structures. It is difficult to give an exact value of B_0 at which jets no longer exist qualitatively, however $7 \times 10^{-3} < B_0 < 10^{-2}$ seems to be an acceptable range. Results found by Tobias et al. give this critical value to be $B_0 = 7.5 \times 10^{-3}$ [43]. This is particularly interesting due to the different parameter regimes used in each in-

vestigation; we have $(\beta, \nu, \eta, L) = (1, 10^{-3}, 10^{-3}, \frac{5}{2\pi})$, whereas Tobias et al. take $(\beta, \nu, \eta, L) = (5, 10^{-5}, 10^{-4}, \frac{15}{2\pi})$, leaving them in a far more turbulent regime (note that both simulations make use of a ring forcing; see section 4.7). The similarities in the resulting 'cut off' B_0 are surprising; even supposing ν and η have no effect on this value, we would expect β to. However, it is possible that a balancing of the parameters has occured (particularly β and L), leaving the relevant non-dimensional quantities at similar values. Indeed, Tobias et al. conjecture that, to leading order, the cut-off is controlled by the magnetic Reynolds number, R_m.

In order to distinguish between the previously explored cases in more detail, we plot short time velocity profiles for four values of B_0. In figure 7.20a we see the zonal jets typical of simulations with $B_0 \leq 10^{-3}$. As we look at the $B_0 = 10^{-2}$ case in more detail, figure 7.20b reveals that the weakly jet-like structures exhibited are sustained for $O(10^3)$ units of time; still many times larger than the forcing correlation time ($T_c = 1$). Whether or not we consider such flows to be true 'jets' is a matter previously discussed in chapter 5.

We can now distinguish between the $B_0 = 1.5 \times 10^{-2}$ and $B_0 = 2 \times 10^{-2}$ cases; the flows making up the former generally persist for longer times than the latter, and seem to be of a slightly larger vertical size. It seems that the decrease in time and length scales as our parameter is increased is something that both α and B_0 have in common. In contrast, while the length scale of the flow is decreased as β is increased (as per the Rhines scale), we find that the time scale over which the jets occur increases with the parameter.

Qualitatively, these results resemble those given by Tobias et. al [44], despite a difference in parameter values. Although our simulations deal with lower Reynolds number and generally larger scale flows (with more vortex-like motion as opposed to turbulence; see e.g. figure 7.22), the breaking up of the jets with B_0 is clear. Indeed, the breakdown of the mean flow to smaller scales and amplitudes as B_0 is increased is also apparent in both works.

Having discussed the general structure of the flow over the range $0 \leq B_0 \leq 0.02$, we now look at the how the flux changes over this parameter range with the

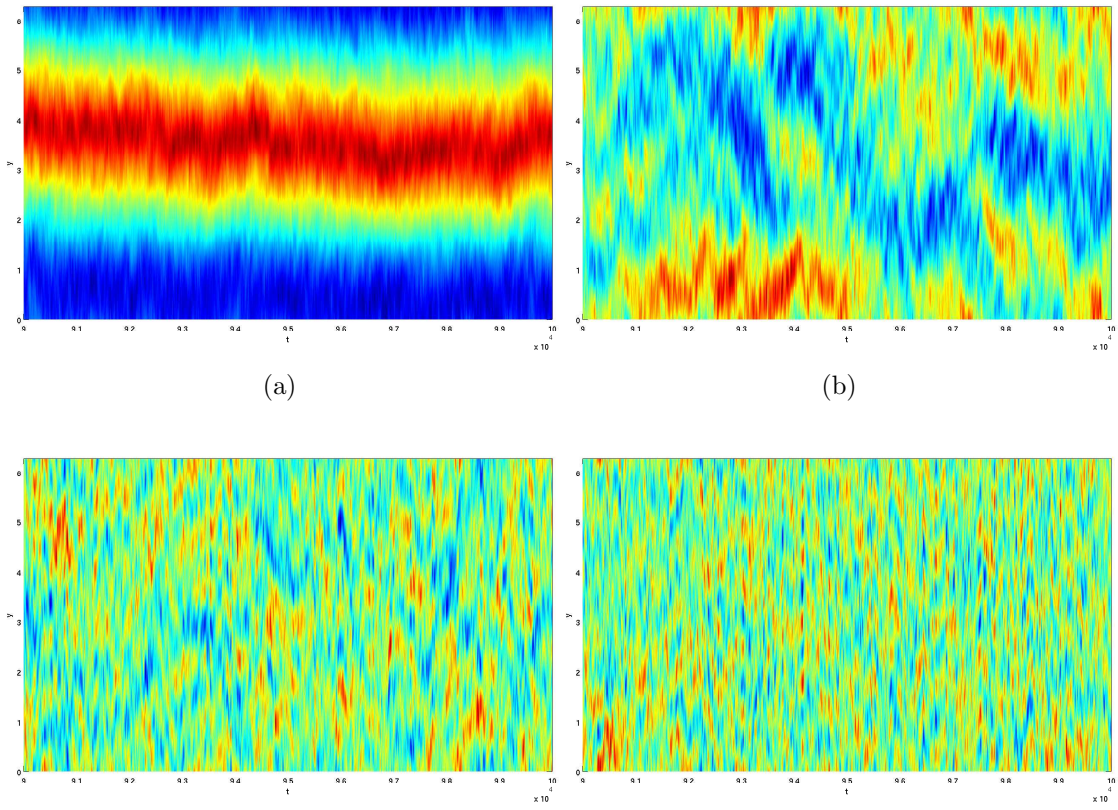

(a) (b)

(c) (d)

Figure 7.20: Contour plot of the evolution of the mean (x-averaged) profile of velocity over 10^4 units of time starting at 9×10^4, for (a) $(\alpha, \beta, B_0) = (0, 1, 10^{-3})$, (b) $(\alpha, \beta, B_0) = (0, 1, 10^{-2})$, (c) $(\alpha, \beta, B_0) = (0, 1, 1.5 \times 10^{-2})$, (d) $(\alpha, \beta, B_0) = (0, 1, 2 \times 10^{-2})$, and all other parameters defined as in table 7.1. Note that (a), (b), (c) and (d) are produced from the data used to make figures 7.18b, 7.19b, 7.19c, 7.19d respectively.

diagram given by figure 7.21. We observe that in the presence of a background vorticity gradient, $\beta = 1$, the flux diagram is a lot more complicated than both the $(\alpha, \beta) = (0, 0)$ and $(\alpha, \beta) = (0.1, 0)$ cases. At small values of B_0, the flux makes the usual transition from a relatively B_0 independent state to one where the parameter has an effect. Unlike the previous cases, the flux actually increases as the magnetic field grows; the field acts to destabilize the jet-like flow associated with the β-plane. Often, this type of behaviour is the result of some kind of resonance in the flow. It is not clear what causes the resonance takes place; certainly the vorticity gradient

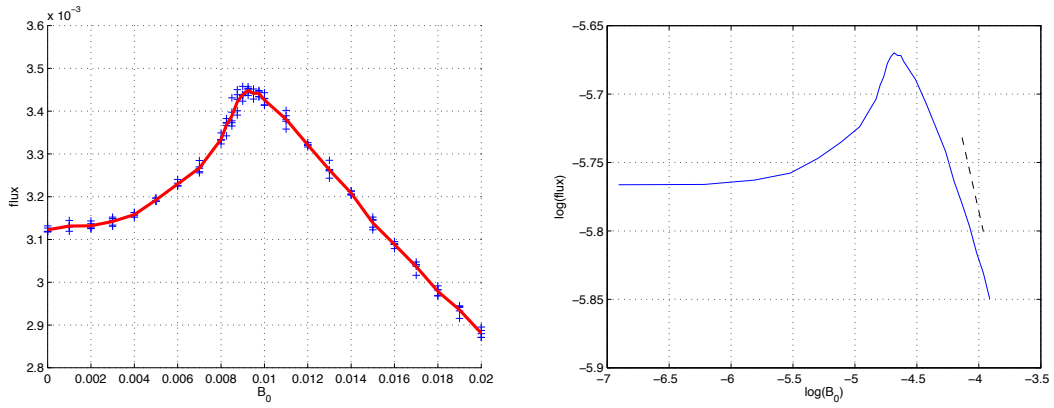

(a) (b)

Figure 7.21: Spatially and temporally averaged passive scalar flux plotted as a function of B_0 with $(\alpha, \beta) = (0, 1)$. Time-averaging is performed by taking the mean of the flux over the previous 50% of the simulation. This is averaged over a number of randomized simulations, each represented in (a) by a blue cross. The ensemble average is plotted in red in (a), while the log-log relationship of this line is given in (b), with $B_0^{-2/5}$ given by the dashed line. A denser selection of points is used for $8 \times 10^{-3} \leq B_0 \leq 10^{-2}$ in order to properly establish the relationship between B_0 and the flux.

and magnetic field are involved, but so might be the body force. It is also possible that, while two of these effects create an instability, the other acts to amplify it. It is difficult to pull apart the complicated interactions causing this result.

The dynamical behaviour reflecting this can be seen in the comparison of figures 7.20a and 7.20b; the pair of zonal jets occuring at $B_0 = 10^{-3}$ become distorted as B_0 is increased, allowing for more vertical transport across the flow. Note that $B_0 = 10^{-2}$ corresponds roughly to the peak of flux seen in figure 7.21a. The rise in flux over this range of B_0, doesn't seem to correspond to any single power law, as seen in 7.21b.

As we increase B_0 past 10^{-2}, the behaviour of the flow changes and the flux begins to drop. Despite the zonal flow continuing to break down, as shown in figures 7.20c and 7.20d, the flux now dissipates as the flow is stretched out and

regulated by the magnetic field. In figure 7.21a it appears that the flux decreases at a roughly constant rate; however inspection of 7.21b indicates that the relation between the flux and B_0 appears to be heading towards a power law as the strength of the magnetic field increases. At $B_0 = 2 \times 10^{-2}$, this power law is approximately $F \propto B_0^{-2/5}$. However, the power law exponent appears to still be decreasing with B_0 at this point.

Whether or not this power law exponent stabilizes to a single value is currently unknown to us. As the magnetic field is increased, the structures of the flow are stretched into finer, small-scale turbulent features, massively increasing the computational strain. For $B_0 > 0.02$, numerical grids consisting of at least 512^2 points are required for the simulation to be fully resolved; each individual run then requires enough computation time that obtaining an ensemble of accurate data is not achievable at the scale of our current investigation. As such, for now we can only speculate on the nature of the flow beyond this point in the parameter space.

The two likely options for the relationship between the flux and the magnetic field for large B_0 are that: for large enough B_0 the vorticity gradient becomes negligible and the power law eventually reaches the $F \propto B_0^{-1}$ law seen in figure 7.4, or that alternatively the vorticity gradient and magnetic field interact to modify the behaviour of the flow in such a way that the power law changes (with the possibility that no constant power law is ever reached). Of course, in either case it is also possible that further changes to the flux, such as regions of B_0 independence, may occur before a constant power law is attained.

When looking at the vorticity field at a single point in time for several values of B_0, we see that it is difficult to distinguish between cases with a mix of β and B_0, and the corresponding individual β and B_0 simulations. For example, figure 7.22a is comparable to those given in the purely hydrodynamical case; the weak magnetic field appears to stretch out the vortices horizontally, giving the flow an added degree of anisotropy without effecting the mean jet-like state. Meanwhile, figures 7.22c and 7.22d are similar to each other and figure 7.8c, the $(\alpha, \beta, B_0) = (0, 0, 10^{-2})$ case. The effect of β here seems to be relatively small in comparison to B_0, with

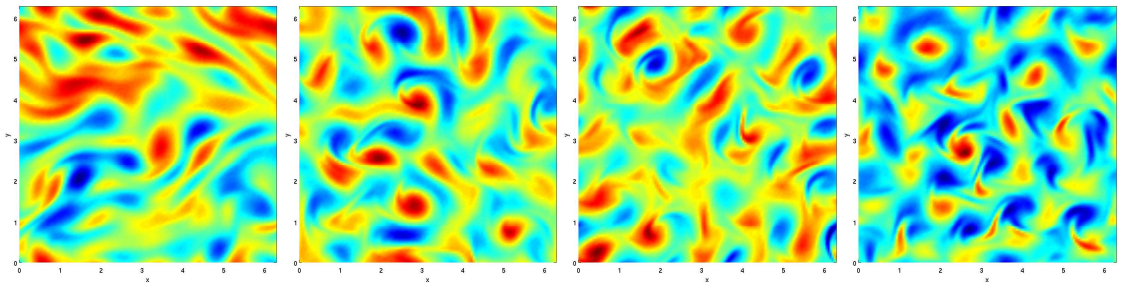

(a) (b) (c) (d)

Figure 7.22: Contour plot of the perturbations of the vorticity field at $t = 10^5$ for (a) $(\alpha, \beta, B_0) = (0, 1, 10^{-3})$, (b) $(\alpha, \beta, B_0) = (0, 1, 10^{-2})$, (c) $(\alpha, \beta, B_0) = (0, 1, 1.5 \times 10^{-2})$, (c) $(\alpha, \beta, B_0) = (0, 1, 2 \times 10^{-2})$, with all other parameters defined as in table 7.1. Note that (a), (b), (c) and (d) are produced from the data used to make figures 7.18b, 7.19b, 7.19c and 7.19d respectively.

the difference in length scale between the three figures coming solely from the difference in the strength of the magnetic field.

The main point to be made here is that snapshots of the vorticity profile at a single point in time do not give a huge amount of information about the statistics of the flow, particularly the more subtle interactions between parameters (despite often being solely relied on in the literature). We emphasize the importance of using data which conveys time-dependent information (such as the mean profile evolution contour plots given throughout this thesis) in order to determine the form of the flow.

Each plot given in figure 7.22 represents a different section of the flux diagram given in figure 7.21, with $B_0 = 10^{-2}$ corresponding roughly to the peak of flux, $B_0 = 2 \times 10^{-2}$ giving the least flux on our current range, and the remaining two figures representing points in the parameter space with comparable amounts of transport, yet very different behaviour. We take this into account as we look at the magnetic field for these simulations, as given in figure 7.23. As previously mentioned, we find that generally the magnetic field is not particularly similar to the vorticity field. This is in contrast to the evolution of the passive scalar field in the purely hydrodynamical simulations, where the vorticity and passive scalar

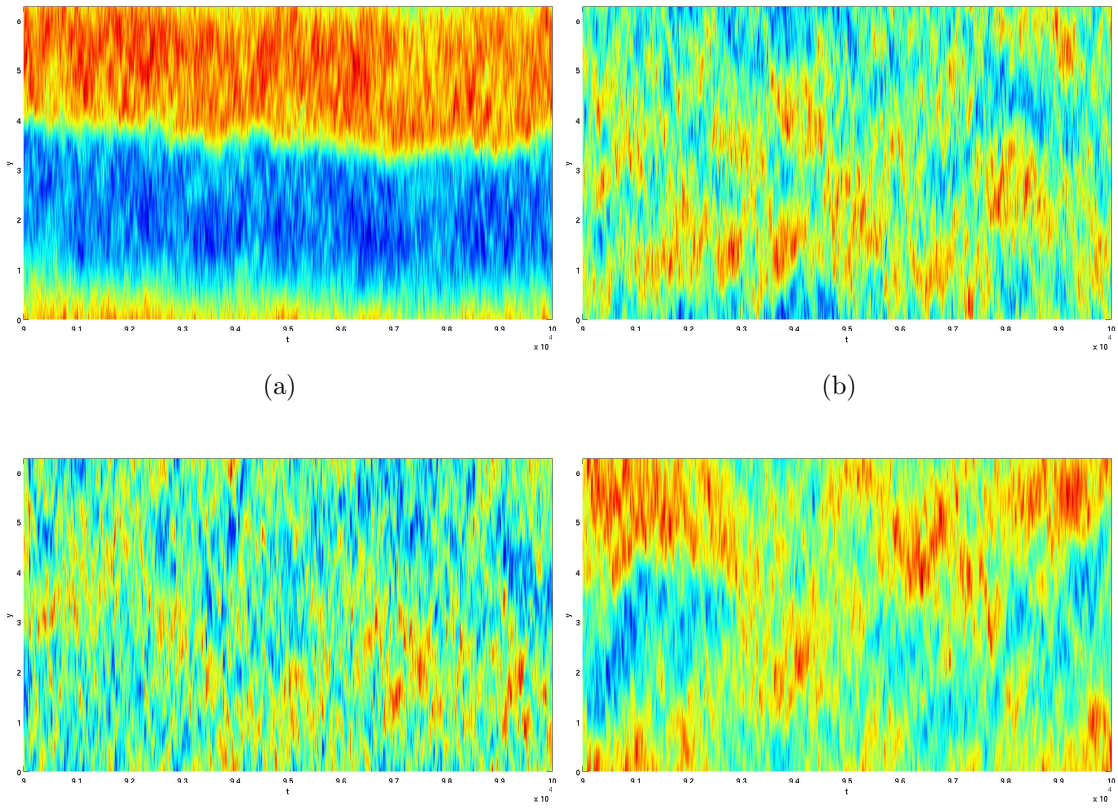

(a) (b)

(c) (d)

Figure 7.23: Contour plot of the evolution of the mean (x-averaged) profile of magnetic potential over 10^4 units of time starting at 9×10^4, for (a) $(\alpha, \beta, B_0) = (0, 1, 10^{-3})$, (b) $(\alpha, \beta, B_0) = (0, 1, 10^{-2})$, (c) $(\alpha, \beta, B_0) = (0, 1, 1.5 \times 10^{-2})$, (d) $(\alpha, \beta, B_0) = (0, 1, 2 \times 10^{-2})$, and all other parameters defined as in table 7.1. Note that (a), (b), (c) and (d) are produced from the data used to make figures 7.18b, 7.19b, 7.19c and 7.19d respectively.

correlated well. Comparing with figure 7.21, we see that for the smaller values of B_0 the two variables can be related, with strong regions of vorticity corresponding to weak regions of A. This certainly seems to hold for $B_0 \leq 10^{-2}$, with the relationship becoming less well defined for figures 7.20c and 7.23c. However, as we increase B_0 to 2×10^{-2}, we see that the relationship is lost, with the vorticity taking on a very short (time and length) scale structure, while the A-field actually tends towards a weakly zonal profile.

This can be seen in the individual time plots of the magnetic potential, given

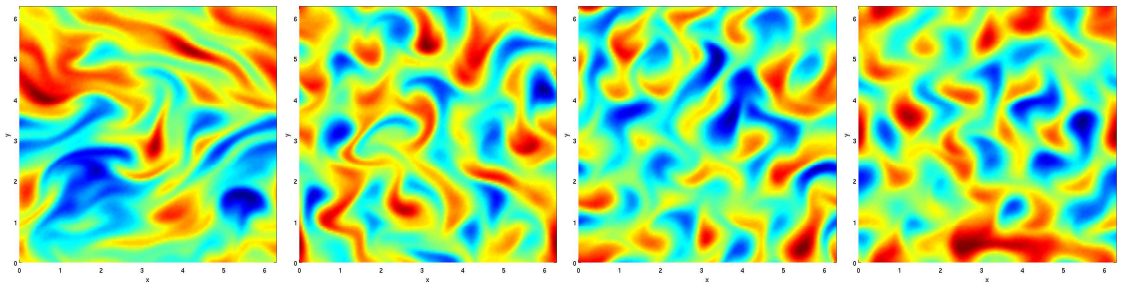

(a) (b) (c) (d)

Figure 7.24: Contour plot of the perturbations of the magnetic potential field at $t = 10^5$ for (a) $(\alpha, \beta, B_0) = (0, 1, 10^{-3})$, (b) $(\alpha, \beta, B_0) = (0, 1, 10^{-2})$, (c) $(\alpha, \beta, B_0) = (0, 1, 1.5 \times 10^{-2})$, (d) $(\alpha, \beta, B_0) = (0, 1, 2 \times 10^{-2})$, with all other parameters defined as in table 7.1. Note that (a), (b), (c) and (d) are produced from the data used to make figures 7.18b, 7.19b, 7.19c and 7.19d respectively.

in figure 7.24. Each plot seems similar to its vorticity counterpart (given in figure 7.22), although the magnetic field lacks the stretched and twisted elements which characterize the vorticity field for strong B_0. However, for $B_0 = 2 \times 10^{-2}$, the two variables become distinct, with the magnetic field reverting to a form closer to that of the small B_0 case given in 7.22a.

This is particularly interesting when taking into consideration the passive scalar flux diagram in figure 7.21. As previously discussed, the passive scalar and magnetic field differ only by scale in our current simulations, due to our choice of diffusive parameters. As such, our measurement of the flux of passive scalar is proportional the magnetic potential flux. Of the three previously discussed figures, 7.22 – 7.24, parts (a) correspond to the constant level of flux apparent in a standard β-plane system. The peak of the flux is reached in (b), and then an equal level to that of (a) is found in (c). Finally, (d) corresponds to a region of continually decreasing flux. It is interesting that in this region of decreasing flux, the behaviour that the flux corresponds to appears to be the formation of zonal structures. Again, whether or not this behaviour continues is unknown to us due to the limit of our computations. However, we might speculate that zonal jets of a different type are becoming the new barriers to transport in this MHD system.

During this section, we have explored interesting phenomena that occur when applying a magnetic field to a β-plane system. We have seen how the field disrupts the β-plane jets as B_0 is increased, and how the effective transport mechanism bought in by these flows is disrupted by small values of B_0. The flux decreases once it passes a peak (which may correspond to resonance-like behaviour), possibly going on to form a power law scaling. Over this parameter range, the flow moves to increasingly small scales, while the magnetic potential undergoes an interesting change of behaviour; from a strong jet-like state, to close to homogenous behaviour, then back to a weakened zonal structure. Due to the relationship between the passive scalar flux and the magnetic flux (see equation (7.1)), the flux diagram seems to aptly describe the behaviour of the magnetic field. We are unable to answer intruiging questions regarding the nature of the flow as B_0 is increased further (such as whether the zonal state of A persists, and what power law relating F to B_0 is reached), due to the intensive requirements of running the large B_0 simulations.

7.5 Conclusion

In this chapter we have discussed the following results:

- We found that for two-dimensional MHD turbulence, the vertical transport of a passive scalar carried by the flow is supressed at a rate $F \propto B_0^{-1}$. For small values of B_0 the time it takes for the flux to stabilize dramatically increases (similarly to α and β in chapter 5).

- For our parameter choice, the flux of the passive scalar field is proportional to the flux of the magnetic field, and so the power law given above tells us that the magnetic flux scales with B_0^0. Generally, the mean profile of the field is observed to exhibit larger scale motion than the vorticity, indicating that it may have a relatively small effect on the flow.

- When introducing a sheared flow, B_0 suppresses vertical transport further, reaching the $F \propto B_0^{-1}$ power law seen in the non-sheared case.

- For large values of B_0 the flow actually begins to exhibit zonal behaviour, comparable (although not as steady) as that seen for β-plane jets. The magnetic field and flow begin to take on a similar form in this case, indicating that the shear helps reinforce the effect of the field on the flow (through the Lorentz force). Unfortunately, the simulations become hard to resolve when this behaviour starts to occur.

- Introducing a magnetic field to a β-plane flow has the initial effect of increasing transport, possibly by some resonance between the two phenomena. This comes about from the breaking up of the zonal jets which normally maintain the flux in the HD case. To our knowledge, this has yet to be observed elsewhere in the literature, and may have implications for research on rotating two-dimensional MHD phenomena.

- As B_0 is increased further, the flux begins to decrease again. We measure a $F \propto B_0^{-2/5}$ trend, however the exponent appears to still be decreasing at the largest values of B_0 we are able to simulate.

- Although the flow becomes increasingly turbulent as B_0 is increased, the magnetic field goes through stages of initially breaking up (when the flux is at its peak), then beginning to form weakly zonal regions at higher values of $B_0 \approx 0.02$. We reach our computational limit at this point in the parameters, and so are unable to thoroughly investigate these phenomena.

We now proceed to the final chapter of this report, we we present a summary of our findings, and attempt to correlate some of these results.

Chapter 8

Concluding Remarks

In this thesis we have found a variety of results from both analytical and computational methods. In this final chapter, we discuss and compare these results, providing implications for current research on geophysical and astrophysical phenomena. For clarity we split this discussion into two sections; purely hydrodynamical (HD) results and magnetohydrodynamical (MHD) results. Following this, we elaborate on future research directions it may be interesting to pursue following from the material covered in this thesis.

8.1 Hydrodynamics

We have looked at various features of hydrodynamical flows throughout this work. In particular, we have focused on the effects of mean flows and vorticity gradients, with an emphasis on transport and fluxes as diagnostic tools. In chapter 2 we gave the vorticity flux, F, of a flow in terms of the vorticity (or stream function) and the background mean flow, $U(y)$ (see equation (2.35)), which plays a key part in the evolution of the mean flow. We used this result when looking at several different approximations to the quasi-linear equations, (2.31 – 2.33).

For a large-scale expansion (corresponding to the effect of launching small length scale waves on a large-scale background flow), we found that regions in the flow where $U' = 0$ tend to correspond to strong spikes of flux. Given the form of the mean flow, this implies that the feedback from the waves onto the mean causes it to self-maintain, or possibly self-narrow, strengthening the original zonal flow. Similar results were found for a short-time expansion, where for waves smaller than the mean flow the flux has a leading order anti-diffusive effect, reinforcing the initial mean profile. These results both indicate that mean flows will, in general, resist changes to flow structure, and possibly even be strengthened when perturbed at small scales.

Returning again to the large-scale expansion, we found that frictional forces such as bottom drag, λ, and viscosity, ν, cut off the effect of the small-scale waves before they can produce a diffusive feedback, i.e. allowing only the initial anti-diffusive behaviour. The interesting and somewhat counter-intuitive result of this

is that diffusive parameters can potentially encourage the persistence of zonal flows, by reinforcing the original structure of the mean profile of the flow. However, this may have important consequences on the use of unphysical diffusive effects in the literature; techniques such as the implementation of hyper-viscosity may modify this feedback, possibly altering the statistics of the jets observed in these flows. More research would be required to fully investigate this issue.

Finding the effect of the vorticity gradient on the mean flow evolution has proven more difficult; the coefficient of the vorticity gradient, β, does not appear in the leading order expansions of the large-scale or short-time fluxes. For the former, the effect comes in at second order and appears to cause small-scale oscillations in the flux, with a sharper central jet possibly indicating further self-narrowing of the mean flow. However, we found that at long times the behaviour at these points (where $U' = 0$) became complicated, requiring further investigation. Reducing the expansion at these points to a single-parameter linear PDE, we found numerical solutions dependent on β, which produced an oscillatory feedback on the flow. Note also that the sign of β was important here; the parameter does not act symmetrically on maxima/minima in the mean flow profile. For the short time expansion, we found that at second order the β-effect leads to symmetries in the flow being broken, which allows for anisotropic behaviour, with strong jets in one direction, and weak jets elsewhere.

In chapters 4 and 5 we formulated numerical methods with which to solve the nonlinear governing equations for a flow on a β-plane under the influence of linear shear. We made use of a shearing box coordinate system, and put considerable effort into determining the best choice of body force for a sheared system, ultimately implementing a ring forcing which followed the shear flow. As in chapter 2, we found that the vorticity flux for a linear shear flow averaged to zero, and so we looked instead at the flux of a passive scalar field as our transport diagnostic. In the literature, many attempts have been made to simulate large, computationally demanding flows (albeit at parameter values far removed from their physical counterparts). We opted instead to investigate a large number of relatively small scale

simulations in order to establish reliable statistical results across a wide range of parameter values. Despite this, many regions of our parameter space required long integration times to produce fully developed statistical averages, and as such we also performed a large number of long-time calculations.

As we have avoided using a very small value for the viscosity, the flows that we have explored are more vortex-dominated than the typically turbulent regimes seen elsewhere in the literature. Nonetheless our simulations contain much the same phenomena, in particular zonal jet-like structures. This can be linked with our quasi-linear results, which as discussed previously, showed that viscosity can actually promote anti-diffusive behaviour and reinforce zonal flows. That isn't to say that increasing ν will cause stronger jets; rather that decreasing ν may have less of a jet-enabling effect.

For moderate values of β, we have established that there is an approximate $F \propto \beta^{-5/4}$ power law; a result we have yet to encounter elsewhere in the literature. For weaker vorticity gradients, the total time scales of the flow increase, such that it becomes difficult to accurately measure a stable value of the flux. We speculate that, due to the random nature of the body force, G, the averaging time required for the flux to reach a constant value (with a set degree of accuracy) will peak at $\beta = 0$, as opposed to a constant non-zero value of β. This is due to the fact that the variance of values of F increases as $\beta \to 0$ (and also decreases over time). Such a result would indicate that β is never negligible in comparison to G, rather that the time scales over which the effect of the vorticity gradient can be observed dramatically increase as β is decreased. However, further research would be required to confirm this hypothesis, with an emphasis on the probability distribution of the flux over β.

When investigating sheared turbulence (by use of the shearing box coordinate system; see chapter 4), we found a generally simpler effect on the flow. The shear, the strength of which is represented by α, tips over and shears out the vortices created by the body force, with an overall suppresion rate of approximately $F \propto \alpha^{-5/3}$, another result we have yet to see in the literature. Occasionally the mean

flow appears to take a jet-like structure, however this is due to the shearing out of vortices into horizontal structures. These 'shear-jets' are characteristically different to β-plane jets in terms of their relatively short time scales and tendency to have the fastest part of the jet at the top rather than the centre of each individual structure.

When adding a shear flow to a β-plane system, we observe a disruption to the formation and persistence of zonal jets. For a strong shear, the $F \propto \alpha^{-5/3}$ scaling is regained as β has negligible effect. However, for smaller values of α, more complicated behaviour occurs. For very small values of α, the shear actually increases transport in the jet-regulated flow, by the above mentioned disruption mechanism. As the shear is increased, the flux is generally reduced, however for certain regions of α, the flux goes unchanged across a short range of the parameter. We have found these 'flux plateaus' difficult to explain, in part due to the small (yet relevant) range of α over which they exist, and the complicated interactions taking place between the vorticity gradient, shear flow and body force; the latter may play an important part in the occurence of these phenomena.

We emphasize the importance of establishing strong statistical results which relate to the physical phenomena being researched. Likewise, exploring the fundamental mechanisms which drive zonal flows is ongoing investigation, on which our quasi-linear analysis has given added perspective. In particular, the quasi-linear results should correlate to very high Reynolds number systems, where eddy-eddy interactions provide little impact on the flow. Note that to our knowledge, there has been no previous investigations into the effect of shear on β-plane flows.

8.2 Magnetohydrodynamics

Throughout this thesis we have researched the MHD system with similar goals to the original hydrodynamical investigation; to explore the modification of transport in two-dimensional flows. In chapter 3, we made the MHD extension to the research presented in chapter 2. Rather than having a single flux govern the feedback on the mean flow, we found that the Lorentz force also contributed to this feedback, while

an additional magnetic flux, F_M, determined the feedback on the mean magnetic field (see equations (3.51) and (3.48)).

Like the HD case, we found that a linear shear flow will produce zero kinetic flux, and also no Lorentz force feedback. However, the magnetic flux will generally be non-zero, and its components are each governed by a second order ODE. At the leading order of the large-scale expansion of the quasi-linear equations the same ODE is obtained (in the absence of additional parameters, e.g. ν, etc). Solutions to this ODE (required to give a meaningful form of the flux) can only be obtained numerically; we have refrained from exploring this in our current work.

Instead, we have investigated the short-time expansion of the MHD quasi-linear equations. We found that the magnetic field has no influence on the mean flow feedback at leading order, but at second order will bring about an anti-diffusive effect. For small-scale waves on a large background flow, this will reinforce the leading order anti-diffusion, potentially promoting zonal flows. This is in contrast to nonlinear MHD simulations, which (including our own) show that the field suppresses zonal flows. However, we note that the effects of each feedback becomes harder to determine in the MHD case; the feedback produced by F_M will influence F, which in turn will have an effect on F_M. As such, either flux could ultimately be the cause of jet-suppresion by the magnetic field.

While B_0 has no leading order effect on the magnetic flux, at lower orders it produces fluctuations in the mean field at smaller length scales than that of the mean flow. For the reasons given above, we hypothesize that this is the mechanism by which zonal flows are dissipated by the magnetic field; the resultant small-scale $B(y)$ produces more complicated small-scale behaviour in F. However, we again emphasize the difficulty in confirming results in this complicated analytical system.

The effect of β on the mean flow remains the same as in the HD case. For the magnetic field, it introduces terms which, in combination with B_0, make it possible for strong jet-like behaviour to occur. This possibly relates to the weakly jet-like behaviour observed for large B_0 on the MHD β-plane discussed in section 7.4, however any link here is tentative.

In chapters 6 and 7, we investigated the nonlinear MHD equations with the effect of a vorticity gradient and linear shear flow. When averaged over a periodic domain we find that the vorticity flux again results in zero, as do the contributions to the feedback via the Lorentz force. The magnetic flux, however, does have a non-zero value; for our choice of parameters, it will be exactly B_0 multiplied by the passive scalar flux, F.

We found that MHD turbulence suppresses the passive scalar flux with a rate of approximately $F \propto B_0^{-1}$. Generally, the field stretches out and destroys vortex motion. Also, we made observations that the scale of the mean flow and mean field tend to be different. When introducing B_0 to a sheared flow, we found that the $F \propto B_0^{-1}$ scaling was regained for large values of B_0. We also saw that at these values, the flow appeared to organise into zonal structures. This was the result of the combined 'stretch and shear' effect of B_0 and α on the vortices created by the body force. These flows persisted for relatively long time scales (despite no anchor to a particular position in y), and could be directly related to the mean magnetic field, suggesting that the field plays a larger role in the evolution of these sheared MHD systems.

While investigating the MHD β-plane system, we found that for moderate values of B_0, the transport in the flow increases before being suppressed by the magnetic field. This behaviour, depicted in figure 7.21, appears resonance-like, and is caused by the field disrupting jet-like flow before becoming the dominating effect in the system. We note that a similar effect occurs for the shear in the HD case (see section 5.5). As B_0 is increased, an $F \propto B_0^{-2/5}$ power law is observed, although it appears that the exponent of this is still decreasing when we reach our computational limit. Although the mean flow becomes increasingly turbulent for large B_0, the magnetic field goes from a zonal state (at $B_0 = 0$), to a turbulent one (coinciding with the peak of flux), then back to a weakly zonal state. This behaviour could possibly be explained by our quasi-linear analysis, where we found that β and B_0 can interact to potentially break the symmetry of the mean field (see equation (3.126) and figure 3.5). This is similar to the way β interacts with the mean flow to break the flows

own symmetry in the HD case; however further research would be required to test this simplified explanation.

Although MHD turbulence has been investigated in the literature in some detail, there has been little work presented on sheared two-dimensional MHD turbulence, to which our research offers important observations of transport. The MHD β-plane has been subject to very little prior exploration, and our observation of the peak in flux at non-zero B_0 provides an important result. To our knowledge, this is the first time such an effect has been observed, and it may have important results for MHD β-plane studies, such as those focusing on the solar tachocline.

8.3 Future Research

Following from the methods and results presented in this thesis, there are numerous investigations that can be explored in more detail. In this section we discuss the possible research that might follow on from our work.

- We found in sections 2.3 and 4.3 that a linear shear has no effect on the vorticity flux of a system. As such, our quasi-linear approximation focused on the feedbacks produced by taking perturbations to mean flows dependent on y. These results could be expanded on in more detail by simulating the nonlinear two-dimensional flows subject to a mean background flow, e.g. $U(y) = -\cos(y)$, while varying the relevant parameters. The shearing box coordinate system could not be implemented for these flows, meaning more computational power might be needed. Also, the quasi-linear results are most relevant in high Reynolds number flows, which again will require a larger scale numerical investigation.

- In chapter 2 we found that frictional forces have an important effect on cutting off diffusive feedbacks from a mean flow onto itself. This may have consequences for the use of unphysical damping methods, such as hyperviscosity. Further investigation into this using the quasi-linear framework may prove insightful.

- Equation (2.21) describes the effect the integrated flux has on the evolution of the mean profile in the quasi-linear system. It would be interesting to introduce this feedback into the governing system of equations (with a now time dependent $U(y,t)$). However, we note that this may prove difficult due to the anti-diffusion present in the system, which may lead to instabilities in the results (possibly including the zonostrophic instability). Also, only the large-scale expansion would be useful here, as integrating over the short-time approximation would likely lead to spurious results. Regardless, exploring the continual evolution of the mean flow in more detail would provide interesting research.

- In section 2.5 we looked at the effect of a turning point in the mean flow, finding that the behaviour here is determined by a single parameter PDE, (2.93). Although we have looked briefly at numerical solutions to this equation, more work is required to fully investigate the effect the vorticity gradient has at these points. In particular, it may be possible to give analytical solutions to this equation (although difficult due to its complexity). Note that we have been unable to find references to this equation elsewhere in the literature.

- It is possible to use the quasi-linear framework to investigate the flux of a passive scalar field carried by the flow, which may provide results comparable to those seen in our numerical simulations. Unlike the vorticity flux, the passive scalar flux will not relate directly to the feedback on the mean flow (although it can be related to the effective diffusivity [25]), and will generally be non-zero for a linear shear flow. However, as the system of governing equations will be expanded (to include the passive scalar equation), results for general mean flow profiles will likely be more complicated.

- In our direct numerical simulations, we found that when α and β appear together, there are regions in the flux diagram where the general power law trend was broken, and the flux was not suppressed across a small range of α. Complicated dynamics occured at these points, with the resultant 'flux

plateaus' possibly occuring due to interactions with the body force. More work on this system would be needed to explain these phenomena.

Each of the above points can be investigated (where relevant) with regard to the MHD extension. In addition, there are several areas of future research which apply only to the MHD case:

- In chapter 3 we found that, while the mean flow feedback is zero for a linear shear (like the HD case), the magnetic flux is not necessarily zero. Here, the vorticity and magnetic field can each be calculated from a single second order ODE (see equations (3.61 – 3.62)), which also corresponds to the leading order result of the large-scale expansion. We found that these ODEs could not be written in terms of standard functions, and so giving a meaningful analytical solution to the flux is impossible. However, these equations can be solved numerically; the results of which could be used to evolve the mean field (see the first point in this section).

- The interesting interactions between β and B_0 lead to an initial increase in transport with B_0 (see section 7.4), which requires further exploration. In particular, the system may be sensitive to changes in the viscosity and magnetic diffusivity, and may have applications to the rotating plasmas observed in astrophysical flows.

- The behaviour at large B_0 becomes increasingly hard to simulate due to the fast turbulent motions taking place in the flow. In particular, we have been unable to establish the large B_0 statistics of the flow for the $\alpha \neq 0$ and $\beta \neq 0$ cases. For the latter, we have also observed interesting zonal effects in the magnetic field; more powerful simulations of these flows would allow us to investigate this in more detail. Likewise, for the sheared MHD case, interesting zonal features begin to occur at larger values of B_0, which may or may not persist as the field is increasingly strengthened.

Appendix A

A.1 Proof of zero vorticity flux for sheared systems

In chapter 4, we implement the shearing box coordinate system via the use of the Fourier transform defined by

$$h(x,y,t) = \sum_{m,n} \hat{h}_{m,n}(t) e^{imx+i(n-\alpha mt)y}. \tag{A.1}$$

We take the Laplacian of $h(x,y,t)$ to be

$$\nabla^2 h = \frac{\partial^2 h}{\partial x^2} + \frac{\partial^2 h}{\partial y^2}. \tag{A.2}$$

Defining $< \cdot >_{x,y}$ to be the spatial average of its components (across x and y) we have the following relationship:

$$\begin{aligned}
\left\langle (\pm\nabla^2 h)\partial_x h \right\rangle_{x,y} &= \left\langle \left(\sum_{m,n} \pm\hat{\nabla}^2 h e^{imx+i(n-\alpha mt)y} \right) \left(\sum_{m,n} (\hat{\partial_x} h) e^{imx+i(n-\alpha mt)y} \right) \right\rangle \\
&= \left\langle \left(\sum_{m,n} \mp(m^2 + (n-\alpha mt)^2) \hat{h} e^{imx+i(n-\alpha mt)y} \right) \right. \\
&\quad \left. \times \left(\sum_{m,n} im\hat{h} e^{imx+i(n-\alpha mt)y} \right) \right\rangle \\
&= \sum_{m,n} \left[\mp(m^2 + (n-\alpha mt)^2) \hat{h} (im\hat{h})^\star + \text{c.c.} \right] \\
&= \sum_{m,n} \left[\pm im(m^2 + (n-\alpha mt)^2) |\hat{h}|^2 \mp im(m^2 + (n-\alpha mt)^2) |\hat{h}|^2 \right],
\end{aligned} \tag{A.3}$$

where c.c. refers to the complex conjugate of the previous terms. The result is then

$$\left\langle (\pm\nabla^2 h)\partial_x h \right\rangle_{x,y} = 0. \tag{A.4}$$

Note that when $h = \omega$, the fluid vorticity, this corresponds to the vorticity flux.

A.2 Testing the shearing box coordinate system

To find out if the shearing box method given in chapter 4 is accurate, efficient and correctly implemented, we test it by using a single harmonic mode as the initial

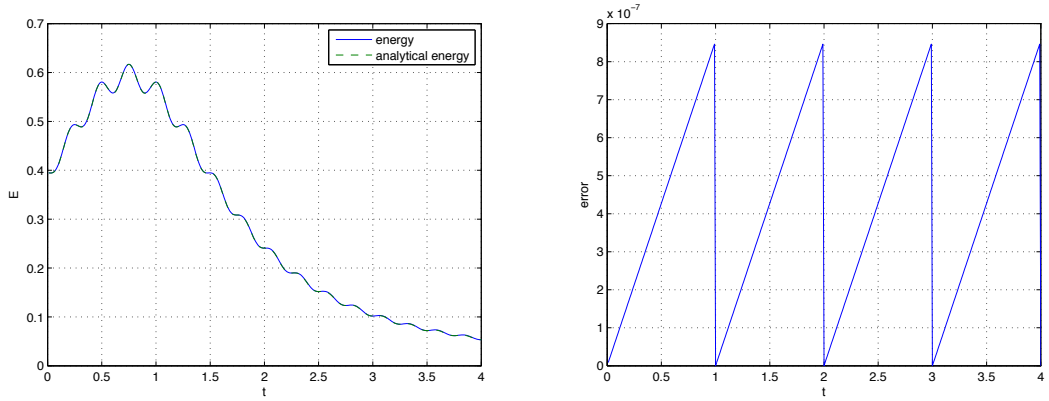

(a) (b)

Figure A.1: Graphs describing the evolution of a single sheared mode using the shearing box coordinate system. Specifically, (a) gives the kinetic energy of the mode as compared to its analytical solution (see equation (A.7)), while (b) gives the normalized 2-norm relative error of the vorticity field, as described in equation (A.8).

value of the vorticity, ω:

$$\begin{aligned}\omega(x,y,t=0) &= \cos(Ax+By),\\ \psi(x,y,t=0) &= -\frac{1}{A^2+B^2}\cos(Ax+By),\end{aligned} \tag{A.5}$$

in absence of any body forces. The nonlinear Jacobian is then analytically identical to zero, making it easy to compare with our numerical results. The exact solution to equation (4.42), with the initial results given by (A.5) is

$$\omega_\star(x,y,t) = \frac{1}{2}\exp\left\{\int S_{A,B}(t)dt\right\}\exp\{iA(x-\alpha ty)+iBy\} + \text{c.c.}, \tag{A.6}$$

where $\int S_{A,B}(t)dt$ is given by equation (4.65) evaluated at $(m,n) = (A,B)$, and c.c. denotes the complex conjugate of the preceding terms. In general, we use the lower case star to describe analytical results.

We use this to evaluate the effectiveness of our 'un-shearing' methods. We use the kinetic energy, defined as

$$E(t) = \frac{1}{2}\int\int_{x,y} |\mathbf{u}(t)|^2 dxdy, \tag{A.7}$$

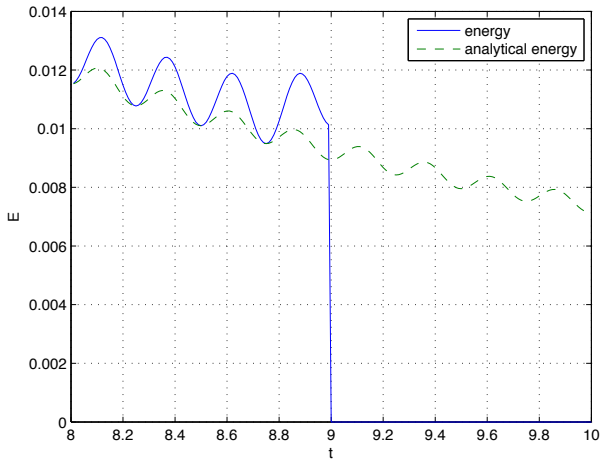

Figure A.2: Kinetic energy of a single mode as it is 'sheared off the grid' of Fourier space by the mode resetting mechanism used in implementing a shearing box coordinate system. Note that this is a continuation of figure A.1a.

and use $E_\star$ to refer to the analytical kinetic energy. We also use the relative 2-norm error in the computed vorticity:

$$e(t) = \sqrt{\frac{|\omega_\star(t)^2 - \omega(t)^2|}{\omega_\star(t)^2}}. \tag{A.8}$$

While the kinetic energy is calculated as an integral of the velocity field, we take the sum of each point on a computational grid when calculating the error, normalizing by the number of grid points in order to maintain our results across various grid sizes.

In the absence of viscosity and the β-effect, we have the solution

$$\omega_\star(x, y, t) = \cos\left(A(x - \alpha t y) + By\right). \tag{A.9}$$

Taking $\alpha = 1$ gives us a shear turnover time $T_\alpha = 1/\alpha = 1$. As such, the grids of the shearing box will align with a standard Cartesian system whenever $t = T_\alpha k = k, k \in \mathbb{N}$. We assign $(A, B) = (4, 3)$; this choice, although arbitrary, coincides with the typical length scales implemented in our body force, as discussed later in this chapter.

In figure A.1 we can see the accuracy of the shearing box for simulating the above mode for the first few turnover times. In figure A.1a the difference between

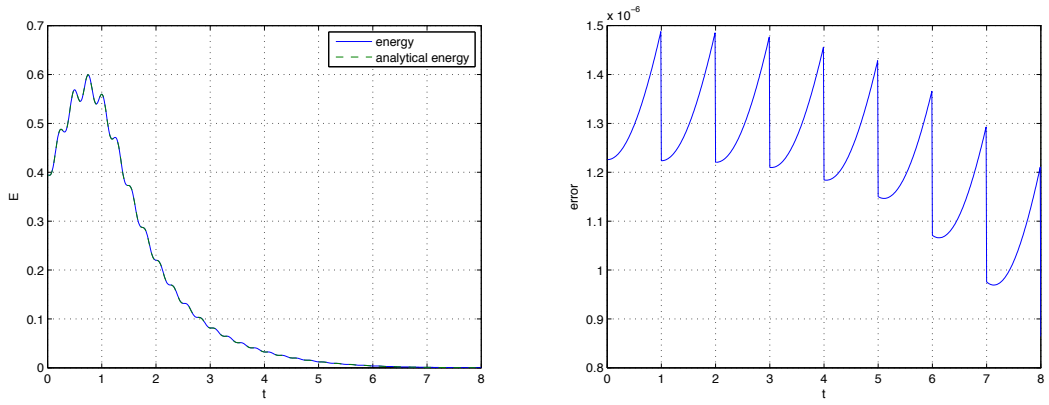

(a) (b)

Figure A.3: Graphs describing the evolution of a single sheared mode under the influence of viscosity, using the shearing box coordinate system. Specifically, (a) gives the kinetic energy of the mode as compared to its analytical solution (see equation (A.7)), while (b) gives the normalized 2-norm relative error of the vorticity field, as described in equation (A.8).

the numerical and analytical kinetic energies is not readable due to its small magnitude. Indeed, figure A.1b illuminates this, showing that even at its largest value, the difference in vorticity fields is $\sim 10^{-6}$ times smaller than the magnitude of the analytical voricity.

Interestingly, this relative error seems to display linear growth during each shear turnover time, with the mode reset acting to also bring the computational vorticity back in line with the actual solution. Despite the energy of the field dissipating as the mode is sheared out, this trend seems to be relatively stable.

Each time the modes are reset, our sheared mode is dragged down the grid to where it should exist in standard Fourier space. This corresponds to the $n - \alpha mt$ term in our sheared wavenumbers, meaning that at each shearing turnover time, the position of the mode will be

$$(m, n) = (A, B - \alpha A). \tag{A.10}$$

So, for our initial mode $(A, B) = (4, 3)$, after the first reset (with $\alpha = 1$), the mode will have position $(4, -1)$. Depending on the size of our numerical grid, the mode

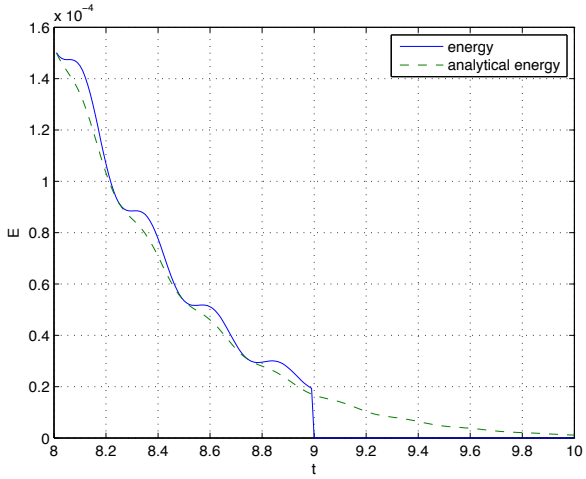

Figure A.4: Kinetic energy of a single mode under the effect of viscosity as it is 'sheared off the grid' of Fourier space by the mode resetting mechanism used in implementing a shearing box coordinate system. Note that this is a continuation of figure A.3a.

will eventually reach a point where it can no longer be stored computationally, and as per figure 4.2, will be discarded. For the 64^2 grid points used for our current example, this will happen after 9 shear turnover times. This can be seen in figure A.2, where the computational energy drops to zero after the final mode reset discards the sheared mode.

Of course, a general assumption of working with Fourier space is that energy in the smallest-scale motions needs to dissipate in order to keep the system from becoming computationally unstable. To an extent, this is facilitated by the shear; as can be seen by comparing figures A.1a and A.2, the energy of the vorticity field has dropped extensively (even before the mode reset) due to the shearing out of velocity. This shear-diffuse mechanism comes about by the α terms in equations (4.65) and (4.68), and strongly suppresses the flow for $\alpha > 0$. However, more generally the dissipation comes about due to fluid viscosity.

Considering the same initial mode, $(A, B) = (4, 3)$, with $\alpha = 1$ and now under the effect of viscosity, $\nu = 10^{-3}$ (again, a typical value used in this thesis, as will be seen later in this chapter), we plot the kinetic energy and error in figure A.3.

We have shown more shear turnover times in order to display the rate at which viscosity dissipates the energy, noting that the difference in energies are again very small. The relative error no longer grows linearly during the turnover time, with the computational result also not matching the analytical result perfectly at mode resetting times. The error is also marginally larger at its greatest magnitude, although still of the order 10^{-6}.

Key to our consideration is the magnitude of the mode when it is discarded by the mode resetting system. In figure A.4 we plot the kinetic energy at later times. As can be seen, by the time the mode is lost its energy is already approximately 10^{-4} times smaller than it originally was, and is significantly smaller than the energy of new modes being introduced by the body force in the full system.

Bibliography

[1] D. J. Acheson. *Elementary Fluid Dynamics*. Oxford University Press, 1990.

[2] S. A. Balbus and J. F. Hawley. Instability, turbulence, and enhanced transport in accretion disks. *Rev. Mod. Phys.*, 70, 1998.

[3] S. A. Balbus and P. Henri. On the magnetic prandtl number behaviour of accretion disks. *Atrophys. J.*, 674, 2008.

[4] G. K. Batchelor. *An introduction to fluid dynamics*. Cambridge University Press, 2000.

[5] G. Bodo, F. Cattaneo, A. Ferrari, A. Mignone, and P. Rossi. Symmetries, scaling laws, and convergence in shearing-box simulations of magneto-rotational instability driven turbulence. *Astrophys. J.*, 739, 2011.

[6] K. A. Brucker, J. C. Isaza, T. Vaithianathan, and L. R. Collins. Efficient algorithm for simulating homogeneous turbulent shear flow without remeshing. *J. Comp. Phys.*, 225, 2007.

[7] E. Buckingham. On physically similar systems; illustrations of the use of dimensional equations. *Phys. Rev.*, 4, 1914.

[8] F. Cattaneo. On the effects of a weak magnetized field on turbulent transport. *Astrophys. J.*, 376, 1991.

[9] F. Cattaneo and S. I. Vainshtein. Suppresion of turbulent transport by a weak magnetic field. *Astrophys. J.*, 376, 1991.

[10] D. Chung and G. Matheou. Direct numerical simulation of stationary homogeneous stratified sheared turbulence. *J. Fluid Mech.*, 696, 2012.

[11] N. C. Constantinou, B. F. Farrell, and P. J. Ioannou. Emergence and equilibration of jets in beta-plane turbulence: applications of stochastic structural stability theory. *J. Atmos. Sci.*, 71, 2014.

[12] B. Cushmam-Roisin and J. Beckers. *Introduction to Geophysical Fluid Dynamics: Physical and Numerical Aspects*. Academic Press, 2nd edition, 2011.

[13] S. D. Danilov and D. Gurarie. Quasi-two-dimensional turbulence. *Usp. Fiz. Nauk.*, 170, 2000.

[14] D. del Castillo-Negrete. Chaotic transport in zonal flows in analogous geophysical and plasma systems. *Phys. Plasmas*, 7, 2000.

[15] D. G. Dritschel and M. E. McIntyre. Multiple jets as pv staircases: The philips effect and the resilience of eddy-transport barriers. *J. Atmos. Sci.*, 65, 2008.

[16] D. G. Dritschel and R. K. Scott. Jet sharpening by turbulent mixing. *Philosophical Transanctions of the Royal Society of London A: Mathematical, Physical and Engineering Sciences*, 369, 2011.

[17] T. J. Dunkerton and R. K. Scott. A barotropic model of the angular momentum-conserving potential vorticity staircase in spherical geometry. *J. Atmos. Sci.*, 65, 2008.

[18] M. Frigo and S. G. Johnson. *FFTW user's manual*. Massachusetts Institute of Technology, 1999.

[19] A. E. Gill. *Atmosphere-Ocean Dynamics*. Academic Press, 1982.

[20] D. Gottlieb and S. A. Orszag. *Numerical Analysis of Spectral Methods: Theory and Applications*. SIAM, 1977.

[21] J. F. Hawley, C. F. Gammie, and S. A. Balbus. Local three-dimensional magnetohydrodynamic simulations of accretion disks. *Astrophys. J.*, 440, 1995.

[22] P. H. Haynes, D. A. Poet, and E. F. Shuckburgh. Transport and mixing in kinematic and dynamically consistent flows. *J. Atmos. Sci.*, 64, 2007.

[23] W. Lyra, A. Johansen, H. Klahr, and N. Piskunov. Global magnetohydrodynamical models of turbulence in protoplanetary disks. *Astronomy and Astrophysics*, 479, 2008.

[24] M. S. Miesch and J. Toomre. Turbulence, magnetism, and shear in stellar interiors. *Annual Review of Fluid Mechanics*, 41, 2009.

[25] H. K. Moffat. Transport effects associated with turbulence with particular attention to the influence of helicity. *Rep. Prog. Phys.*, 46, 1983.

[26] N. Nakamura and D. Zhu. Formation of jets through mixing and forcing of potential vorticity: analysis and parameterization of beta-plane turbulence. *J. Atmos. Sci.*, 67, 2010.

[27] NASA, ESA, M. H. Wong, A. A. Simon-Miller, H.B. Hammel, and Jupiter Impact Science Team. Hubblesite - newscenter - mysterious flash on jupiter left no debris cloud (06/16/2010) - release images, June 2010.

[28] A. P. L. Newton and E. Kim. Resonance enhanced turbulent transport. *Phys. Plasmas*, 14, 2007.

[29] A. P. L. Newton and E. Kim. Investigation into the dual role of shear flow in 2d mhd turbulence. *Phys. Rev.*, 102, 2009.

[30] A. P. L. Newton and E. Kim. A generic model for transport in turbulent shear flows. *Phys. Plasmas*, 18, 2011.

[31] A. P. L. Newton, E. Kim, and H. L. Liu. On the self-organizing process of large scale shear flows. *Phys. Plasmas*, 20, 2013.

[32] W. M. Orr. The stability or instability of the steady motions of a liquid, parts i and ii. *Proceedings of the Royal Irish Academy, Section A*, 27, 2007.

[33] J. Pedlosky. *Geophysical Fluid Dynamics*. Springer, 1987.

[34] P. B. Rhines. Waves and turbulence on a beta-plane. *J. Fluid Mech.*, 69, 1975.

[35] R. K. Scott and D. G. Dritschel. The structure of zonal jets in geostrophic turbulence. *J. Fluid Mech.*, 711, 2012.

[36] R. K. Scott and L. M. Polvani. Forced-dissipative shallow-water turbulence on the sphere and the atmospheric circulation of the giant planets. *J. Atmos. Sci.*, 64, 2007.

[37] J. V. Shebalin, W. H. Matthaeus, and D. Montgomery. Anisotropy in mhd turbulence due to a mean magnetic field. *J. Plasma Phys.*, 29, 1983.

[38] A. P. Showman. Numerical simulations of forced shallow-water turbulence: Effects of moist convection on large-scale circulation of jupiter and saturn. *J. Atmos. Sci.*, 64, 2007.

[39] K. S. Smith. A local model for planetary atmospheres forced by small-scale convection. *J. Atmos. Sci.*, 61, 2004.

[40] K. Srinivasan and W. R. Young. Zonostrophic instability. *J. Atmos. Sci.*, 69, 2012.

[41] G. R. Stuhne. One-dimensional dynamics of zonal jets on rapidly rotating spherical shells. *Physica D: Nonlinear Phenomena*, 149, 2001.

[42] S. M. Tobias, K. Dagon, and J. B. Marston. Astrophysical fluid dynamics via direct statistical simulation. *Astrophys. J.*, 727, 2011.

[43] S. M. Tobias, K. Dagon, and J. B. Marston. Zonal flow suppresion on a turbulent magnetised beta-plane. Unpublished results received via personal correspondance., 2013.

[44] S. M. Tobias, P. H. Diamond, and D. W. Hughes. β- plane magnetohydrodynamic turbulence in the solar tachocline. *Astrophys. J.*, 667, 2007.

[45] G. K. Vallis. *Atmospheric and Oceanic Fluid Dynamics*. Cambridge University Press, 2006.

[46] G. K. Vallis and M. E. Maltrud. Generation of mean flows and jets on a beta plane and over topography. *Journal of Physical Oceanography*, 23, 1993.

[47] E. S. Warneford and P. J. Dellar. Thermal shallow water models of geostrophic turbulence in jovian atmospheres. *Phys. Fluids*, 26(016603), 2014.

[48] F. M. White. *Viscous Fluid Flow*. McGraw-Hill, 2nd edition, 1991.

[49] R. D. Wordsworth. A phase-space study of jet formation in planetary-scale fluids. *Phys. Fluids*, 21(056602), 2009.